Parson, L., Hawkins, J., Allan, J., et al., 1992
Proceedings of the Ocean Drilling Program, Initial Reports, Vol. 135

9. SITE 839[1]

Shipboard Scientific Party[2]

HOLE 839A

Date occupied: 15 January 1991

Date departed: 17 January 1991

Time on hole: 1 day, 17 hr, 55 min

Position: 20°41.531′S, 176°46.492′W

Bottom felt (rig floor; m, drill-pipe measurement): 2628.5

Distance between rig floor and sea level (m): 11.14

Water depth (drill-pipe measurement from sea level, m): 2617.4

Total depth (rig floor; m): 2846.70

Penetration (m): 218.20

Number of cores (including cores with no recovery): 25

Total length of cored section (m): 218.20

Total core recovered (m): 98.1

Core recovery (%): 45.0

Oldest sediment cored:
Depth (mbsf): 206.00
Nature: vitric sand and silt
Earliest age: late Pliocene
Measured velocity (km/s): 2.0–2.2

Hard rock:
Depth (mbsf): 206.00
Nature: sparsely phyric olivine basalt
Measured velocity (km/s):

HOLE 839B

Date occupied: 17 January 1991

Date departed: 23 January 1991

Time on hole: 6 days, 9 hr

Position: 20°42.539′S, 176°46.501′W

Bottom felt (rig floor; m, drill-pipe measurement): 2628.5

Distance between rig floor and sea level (m): 11.20

Water depth (drill-pipe measurement from sea level, m): 2617.3

Total depth (rig floor; m): 3145.70

Penetration (m): 517.20

Number of cores (including cores with no recovery): 45

Total length of cored section (m): 356.6

Total core recovered (m): 25.2

Core recovery (%): 7.1

Oldest sediment cored:
Depth (mbsf): 257.00
Nature: clayey nannofossil ooze with foraminifers and glass
Earliest age: late Pliocene
Measured velocity (km/s): 1.9

Hard rock:
Depth (mbsf): 214.00
Nature: aphyric basalt
Measured velocity (km/s): 3.73–4.91

Basement:
Depth (mbsf): 266.00
Nature: aphyric basalt
Measured velocity (km/s): 4.31

Principal results. Site 839 is situated in the central Lau Basin about 225 km east of the axis of the Lau Ridge (the remnant arc) and approximately 70 km west of the Eastern Lau Spreading Center (ELSC). The site is located in an irregular, elongated basin that trends northeasterly and is about 11 km wide at the 2500-m isobath. The basin extends to the northeast beyond the area for which we have bathymetric data, but is at least 15 km long. The basin is segmented into a western part with maximum depths of about 2600 m and an eastern part with depths down to nearly 2800 m. The age of the crust at Site 839 was estimated to be about 2 m.y. old on the basis of regional patterns of magnetic anomalies. The scientific objectives for the site were to core the sediment column and to sample the igneous basement, with the goal of interpreting the geologic history of this part of the Lau Basin. A summary of some of the results of the coring at Site 839 is in Figure 1.

The sedimentary sequence at Site 839 consists of clayey nannofossil ooze, turbiditic glass-rich sands and silts, pumiceous volcaniclastic gravels, and rare pyroclastic air-fall ashes. Three major units were recognized on the basis of changes in lithology, in particular on the presence or absence of volcaniclastic sands and silts. Unit I (middle Pleistocene) comprises 17.85 m of iron-oxyhydroxide-stained clayey nannofossil ooze with occasional layers of vitric sand and silt. Unit II (late Pliocene) is 81.65 m thick and is distinguished from Unit I by its very high content of volcaniclastic material. It comprises thick to very thick-bedded vitric sands and silts (turbidites) with some interbeds of clayey nannofossil ooze. The unit is subdivided into six subunits with upward-fining sedimentary cycles. Unit III groups all sediments below 99.5 mbsf. It comprises late Pliocene nannofossil clays, clays, vitric silts and sands, and volcanic gravel. Poor core recovery did not allow further separation of the unit.

The biostratigraphic and paleomagnetic studies were key factors in interpreting the history of the Lau Basin as recorded at Site 839. The calcareous nannofossils and planktonic foraminifers range in age from the middle Pleistocene to the late Pliocene (CN14b–CN12d). The Pliocene/Pleistocene boundary occurs in Core 135-839A-7H. The remainder of the sedimentary sequence at the site is late Pliocene. Microfossils from the sediment in Section 135-839B-10R-CC, 6 m above igneous Unit 2 in Hole 839A, are latest Pliocene (CN13b) in age. Sample 135-839B-17R-CC immediately overlies basalts of Unit 2 in Core 135-839B-18R and is late Pliocene in age (CN12d). Sediments younger than middle Pleistocene were not recovered in the drilling operation.

The sedimentary accumulation rates at Site 839 varied widely and show a correlation to the abundance of ash beds. In the lower part of the sequence (213.5–56 mbsf), where the main ash beds are found, the rate is 882 mm/k.y. Between 56 and 25 mbsf, the rate decreases to about 51 mm/k.y. In this range the ash beds are thinner. Above 25 mbsf, where ash beds are rare, the rate is 9 mm/k.y.

Magnetic polarity measurements of sediments show normal polarity intervals (at 0–16, 35.2–38.3, and 40.9–41.4 mbsf) corresponding to the Brunhes Chron (0–0.73 Ma), the Jaramillo Subchron (0.91–0.98

[1] Parson, L., Hawkins, J., Allan, J., et al., 1992. *Proc. ODP, Init. Repts.,* 135: Ocean Drilling Program (College Station, TX).
[2] Shipboard Scientific Party is as given in the list of participants preceding the contents.

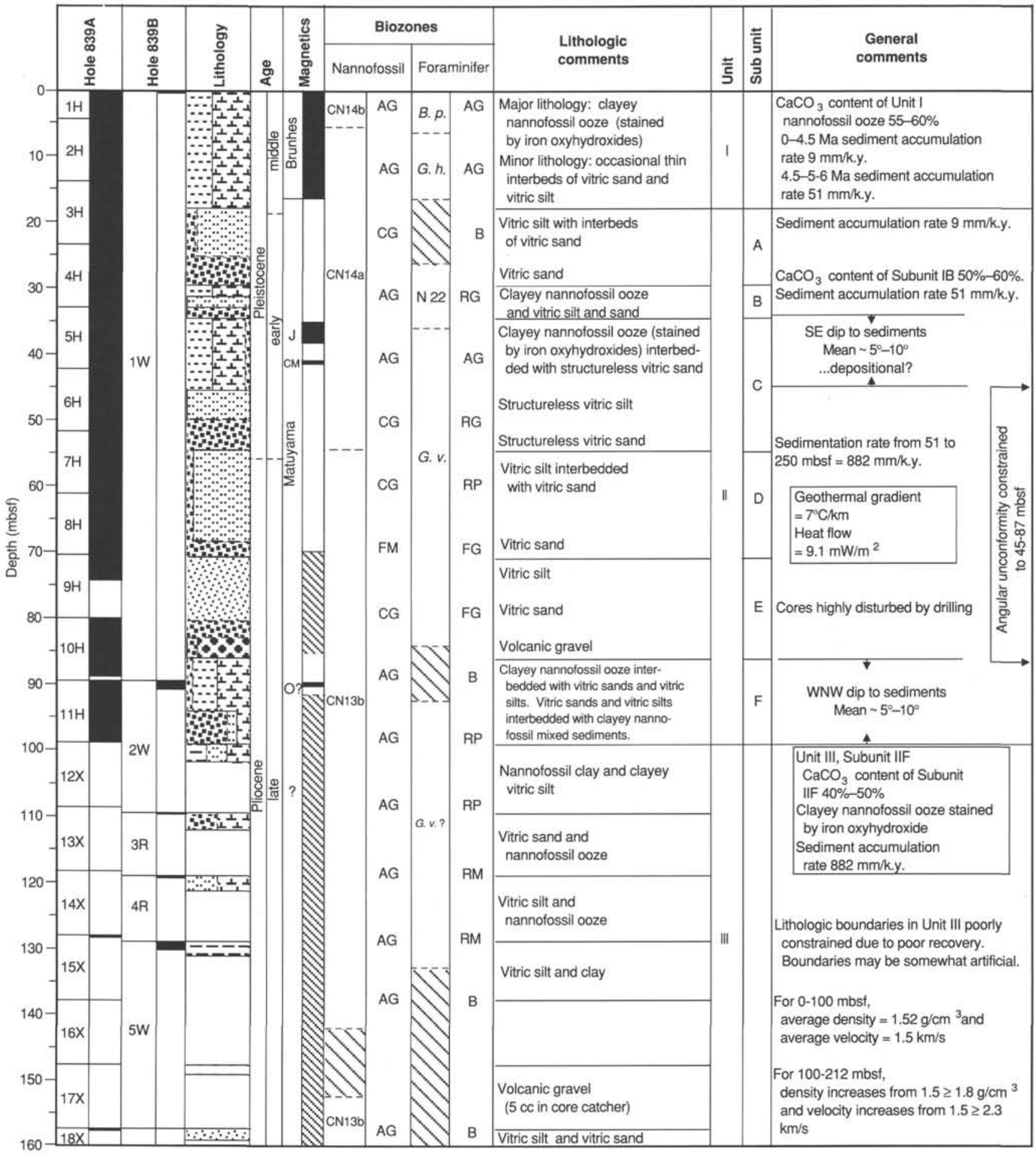

Figure 1. Site summary figure for Site 839. Abbreviations for abundance are as follows: A = abundant, C = common, F = few, and R = rare, and B = barren. Those for preservation are as follows: G = good, M = moderate, and P = poor. Planktonic foraminifer zones are abbreviated as follows: *B. p.* = *Bolliella praeadamsi*, *G. h.* = *Globorotalia crassaformis hessi*, *G. v.* = *Globorotalia crassaformis viola*, and *G. q. f.* = *Globigerinoides quadrilobatus fistulosus*.

Ma), and the Cobb Mountain Event (1.12 Ma). Lower in the core, another normal polarity interval was found and is interpreted to be either the Olduvai Subchron (1.66–1.88 Ma) or the Réunion Subchron (2.01–2.14 Ma). The paleomagnetic studies of basalt and basaltic andesite recovered from between 256 and 213 mbsf yielded anomalously low inclinations (between –5° and 15°), suggesting that they cooled during a magnetic polarity transition. A sediment layer beneath these lavas at about 257 mbsf has reversed polarity; lavas from still deeper levels have normal polarity. Biostratigraphic data constrain the reversely polarized sediments to the Matuyama Chron between the Olduvai and Réunion subchrons. Thus, at the deepest level, normally polarized basaltic andesites are likely to represent either the Réunion Subchron (2.01–2.14 Ma) or the Gauss Chron (2.48–2.92 Ma). The magnetic susceptibility record appears to be a good indicator of major

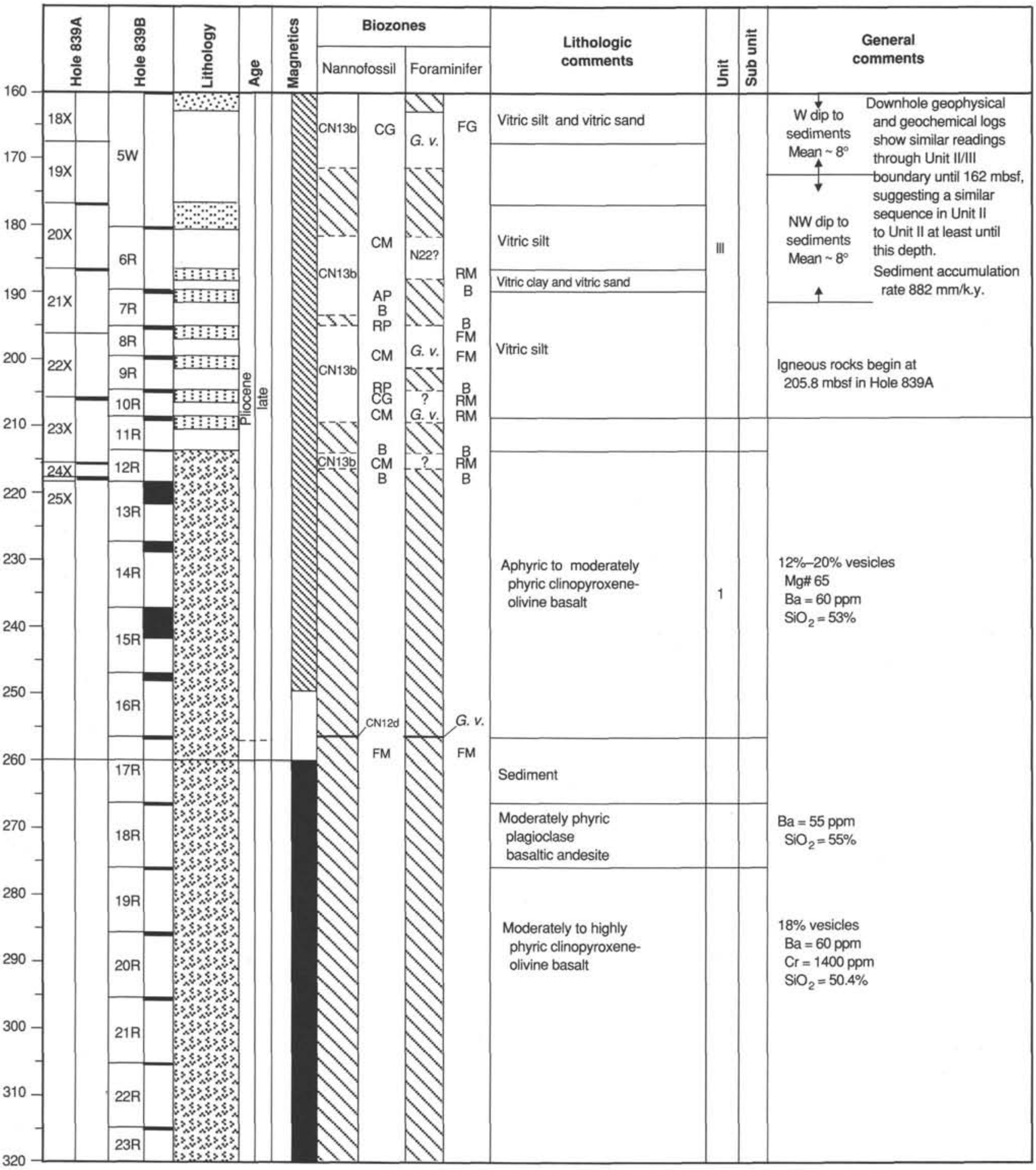

Figure 1 (continued).

ash layers. As at previous sites, cyclic variations in the modified Q-ratio (1-mT alternating-field-cleaned remanent intensity/susceptibility) may indicate a Milankovitch climatic cyclicity present in the nannofossil ooze sediments.

Hydrocarbon analyses of the core showed only background levels as at the other sites. Analyses of the pore-water fluids showed that, except for dissolved Mn, they were indistinguishable from average seawater and are like the values for the other sites. The Mn concentrations showed an initial downcore increase, reaching a maximum value at 48.5 mbsf, before decreasing downcore again toward the base of the sediment.

Igneous rocks that form the basement to the sedimentary section were recovered between 205.85 and 497.26 mbsf. The hole was terminated because of drilling difficulties at 497.26 mbsf. Chilled margins and quenched mineral textures suggest that many of the cooling units recovered were parts of extrusive flows and pillow complexes. All of the rocks recovered are highly vesicular (10%–25%), attesting to their high volatile content at the time of eruption.

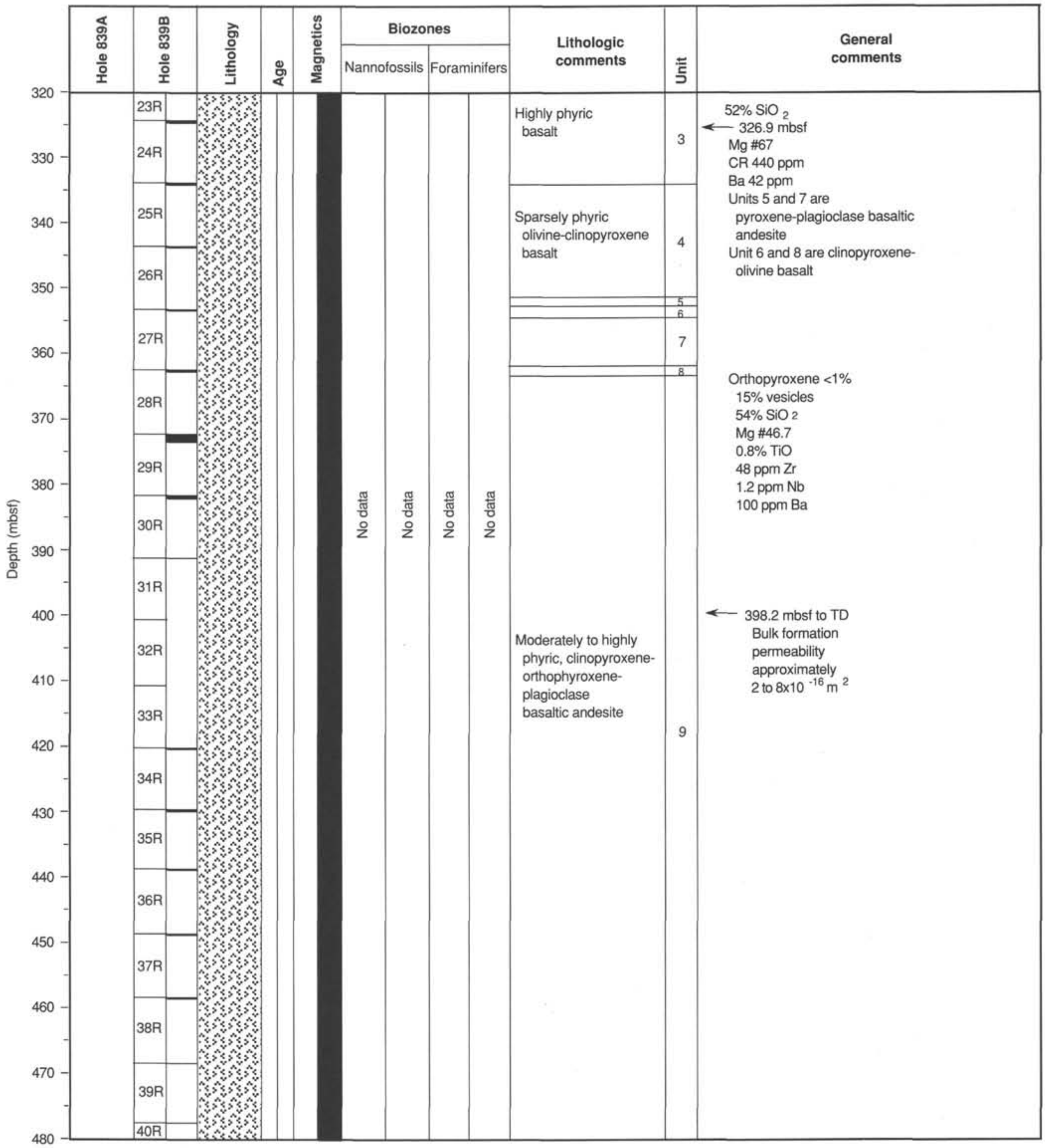

Figure 1 (continued).

Two main petrologic varieties are present; olivine and clinopyroxene phyric basalt and orthopyroxene-clinopyroxene-plagioclase phyric basaltic andesite. The latter type was not encountered at any of the other sites. Nine units were recognized on the basis of texture, mineralogy, and mineral proportions. The lowermost part of the section recovered comprises a series of flows of moderately to highly phyric clinopyroxene-orthopyroxene-plagioclase basalts having high ratios of plagioclase to pyroxene. They resemble many of the rocks of the Tofua Arc. These are overlain by three major eruptive units comprising numerous flows of very Mg-rich, aphyric to highly phyric, clinopyroxene-olivine basalts with minor interbeds of basaltic andesite and very rare sediment layers. The overall geochemical signature of the entire mafic rock series at Site 839 has many similarities to island-arc tholeiite magmas. Some of the basalts have very high concentrations of Mg, Cr, and Ni and are the most primitive igneous rocks found in the Leg 135 cores. They may represent near-parental (primary?) magmas for some of the volcanic units in the Lau Basin that have an arclike geochemical signature.

Physical properties of the sediments show a good correlation with lithologic types. A cyclical change in grain-size results is mirrored in increasing density and decreasing water content, porosity, and void ratio. The *P*-wave logger, compressional wave velocity data varies with the alternation of silts and sands interbedded with the dominant nannofossil ooze. There is also an excellent correlation between grain density and velocity in the basalt samples, but the correlation between bulk density and velocity is poor. This may be because of the random distribution of vesicles. The temperature gradient of 7.1°C/km, and the derived heat-flow value of 9.3 W/m^2, are the lowest values measured in the Lau Basin during Leg 135.

Bathymetric profiles show that Site 839 is situated in a basin that is bounded on the northwest by a 200–300-m-high, northeast-trending scarp. This feature is clearly visible on GLORIA sidescan sonar records. Seismic reflection profiles suggest that the scarp is coincident with a fault zone, and seismic profile data clearly show an angular unconformity within the sedimentary fill of the basin. The lowermost identifiable reflectors dip at about 4° toward the northwest and are onlapped from the west by a second seismic unit. This whole lower section is overlain by a "drape" of reflectors that extends up to the seafloor, which is itself apparently inclined at about 1° toward the northwest.

Bedding orientations were measured in cores from both holes in the interval between 0 and 250 mbsf. Dips were recorded mainly from bases of individual volcaniclastic turbidite horizons; many of these have erosive bases and some component of depositional dip may be included in the dip measurements. The sediments between 30 and 50 mbsf have an average southeasterly dip of about 7.4°. Between 90 and 100 mbsf, the average dip is about 9.6° to the west or west-northwest. This change in dip direction may correspond to the unconformity observed in the seismic data. A possible candidate for the sedimentary horizon marking the base of the unconformity is a 5-m-thick zone of poorly sorted volcanic gravel at 82–87 mbsf. The gravel deposit and oozes beneath it are all of uppermost Pliocene age (nannofossil Subzone CN13b).

BACKGROUND AND OBJECTIVES

Background

Location and Bathymetry

Site 839 is in the central Lau Basin at 20°42.5′S, 176°46.5′W. This is about 225 km east of the Lau Ridge remnant arc and approximately 55 km west of the axial rift zone of the ELSC (Fig. 2). The ELSC is the presently active site of generation of new backarc basin crust at the latitude of the drill site. Site 839 is located in a region of north to northeasterly trending ridges and deeps interpreted as horsts and grabens or half-grabens (Parson et al., this volume). The site was selected in the hope that it would yield data on a part of the Lau Basin crust that had been estimated to be intermediate in age between the oldest backarc crust (e.g., Site 834) and young crust formed at the axial rift of the ELSC.

The bathymetric relief in the area is about 500–600 m, with ridges shoaling to <2200 m, rising above basins that can exceed 2800 m depth. In this discussion, we will use the term "Basin 839" for the irregularly shaped, narrow, linear, sedimented trough in which the site is located. Basin 839 is at least 15 km long in a northeast-southwest direction and about 5 km wide at its maximum northwest-southeast dimension (Fig. 3). Basin 839 is separated from Basin 838 by an east-facing scarp that strikes north-south. On GLORIA sidescan sonar records the scarp appears to truncate the northeast-southwest lineaments defined by the ridge-basin topography of the area.

Geologic Setting

Site 839 is located on crust estimated to be <1 m.y. old because it is approximately along-strike from lineated crustal fabric at Site 836 identified as having been formed in the Brunhes magnetic epoch (<0.7 Ma). Magnetic profiles have proved inconclusive in interpreting the regional tectonic/magnetic fabric. Two general trends are suggested by the sketch map showing an interpretation of the morphology and tectonic features near Site 839 in Figure 4. East of 177°W, including the area of Basin 839, there is a pronounced northeast trend to the anomalies; west of 177°W the pattern is less distinct because of a lack of data, but there is a suggestion of a more northerly trend to the anomalies. As discussed in the "Introduction and Principal Results" chapter (this volume), these northerly trends may not represent magnetic anomalies generated by seafloor spreading.

Although no samples of the crust had been collected near this site, it was assumed that the seafloor would be basalt overlain by a thin cover of clayey carbonate ooze. The site lies between the active axial zone of the ELSC, where tholeiitic basalt is erupted, and the western Lau Basin where rocks intermediate in composition between arclike and MORB-like have been recovered (see discussion in the "Background and Objectives" section, "Site 836" chapter, this volume). Thus, it seemed likely that Site 839 igneous rocks would show some affinity to arc samples.

Regional Structural Synthesis

The regional structural setting has been interpreted using good coverage with GLORIA data combined with limited SeaBeam and single-channel seismic records (Parson et al., 1990; Hawkins, 1976). The pre-drilling survey tracks used and resulting profiles are shown in Figures 5 and 6. Basin 839 is constrained on the northwest by a major fault scarp that dips to the east southeast. As described above, an east-facing scarp separates Basin 839 from Basin 838 that lies to the west. On the east side, the basin is cut by another steep, easterly dipping normal fault. This latter fault drops about 100 m into a flat-bottomed, channel-like structure about 3 km wide (Fig. 6).

Estimates of the age of the crust in this area have been summarized in the "Introduction and Principal Results" chapter (this volume) and are discussed in more detail in the "Background and Objectives" sectionof the Site 836 chapter.

Seismic Stratigraphy

Before drilling, seismic profiler records were interpreted using average seismic velocity values as determined from traveltimes and actual depths to horizons encountered drilling earlier sites on this leg. For post-drilling interpretations, we were able to correct our estimates by using additional seismic velocities obtained from downhole measurements and direct physical properties measurements. As at several of the previous sites, we recognized seismic Units A and B and an acoustic basement referred to as Unit C (see Figs. 6 and 7; also see the "Introduction and Principal Results" chapter, this volume). We estimated acoustic basement to be at a depth of 213 m, based on an average velocity of 1700 m/s, and a basement depth of around 0.25 s two-way traveltime (TWT; Fig. 7). The 3.5-kHz profiler records across the channel floor indicate a hard, strongly reflective surface indicative of a scoured channel floor, or one filled with sands or gravels. No correlation can be made between the 3.5-kHz records and variations in surface backscattering on the GLORIA images. The floor of the basin slopes toward the northwest at an average angle of about 1°. The seismic reflection profiler recorded a complex internal structure that suggests several episodes of basin faulting and sedimentation. The rotated downdropped basement block (seismic Unit C) dips northwesterly at about 4° and is covered by a sequence of parallel-bedded planar reflectors approximately 0.12 s TWT thick. These we tentatively interpret as equivalent to seismic Unit B. Overlying this unit is a westerly onlapping sequence of beds, approximately 0.1 s TWT thick (Fig. 7). The basal part of this sequence is an acoustically semitransparent wedge, pinching out on the basal unit with a sharp angular unconformity. Thus, this sequence of flat-lying reflectors that we refer to as seismic Unit A suggests a gradual sediment fill of a rapidly formed half-graben, rather than syntectonic deposition that would have been likely to

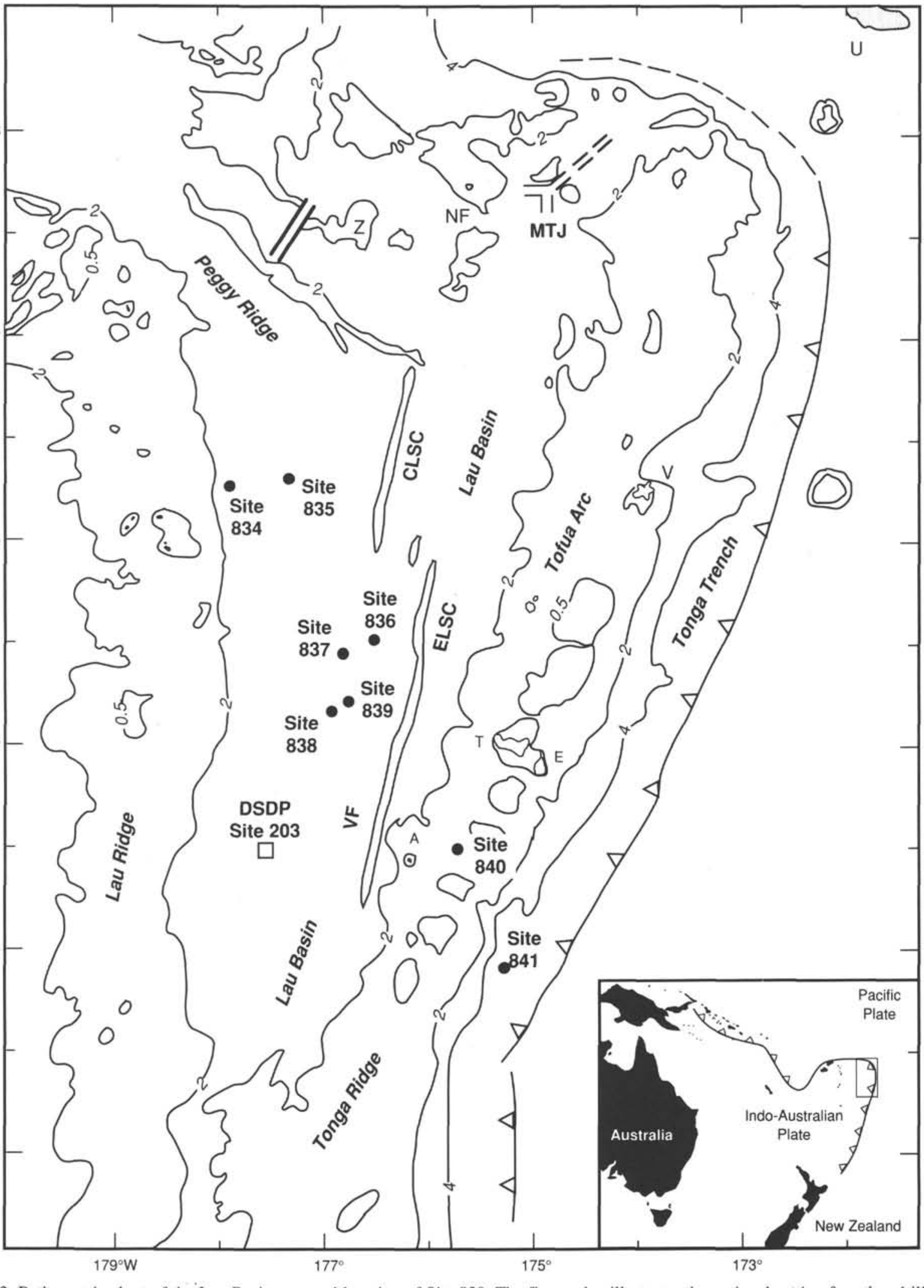

Figure 2. Bathymetric chart of the Lau Basin area and location of Site 839. The figure also illustrates the regional setting for other drill sites in the Lau Basin and the major geologic features of the Tonga Trench and Lau Basin system. Z = Zephyr Shoal; islands shown are T = Tongatapu, E = 'Eua, V = Vavau, NF = Niua Fo'ou, A = Ata, and U = Upolu. Locations of the Central Lau (CLSC) and Eastern Lau (ELSC) spreading centers, Valu Fa (VF) Ridge, and Mangatolu Triple Junction (MTJ) are from von Stackelberg (1990), Parson et al. (1990), Hawkins et al. (1989), and Nilsson et al. (1989). The location of DSDP Site 203 is shown as an open square. Contour intervals in thousands of meters.

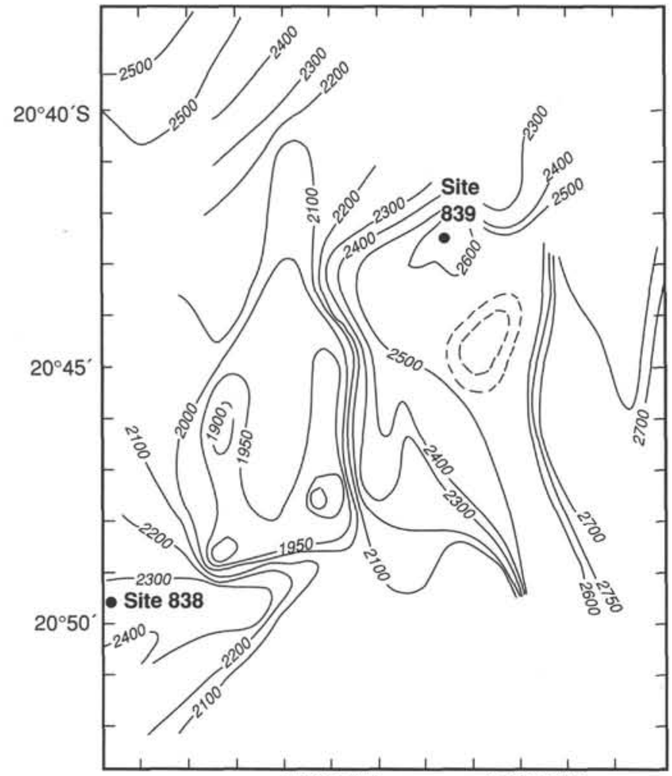

Figure 3. Detailed bathymetry based on SeaBeam and GLORIA imagery for the area near Site 839. Contours in meters below sea level.

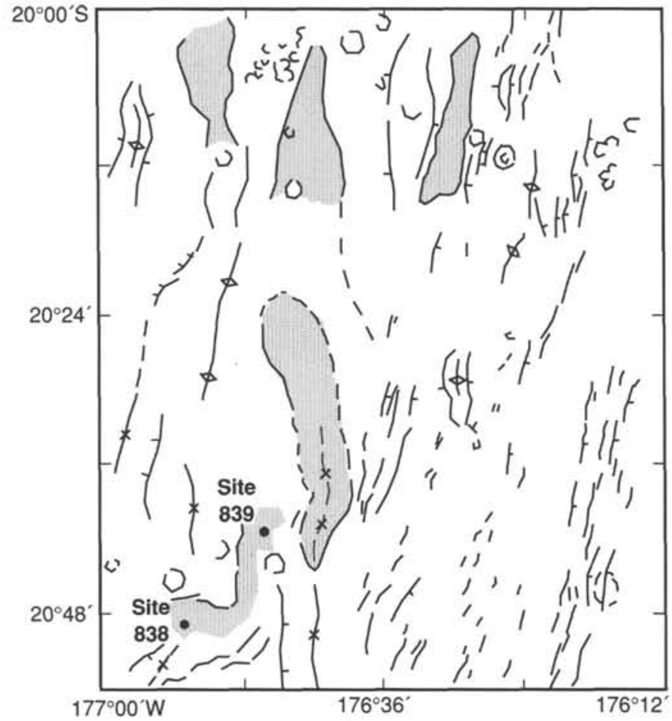

Figure 4. Sketch map of morphologic and tectonic features near Site 839. Stippled area denotes planar, flat-lying sediments without surface faulting.

form nonparallel sequences against a growth fault. A 0.07-s-TWT-thick, parallel-bedded unit, which covers both the basement highs and the basin floor as a pelagic drape and is correlated with seismic Unit A, overlies and is conformable with the upper surface of the onlap unit. A more detailed discussion of the sub-bottom structure appears in the "Structural Studies" section.

A seismostratigraphic interpretation for Site 839 is given in Figure 7B.

Scientific Objectives

The primary objectives of Site 839 were the same as those for Site 836 and the other central Lau Basin sites. These are discussed in the "Background and Objectives" section for Site 836 (this volume).

OPERATIONS

Introduction

The 24-nmi transit from Site 838 to Site 839 began at 0615 UTC, 15 January 1991, and took 4.3 hr at an average speed of 5.6 kt. Site 839 shared the same objectives as Site 838 and was cored primarily to reach the basement objectives missed at Site 838 because of hole termination caused by very poor sediment recovery.

Site Approach and Site Survey

Site 839 is situated in the central Lau Basin at approximately 20°42.5'S, 176°46.5'W, about 75 km west of the ELSC. It is located in a north-trending basin, 5 km wide and at least 15 km long, which we refer to as Basin 839. This narrow depression is one of many north- to northeast-trending fault basins occurring in this portion of the Lau Basin. Site surveys for Site 839 were completed in two stages. The first, a reconnaissance program, took place between 1030 and 1400 UTC, 10 January 1991, during the seismic survey for Site 838 (Fig. 5B). The second survey was completed immediately before the site approach and occupation of Site 839, and took place between 0800 and 1030 UTC, 15 January 1991 (Fig. 5C).

After slowing to deploy two 80-in.[3] water guns, a single-channel 60-element Teledyne streamer, and a Geometrics 801 proton precession magnetometer, the ship completed this second pre-site survey, crossing the site twice (Fig. 5C). After the second crossing, the ship made a Williamson turn and adopted a reciprocal course to mark the site; a beacon was dropped at 0945 UTC (Fig. 6). Underway geophysical gear was recovered immediately afterward, with the ship returning to the site to begin coring operations. The geophysical data from these surveys have been combined with existing single-channel seismic profiles and long-range sidescan sonar to produce a morphotectonic framework for the site (Fig. 4).

Drilling and Logging Summary

Our original plan was to drill two adjacent holes at Site 839, with the principal objective of reaching more than 50 m into basement. Hole 839A was planned to be an APC/XCB/MDCB hole, with the goal of obtaining as complete and relatively undisturbed a sediment section from the site as possible. It was hoped that the motor-driven core barrel (MDCB) would sample a short section of basement underlying the sedimentary section, estimated from the 0.25-s two-way traveltime to be about 200 m thick. Hole 839B was to be a rotary core barrel (RCB) hole that washed through most of the sediments, beginning coring just above the sediment/basement interface and continuing to 200-m basement penetration or drill-bit destruction. Hole 839B would then be logged. After logging had determined that acceptable hole conditions existed, a packer experiment was planned that, if successful,

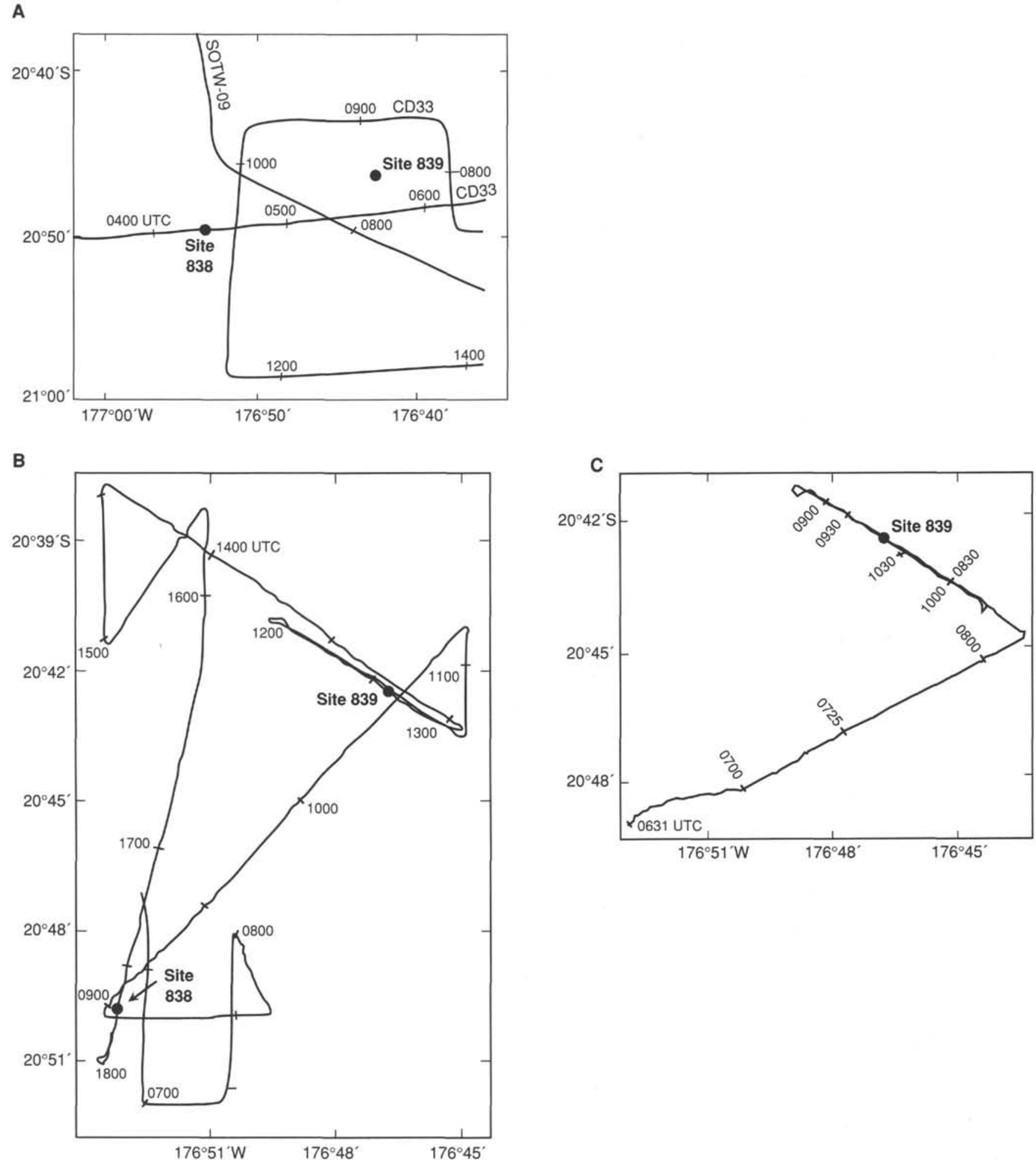

Figure 5. Track charts showing the locations of the seismic lines used to select Site 839. **A.** Tracks available before Leg 135, taken from *Charles Darwin* (CD33; Parson et al., 1989) and SOUTHTOW cruise (SOTW-9; Hawkins, 1976). **B.** *JOIDES Resolution* tracks with seismic reflection profiles recorded during site survey. **C.** Approach of *JOIDES Resolution* to Site 839.

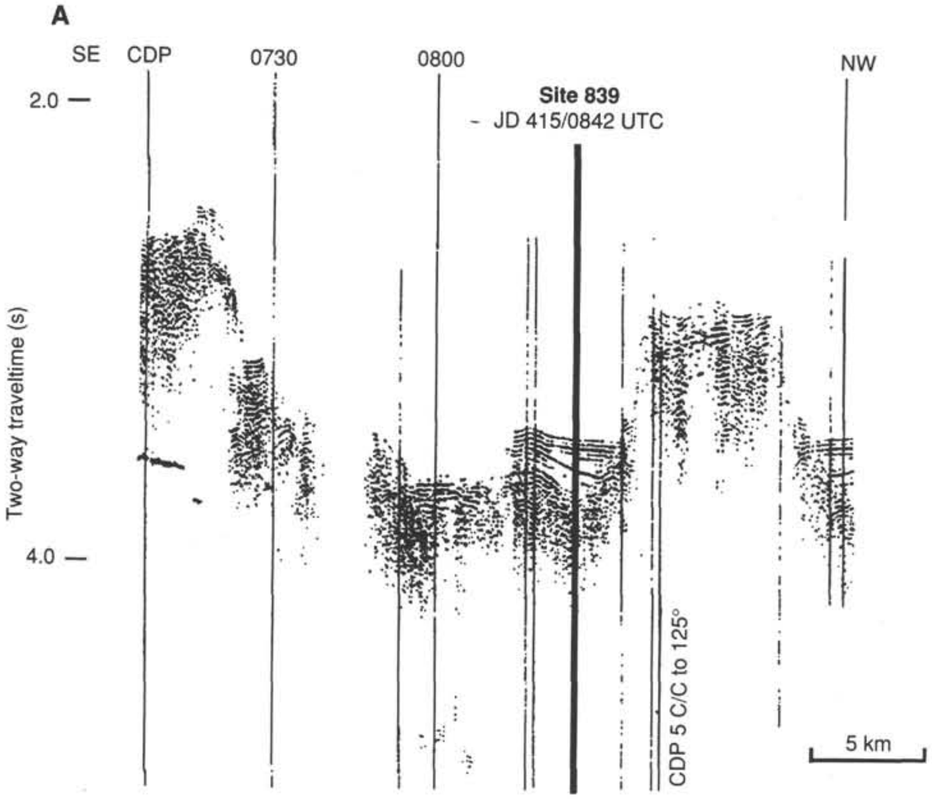

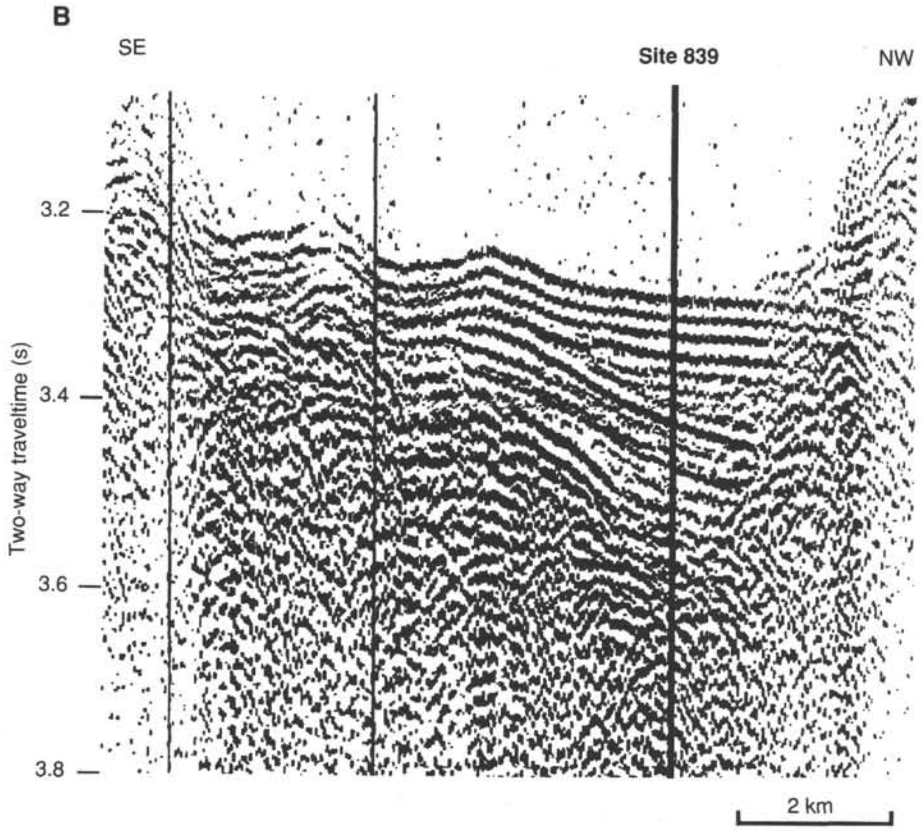

Figure 6. **A.** Seismic reflection profile recorded by *JOIDES Resolution* across Site 839, illustrating fault-bounded position of sedimentary basin and the location of down-dropped "channel" east of Site 839. **B.** Enlarged portion of the seismic reflection profile across Site 839, illustrating seismic stratigraphy of the basin.

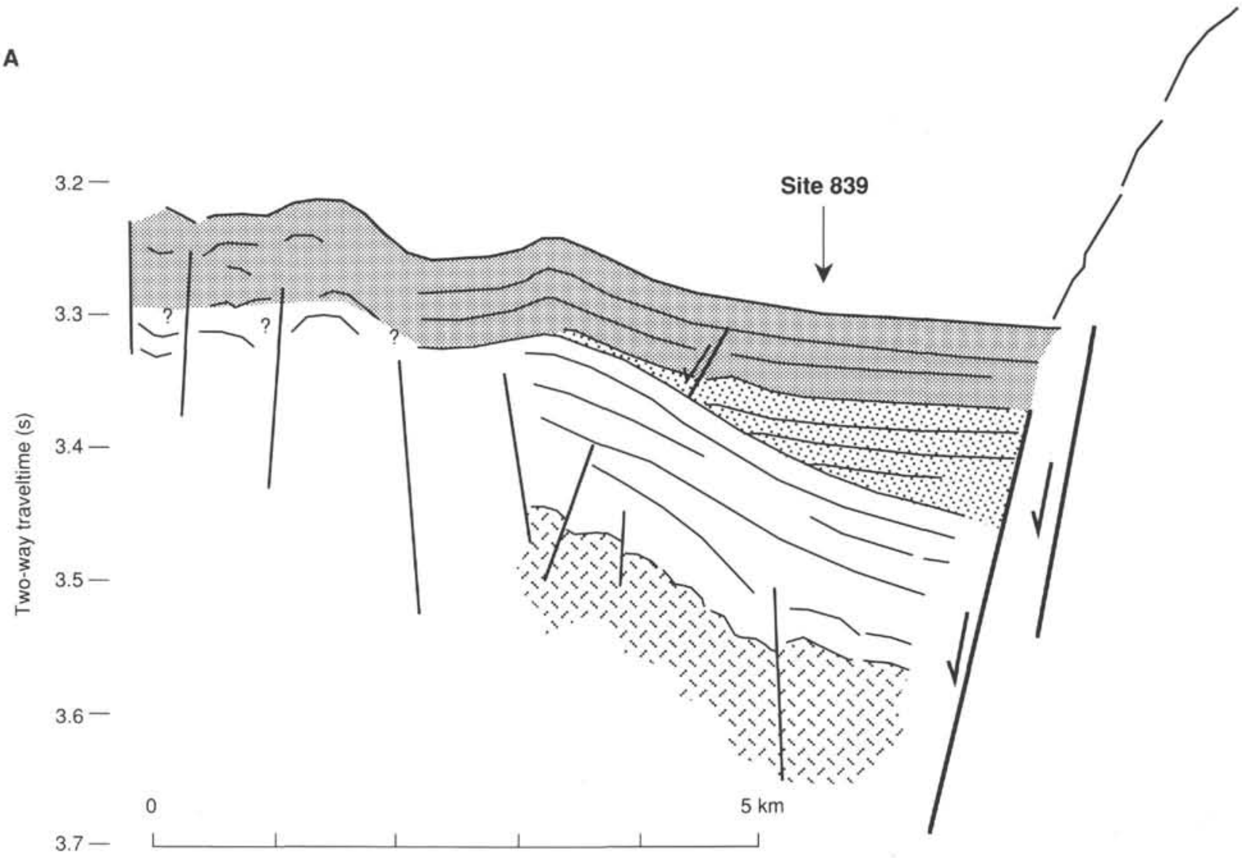

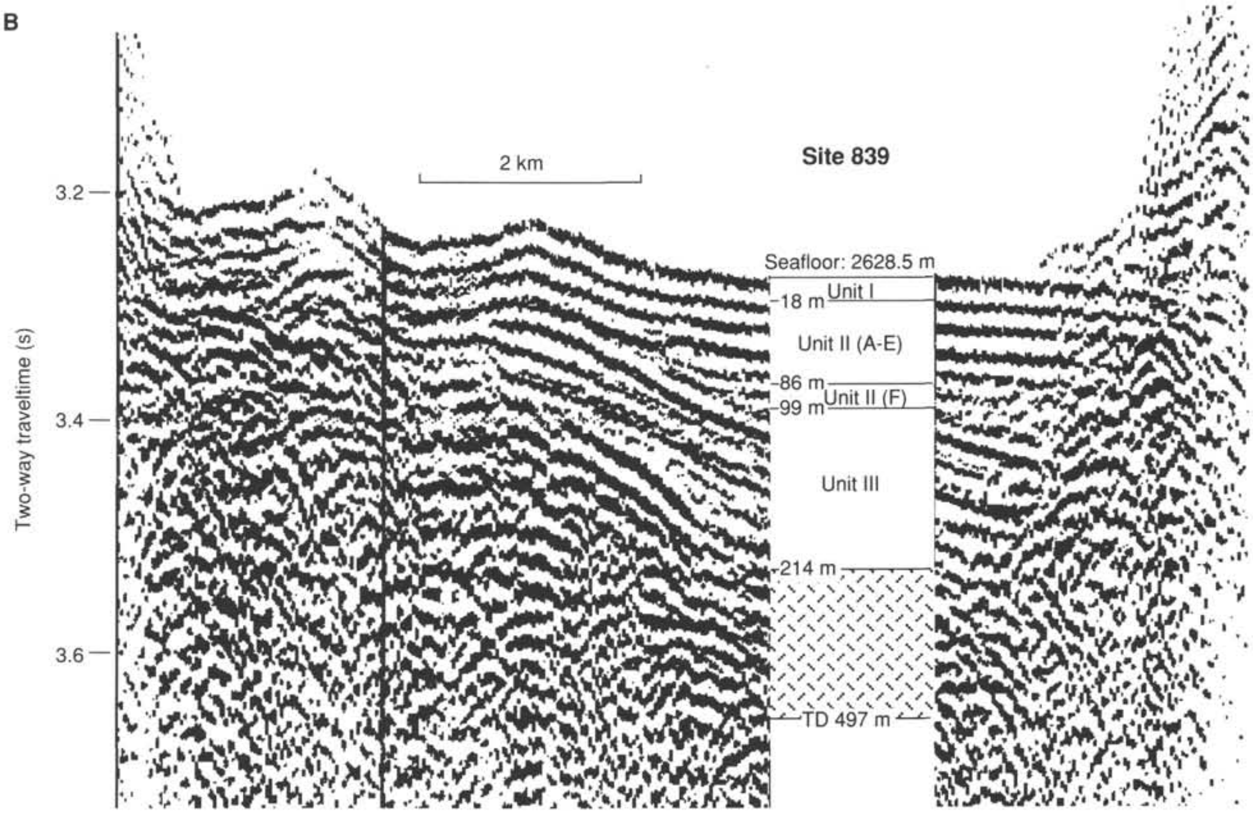

Figure 7. **A.** Line drawing interpretation of the seismic profile in Figure 6B. Dashed ornament marks Seismic Unit C (acoustic basement); unornamented sediments are probably Seismic Unit B; stipple marks lower sediment fill of half graben by Seismic Unit A′; dark stipple locates Seismic Unit A. **B.** Seismostratigraphic interpretation of seismic reflection profile presented in Figure 6B. TD = total depth.

would provide the first bulk crustal permeability measurements from a backarc setting.

Hole 839A

Hole 839A was spudded in at 1623 UTC, 15 January 1991, at a position of 20°42.531′S, 176°46.492′W. A mud-line core established the seafloor depth as 2628.5 m below the driller's datum. Eleven cores were taken with the advanced hydraulic piston corer (APC), to a depth of 99.5 mbsf. A nonmagnetic drill collar was used to minimize the drill-string magnetic overprint on the cores. The multishot tool provided orientation data for Cores 135-839A-4H and -11H, and temperature measurements were made at 33.0, 52.0, 71.0, and 90.0 mbsf using the WSTP tool. Recovery using the APC was excellent, with 94.4 m recovered (94.9% recovery). Because of stiffening of the sediments, a change was made to the extended core barrel (XCB) at Core 135-839A-12X (Table 1). Thirteen cores of sediments were taken with the XCB, with poor recovery (1.46 m recovered, 2.7% recovery) to a depth of 217.7 mbsf. At 206 mbsf, igneous rocks (basalt) were encountered and the decision was made to continue coring for several basalt cores with the motor-driven core barrel (MDCB) before ending the hole and beginning rotary coring in Hole 839B. Core 135-839A-25N succeeded in recovering 0.45 m of vesicular basalt before failing. There was some uncertainty as to the actual amount of formation penetrated during core cutting, but at least 0.5 m (the official estimate) was cored. During coring, the core bit separated from the core barrel because of overloading, overtorquing, a bit defect, or a combination of these factors. The hole was then abandoned because of blocking by the MDCB bit.

Hole 839B

The ship was moved 20 m to the southwest, and Hole 839B was spudded at 0855 UTC, 17 January 1991, at 20°42.539′S, 176°46.501′W. A 9⅞-in. RCB bottom-hole assembly (BHA) was used. The seafloor was estimated to be at 2628.5 mbrf, and the hole was washed from 0.0 to 110.0 mbsf, recovering two wash cores. Cores 135-839B-3R and -4R were taken from 110.0 to 129.4 mbsf, with 19.4 m cored and 0.49 m recovered (recovery of 2.5%). Another wash core (135-839B-5W) was then taken from 129.4 to 180.0 mbsf. Coring then continued, with Cores 135-839B-6R to -28R taken from 180.0 to 372.6 mbsf, with 192.6 m cored and 21.2 m recovered (recovery of 9.1%). Mud was pumped down the hole after Cores 135-839B-26R and -28R to stabilize the hole. While we recovered Core 135-839B-28R, the drill-string driver motor stalled, and the drill string stuck despite 100,000 lb of overpull. After the drill string was finally worked free, hole conditions steadily deteriorated (probably because of unstable basalt fragments falling into the hole), requiring a wiper trip with the drill string up to 202.5 mbsf to improve the hole. At this point, permission was asked and received for approval to deepen Hole 839B to bit destruction, instead of stopping at 400 mbsf as originally planned. Coring with the RCB continued with Cores 135-839B-30R and -45R taken from 382.2 to 517.2 mbsf, with 135.0 m cored and 1.86 m recovered (1.38% recovery). Mud was pumped downhole with each core to reduce sticking of the drill string. From 400 mbsf to the total depth of 517.2 mbsf, recovery was very poor to none (1.75 m or 1.49% recovery from unstable, fractured, vesicular basalts). Coring was terminated both because of poor hole conditions and to save time for future sites. Overall, 160.6 m was washed, 356.6 m was cored, and 25.1 m was recovered (7.0% recovery) in Hole 839B.

After conditioning the hole for logging with a short trip of the drill string, the bit was dropped with the mechanical bit release (MBR). The open end of the pipe was pulled to 90.0 mbsf, and logs were run as follows:

Run No. 1: Induction/sonic/caliper. The log found bottom 44.3 m above the driller's total depth and required 3.50 hr to run.

Run No. 2: Density/neutron. The log found bottom 46.6 m above the driller's total depth and required 3.75 hr to run.

Run No. 3: Geochemical. The log found bottom 47.9 m above the driller's total depth and required 4.9 hr to run.

Run No. 4: Formation microscanner (FMS)/gamma ray. The log found bottom 51.3 m above the driller's total depth and required 4.23 hr to run.

The logs were then reviewed to determine if suitable seats could be found for the packer measurements. Three potential setting depths were identified, and the decision was made to proceed with the packer measurements. To allow reentry of the drill string, a free-fall funnel (FFF) was dropped at 0750 UTC, January 22. The fifth logging run used the analog borehole televiewer (BHTV), and preparations were made for the packer measurements. The BHTV log found bottom 56.5 m above the driller's datum and required 5.83 hr to run. The BHTV log quality was hampered by a hole enlarged to 14 in. in both sediments and the unstable basalts. The hole was left full of seawater, and the MBR cleared the seafloor at 0308 UTC, January 22, and reached the rig floor at 0725 UTC.

Packer Measurements

A single-element, nonrotating TAMU packer was run into Hole 839B following logging. The objectives of the packer experiment were to measure the bulk permeability and pore pressure in the basalt between the packer element and the bottom of the hole. The plan was to attempt to set the packer at two different depths (three if time and equipment allowed) to determine the permeability changes through the formation.

Rock samples recovered in cores from this hole are highly porous, highly fractured, and highly vesicular basalt. As a result, they were expected to exhibit a high degree of vertical and horizontal permeability. The FMS caliper log and the BHTV monitor were used to identify the smoothest and narrowest portions of the hole. Three packer setting depths were selected in relatively smooth, 11- to 13-in.- wide regions of the hole in basalt.

The packer and drill-string assembly reentered the FFF at 1143 UTC, January 22. After running in of the pipe, the packer was lowered to 398.2 mbsf for the first packer seating. At 1810 UTC, the go-devil with the attached Kuster pressure recorders was dropped. Both recorders were set with 6-hr clocks. Successful inflation and setting of the packer was achieved at 1847 UTC, with a 1500 PSI packer element inflation pressure and 15,000 lb of overlying weight, later raised to 17,000 lb. All signs indicated that the set was good. A pulse test at 500 psi was then run at 1910 UTC, with an immediate decay of pressure to 0 psi. After a 10-min wait, a second pulse test was run at 1000 psi, also showing an immediate decay of pressure to 0 psi. At this point, a packer leak was suspected, but it was decided to run two constant-flow injection tests in the event that highly permeable basalt was taking all of the water being pumped.

The first of these injection tests was run at 50 strokes/min (50 strokes = 250 gal/min or 946.5 L/min) for 41 min (1940–2021 UTC). A flat pressure response was obtained, with no significant rise or drop of pressure in the hole. The pump pressure measured at the drill floor was within the range of 365–375 psi for the entire test after the initial pressure buildup, and pressure decayed to 0 psi when the pumping stopped.

After a 20-min wait to allow borehole pressure to decay, a second, 33-min injection test was run at 100 strokes/min (100 strokes = 500 gal/min or 1893 L/min). As before, a flat pressure response was obtained, with only small rises and drops of pressure

Table 1. Coring summary, Site 839.

Core no.	Date (Jan. 1991)	Time (UTC)	Depth (mbsf)	Cored (m)	Recovered (m)	Recovery (%)	Age
135-839A-							
1H	15	1640	0.0–4.5	4.5	4.53	100.0	middle Pleistocene
2H	15	1715	4.5–14.0	9.5	9.45	99.5	middle Pleistocene
3H	15	1750	14.0–23.5	9.5	9.96	105.0	middle Pleistocene
4H	15	1840	23.5–33.0	9.5	9.53	100.0	
5H	15	2025	33.0–42.5	9.5	9.76	103.0	
6H	15	2110	42.5–52.0	9.5	9.81	103.0	
7H	15	2330	52.0–61.5	9.5	10.10	106.3	upper Pliocene
8H	16	0025	61.5–71.0	9.5	9.50	100.0	upper Pliocene
9H	16	0245	71.0–80.5	9.5	3.91	41.1	upper Pliocene
10H	16	0335	80.5–90.0	9.5	8.90	93.7	upper Pliocene
11H	16	0545	90.0–99.5	9.5	9.67	102.0	upper Pliocene
12X	16	0650	99.5–109.2	9.7	0.34	3.5	upper Pliocene
13X	16	0730	109.2–118.9	9.7	0.00	0.0	
14X	16	0805	118.9–128.5	9.6	0.00	0.0	
15X	16	0850	128.5–138.2	9.7	1.17	12.0	upper Pliocene
16X	16	0940	138.2–147.9	9.7	0.00	0.0	
17X	16	1025	147.9–157.6	9.7	0.01	0.1	upper Pliocene
18X	16	1115	157.6–167.3	9.7	0.36	3.7	upper Pliocene
19X	16	1205	167.3–176.5	9.2	0.00	0.0	
20X	16	1255	176.5–186.2	9.7	0.34	3.5	upper Pliocene
21X	16	1355	186.2–195.9	9.7	0.38	3.9	upper Pliocene
22X	16	1510	195.9–205.6	9.7	0.05	0.5	upper Pliocene
23X	16	1650	205.9–215.2	9.3	0.32	3.4	upper Pliocene
24X	16	1830	215.2–217.7	2.5	0.28	11.2	
25N	16	2120	217.7–218.2	0.5	0.45	90.0	
Coring totals				217.9	98.82	45.4	

in the hole. The pressure was essentially constant throughout the test, mainly between 1365 and 1370 psi. An immediate decay of pressure to 0 psi followed when the pumping stopped. The first packer test ended at 2123 UTC.

The packer was then deflated and unseated while retrieving the go-devil and the attached Kuster pressure gauges. The pressure chart records showed a small increase in pressure during the pulse and injection tests, with a maximum pressure of 33–50 psi over hydrostatic pressure during the 50 strokes/min test, and a constant pressure of 65–71 psi over hydrostatic pressure during the 100 stroke/min injection test. A gradual pressure rise was present on the Kuster chart records for the first injection test and with further analysis should provide a measure of the bulk formation permeability.

The packer was then pulled up to 326.9 mbsf at 0015 UTC, 23 January 1991, for the second seat in basement. The packer was successfully set at an inflation pressure of 1500 psi with 18,000 lb of overlying weight. At 0108 UTC, a pulse test at 500 psi was run, yielding a rapid decay of pressure (to 0 psi in <10 s) after the pumps were turned off. After waiting for 10 min to allow the residual borehole pressure to decay, a second pulse test was run at 1000 psi, again yielding an equally rapid decay of pressure. A packer leak was suspected again, but three constant-flow tests were run in the event that highly permeable basalt was taking all of the pumped water flow.

The first injection test began at 0131 UTC, with the goal of pumping 100 strokes/min (100 strokes = 500 gal/min or 1893 L/min). An immediate pressure buildup to 2530 psi caused the test to be stopped at 50 strokes/min, as the mud pumps are only rated to 3000 psi. There was an immediate decay of pressure to 0 psi when the pumps were shut off. After waiting 20 min for the residual borehole pressure to decay, the second injection test was run at 35 strokes/min (35 strokes = 175 gallons/min or 663 L/min) for 20 min, yielding a flat pressure response of around 1205–1235 psi. After we waited another 20 min to allow the residual borehole pressure to decay, a third injection test was run at 45 strokes/min (45 strokes = 225 gal/min or 852 L/min) for 30 min. Again, there was a flat pressure response (to around 1805–1820 psi), with a subsequent 20-min. wait in the testing to allow the residual borehole pressure to decay.

The decision was then made to pump at the maximum possible pressure for an hour to try to reach the limits of what the formation could absorb. The fourth injection test began at 0343 UTC, with 59 strokes/min (59 strokes = 295 gal/min or 1117 L/min) being pumped for 60 min. On this test, a pressure of 2940–2960 psi was reached. Again, there was a flat pressure response throughout the duration of the test, with only minor fluctuation around 2950 psi.

The packer was then unseated, and 30 min was allowed for its deflation. The Kuster pressure recorders from the second seating were left in the packer to speed pulling the packer out of the hole. The packer was pulled without incident to 2958–2902 m, where 50,000 lb of pull on the drill string was required to continue pulling out of the hole. Another overpull of 40,000 lb occurred at 2721 m. When the packer cleared the rig floor at 1330 UTC on January 23, the packer rubber was found to have been pulled inside-out and over itself. Several steel cables had been broken, perhaps while the drill string was pulled through the tight spots in the hole.

The pressure gauges from the second packer seating indicated that the formation below the packer had been exposed to pressures only slightly above hydrostatic pressure; the maximum pressure rise on the Kuster chart records was 14 psi over the hydrostatic pressure. Two possibilities to explain this small pressure rise were considered. A first explanation is that all of the water pumped down the pipe during the second packer set may in some way have vented out of the system before going through the packer. Theoretical pressure drop calculations at the second packer set indicate that the pumping pressures could be explained if there was circulation through the four 0.23-in. equalization ports connecting the drill pipe to the annulus, that is, if the shifting sleeve was not completely closed. When weight is set on the packer to allow the expanded packer element to grip onto the borehole wall, the shifting sleeve briefly closes off the borehole and allows venting through these ports to prevent an unwanted pulse test into the borehole during setting. If this sleeve jams halfway down in its stroke, then the vent ports would be left open. The borehole would

Table 1 (continued).

Core no.	Date (Jan. 1991)	Time (UTC)	Depth (mbsf)	Cored (m)	Recovered (m)	Recovery (%)	Age
135-839B-							
1W	17	1045	0.0–90.0	90.0	0.57	(wash core)	
2W	17	1150	90.0–110.0	20.0	1.30	(wash core)	
3R	17	1305	110.0–119.7	9.7	0.25	2.6	upper Pliocene
4R	17	1420	119.7–129.4	9.7	0.24	2.5	upper Pliocene
5W	17	1645	129.4–180.0	50.6	1.78	(wash core)	
6R	17	1820	180.0–189.7	9.7	0.29	3.0	upper Pliocene
7R	17	1930	189.7–194.7	5.0	0.54	10.8	barren
8R	17	2030	194.7–199.3	4.6	0.67	14.5	upper Pliocene
9R	17	2200	199.3–204.3	5.0	0.64	12.8	Indeterminate
10R	17	2300	204.3–208.5	4.2	0.16	3.8	upper Pliocene
11R	18	0010	208.5–213.5	5.0	0.84	16.8	barren
12R	18	0150	213.5–218.2	4.7	2.10	44.7	
13R	18	0500	218.2–227.2	9.0	3.46	38.4	
14R	18	0705	227.2–237.3	10.1	1.66	16.4	
15R	18	0910	237.3–247.0	9.7	4.76	49.1	
16R	18	1040	247.0–256.7	9.7	1.30	13.4	
17R	18	1150	256.7–266.4	9.7	0.50	5.2	
18R	18	1330	266.4–276.0	9.6	0.45	4.7	
19R	18	1515	276.0–285.7	9.7	0.47	4.8	
20R	18	1640	285.7–295.3	9.6	0.58	6.0	
21R	18	1800	295.3–305.0	9.7	0.50	5.2	
22R	18	1915	305.0–314.6	9.6	0.25	2.6	
23R	18	2050	314.6–324.3	9.7	0.52	5.4	
24R	18	2215	324.3–334.0	9.7	0.23	2.4	
25R	18	2335	334.0–343.6	9.6	0.34	3.5	
26R	19	0140	343.6–353.3	9.7	0.28	2.9	
27R	19	0255	353.3–362.9	9.6	0.31	3.2	
28R	19	0420	362.9–372.6	9.7	0.24	2.5	
29R	19	0750	372.6–382.2	9.6	1.06	11.0	
30R	19	1055	382.2–391.9	9.7	0.55	5.7	
31R	19	1235	391.9–401.6	9.7	0.11	1.1	
32R	19	1405	401.6–411.3	9.7	0.00	0.0	
33R	19	1540	411.3–420.9	9.6	0.00	0.0	
34R	19	1820	420.9–430.3	9.4	0.16	1.7	
35R	19	2005	430.3–439.6	9.3	0.49	5.3	
36R	19	2200	439.6–449.2	9.6	0.30	3.1	
37R	20	0000	449.2–458.9	9.7	0.38	3.9	
38R	20	0125	458.9–468.6	9.7	0.16	1.7	
39R	20	0245	468.6–477.9	9.3	0.06	0.7	
40R	20	0410	477.9–487.5	9.6	0.00	0.0	
41R	20	0540	487.5–497.2	9.7	0.14	1.4	
42R	20	0710	497.2–502.2	5.0	0.06	1.2	
43R	20	0830	502.2–507.2	5.0	0.00	0.0	
44R	20	1000	507.2–512.2	5.0	0.00	0.0	
45R	20	1215	512.2–517.2	5.0	0.00	0.0	
Coring totals				356.6	25.05	7.0	
Washing totals				160.6	3.65		
Combined totals				517.2	28.70		

therefore be closed off, and none of the pumped water would have gone to the hole.

A second explanation for the small pressure rise recorded on the Kuster charts is possible. On recovery of the packer after the measurements, the seal separation ring on the go-devil was found to have rotated 45° with respect to the mandrel flow holes. If the ring was in the rotated position during the injection tests, pressure would be required to pump water through the plugged go-devil flow holes; calculated pressure losses due to this phenomenon are only about half of the observed standpipe pressure (water pressure being pumped down the interior of the drill string). In this case, however, fluid would have gone into the borehole below the packer element, with the minimal pressure rise on the Kuster recording gauges indicating a large formational permeability. As these flow holes are also used in deflating the packer element, partial blockage of them could lead to only partial deflation of the packer element, resulting in damage to the element while it was pulled out of the hole.

At the end of Leg 135, both of these possible malfunctions were experimentally tested. The pressure rise obtained when the seal separation ring on the go-devil was rotated 45° and closed off the mandrel flow holes was 2955 psi at 50 strokes/min, very similar to what was observed during the second packer set. The pressure rise caused by a stuck shifting sleeve in the packer was 1500 psi at only 16 strokes/min; this test was terminated due to possible dangers to personnel and equipment. The experimentally measured pressures, combined with the observation of a rotated seal separation ring, indicate that the rotated ring was the cause of the high pressures observed during the second packer set. Therefore the pumped water went into the borehole, and assuming a packer seal, the second packer set should also provide a valid measure of hole permeability.

Examination of the surface of the recovered packer element showed no signs of water jet damage as would be expected if all the water pumped during the first set had gone by a leak in the packed section. The element was worn, abraded, and slightly striated, but otherwise appeared to be in good condition with no holes or tears. A more complete description and interpretation of the packer results is given in the "Physical Properties" section (this chapter).

LITHOSTRATIGRAPHY

Introduction

The sedimentary sequence recovered at Site 839 consists of 214.71 m of clayey nannofossil ooze, turbiditic vitric sands and silts, volcanic gravels, and rare pyroclastic fallout ashes. The age of the sedimentary sequence ranges from the middle Pleistocene to the upper Pliocene. Basalt was reached at 206 mbsf in Hole 839A and 214 mbsf in Hole 839B, but intra-lava sediment was recovered from as deep as 256.7–266.4 mbsf in Hole 839B. Sediment recovery was almost 96% from 0 to 99.5 mbsf in Hole 839A; thereafter, however, it decreased to only 3%–4%. We have divided the sedimentary sequence into three lithologic units, based primarily on the presence or absence of volcaniclastic sands and silts (Fig. 8). Because of poor recovery and the consequent lack of constraint on lithologic boundaries, all sediments recovered from below 99.5 mbsf have been grouped together into a single unit (Unit III).

Figure 9 displays graphically the relationship between the cycles of sedimentation as defined by our subunit divisions, their $CaCO_3$ content, magnetic susceptibility, and *P*-wave velocity. Unit I and the upper parts of Subunits IIB, IIC, and IIF show high $CaCO_3$ contents (50%–60%) caused by their high proportion of clayey nannofossil ooze. Magnetic susceptibility correlates well with the lithologic cycles we define. High magnetic susceptibility in the nannofossil oozes is probably a result of the iron-oxyhydroxide staining of these sediments. Vitric silts and sands generally show lower values. Higher values often occur in the bases of graded intervals because of concentrations of iron-bearing accessory minerals. *P*-wave velocities also show a close correspondence to the defined subunits. Sharp drops in *P*-wave velocities frequently correspond to the bases of vitric sands, interpreted as turbidite bases.

Unit I

Intervals: Sections 135-839A-1H-1, 0 cm, to -3H-3, 85 cm
Depth: 0–17.85 mbsf

Unit I is 17.85 m thick and is composed predominantly of dark yellowish brown to dark-brown (10YR 3/3 to 10YR 3/4), iron-oxyhydroxide-stained, clayey nannofossil ooze containing occasional thin vitric sand and silt layers. Apart from these ash layers, volcaniclastic material is rare. Paleomagnetic and biostratigraphic data indicate that the age of the sediments recovered from Unit I is middle Pleistocene (see "Sediment Accumulation Rates" section, this chapter). Late Pleistocene to Holocene surface sediments were not recovered because of the dispersion of surface sediments during emplacement of the drill string on the seafloor.

The clayey nannofossil ooze contains about 35%–40% clay-size material, with the rest of the sediment being composed primarily of calcareous nannofossils (55%–60 vol%) and planktonic foraminifer tests and test debris (4–6 vol%). The clayey nannofossil oozes commonly appear homogeneous over long intervals, although sometimes barely discernible mottled intervals are common. Isolated angular to rounded, commonly altered pumice clasts (up to 3 cm in diameter) occur scattered throughout the sediment. The clayey nannofossil oozes comprise about 55%–60% $CaCO_3$, although there seems to be some variability (Fig. 9).

Several volcaniclastic layers occur within Unit I. The uppermost of these is an 8-mm thick, coarse vitric sand (1.66 mbsf) comprising 80 vol% volcanic glass shards and 15 vol% foraminifer tests, with the remaining 5% including feldspar, accessory minerals, and clay-size material. This lies 30 cm above a 4-cm thick band of clay (1.94–1.98 mbsf) containing minor amounts of volcanic glass (15 vol%), feldspar (15 vol%), foraminifers (15 vol%), and nannofossils (10 vol%). This is interpreted as a possible altered, relict pyroclastic ash layer. Three thin, normally graded vitric sands (2–9 cm thick) occur in Section 135-839A-2H-1 (at 4.87–4.96, 5.05–5.07, and 5.41–5.45 mbsf, respectively). These largely consist of sand-size glass shards with minor amounts of foraminifers, clay, and feldspar. Another normally graded vitric ash bed (9 cm thick) occurs at 7.48–7.57 mbsf. Some of these beds may represent thin volcaniclastic turbidites; others may represent fallout ashes. A diffuse, 6-cm thick, vitric ash band at 16.82–16.88 mbsf, with gradational lower and upper boundaries and comprising 95 vol% volcanic glass, is interpreted as a pyroclastic ash layer.

Unit II

Intervals: Sections 135-839A-3H-3, 85 cm, to -11H-7, 64 cm
Depth: 17.85–99.5 mbsf

Unit II is 81.65 m thick and is distinguished from Unit I by its very high content of volcaniclastic material. The unit comprises a sequence of generally thick- to very thick-bedded vitric sand and silts, with some clayey nannofossil ooze interbeds. A very thick-bedded volcanic gravel is also present within the sequence. Clayey nannofossil ooze comprises about 25%–30% of the sequence. Unit II is divided into six subunits (Subunits IIA–IIF) based on general upward-fining cycles, although within any one subunit a number of upward-fining intervals may be present. Between 66 and 82 mbsf, drilling disturbance and poor recovery in Core 135-839A-9H has resulted in very disturbed "soupy" and slightly less disturbed intervals, in which most, if not all, primary structures have been destroyed. Consequently, bed boundaries may have originally existed within this interval that we have been unable to recognize. Paleomagnetic and biostratigraphic data indicate that the age span of Unit II ranges from the middle Pleistocene to the late Pliocene (see "Biostratigraphy" and "Paleomagnetics" sections, this chapter).

Subunit IIA

Intervals: Sections 135-839A-3H-3, 85 cm, to -4H-4, 140 cm
Depth: 17.85–29.40 mbsf

Subunit IIA is 11.55 m thick and comprises a 4.4-m-thick olive gray (5Y 5/2), normally graded, but otherwise generally structureless vitric sand, which grades upward into a 2.14-m-thick light-grayish brown vitric silt (2.5Y 6/2) that appears structureless except for intervals (up to 10 cm thick) of very faint planar laminae. This bed is overlain by a series of interbedded vitric sands and silts (1–90 cm thick). Subunit IIA is entirely volcaniclastic in composition and contains no clayey nannofossil ooze.

The basal olive gray (5Y 5/2), normally graded, vitric sand (25.0–29.4 mbsf) has a 37-cm-thick, planar-layered base, with alternating dark and light layers. The darker layers are enriched with accessory minerals (mainly pyroxenes) whereas the lighter layers are pure glass sands. The sand above the laminated base is graded for at least 1 m and then passes upward into a structureless sand, which consists of 75%–80% glass shards and minor amounts of feldspar (5–7 vol%), accessory minerals (10 vol%), foraminifers (3–5 vol%), and up to 5% clay-size material. The sand grades upward into a very disturbed, light grayish brown, soft and structureless vitric silt.

The vitric silt is overlain by a sequence of interbedded, light brownish gray to grayish brown vitric sands and silts (17.85–22.86 mbsf), the individual beds of which are up to 90 cm thick. The sand beds show sharp basal contacts with the underlying beds and are usually normally graded. Individual sand beds are separated by longer intervals of homogeneous vitric silt. The vitric

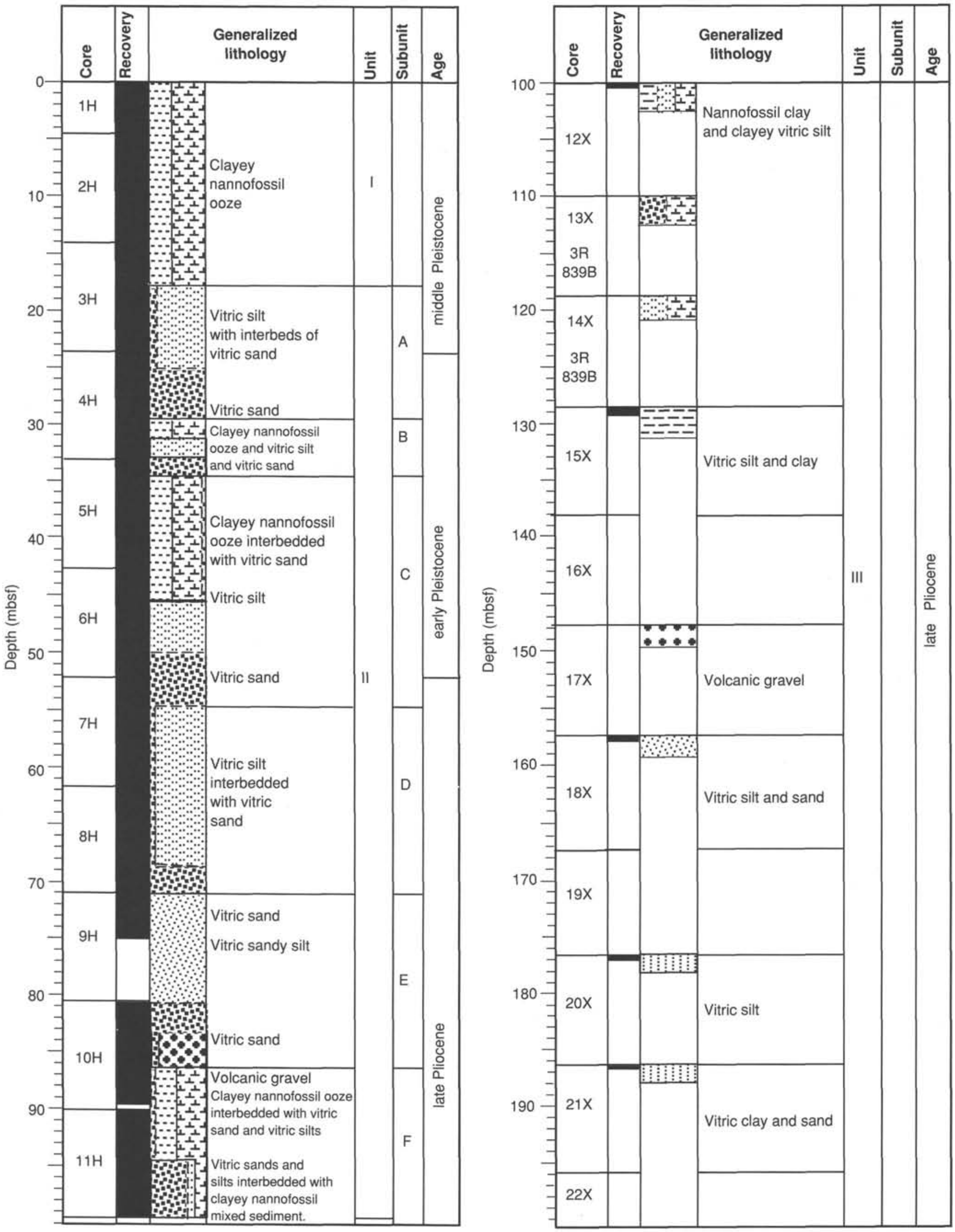

Figure 8. Lithologic summary for Hole 839A, indicating the main lithologic units identified with age as well as a generalized lithology for Site 839.

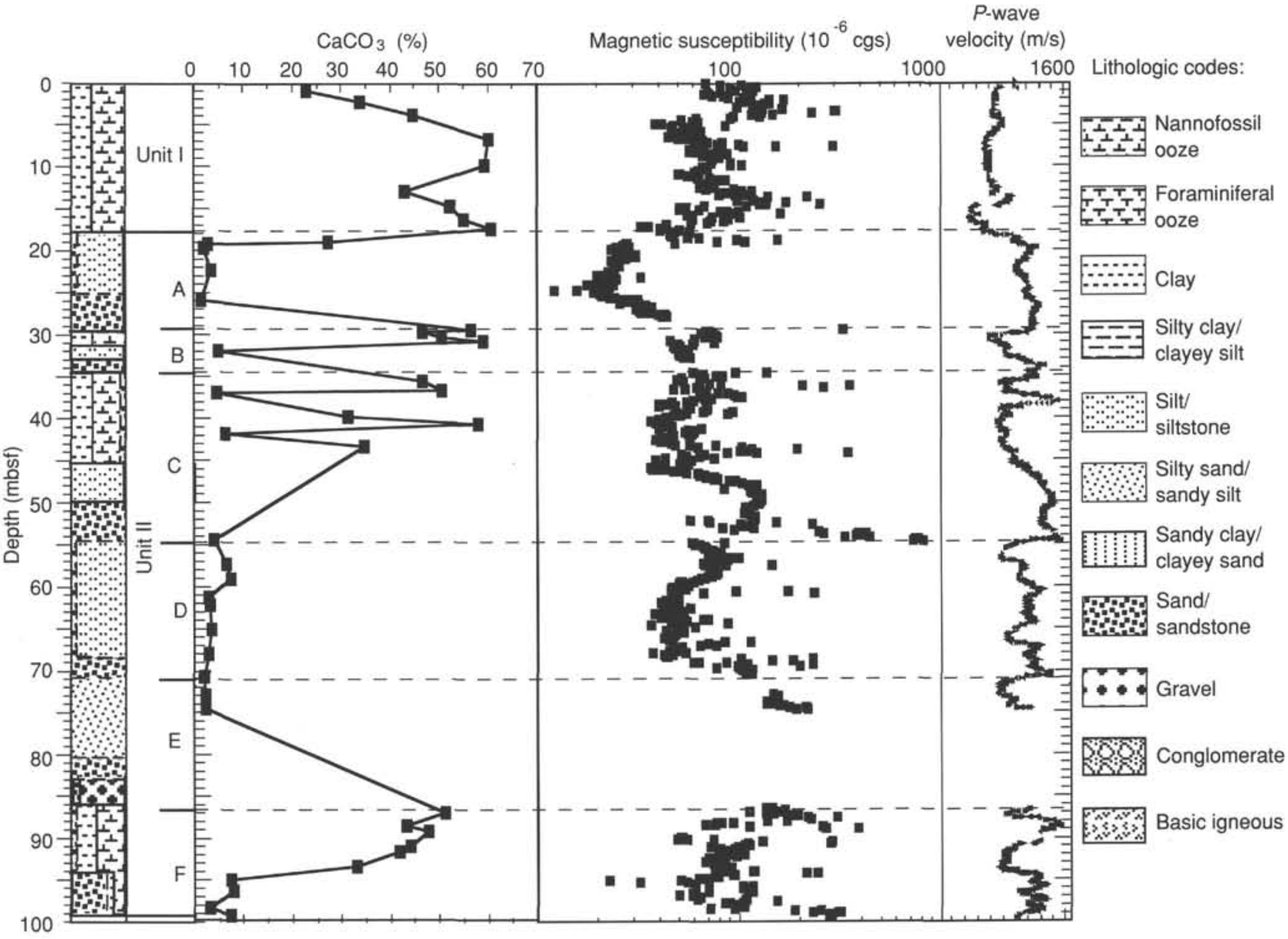

Figure 9. Diagram showing variations in $CaCO_3$ content, magnetic susceptibility, and *P*-wave velocity vs. depth and lithology within Units I and II of Hole 839A. Note the high susceptibility and *P*-wave velocity at the base of each graded unit, decreasing upsection as the sediment fines. The high magnetic susceptibility of the clayey nannofossil oozes in Unit I is attributed to iron oxyhydroxide staining of the sediment.

silts consist primarily of volcanic glass shards (typically 75 vol%), together with minor quantities of calcareous nannofossils (typically 10 vol%) and small amounts of feldspar, clay, foraminifers, and accessory minerals (each up to 5 vol%). The sands consist of up to 90% volcanic glass by volume; the rest consists of feldspar, foraminifers, and accessory minerals.

Subunit IIA is interpreted as a series of volcaniclastic turbidites. The absence of clayey nannofossil ooze interbeds between the vitric sands suggests that they may have been emplaced in rapid succession. However, erosion of underlying sediment by the turbidity currents may have dispersed any pre-existing pelagic sediments before being deposited.

Subunit IIB

Intervals: Sections 135-839A-4H-4, 140 cm, to -5H-2, 17 cm
Depth: 29.40–34.67 mbsf

Subunit IIB is 5.27 m thick and consists of a sequence of vitric sand and silt overlain by clayey nannofossil ooze. The basal bed of the subunit is a 1.67-m-thick, gray, structureless vitric sand (33.0–34.67 mbsf). The sand consists of 95% volcanic glass shards by volume; the remainder consists of angular to subrounded feldspar grains. This bed is overlain by 1.77 m of vitric silt of similar composition, which contains five thin, normally graded layers of vitric sand (1–5 cm thick). These have sharp basal contacts with the underlying silt. The bases of these thin graded units contain sand-size grains. Smear slides show that the silt has a composition similar to the underlying sand. The silt is overlain by 1.83 m of dark-brown (10YR 4/3), iron-oxyhydroxide- stained, clayey nannofossil ooze. The ooze contains rare, isolated pumice clasts up to 3 cm across but otherwise appears homogeneous with no discernible mottling. In the clayey nannofossil ooze, 48 cm beneath the base of the overlying volcanic sand of Subunit IIA (at 29.40 mbsf), there is an abrupt color change to brownish yellow (10YR 6/6) that is interpreted as a redox-related chemical front.

Subunit IIC

Intervals: Sections 135-839A-5H-2, 17 cm, to -7H-2, 111 cm
Depth: 34.67–54.61 mbsf

Subunit IIC is 19.94 m thick and consists of a sequence of very thickly bedded vitric sands and silts overlain by very thickly bedded clayey nannofossil ooze containing thin to thick vitric sand interbeds.

The basal bed in Subunit IIC is a 4.66-m-thick, light gray (5Y 6/1), normally graded vitric sand (49.95–54.61 mbsf). The basal part has been greatly disturbed by drilling, and water saturation has destroyed most of the primary sedimentary structures so that above the normally graded base the sediment appears quite structureless. The lower part of the sand consists mainly of volcanic glass (70 vol%), with smaller amounts of feldspar (20 vol%), accessory minerals (5 vol%), and clay (5 vol%). The upper part of the sand consists of nearly 95% glass shards. The vitric sand grades upward into a 4.37-m-thick, light-olive gray (5Y 6/2), vitric silt, which apart from a few short intervals of faint burrow mottling appears homogeneous.

These volcaniclastic beds are overlain by 10.91 m of iron-oxy-hydroxide-stained, clayey nannofossil ooze, containing thin- to thick-bedded vitric sand interbeds. Where the sand interbeds are thick (>0.4 m), the underlying clayey nannofossil ooze shows a sharp color change 68–97 cm below the sand bed. Above this color change, the sediment is yellowish brown (10YR 5/6), grading upward to a pale olive color (5Y 6/3). Below the color change, the clayey nannofossil ooze is dark brown (10YR 4/3) in color. We interpret this color change as a redox-related chemical front. The clayey nannofossil ooze appears homogeneous over long intervals, although there are a few short intervals showing faint mottling. The ooze also contains a few isolated, commonly altered pumice clasts. The clayey nannofossil ooze contains 55%–60% $CaCO_3$ (Fig. 9), and smear slides show that it comprises 50% calcareous nannofossils and up to 10% planktonic foraminifers and test debris. The noncarbonate fraction consists of clay (35–40 vol%) and accessory minerals, mainly pyroxenes (up to 5%). Higher in the section, the clayey nannofossil ooze contains up to 15 vol% volcanic glass shards.

The clayey nannofossil ooze contains ten interbeds of grayish brown to black (2.5Y 2/0), normally graded vitric sand. Most of the beds are 3–17 cm thick, but two are 35 and 64 cm thick. The thicker interbeds have planar-laminated sandy bases. These sands are mainly composed of volcanic glass shards (up to 75 vol%), the remainder consisting of accessory minerals, mainly pyroxenes (up to 10 vol%), foraminifers (up to 10 vol%), and smaller amounts of feldspar, clay-size material, and nannofossils. These interbeds are interpreted as volcaniclastic turbidites or, in some cases, possibly pyroclastic fallout ashes.

Subunit IID

Intervals: Sections 135-839A-7H-2, 111 cm, to -8H-CC, 15 cm
Depth: 54.61–71.0 mbsf

Subunit IID is 16.39 m thick and consists of a sequence of vitric sands and silts. Between 66.0 and 71.0 mbsf, drilling disturbance has resulted in very disturbed "soupy" intervals and other slightly less disturbed intervals that may have resulted in the destruction of some primary structures. Consequently, bed boundaries are uncertain within the disturbed lower part of the subunit.

The basal unit is a 2.41-m-thick, light gray (5Y 6/1), apparently structureless vitric sand composed primarily of volcanic glass shards (about 90 vol%) and accessory minerals, principally pyroxenes (up to 10 vol%). This grades upward into a light-gray, very disturbed (5Y 6/1), structureless vitric silt. Between 54.61 and 64.75 mbsf, a series of three vitric sand beds (25–33 cm thick) occur, each of which grades upward into thick- to very thick-bedded vitric silts. The uppermost of these beds consists of a 33-cm-thick, gray (5Y 5/1), normally graded vitric sand that grades upward into 6.22 m of light gray/gray (5Y 6/1), structureless vitric silt. This whole sequence is interpreted as a series of volcaniclastic turbidites. The lack of interbeds of clayey nannofossil ooze suggests that emplacement may have been relatively rapid, although erosion at the bases of individual turbidites may have removed any pre-existing ooze.

Subunit IIE

Intervals: Sections 135-839A-9H-1 to -10H-4, 120 cm
Depth: 71.0–86.2 mbsf

Subunit IIE is 15.2 m thick and consists of a single overall upward-fining sequence of very thick pumiceous vitric gravel mixed with very coarse hyaloclastite sand (10 vol%). This grades up into very coarse vitric sand with gravel and then to very coarse-grained vitric sand and then to vitric silty sand.

The basal gravel is 3 m thick and consists predominantly of light gray, angular to well-rounded granules and clasts of pumice (up to 3 cm across), mixed with black, angular, coarse vitric sand. The vitric sand forms approximately 10% by volume of the deposit. The lowermost 25 cm of the unit is dominated by black glassy granules and fragments. The gravel is crudely normally graded and passes upward into a light olive gray to olive gray (5Y 5/2 to 5Y 6/2), very coarse vitric sand mixed with light-gray pumice granules. Isolated pumice clasts, up to 3 cm across, occur within this part of the subunit. The coarse sand-size particles are predominantly angular grains of black volcanic glass of varied vesicularity. The sand shows faint traces of planar bedding, but drilling disturbance may have destroyed much of the primary sedimentary structures. The coarse sand with gravel grades upward into a coarse vitric sand consisting almost entirely (97%) of volcanic glass shards, with the remainder consisting of subhedral to anhedral feldspar and accessory minerals. The glass shards are mainly clear and colorless, although these are mixed with lesser amounts of brown glass. The coarse vitric sand grades upward into a vitric silty sand of similar composition. Drilling disturbance and poor core recovery (41%) in Core 135-839A-9H has resulted in the silty sand being very disturbed with the destruction of all primary structures.

Subunit IIF

Intervals: Sections 135-839A-10H-4, 120 cm, to -11H-7, 64 cm
Depth: 86.2–99.5 mbsf

Subunit IIF is 13.3 m thick. The lower part consists of a sequence of thick-bedded vitric sands and silts interbedded with thick-bedded clayey nannofossil mixed sediments (94.8–99.5 mbsf). This is overlain by a 6.97-m-thick upper sequence of generally thick-bedded clayey nannofossil oozes and clayey nannofossil mixed sediments, with occasional thin- to thickly bedded vitric sand and silt interbeds (86.2–94.8 mbsf).

The lowermost beds in the lower part of Subunit IIF consist of a sequence of very thinly bedded, dark-gray to very dark-gray (5Y 4/1 to 5Y 3/1), normally graded, vitric silts (98.85–99.5 mbsf). Individual beds are 1–5 cm thick (Fig. 10). The normally graded bases of these beds typically consist of volcanic glass shards (57 vol%), clay (20 vol%), and feldspar (15 vol%) with small amounts of foraminifers (3 vol%) and accessory minerals (5 vol%). Above the graded bases, the beds consist of volcanic glass (45 vol%), clay (25 vol%), and calcareous nannofossils (25 vol%), with smaller amounts of foraminifers (5 vol%). This series of thin beds is overlain by a thin homogeneous vitric clay and a thin clayey nannofossil ooze, which contains several angular pumice clasts up to 2 cm across. These beds are overlain by a 1.06-m-thick, normally graded, planar-laminated vitric sand, consisting of 90% volcanic glass shards by volume. This sand is overlain by 56 cm of homogeneous vitric silt, above which there is a thick-bedded, laminated vitric silt, again composed mainly of clear, colorless volcanic glass but also containing clear, unaltered brown shards. This silt grades upward into a clayey nannofossil mixed sediment, containing minor amounts of very fine-grained, colorless volcanic glass (up to 10% by volume). This is overlain by a 0.75-m-thick, normally graded, vitric silty sand. Above this is a 0.77-m-thick sequence of vitric silty sands interbedded with thin intervals of clayey nannofossil ooze (up to 15 cm thick).

The upper part of Subunit IIF (86.2–94.8 mbsf) consists of a sequence of dark-brown, iron-oxyhydroxide-stained, clayey nannofossil oozes and mixed sediments with some thin to thick interbeds of graded vitric sand and silts. The thickest of these interbeds are laminated, and all of the interbeds are composed of colorless and brown volcanic glass shards, together with minor

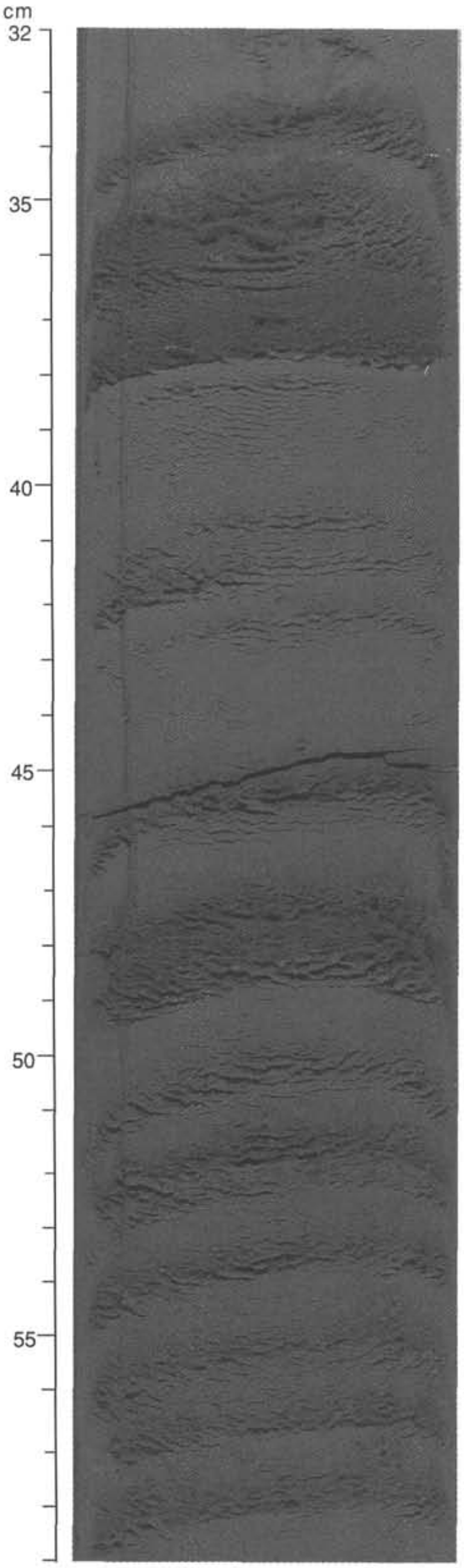

Figure 10. Photograph of Section 135-839A-11H-7, 32–59 cm, illustrating a sequence of very thinly bedded dark gray to very dark gray, normally graded vitric turbidites with dark silty bases (98.6–99.2 mbsf). Individual beds are 1–5-cm thick and are stacked directly on top of one another.

amounts of feldspar and accessory minerals (mainly pyroxenes). These vitric interbeds are interpreted as turbidites.

Unit III

Intervals: Sections 135-839A-12X-1, 0 cm, to -23X-CC, 24 cm, and Sections 135-839B-3R-CC to -11R-1 and 135-839B-17R-1
Depth: 99.5–266.38 mbsf

We have grouped all of the sediments recovered from below 99.5 mbsf in Holes 839A and 839B into a composite Unit III, because of the poor recovery and, therefore, the lack of constraint on the lithologic boundaries. Below 99.5 mbsf in Hole 839A, the hole was extended with the XCB to 218.2 mbsf. Recovery from Unit III was very poor. Only 2.89 m of sediment was recovered from 106.74 m of sediment drilled by the XCB in Hole 839A below 99.5 mbsf (2.7% recovery). Recovery of Unit III in Hole 839B was marginally better. From this hole, 6.47 m of sediment was recovered from below 99.5 mbsf out of 114.81 m of sediment drilled below this depth by the RCB (5.6% recovery). The sediments recovered from Unit III in Hole 839A consist of nannofossil clays, clays, vitric silts and sands, and volcanic gravel. The sediments are firm or indurated. In Hole 839B, sediments recovered from Unit III comprise ashy claystones, vitric siltstones, and sandstones and clayey nannofossil ooze.

The vitric silts recovered from Hole 839A consist predominantly of colorless glass shards, although some contain up to 40 vol% of plagioclase feldspar. Volcanic sand and silt intervals have sharp basal contacts. Immediately above the basement in Hole 839A, a normally graded interval of very dark grayish brown vitric silt with nannofossils, clay, and feldspar that grades up into dark-brown to brown clayey nannofossil chalk is present.

In Hole 839B, where clayey vitric siltstone is the dominant lithology recovered, sedimentary structures are commonly preserved. These include burrows, planar lamination, and ripple cross-bedding. Thin interbeds of vitric sand often occur within the silts, and a 29-cm-thick bed of polymict, matrix-supported breccia was recovered in Section 135-839B-11R-1, 31–50 cm. The polymict breccia shows crude normal grading and contains angular clasts of vesicular basalt and laminated vitric siltstone set in a clayey vitric sandy matrix. Between 31 and 43 cm in this core section, the clasts are very coarse sand to granule-size (up to 3 mm across); however, in the interval from 43 to 50 cm, the individual clasts are much larger, ranging up to 22 mm across. In Section 135-839B-17R-1, 41 cm of clayey nannofossil ooze with foraminifers and glass was recovered, intercalated between basalt lava flows (256.7–266.4 mbsf). This was the deepest sediment recovered at Site 839.

Sediments recovered from Unit III (nannofossil clays, clays, vitric silts, and sands and volcanic gravels) are similar to those of Unit II, suggesting that the sedimentary sequence below 99.5 mbsf may be similar to, and a continuation of, Unit II. If so, Unit III may be dominated by epiclastic volcanic sediments similar to Unit II in Hole 839A (see above). Indeed, this is supported by the downhole geophysical and geochemical logs, which show similar readings through the Unit II/III boundary until 162 mbsf (see "Downhole Measurements" section, this chapter). The cause of a major change in the resistivity, velocity, gamma-ray, bulk density, and photoelectric effect logs at 162 mbsf is unknown, as this interval was not recovered. However, sediments recovered from below this depth are similar in lithology to those recovered above.

Volcaniclastic Sediments

Sixty-five percent of the sediments in the upper 100 m of Hole 839A contain more than 80% volcaniclastic material. Table 2 summarizes the characteristics of volcaniclastic turbidites and pyroclastic ash layers recovered in Units I and II. Figure 11 shows the variation in volcaniclastic bed thickness with depth in Hole

Table 2. Characteristics of volcaniclastic ash layers and epiclastic turbidites in Units I and II, Hole 839A.

Core section, depth	Depth to top (mbsf)	Depth to base (mbsf)	Smear slide	Thickness (cm)	Type of unit	Maximum glass (vol%)	Maximum grain size (µm)	Igneous minerals present (>1 vol%)
135-839A-								
1H-3, 1	3.00	3.01	1	1	P, H	80	300	plag, cpx, opx
1H-3, 32	3.29	3.33	1	4	P, H	15	70	
2H-1, 45	4.87	4.96	1	9	E, G	73	700	plag (very rare)
*2H-1	5.05	5.07		2	E, G			
*2H-1	5.41	5.45		4	E, G			
2H-3, 7	7.48	7.57	1	9	P, G	60	300	plag, cpx
3H-2, 135	16.82	16.88	1	6	P, H	95	200	
3H-3, 130	17.85	18.43	1	58	E, G	75	250	
3H-4, 24	18.46	18.75	1	29	E, G	70	1200	plag, cpx
*3H-4 to 4H-4	19.14	29.42	5	1028	E, G	90	1000	plag, cpx, opx
*4H-6	31.10	34.67	2	357	E, G	95	450	
*5H-3	36.09	36.26		17	E, G			
5H-3, 90	36.74	37.38	1	64	E, G	80/75	400/1000	plag (rare)
*5H-5	39.20	39.23		3	P, G			
*5H-5	39.33	39.34		1	P, H			
5H-5, 68	39.64	39.69	1	5	E, G	75	550	plag (rare)
*5H-6 to 5H-7	41.70	42.05		35	E, G			
*6H-1	43.66	43.67		1	P, G			
*6H-2	44.08	44.09		1	P, G			
6H-2, 24	44.21	44.28	1	7	E, G	70	1100	plag, cpx, opx
*6H-2	44.70	44.78		8	E, G			
*6H-2 to 7H-2	44.86	54.23	3	937	E, G	90	1100	plag
*7H-2	54.23	54.60		37	E, G	90		
*7H-2 to 7H-6	54.61	60.83	2	622	E, G	90	400	plag, cpx
*7H-6 to 8H-1	60.63	62.65	1	202	E, G	90	800	
*8H-1 to 8H-3	62.65	64.90		235	E, G	90		
*8H-3 to 10H-4	64.90	86.20	5	2130	E, H	97	1000	plag, cpx
*10H-5	87.32	87.80	2	48	E, G	60	300	plag, cpx, opaques
10H-6, 97	88.68	88.85	1	17	E, G	55	1200	cpx
11H-1, 70	90.66	90.72	1	6	E, G	25	700	plag, cpx
11H-2, 88	92.30	92.38	1	8	P(?), G	85	700	plag
*11H-4	94.50	95.27	3	77	E, H	91		
11H-4, 141	95.27	96.02	1	75	E, H	82	600	minor plag, augite
11H-5, 69	96.45	97.56	1	111	E, G	88		
11H-6, 48	97.56	98.02	1	46	E, G	85	1000	minor augite
11H-6, 95	98.02	98.51	1	49	E, G	90	1200	minor plag, augite
*11H-6 to 11H-7	98.51	99.50	3	99	E, G	57	500	plag, augite, lithics
*15X-1	128.50	129.50	1	100	E, H			
*18X-CC	157.61	157.81		21	E, H			
*20X-CC	176.50	176.84		34	E, H			plag, cpx, opx(?)

Notes: An asterisk (*) indicates ash layer from which no smear slide was made; only the core and section in which the ash layer occurs are indicated. Type: P = pyroclastic, E = epiclastic, H = homogeneous, and G = graded. Glass (vol%): Glass content normally indicates maximum mode estimated from smear slides. However, glass content may be highly variable in individual units, especially in the graded sequences. Igneous minerals present: Igneous mineral content is noted when more than trace amounts (>1%) are present. Key: plag = plagioclase, cpx = clinopyroxenes, and opx = orthopyroxenes.

839A. Volcaniclastic beds occur mainly in Unit II, which corresponds to an age span of approximately 1.7–0.6 Ma. No volcaniclastic sediment (except for isolated pumice clasts) has been deposited at this site since about 330 Ka. Before this time the quantity of redeposited volcaniclastic material within the sequence had already greatly decreased since 500 Ka. Little is known about the volcaniclastics of Unit III because of poor recovery. Most of the volcaniclastic material recovered is epiclastic in origin, as at previous drill sites within the Lau Basin, and occurs as three different types of deposit: (1) thick, massive, volcanic sands and silts, often several meters thick; (2) thin turbidites with glass-rich bases (typically >20 cm thick); and (3) rare, thin, primary fallout tephra layers.

Thick, Massive Volcanic Sands and Silts

Massive volcanic sands and silts occur as typically graded but otherwise structureless beds that are often several meters thick. They are absent from Unit I, but are very common in Unit II and probably Unit III. Volumetrically, they are the most important type of volcaniclastic sediment, comprising about 65% of the total sediment in Unit II. Internally, they generally lack sedimentary structures, although parallel planar lamination is often present in the lower parts of the deposits. The laminated bases often consist of alternating light and dark laminae, 5–15 mm thick. The light-colored layers are predominantly pure, colorless glass (90–95 vol%), whereas the dark layers contain abundant fragments of greenish brown glass with lesser amounts of subangular augite, plagioclase, and opaque oxide minerals. Short intervals of faint planar laminae also occasionally occur in the upper parts of some of the thicker beds. The thick massive sands and silts have sharp, sometimes scoured, basal contacts and gradational upper boundaries.

The massive volcanic sands and silts consist primarily of fresh, colorless glass shards (typically 70–95 vol%); the remainder consists of anhedral to subhedral feldspar and accessory minerals (particularly pyroxenes), foraminifer tests and test debris, calcareous nannofossils, and clay-size material. The glass debris in the vitric turbidites consists of vesicular pumice, fibrous pumice containing elongate tubular vesicles, and both bubble-wall and bubble-junction shards. Some of the silt-size, platy, vitric debris appears to be derived from the breakdown of larger shards. Nevertheless, much of the silicic glass debris bears little evidence of

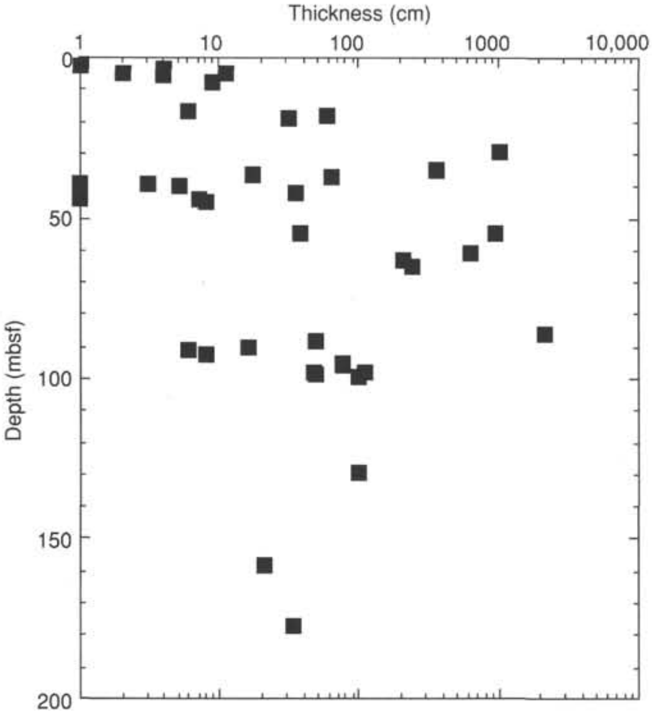

Figure 11. Variation of volcaniclastic bed thickness with depth in Hole 839A.

a long history of water-born transport, as delicate elongate shards are often preserved.

A single, 15.2-m-thick, mass-gravity-flow deposit forms Subunit IIE (Sections 135-839A-9H-1 to -10H-4). This bed consists of a disorganized pumiceous gravel that grades upward into a coarse vitric sand and then into vitric sandy silt. Most of the deposit is structureless, although a few faint planar laminae occur where the gravel grades up into a coarse sand. The gravel consists mainly of light gray, subangular to well-rounded pumice clasts (up to 3 cm across) but also contains black hyaloclastite coarse sand, which is concentrated toward the base of the bed.

The epiclastic sands and silts are interpreted as turbidites on account of their sedimentary structures. However, most beds show only partial Bouma sequences (Bouma, 1962). Planar-lamination is the most commonly observed sedimentary structure. This reflects deposition involving traction of grains on the bed and represents the "upper plane bed" of experimental work (Harms et al., 1982). However, many of the thick sand and silt beds are almost totally structureless and therefore fall into the massive sandstone facies rather than classical turbidites in the scheme introduced by Walker (1978). These beds usually consist of very thick Bouma Ta divisions (up to several meters thick), which were probably rapidly deposited from turbidity currents developing into fluidized flows before being deposited. "Dish" fluid escape structures, which are typical of such deposits (Lowe, 1975), are not seen. However, many of these beds are disturbed, so any such structures, if originally present, may have been lost.

Thin Turbidites with Glass-rich Bases

Thin turbidites with glass-rich bases are found throughout Unit I, within the upper part of Unit II (subunits IIA–IIC), and within subunit IIF. These form a small percentage of the total sediment and are rarely more than 20 cm thick. These beds are grayish brown (2.5Y 5/2) to very dark grayish brown (10YR 3/2) in color, have sharp bases, and show normal grading. Compositionally, the bases of these beds consist mainly of large, angular, platy, colorless or greenish brown glass shards with smaller quantities of pumiceous and fibrous shards. The bases also contain minor quantities of accessory minerals, mainly plagioclase and pyroxenes. The brownish color of many glass fragments is not always linked to lower silica contents (see Table 3), but silica-poor glasses do usually have a greenish brown color.

Primary Fallout Tephra

Pyroclastic intervals are found as thin (up to 5 cm thick) interbeds within nannofossil oozes in Cores 135-839A-1H, 2H, 5H, and 6H. These deposits are very dark grayish brown (10YR 3/2) to black (2.5Y 2/0) in color, and occur as both graded and homogeneous layers. Individual shards within the ash are typically highly angular and fragile, although elongate fibrous shards are common. Although glass is the most common component within these beds, igneous minerals also occur and are more abundant in the tephras than in the glass-rich turbidites. Plagioclase, augite, and hypersthene are present in significant quantities (up to 20%), with the former being the most and the latter the least abundant. The tephras commonly have bioturbated tops. Isolated pumice clasts occur within clayey nannofossil ooze throughout the sequence.

Chemical Composition of the Volcanic Glass

Eight glass-shard samples were taken from volcaniclastic horizons in Units I, II, and III. These were cleaned and sorted by grain size as described in the "Lithostratigraphy" section of the "Site 834" chapter (this volume). The 36–63-μm size fraction was then examined using a petrographic microscope to determine the refractive indices of the constituent glass shards using standard reference index oils. Total silica content was calculated by the method of Church and Johnson (1980) and Schmincke (1981) (Table 3). X-ray fluorescence (XRF) analysis for a single sample from 84 mbsf (70.6 wt% SiO_2) confirmed the general accuracy of the optical SiO_2 determinations (see Fig. 12 and Table 11). There are two glass populations: a colorless, rhyolitic group (SiO_2 content = 70.3–71.1 wt%) and a brownish green, basaltic andesitic group (SiO_2 content = 52.6–56.3 wt%). The former is normally by far the most common (>95%). However, one exception is found in Sample 135-839A-10H-5, 68 cm, where both colorless and greenish brown glass fragments had the same refractive indices, giving compositions of 68.8 wt% SiO_2. In this sample, glass

Table 3. Refractive indices (*n*) and SiO_2 concentrations (estimated from Church and Johnson [1980] and Schmincke [1981]) of vitric shards (63–36 μm size fraction) from volcaniclastic turbidites in Hole 839A.

Core, section, interval (cm)	Depth (mbsf)	Comment	*n*	SiO_2 (wt%)
135-839A-				
2H-1, 44	4.94	Clear, colorless	1.506	71.1
4H-3, 72	24.22	Clear, colorless	1.506	71.1
4H-3, 72	24.22	Greenish brown	1.578	53.4
6H-5, 118	49.68	Clear, colorless	1.509	70.3
6H-5, 118	49.68	Greenish brown	1.582	52.6
7H-2, 90	55.40	Clear, colorless	1.509	70.3
7H-2, 90	55.40	Greenish brown	1.582	52.6
7H-2, 90	55.40	Greenish brown	1.578	53.4
8H-3, 90	65.40	Clear, colorless	1.509	70.3
10H-5, 106	87.56	Clear, colorless	1.514	68.8
10H-5, 106	87.56	Greenish brown	1.514	68.8
11H-7, 49	99.49	Clear, colorless	1.522	66.6
11H-7, 49	99.49	Greenish brown	1.564	56.3
15H-1, 9	128.59	Clear, colorless	1.506	71.1
15H-1, 9	128.59	Greenish brown	1.580	53.0

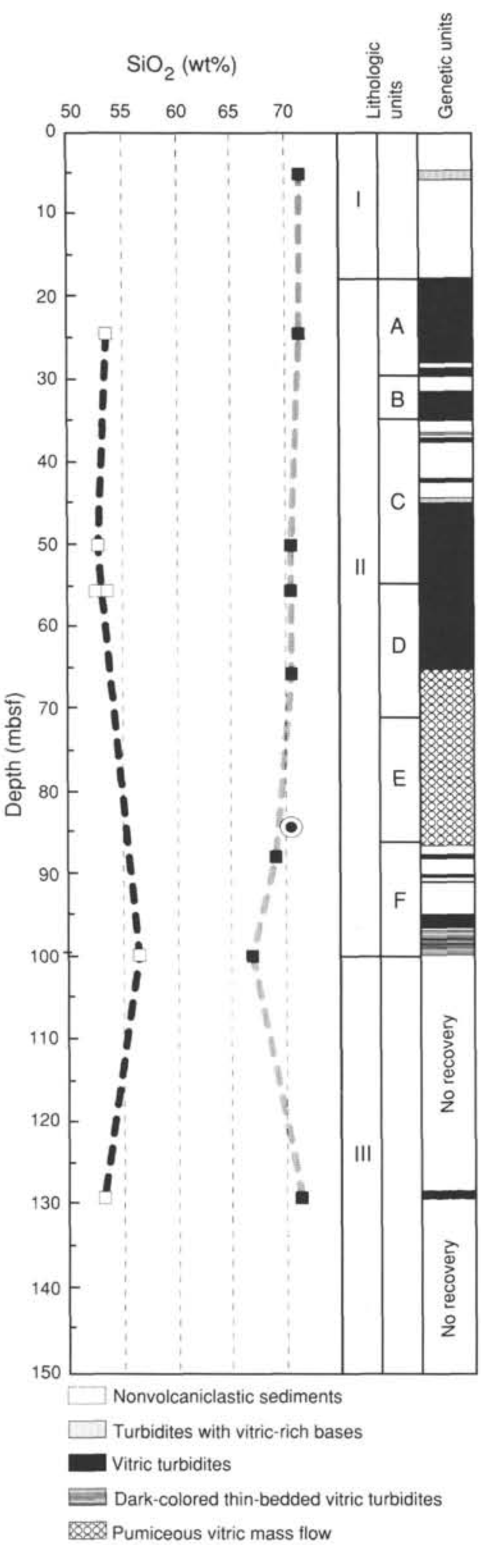

Figure 12. Downcore plot showing variation in silica content of volcanic glass shards from Hole 839A. Downcore log of lithologic and genetic units alongside. Note the presence of two or three different glass compositions in single samples. Dark-shaded squares represent the majority glass group and white squares the majority group within any one sample. Black dot with concentric ring at 84 mbsf indicates results from X-ray-fluoresence sample. Dark- and light-shaded dashed lines show the trend of high- and low-silica glass groups throughout the sequence.

shards comprise >95% of all volcanic detritus. Another important, but volumetrically small, type of glass-rich sand interval (e.g., 135-839A-3H-7, 17–27 cm) occurs as dark gray to black, thin, normally graded, fine-grained beds. Smear-slide analyses showed that these contain abundant augite, plagioclase, and dark greenish brown glass with only a few clear colorless shards.

The little chemical variation from top to bottom of Hole 839A (Fig. 12) suggests that the nature of the sources has not changed through the depth interval sampled (5–130 mbsf). However, all but the top two samples were deposited over a relatively short time interval (0.94–1.76 Ma) because of the high sedimentation rates at this site during the late Pliocene (see "Sedimentation Accumulation Rates" section, this chapter). The chemical composition of glass shards analyzed from Site 839, when compared with those from Sites 834–838, shows that the compositional range (from dacite to basaltic andesite) is approximately constant throughout the basin. Most samples are either dacites or basaltic andesites; there are few andesites. In this respect, Site 839 appears to be typical of the other Lau Basin Leg 135 drill sites.

The predominance of silicic glass within the volcaniclastic turbidites suggests that the Lau Ridge could have been the principal source for the volcaniclastic material, but we cannot discount the Tofua Arc or contributions from silicic extrusives on intrabasin centers such as Zephyr Shoal or Valu Fa Ridge and other intrabasin seamounts. The long transport distance from the Lau Ridge to Site 839 makes derivation from the Lau Ridge problematical. In all these cases, the proportion of rhyolite relative to basaltic andesite within any source may be much less than that represented in the volcaniclastic sediments of the Lau Basin. This is attributed to the relatively explosive nature of silicic eruptions causing tephra of this composition to be more effectively transported and thus preferentially deposited (and hence redeposited) in the basin.

Glass fragments show little alteration in the upper parts of the sequence but are optically less clear at lower depths. Shards showing low birefringence were seen in several samples from Unit II; they indicate early stages of devitrification.

Depositional History

The earliest sedimentation recorded at Site 839 is dated as late Pliocene in age (about 1.9 Ma). Pelagic clayey nannofossil oozes with pelagic foraminifers occur as intra-lava sediments, deposited during eruption of the basaltic basement. Following the cessation of volcanism, the late Pliocene was characterized by deposition of clayey nannofossil ooze and clayey, fine-grained, volcaniclastic turbidites. Thick turbidites and other sediment gravity flow deposits were deposited at this time. Sedimentation rates were very high.

Toward the end of the late Pliocene, extensional faulting caused downfaulting and tilting of the sub-basin. This is reflected by the presence of an angular unconformity (82–87 mbsf), seen on seismic records and downhole dipmeter readings (see "Background and Objectives" and "Structural Geology" sections, this chapter). Sedimentation began again with coarse volcaniclastic turbidite sands and gravels. The volcanic debris appears to have been derived principally from a bimodal volcanic source supplying both basaltic andesitic and rhyolitic material. Individual beds, however, also contain vitric debris of intermediate composition. The Lau Ridge and Tofua Arc may have been sources of much of the volcanic material, although the Valu Fa Ridge or other intrabasin volcanic centers may have also contributed. The volume of volcanic debris decreases with time so that the turbidites became thinner and less frequent by the early Pleistocene. Epiclastic sedimentation had almost ceased by middle Pleistocene times, about 500 Ka. This decrease in turbiditic input may be related to (1) establishment of the ELSC, which may have been an effective sediment transport barrier; and/or (2) widening of the Lau Basin east of Site 839 through spreading, thereby increasing the distance between the Tofua Arc and the sub-basin containing Site 839. Primary ash layers are present within upper Pliocene clayey nannofossil ooze sediments, indicating proximity to an active volcanic arc. Sedimentation since the middle Pleistocene has been principally pelagic clayey nannofossil ooze, with rare thin pyroclastic ashes and pumice clasts. Manganese oxide coatings on volcanic sand grains lower in the sequence, and the iron-oxyhydroxide staining of the pelagic nannofossil oozes found at higher levels in the sequence reflect the continuous activity of hydrothermal systems within the basin since the late Pliocene.

STRUCTURAL GEOLOGY

Introduction

Site 839 is located in the western Lau Basin 180 km south of the Central Lau Spreading Center (CLSC) and approximately 70 km west of the Eastern Lau Spreading Center (ELSC). Sea-Beam bathymetric profiles show that Site 839 is situated in a basin that is bounded to the northwest by a 200–300-m-high northeast–southwest-trending scarp (see "Background and Objectives" section, this chapter). The basin is separated from the basin containing Site 838 by a north–south-striking, east-facing scarp that on GLORIA sidescan sonar records appears to truncate the northeast-southwest lineament. Seismic reflection profiles suggest that the northeast-southwest scarp adjacent to Site 839 extends at depth to a steeply inclined normal fault zone. The fault forms the northwest margin of the seismic units comprising the basin fill, and these are described and discussed above in the "Background and Objectives" section (this chapter). The most prominent structure within the basin is the angular unconformity between the underlying upper surface of seismic Unit B, dipping at about 4° toward the northwest, and the onlapping subhorizontal transgressional Unit A (Fig. 7). The overlying pelagic drape (seismic Unit A) itself dips at a low angle (about 1°) to the northwest at the surface.

Sediments

Depth: 0–205.9 mbsf in Hole 839A and 0–214.2 and 256.8–266.4 mbsf in Hole 839B

Bedding orientations were measured from core in Hole 839A from 0 to 187 mbsf, and a further measurement was made on sediment from the interbedded subunit at 257 mbsf in Hole 839B. Use of the multishot orientation tool solely for Cores 135-839A-4H to -11H meant that only those data between 30 and 100 mbsf could be reoriented to geographical coordinates. No dipmeter data are available for the sedimentary section in Hole 839B, as the formation microscanner was unable to operate successfully in the large borehole diameter (see "Downhole Measurements" section, this chapter).

All geographically reoriented data are illustrated in Figures 13 and 14. Mean dips at all stratigraphic levels are greater than the indicated dip of the seismic reflectors. The core dip measurements have mostly been taken from the bases (frequently these are erosional surfaces) of individual volcaniclastic turbidite horizons, and may therefore include some component of depositional dip. The upper parts of the sedimentary succession, between 30 and 50 mbsf, dip southeastward at an average of 7.4°. Between 90 and 100 mbsf, however, inclination of bedding is generally toward the west or west-northwest, although with increased scatter. The average dip of these lower strata is 9.6°.

The changeover between the two clusters of dip orientations could potentially correspond to the unconformity recognized on the seismic records. If so, it must lie below 44.8 mbsf and above 92.4 mbsf. No dips were measurable between 44.8 and 86.7 mbsf. If two beds that occur at 86.7–89.0 mbsf and dip 6° to the east are considered, then the angular discordance is constrained to lie between 89.0 and 92.4 mbsf. This would place it within a uniform sequence of clay/nannofossil ooze, which is not an obvious site for such a discontinuity; however, if these two dip measurements are disregarded, the supposed unconformity could be placed within the overlying 5-m-thick, poorly sorted volcanic gravel deposit (at 82–87 mbsf, the base of lithologic Subunit IIE). This has been regarded as the most favorable model on sedimentological grounds (see "Lithostratigraphy" section, this chapter), and is compatible with the inferred depth of the unconformity on the seismic records, assuming velocities in the region of 1.7 km/s (see "Background and Objectives" section, this chapter).

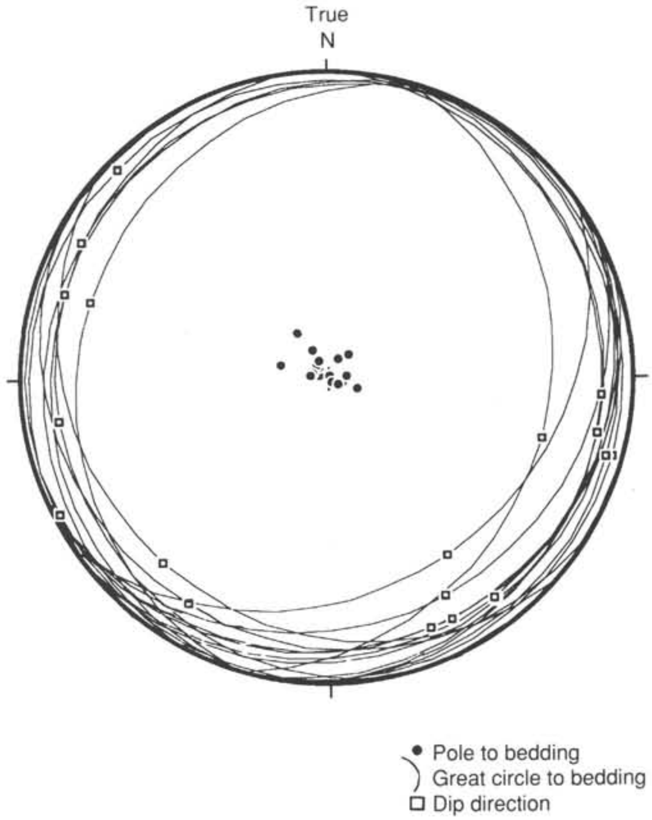

Figure 13. Lower hemisphere equal-angle stereographic projection of sedimentary bedding orientations from Hole 839A. $N = 19$.

The gravel deposit and subjacent oozes are all of latest Pliocene age (nannofossil Subzone CN13b). If they do correspond to the angular discordance recognized on the seismic records, then it appears that fault movement is likely to have occurred along the northeast–southwest structure in the late Pliocene.

The gravels are identical in age to the thick gravel deposits recovered at Site 838 (lithologic Subunit IIC), which may also coincide with changes in sedimentary bedding orientation and possible tectonic activity (see "Structural Geology" section, "Site 838" chapter, this volume).

Igneous Rocks

Igneous rocks were encountered at 205.9–218.2 mbsf in Hole 839A and at 214.2–497.3 mbsf in Hole 839B. A sedimentary interbed was cored from 256.8 to 266.4 mbsf. Core recovery in the igneous section was generally <10%, so that few structures are preserved. Nevertheless, it was possible to recognize subplanar joints traversing the core. These fractures generally dip at a steep angle to the axis of the core and may be coated with zeolite or slightly stained by iron oxide or hydroxide.

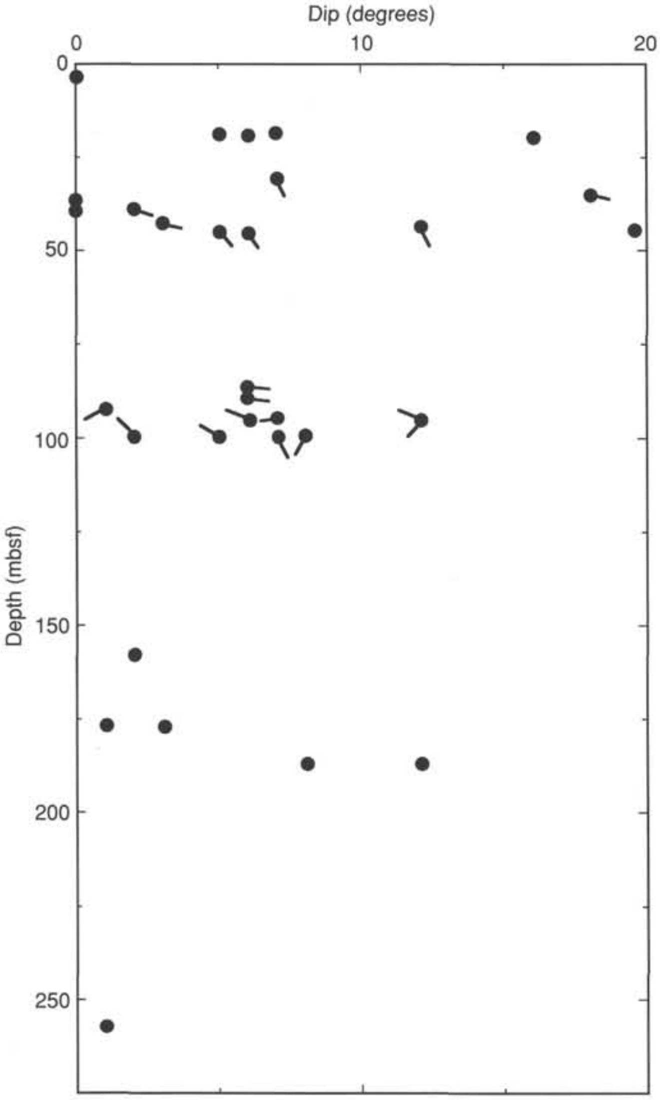

Figure 14. Sediment bedding orientations plotted vs. depth. The angle of the dip is given on the *x*-axis and the dip direction, where known, by the azimuth of the tick. True north is toward the top of the page. Note the change in orientation between the southeasterly dipping strata at above 50 mbsf, and the general westerly dip of strata at approximately 90 mbsf and below. See text for discussion.

The small size of several individual pieces in the igneous section prevented measurement by the cryogenic magnetometer; hence, demagnetization was only conducted on fragments cut by a total of 19 joint planes. Eleven of these were measured in the depth range from 214 to 250 mbsf, within which interval magnetic inclinations close to zero were obtained upon demagnetization (see "Paleomagnetism" section, this chapter). These inclinations suggest an intermediate polarity (i.e., a nondipole magnetic field), perhaps indicating extrusion of this portion of the igneous sequence during the time span of a magnetic reversal (see "Paleomagnetism" section, this chapter). If this is so, magnetic declinations over the same interval cannot be used to orient the core as the geomagnetic field may not have been dipolar or axially symmetric. Thus, we were only able to reorient eight of the measured joint planes back to geographical coordinates using paleomagnetic data.

The remaining eight joint planes that were successfully reoriented to geographical coordinates (true north) are shown in Figure 15. They show a wide range of orientations and are so few in number that they are unlikely to have regional geological significance.

BIOSTRATIGRAPHY

Introduction

The sediments at this site range from middle Pleistocene to late Pliocene in age. The middle Pleistocene assemblages occur in Cores 135-839A-1H and -2H. The middle/early Pleistocene boundary occurs within Core 135-839A-3H. The Pleistocene/Pliocene boundary (base of nannofossil Zone CN14 of Okada and Bukry, 1980) is within Core 135-839A-7H. The remainder of the sedimentary sequence at this site is late Pliocene in age.

The biostratigraphic results for Sites 839A and 839B are summarized in Figures 16 and 17.

Calcareous Nannofossils

Pleistocene

Sample 135-839A-1H-CC contains a flora that includes *Gephyrocapsa oceanica, Helicosphaera inversa,* and abundant small gephyrocapsids, but not *Emiliania huxleyi* or *E. ovata.* On this basis this sample is placed in Subzone CN14b.

Samples 135-839A-2H-CC to -6H-CC yielded floras including *Gephyrocapsa oceanica, G. caribbeanica, Emiliania huxleyi, Pseudoemiliania lacunosa,* and small gephyrocapsids. These samples are assigned to Subzone CN14a.

Pliocene

Samples 135-839A-7H-CC, -12X-CC, -15X-CC, -17X-CC, -18X-CC, -20X-CC, -22X-CC and -23X-CC and Samples 135-

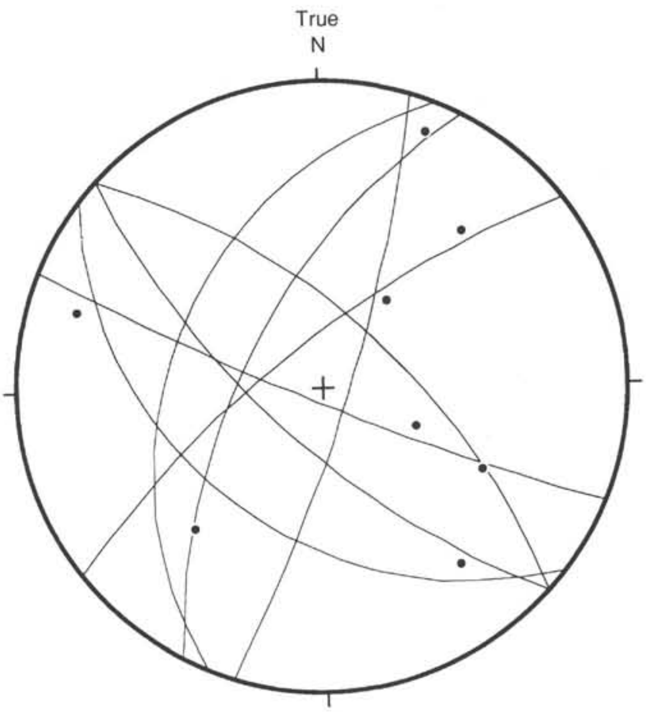

Figure 15. Lower hemisphere equal-angle stereographic projection of pole to joint planes, Hole 839B. $N = 8$.

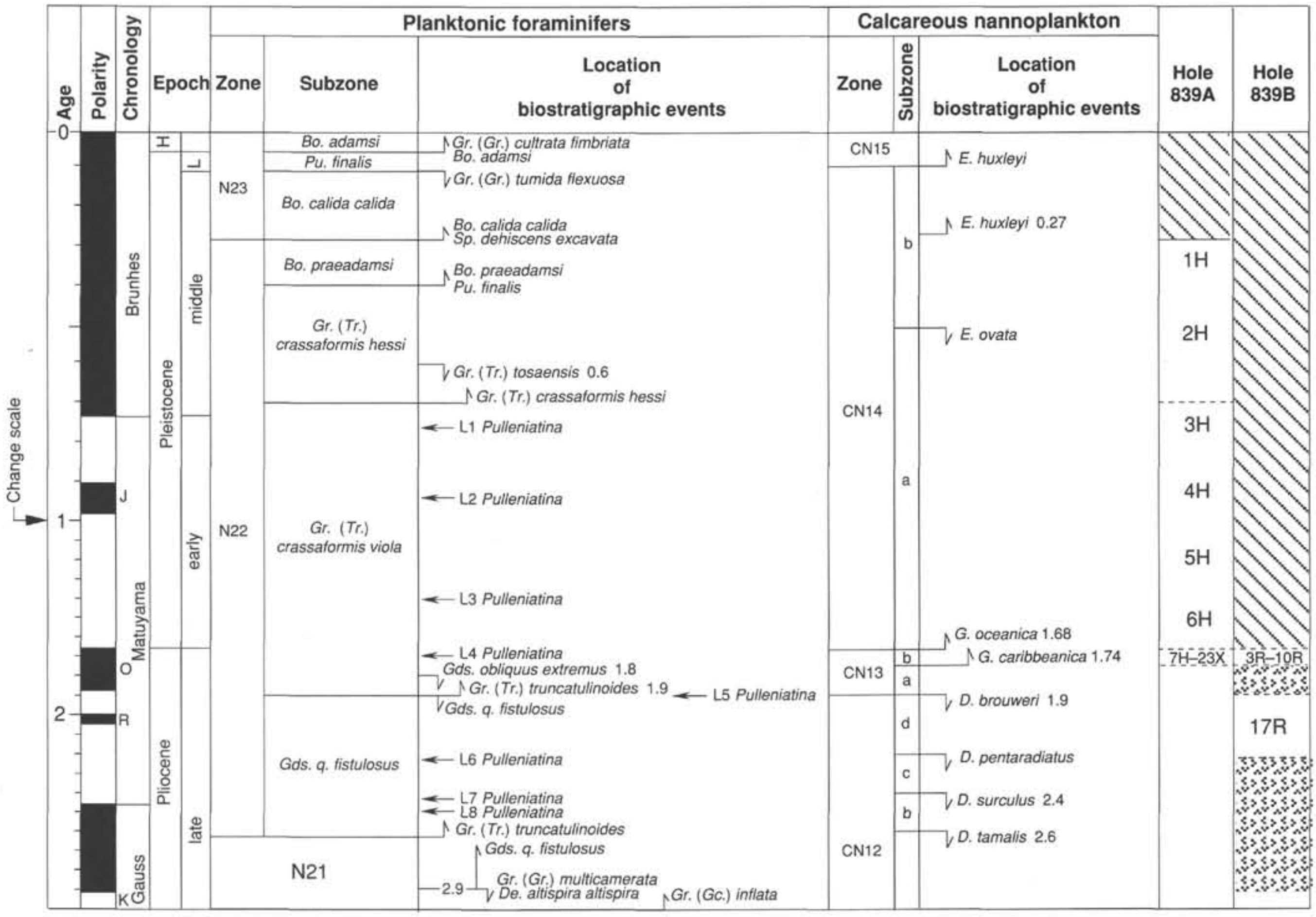

Figure 16. Biostratigraphic results, Site 839.

839B-3R-CC, -4R-CC, -6R-CC, and -10R-CC contain sparse to abundant, moderately to well-preserved floras containing *Gephyrocapsa caribbeanica, Calcidiscus macintyrei, Emiliania ovata, Pseudoemiliania lacunosa*, and small gephyrocapsids, but not *G. oceanica* or *Discoaster brouweri*. These samples have been assigned to Subzone CN13b. Poorly preserved discoasters and sphenoliths included in some of the floras recovered from these samples are considered reworked.

Poorly preserved floras in Samples 135-839A-21X-CC and 135-839B-8R-CC were sufficient to assign those samples to Zone CN13 but not to a specific subzone.

Sample 135-839B-17R-CC contains a sparse, moderately preserved flora including *Discoaster brouweri* and *C. macintyrei*. This sample is assigned to Subzone CN12d.

Planktonic Foraminifers

A total of 29 core-catcher samples were examined for planktonic foraminifers at Site 839. Of these, nine are barren and two others contain faunas too poor to permit any age determination. The pumiceous sands from within Core 135-839A-06H to below Core 135-839A-11H, and the fine ash beds at the lower part of the sedimentary sequence are often barren or, at best, contain low-diversity faunas. The remainder contain faunas that range from the middle Pleistocene to the upper Pliocene. In Hole 839B faunas were obtained from beds immediately overlying the highest basalt flow, as well as from beds separating flows.

Middle Pleistocene

Sample 135-839A-1H-CC contains *Bolliella praeadamsi, Globorotalia (Truncorotalia) crassaformis hessi* and pink forms of *Globigerinoides ruber*, without either *B. calida calida* or *Gr. (Tr.) tosaensis*, indicating the *B. praeadamsi* Subzone of Zone N22. Sample 135-839A-2H-CC contains a similar fauna but lacks *B. praeadamsi*, indicating the *Gr. (Tr.) crassaformis hessi* Subzone of Zone N22.

Lower Pleistocene to Upper Pliocene

The planktonic foraminifer faunas over this interval of time at Site 839 are too poor to permit the separation of the lower Pleistocene and upper Pliocene.

The overlap in ranges of *Globorotalia (Tr.) tosaensis* and *Gr. (Tr.) truncatulinoides* marks the *Gr. (Tr.) crassaformis viola* Subzone, and this assemblage is present in Samples 135-839A-5H-CC to -21X-CC. Below this interval in Hole 839A, faunal assemblages are of low diversity and these two species are absent.

Samples 135-839B-3R-CC to -7R-CC are either barren or contain a fauna with species diversity too low to permit an accurate biostratigraphic assignment. However, from the evidence of samples from Hole 839A, they fall within the *Gr. (Tr.) crassaformis viola* Subzone. Assemblages typical of this subzone are found intermittently in Samples 135-839B-8R-CC to -17R-CC. Other samples within this interval are either barren of planktonic foraminifers or of insufficient diversity to permit a biostrati-

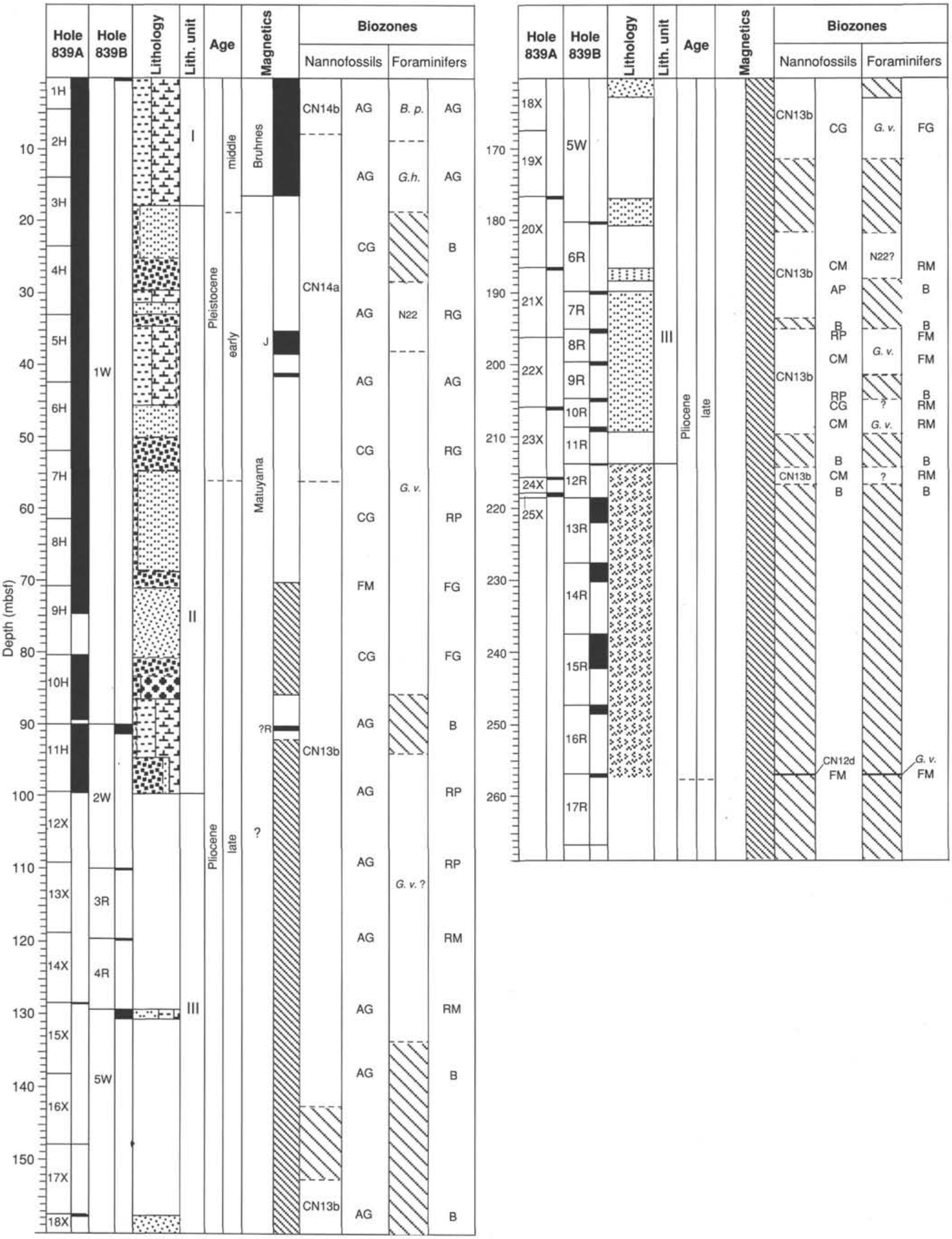

Figure 17. Paleontology summary chart, Site 839. See Figure 1 caption for an explanation of the symbols and abbreviations used.

graphic assignment. The presence of *Globigerinoides obliquus extremus* in Sample 135-839B-3R-CC suggests assignment to the lower part of the *Gr.* (*Tr.*) *crassaformis viola* Subzone.

SEDIMENT ACCUMULATION RATES

The biostratigraphic and paleomagnetic data indicate that the age of the sediments at Site 839 ranges from the middle Pleistocene to the upper Pliocene (Brunhes and Matuyama chrons). The sediment sequence consists largely of tuffaceous sands, with some interbedded calcareous ooze horizons. The amount of volcaniclastic material greatly increases downcore, being concentrated from within Core 135-839A-6H to below Core 135-839A-11H (100 mbsf), an interval with little paleontologic control. Below 100 mbsf, core recovery fell drastically, with biostratigraphic control being restricted to core-catcher samples. Many of these were barren, and others had a rare to common microfossil content.

Table 4 lists depths and ages of bioevents used to plot sediment accumulation rates. Figure 18 presents a graphic presentation of depth and biostratigraphic data from Site 839. As with previous sites, two sets of biostratigraphic data have been used: one based on the extinction level (last appearance datum [LAD]) of *Gr.* (*Tr.*) *tosaensis* at 0.6 Ma (Berggren et al., 1985a, 1985b), and the other with this event being placed at 0.9 Ma (based on the relationship between this event and the paleomagnetic data at Sites 834 and 837). In addition, paleomagnetic data, which are available only for the top 92 m of the core, have also been plotted with the biostratigraphic data.

The sediment accumulation curve can be divided into three sections, illustrating changes in the rates of accumulation. The lowermost part (A), between 213.5 and 56 mbsf, shows very rapid sedimentation rates of about 882 mm/k.y.; the upper part of this interval coincides with the level where the main ash beds are found and the lower part with basalts. Between 56 and 25 mbsf (B), the sedimentation rate decreases to about 51 mm/k.y., marking the interval over which the ash beds are thinner. From levels above 25 mbsf (C), sedimentation rates decrease to 9 mm/k.y., coinciding with levels where ash beds are very rare.

Table 4. Depths and ages of bioevents used to plot sediment accumulation rates for Site 839.

Depth (mbsf)	Age (Ma)	Events
4.5	0.50	LAD *E. ovata*
25.0	0.60	LAD *Gr. (Tr.) tosaensis*
56.0	1.68	LAD *G. oceanica*
250.0	1.90	LAD *D. brouweri*

Note: LAD = last appearance datum.

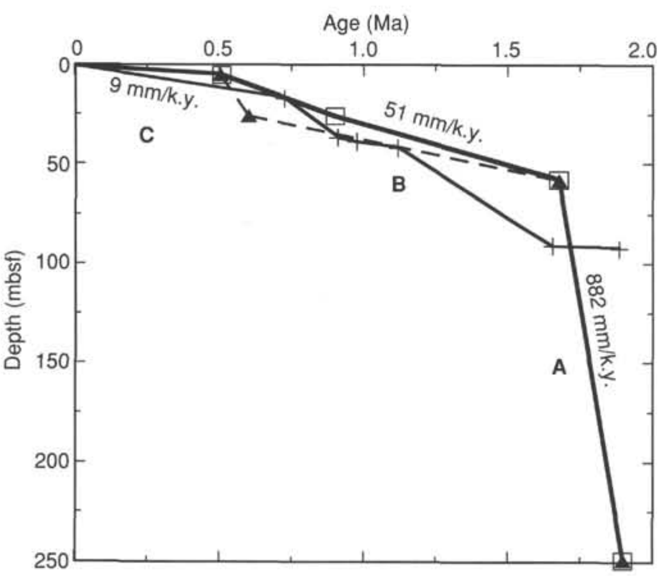

Figure 18. Graphic representation of age vs. depth data illustrating the sedimentation rates at Site 839 by means of the bioevents and depths given in Table 4. A plot of the paleomagnetic data is also included for comparison. Filled triangles = biostratigraphic data, open squares = biostratigraphic data with modified age for *Globorotalia (Truncana) tosaensis*, and plus signs = paleomagnetic data.

PALEOMAGNETISM

Remanent Magnetism

Most remanent magnetization measurements were made with the pass-through cryogenic magnetometer on archive core halves. All measurements were made at a spacing of 5 cm. After measuring the natural remanent magnetism (NRM), alternating-field (AF) magnetic cleaning of sediment cores was done at 15 mT, whereas 5, 10, and 15 mT was used for the basalt cores. A few discrete samples were analyzed using the Molspin Minispin spinner magnetometer and the Molspin pulse magnetizer to investigate the magnetic properties in greater detail.

Sediments in Cores 135-839A-1H through -11H were measured mainly to determine magnetic polarity stratigraphy. Other cores in Hole 839A were not measured because they suffered moderate to severe drilling disturbance and were unlikely to produce reliable results in the pass-through magnetometer. Oriented segments of rotary core barrel (RCB) basalt cores from Hole 839B were also measured with the pass-through cryogenic magnetometer primarily to determine magnetic polarity.

Magnetic Properties

The sediments at Site 839 are strongly magnetic with NRM intensities ranging between 30 and 200 mA/m, with geometric means typically around 50 mA/m. Such strong magnetizations probably result from volcanic material contained in the sediments. Indeed, their color is often dark, reddish brown as a result of abundant iron, probably contained in ferric oxyhydroxides, or light gray to light brownish gray because of the vitric volcanic silt and sand components (see "Lithostratigraphy" section, this chapter). Isothermal remanent magnetization (IRM) acquisition curves (Fig. 19) show a rapid saturation with increasing field strength, indicating that the magnetic grains within these sediments behave like magnetite.

Another factor in producing the strong magnetizations is a pervasive upward overprint that gives the sediments NRM inclinations near –90° and completely masks their polarities. The vertical direction of the overprint implies that it results from exposure of the sediments to strong magnetic fields (an IRM) in the core barrel or drill string. The sediments acquire a strong drill-string IRM because some of their magnetic grains have low coercivities, as shown by typically low mean destructive field (MDF) values (5 mT or less; Fig. 20). Because of this, the sediments can easily acquire an overprint. However, because it resides in low coercivity grains, this overprint is readily removed with moderate AF demagnetization between 5 and 15 mT (Fig. 20), leaving a more stable, characteristic remanence that holds geologic information.

Typical basalt NRM magnetization intensities ranged from about 1 to 20 A/m. These rocks also displayed a drill-string IRM, but to a lesser extent than the sediments from Hole 839A. The amount of overprint was variable. Some samples had low MDFs

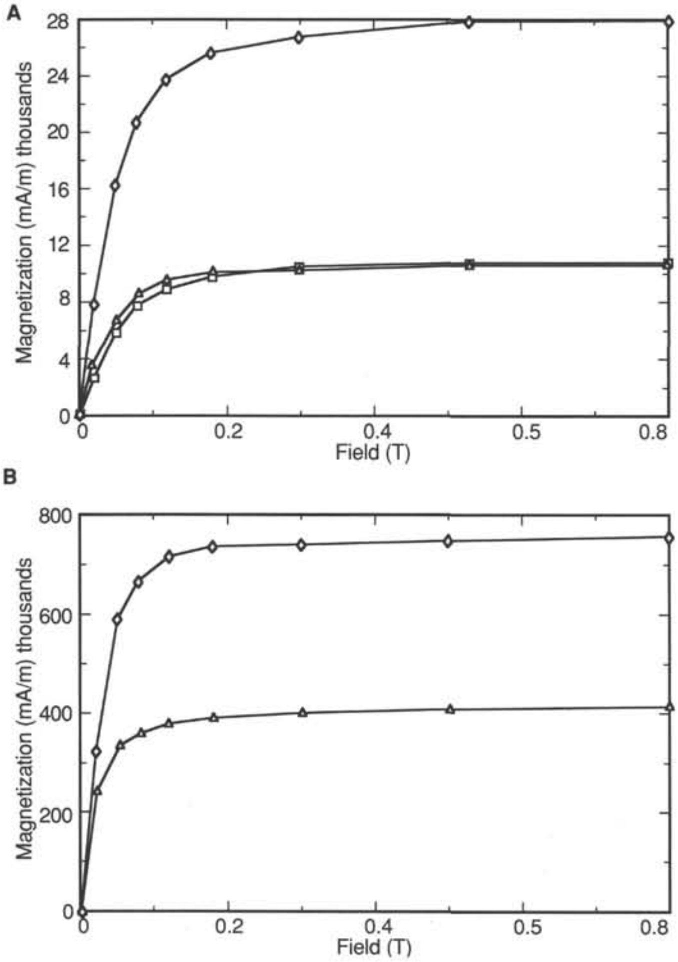

Figure 19. **A.** Isothermal remanent magnetization (IRM) acquisition curves for three nannofossil ooze sediment samples, Hole 839A. Two samples (open squares = Sample 135-839A-3H-1, 88–90 cm, and open triangles = Sample 135-839A-7H-5, 20–22 cm) display saturation in low applied fields, indicating the remanence carrier to be magnetite, whereas a third sample (open diamonds = Sample 135-839A-10H-5, 40–42 cm) saturates above 0.3 Tesla, perhaps indicating that it contains some hematite. **B.** Isothermal remanent magnetization (IRM) acquisition curves for two basalt samples (open diamonds = Sample 135-839B-18R-1, 27–29 cm, and open triangles = Sample 135-839B-19R-1, 44–46 cm), Hole 839B. The samples display saturation in low applied fields, indicating the remanence carrier to be magnetite.

(5 mT or less) and low-coercivity magnetization components, so they acquired a greater drill-string IRM. Other samples had MDFs greater than 15 mT, so they were less affected. As with the Hole 839A sediments, AF demagnetization easily removed the drill-string overprint to reveal a stable characteristic remanent magnetization.

Because AF demagnetization of the core archive halves during Leg 135 was limited to 15 mT, characteristic magnetizations were not always isolated and so the measurements made with the pass-through magnetometer must be regarded as reconnaissance results only.

Magnetic Polarity Stratigraphy

Determination of magnetic polarity stratigraphy was complicated by two factors at Site 839. First, volcaniclastic silt and gravel layers were abundant and often thick (see "Lithostratigraphy" section, this chapter). These sediments were probably deposited rapidly, some perhaps as turbidites. Thus, they probably record the magnetic field only for an "instant" of geologic time. Furthermore, because of their large grain sizes, these sediments are often poor magnetic field direction recorders. Second, as at most other Leg 135 sites, the sediments were prone to acquiring a drill-string-induced IRM overprint that AF demagnetization at 15 mT could not completely remove.

Because the drill-string overprint is directed upward, it gives the sediments an artificial normal polarity (for the Southern Hemisphere), with magnetic inclinations approaching –90°. Furthermore, in the NRM, this overprint entirely masks the inherent polarities of the sediments. Even after AF cleaning to 15 mT, the magnetic inclinations were not distributed symmetrically around zero, as expected if the overprint had been removed. Thus, the magnetic inclinations by themselves were not reliable indicators of polarity. Reversals were not considered reliable unless the magnetic declination changed by approximately 180° and the inclination showed a consistent change from steep negative values to near or greater than zero, or vice versa.

The uppermost 18 mbsf of Hole 839A sediments consist of nannofossil ooze and appear to be accurate magnetic field recorders. They show normal polarity down to 16.3 mbsf (Fig. 21 and Table 5) in Core 135-839A-3H and reversed polarity below (Fig. 21A). This polarity reversal is probably the boundary of the Brunhes and Matuyama chrons. The sediments in the lower part of Core 135-839A-3H through to the bottom of the APC section (Core 135-839A-11H) appear to be predominantly reversed polarity and were probably deposited during the Matuyama Chron. This hypothesis is consistent with biostratigraphic markers (see "Biostratigraphy" section, this chapter).

From the top of the Matuyama Chron downward, two prominent normal-polarity subchrons, Jaramillo and Olduvai, should be encountered in that order. With moderate to high sedimentation rates, two short subchrons, Cobb Mountain and Réunion, might also be seen, the first just below the Jaramillo and the second beneath the Olduvai. The Cobb Mountain subchron has been observed at Sites 834, 835, 837, and 838, whereas the Réunion subchron was observed at Site 834. In Hole 839A, the prevalent volcaniclastic layers yielded spurious magnetic directions, making it difficult to find these subchrons unambiguously. For example, an apparently normal polarity layer occurs between 25.3 and 27.7 mbsf and might be interpreted as the Jaramillo Subchron except that it is in a volcaniclastic gravel layer (Fig. 21A). Instead, the Jaramillo Subchron and underlying Cobb Mountain Event appear to be in a predominantly ooze section at a depth of 35.2–38.3 mbsf in Core 135-839A-5H (Fig. 21).

Beneath the Jaramillo and Cobb Mountain subchrons, the sediments from Hole 839A are probably of reversed polarity. This interpretation is based mainly on the magnetic declinations of oriented cores because the inclinations are variable and usually less than zero, implying that the drill-string overprint is only partially removed. Another apparently normal polarity interval occurs between 48.1 and 54.7 mbsf, but again this is probably spurious because it is within a volcaniclastic silt and gravel layer. A large section of indeterminate polarity characterizes Cores 135-839A-9H and the upper two-thirds of 135-839A-10H because of low recovery in the former and volcaniclastics disturbed by drilling in both.

Below this section a small interval of normal polarity occurs between 90.0 and 91.2 mbsf. It is not easily explained by the magnetic polarity reversal time scale. Being in the Matuyama Chron below the Cobb Mountain Subchron, it should be either the Olduvai or Réunion subchron. If interpreted as the Olduvai Subchron (Model A, Fig. 22), it suggests a sedimentation rate of 5.5 mm/k.y., which is surprisingly low considering the sedimentation

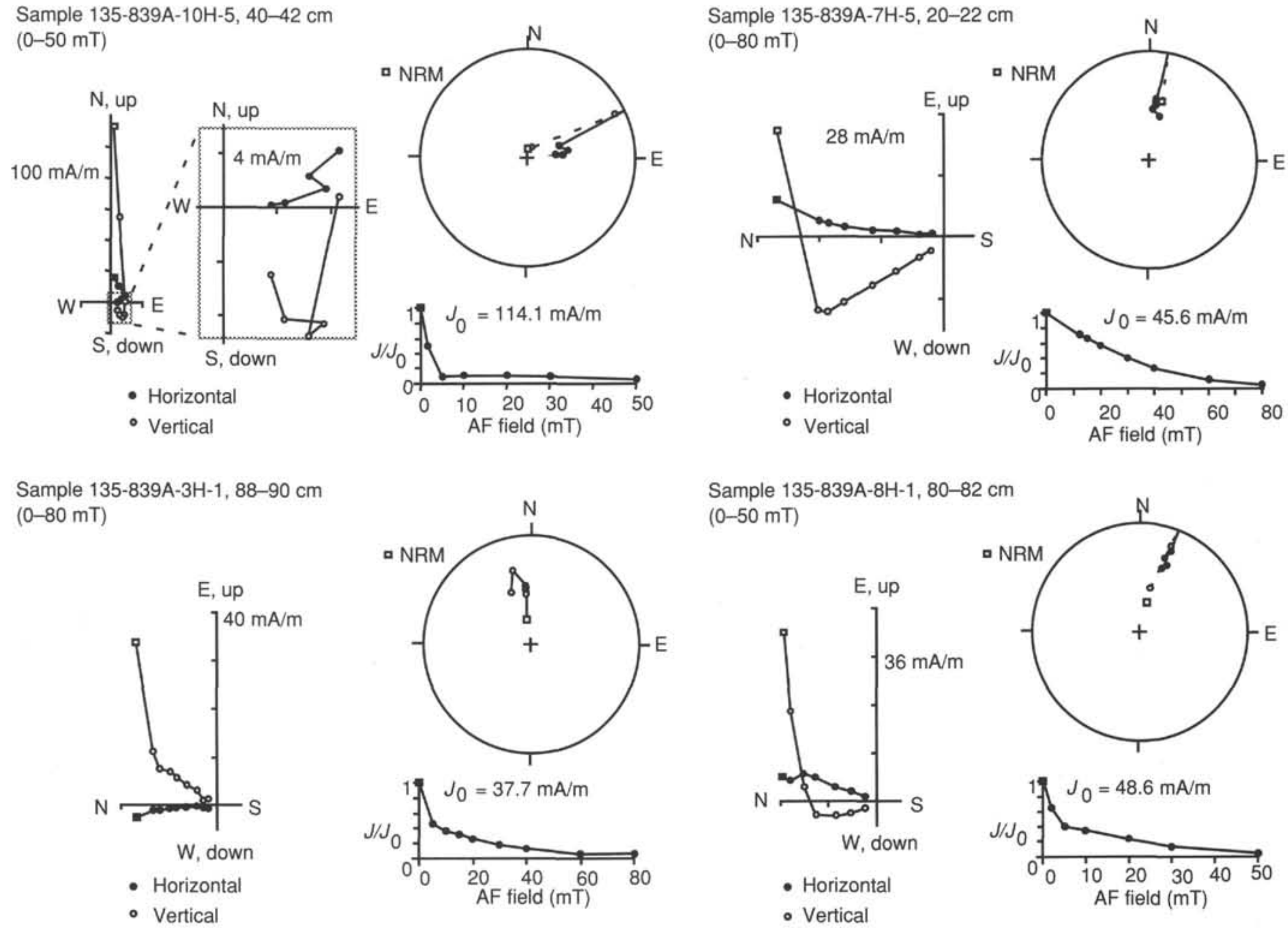

Figure 20. Behavior of two nannofossil ooze samples (left) and two vitreous volcaniclastic silt samples (right) from Hole 839A during alternating-field (AF) demagnetization. In each set of plots, an equal-area stereonet showing magnetization vector endpoints is at upper right; a normalized magnetization decay plot is at lower right; and an orthogonal vector endpoint plot is shown at left. Sample 135-839A-10H-5, 40–42 cm, changes polarity and reveals a characteristic magnetic component above 10-mT AF, although the MDF is as high as 25 mT. Sample 135-839A-3H-1, 88–90 cm, shows the same directional behavior, but the MDF is much lower, only about 4 mT. Sample 135-839A-7H-5, 20–22 cm, changes polarity and reveals a characteristic magnetic component above 10-mT AF; its MDF is low (2 mT). Sample 135-839A-8H-1, 80–82 cm, shows a characteristic stable remanence after 5-mT AF demagnetization, and a low MDF of 5 mT.

rate (112.3 mm/k.y.) implied by the difference in depth between it and the Cobb Mountain Subchron. However, if interpreted as the Réunion Subchron (Model B, Fig. 22), it is older than the deeper sediment found between basalt layers in Hole 839B (see "Biostratigraphy" section, this chapter). Moreover, this model implies that the Olduvai Subchron is missing.

Subtracting the thickness of major volcaniclastic silt, sand, and gravel layers, the magnetic polarity zone depths may be adjusted to reflect more accurately the ooze accumulation rate. This substantially decreases the sedimentation rate in the lower part of Hole 839A and puts the age/depth calibration points very nearly on a straight line (Fig. 22). The upper Matuyama (Brunhes/Matuyama boundary to Cobb Mountain Subchron) sedimentation rate decreases from 69.0 to 25.7 mm/k.y. Moreover, the high sedimentation rate between the Cobb Mountain Subchron and the Olduvai (Model A) or Réunion (Model B) subchrons (112.3 or 51.5 mm/k.y.) is reduced to a rate similar to that in the upper Matuyama Chron. In addition, Model A, in which the normal polarity zone from 90.0 to 91.2 mbsf is interpreted as the Olduvai Subchron, falls more nearly on a straight line extrapolated from the upper Matuyama age/depth points than does Model B. Thus, Model A seems the more plausible.

Using the pass-through cryogenic magnetometer, magnetic polarity measurements were also made on vertically oriented basalt and sediment pieces from the archive halves of Hole 839B cores. Basalt samples recovered between 213.5 and 256.7 mbsf yielded anomalously low inclinations, mainly between −5° and 15° and suggest that these igneous rocks cooled during a magnetic polarity transition (Fig. 23). Several discrete basalt samples from these cores were studied in detail using the spinner magnetometer and AF demagnetization to 100 mT. These measurements show shallow, stable magnetization directions in accord with the pass-through cryogenic magnetometer results (Fig. 24).

Sediments underlying these basalts, in Core 135-839B-17R, 256.7–257.2 mbsf, have reversed polarities. Basalts deeper in Hole 839B are predominantly normally polarized (Fig. 24). The different polarities in these three zones implies a significant age gap between the two basalt layers. Biostratigraphic data constrain the reversely polarized sediments to the lower Matuyama Chron between the Olduvai and Réunion subchrons. This implies that

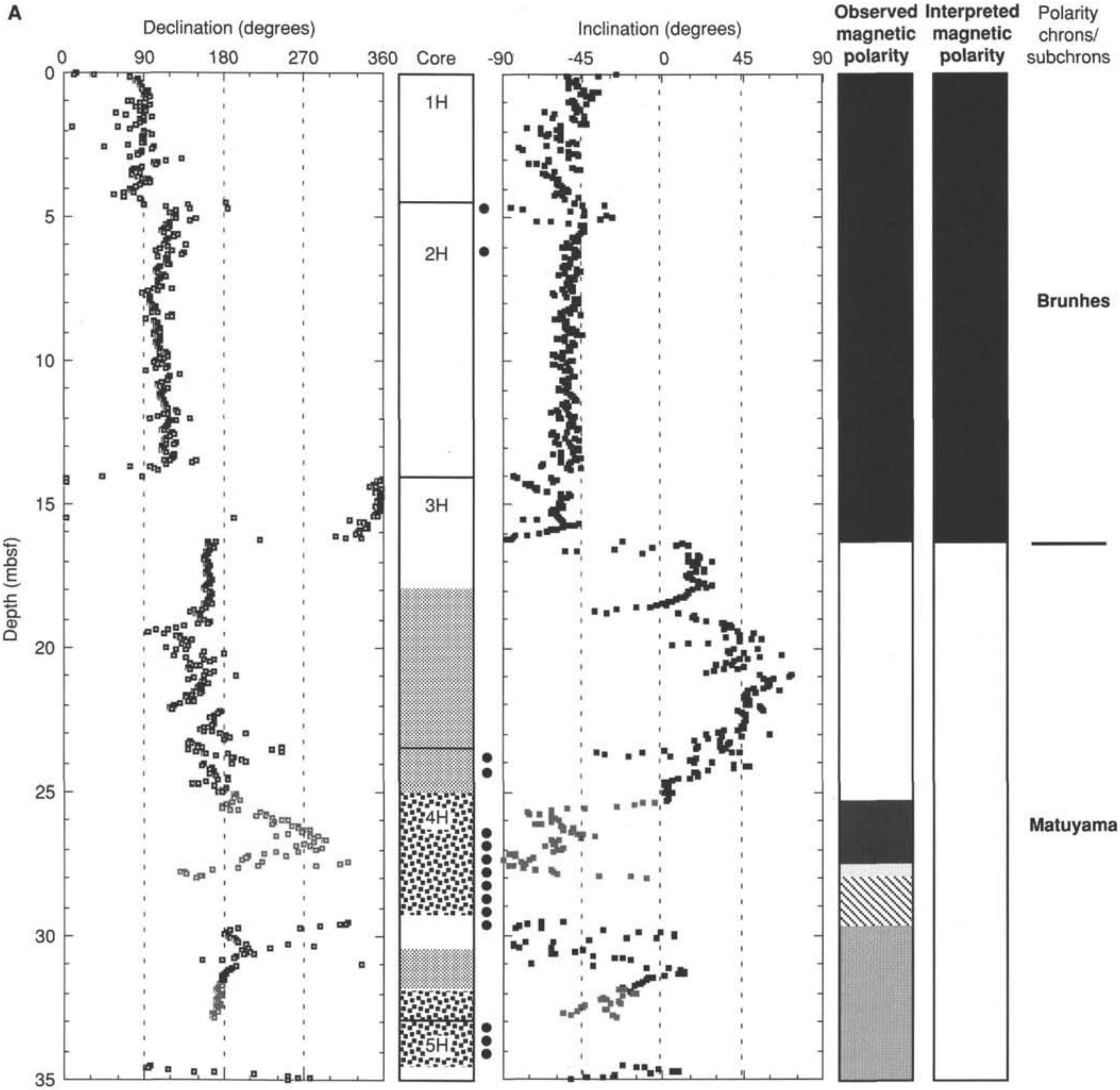

Figure 21. Magnetic polarity stratigraphy, Hole 839A. Wide columns at middle and left show magnetic inclination and declination, respectively. Unreliable inclinations and declinations from volcaniclastic layers are shown in gray. Narrow column in middle shows core boundaries, disturbed core (dots), and volcaniclastic silts, sands (light stipple), and gravels (coarse stipple). Columns at right show observed and interpreted magnetic polarities (black = normal, dark stipple = probably normal, hachure = indeterminate, light stipple = probably reversed, and white = reversed). At far right, chron and subchron names are shown in bold and regular type, respectively.

the normally polarized basalts below were formed either during the Réunion Subchron (approximately 2.01–2.14 Ma; Harland et al., 1982) or perhaps during the previous normal polarity period (i.e., the upper Gauss Chron, 2.47–2.92 Ma; Berggren et al., 1985a, 1985b). The transitional period during which the upper basalt layer was formed is uncertain. It may have been part of the Réunion Subchron (Harland et al., 1982, e.g., divide the Réunion Subchron into two parts), or it may represent the bottom of the Olduvai Subchron.

Magnetic Susceptibility and Q-ratio

Sediments (Level 3)

Volume magnetic susceptibility was measured on a routine basis on whole (i.e., unsplit) core segments of both sediments and basalts from both holes at Site 839, whenever the core sections appeared to be relatively full. Magnetic susceptibility values of Hole 839A sediments range from about 20×10^{-6} to 2000×10^{-6} cgs, and display both long- and short-wavelength variations.

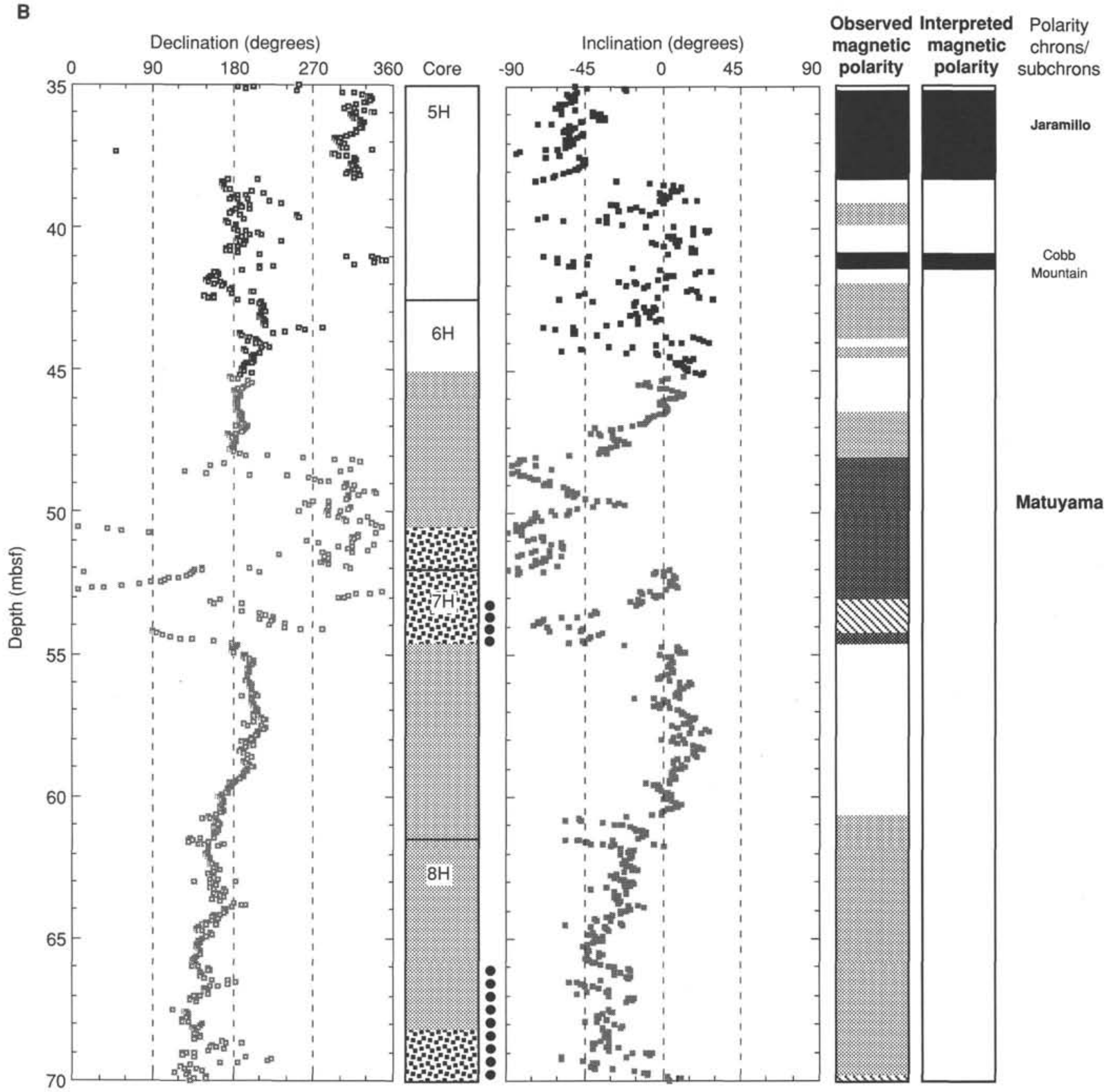

Figure 21 (continued).

The broad-scale variation in susceptibility in Hole 839A sediments (Fig. 25) consists of an order of magnitude oscillation over 10–30 m depth. Most likely, these broad peaks reflect variations in the input of volcanic material, which tends to be strongly magnetic, into the nannofossil oozes, which are typically weakly magnetic. Three to four peaks occur within lithologic Unit I and several peaks are found within Unit II (Fig. 25). The largest of these peaks appear at the bottom of Subunits IIC and IIE where susceptibility values are typically 1000–2000 $\times$ 10^{-6} cgs around 55 mbsf and 82–86 mbsf. Both correlate with the lithologic boundaries.

The most obvious part of the short-wavelength variation also appears to be caused by lithologic variations, in particular the occurrence of ash layers, the thickness of these variations being typically about 2 m. These variations appear superficially similar to those caused by Milankovitch climate variations in other ocean sediments (e.g., Wollin et al., 1971). To investigate possible cyclic variations in the sediment, the modified Q-ratio (Q15 = 15-mT AF-cleaned intensity at susceptibility) was calculated because it is less dependent on material variations than the individual susceptibility and magnetization intensity variations (Fig. 26). The susceptibility and intensity measurements were made at different spacings (3 and 5 cm, respectively), so it was necessary to match the two sets of data by interpolation. Furthermore, because of the wide sensing region of the pass-through magnetometer, the magnetization intensity readings average a parcel of core 10 cm on either side of the measurement depth, so both data sets were filtered through a 10-cm window.

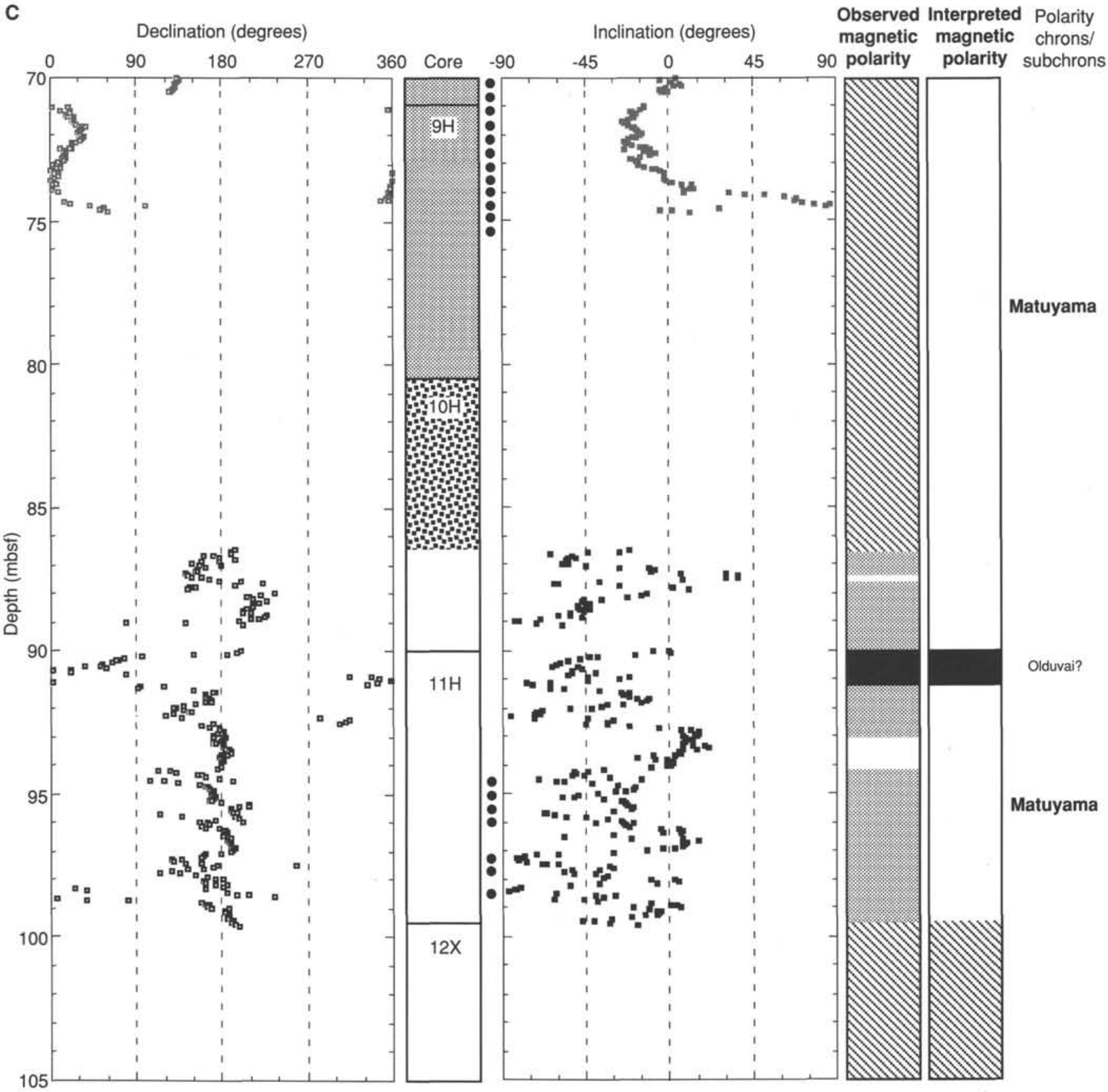

Figure 21 (continued).

Counting the number of Q15 cycles in the top 16.3 m of Hole 839A (i.e., from the beginning of the Brunhes Polarity Chron, at 0.73 Ma) that contain at least two data points (20 cm width) at maximum and also in the adjacent minima, about 20 cycles are found, yielding an average period of about 36 k.y. per cycle, which is similar to the 41-k.y. period of the Earth's tilt (obliquity) in the Milankovitch cycle theory (Berger, 1978; deMenocal et al., 1991). We therefore suggest that these cycles, as in the previous Leg 135 sites, are likely an indication of the magnetic properties mirroring the climatic variations.

Basalts

Magnetic susceptibility values in the basalts of Site 839 were strongly variable, ranging from 20×10^{-6} to 2000×10^{-6} cgs (Fig. 27). Because the cores sometimes contained basalt fragments and were not always full, the whole-core susceptibility measurements must be taken as minimal values and only used for reconnaissance. A broad cyclic variation is noted, with susceptibility peaks at 230 and 370 mbsf. This cyclicity is likely to indicate broad lithologic variations in the basalts (see "Igneous Petrology" section, this chapter), perhaps showing fluctuations in the concentration of iron-bearing minerals.

The susceptibility shows a large jump at the sediment-basalt interface and continues to rise until it reaches a peak of 2000×10^{-6} cgs in the middle of igneous Unit 1 (Fig. 27). Susceptibility values decline through Unit 2 and reach a minimum at about 320 mbsf in Unit 3. They rise again through Units 4–8 and peak in the upper part of Unit 9.

Table 5. Magnetic polarity zones, Hole 839A.

Depth (mbsf)	Polarity	Age (Ma)	Chron/subchron
0.0			
	N		BRUNHES
16.3		0.73	
	R		MATUYAMA
25.3			
	N?		
27.7			
	R?		
28.0			
	I		
29.7			
	R?		
35.2		0.91	
	N		Jaramillo
38.3		0.98	
	R		
39.1			
	R?		
39.9			
	R		
40.9			
	N	1.12	Cobb Mountain
41.4			
	R		
41.8			
	R?		
43.8			
	R		
44.1			
	R?		
44.6			
	R		
46.5			
	R?		
48.1			
	N?		
53.1			
	I		
54.2			
	N?		
54.7			
	R		
60.7			
	R?		
69.8			
	R		
70.6			
	I		
86.5			
	R?		
87.3			
	R		
87.6			
	R?		
90.0		1.66	
	N		Olduvai?
91.2		1.88	
	R?		
92.8			
	R		
94.1			
	R?		
99.5			
	I		
TD			

Notes: Magnetic polarity reversal time scale of Berggren et al. (1985a, 1985b), with Cobb Mountain Subchron age from Clement and Robinson (1987). Chron names in capital letters, and subchron names in lowercase letters. TD = total depth of hole.

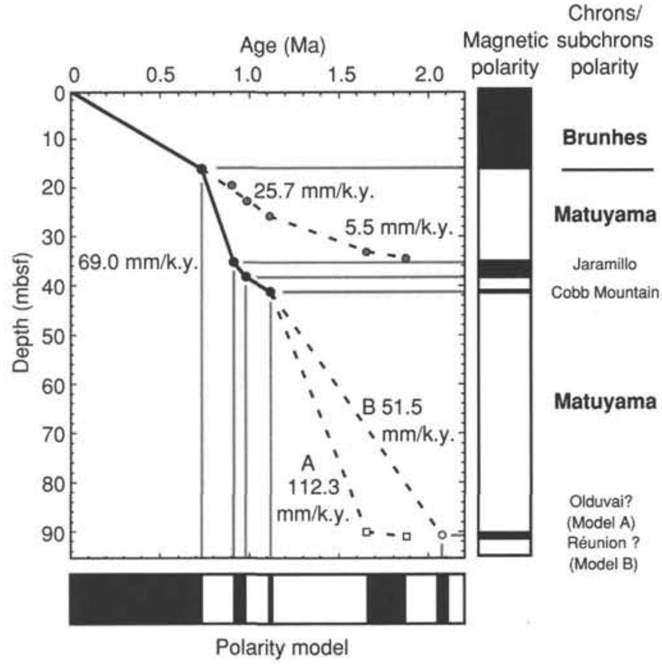

Figure 22. Age vs. depth plot from magnetic polarity stratigraphy, Hole 839A. Reliable age/depth points are shown in black and connected with a solid line. Less reliable points at bottom of hole are denoted by an open circle and open squares. Two possible models are shown (A and B), in which the normal polarity zone at 90 mbsf is interpreted as either the Olduvai Subchron (Model A) or Réunion Subchron (Model B). Gray dots show age/depth points adjusted upward by removing the thickness of volcaniclastic layers to reflect the ooze accumulation rate. Sedimentation rates are also shown.

Core Orientation

Cores 135-839A-4H through -11H were oriented using the multishot camera (see "Explanatory Notes" chapter, this volume). Usable orientation photographs were obtained for all eight cores (Table 6).

INORGANIC CHEMISTRY

Introduction

A total of seven interstitial water samples were collected at Site 839. They were sampled from every core in the uppermost 31 mbsf. Below this depth, samples were taken every second core. Water samples were extracted by means of standard ODP squeezing techniques (see "Explanatory Notes" chapter, this volume). The results are summarized in Table 7, and the depth-concentration distribution is shown in Figure 28.

In Hole 839A, dissolved major constituents (chloride, sodium, calcium, magnesium, potassium, and sulfate) were determined. Subsequent charge-balance calculations yielded sodium concentrations. Ammonia, phosphate, silica, strontium, and manganese were also conducted using colorimetric methods and flame AA spectrophotometry.

Chemical Components

In Hole 839A, chloride, sodium, calcium, manganese, potassium, sulfate, and strontium concentrations are indistinguishable from the average seawater concentration (Fig. 28) and are comparable with those obtained in Holes 834A, 835A, 836A, and 837A.

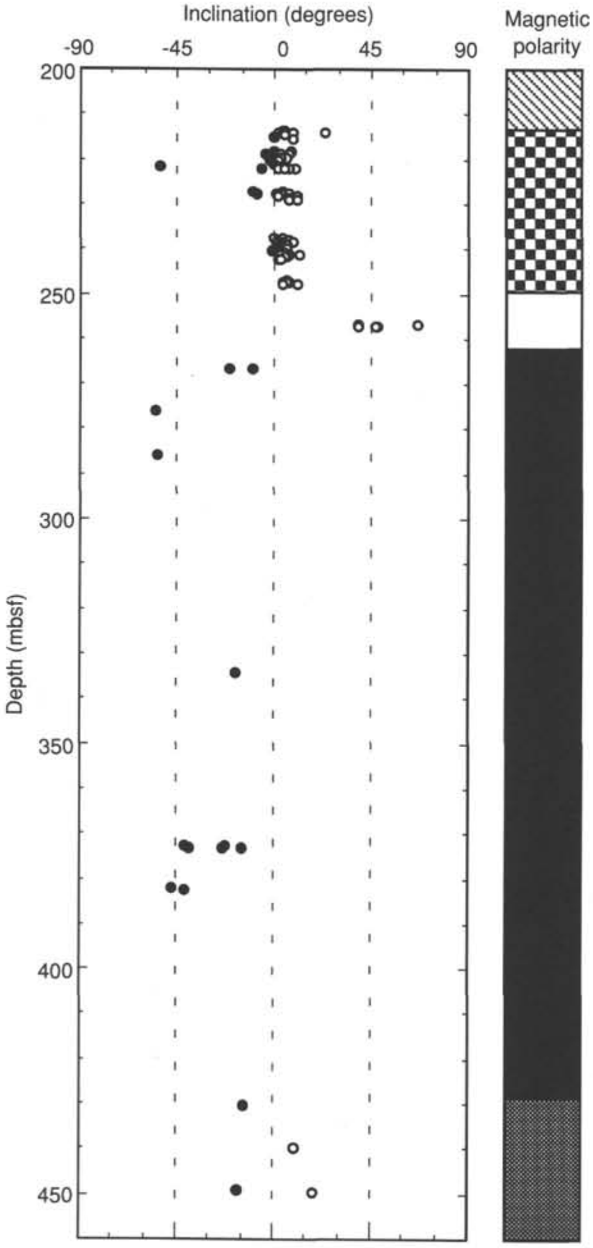

Figure 23. Magnetic polarity, Hole 839B. Measurements were made on basalt and sediment pieces from archive core halves by means of the pass-through cryogenic magnetometer and an AF demagnetization of 15 mT. Column at right shows interpreted magnetic polarity (black = normal, dark stipple = probably normal, transitional = checkerboard, white = reversed, hachures = indeterminate).

As mentioned for the other Leg 135 sites, values of ammonia and phosphate concentrations in pore-water samples from Hole 839A are very low and are consistent with the fairly uniform sulfate data.

The manganese concentration-depth profile at Site 839 is comparable with those obtained at Sites 834, 835, 837, and 838 (at Site 836, Mn concentrations were below the detection limit). At all of these sites, there is an increase of Mn with depth to a maximum (e.g., 88 µM at Site 839 at 48.5 mbsf). Below this Mn maxima a decrease in Mn is observed, with Mn concentration reaching a low value (e.g., 21 µM at Site 839) near the hemipelagic sediment-basaltic basement interface. Low Mn values at the

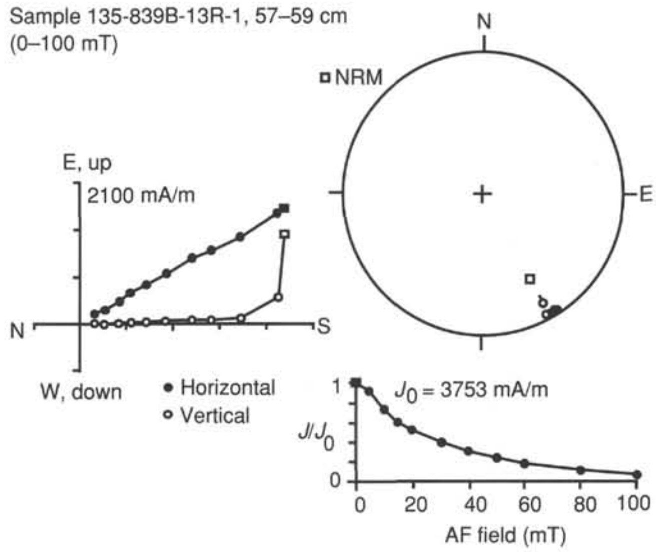

Figure 24. Behavior of a transitional polarity basalt sample from Hole 839B during alternating-field (AF) demagnetization. Figure conventions as in Figure 20.

Table 6. APC core orientation data, Hole 839A.

Core no.	Camera no.	Compass	Inclination Direction	Inclination Drift	Declination
135-839A-					
4H	3209	A	N35°E	1.5°	153°
5H	3209	A	105°	0.8°	93°
6H	3209	A	90°	0.6°	130°
7H	3250	B	60°	1.2°	174°
8H	3250	B	65°	1.0°	112°
9H	3209	A	82°	1.2°	357°
10H	3209	A	100°	1.0°	50°
11H	3250	B	72°	1.4°	172°

Notes: Magnetic declination at Site 839 is 13198E. Compass B was misaligned; to correct its declination values, add 13°. Inclination is the off-vertical angle of the core. Drift and direction are the dip and dip direction measured clockwise from north of a plane perpendicular to the core axis. Declination is the angle between the double line on the core liner and magnetic north (measure clockwise).

base of the sedimentary column also have been observed at Sites 834, 835, and 838 where the basal sediments are characterized by high proportions of volcaniclastic material. However, at Site 838, diffusive exchange with the underlying basalt crust probably affected the seawater signature. At Site 837, the deepest sample analyzed (71 mbsf) shows the highest Mn concentration (87 µM) of this hole. This difference could be related to the lithology of the sedimentary column at Site 837. Indeed, the basal sediments comprised a lesser amount of the volcaniclastic material and a greater clay amount than those observed in the other sites. Hence, the major pathway of the downwelling flow could be probably located in the deeper horizon.

Conclusion

The main features revealed by the interstitial water chemistry data of Hole 839A are as follows:

1. There is a lack of a gradient in the concentration-depth profiles of the major elements.
2. Dissolved Mn reaches a maximum concentration at 48.5 mbsf, yet toward the bottom of the sediment cover, a pore-water

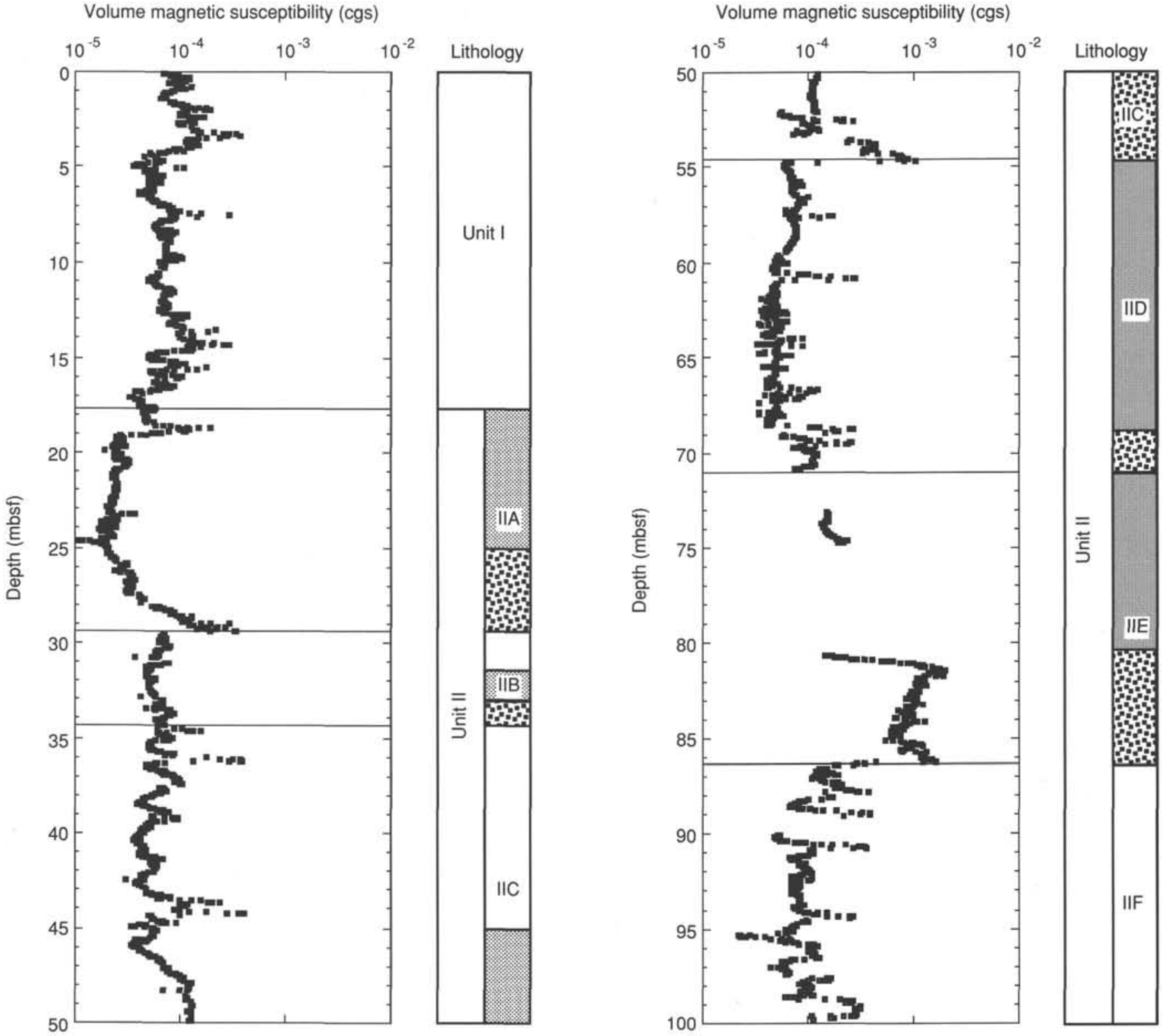

Figure 25. Volume magnetic susceptibility, Hole 839A. Column at left shows susceptibility values, plotted on a logarithmic scale. Column at right denotes stratigraphy. Light stipple areas indicate sections of core containing ash layers, coarse stipple areas indicate volcaniclastic gravel.

Table 7. Interstitial water chemistry, Hole 839A.

Core, section, interval (cm)	Depth (mbsf)	pH	Alkalinity (mM)	Salinity (‰)	Ca^{2+} (mM)	Mg^{2+} (mM)	K^+ (mM)	Cl^- (mM)	SO_4^{2-} (mM)	NH_4^+ (μM)	PO_4^{3-} (μM)	Si^{4+} (μM)	Sr^{2+} (μM)	Mn^{2+} (μM)	Na^+ (mM)
135-839A-															
1H-2, 140–150	3.0	7.62	3.178	35.6	10.5	53.7	10.8	548	27.5	16	5.7	316	103	45.9	465
2H-4, 140–150	10.5	7.44	2.995	35.5	10.3	53.8	11.5	549	28.5	15	2.8	345	101	54.8	464
3H-4, 140–150	20.0	7.61	2.958	35.3	10.5	53.6	9.9	549	28.1	17	2.1	289	99	56.3	467
4H-4, 140–150	31.0	7.53	2.942	35.4	10.4	53.7	10.2	550	27.3	18	2.3	405	101	65.9	466
6H-4, 140–150	48.5	7.86	2.118	35.5	10.4	53.8	11.5	554	28.7	18	1.4	339	100	87.9	465
8H-4, 140–150	67.5	7.94	3.035	36.0	10.6	53.9	10.3	546	28.4	23	1.1	357	93	51.6	465
10H-5, 140–150	88.0	7.66	2.369	35.5	10.3	50.7	11.6	547	27.2	20	1.9	339	97	20.6	468

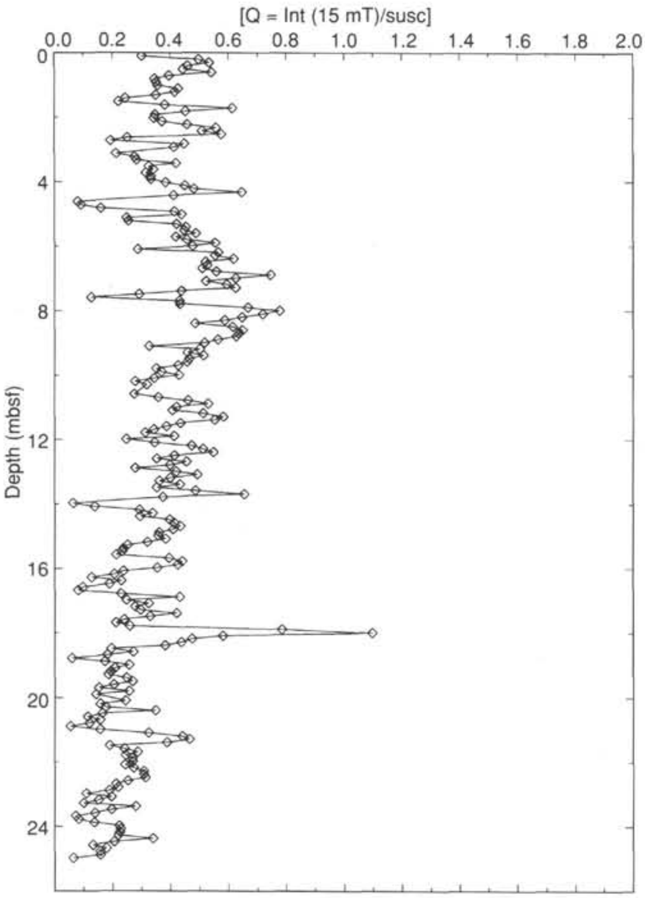

Figure 26. Modified Q-ratio for the upper 25 m of Hole 839A. About 20 cycles are seen in the upper 16.3 m, the depth of the Brunhes-Matuyama Polarity Chron boundary, which has an age of 0.73 Ma. The Q cycles may be Milankovitch cycles.

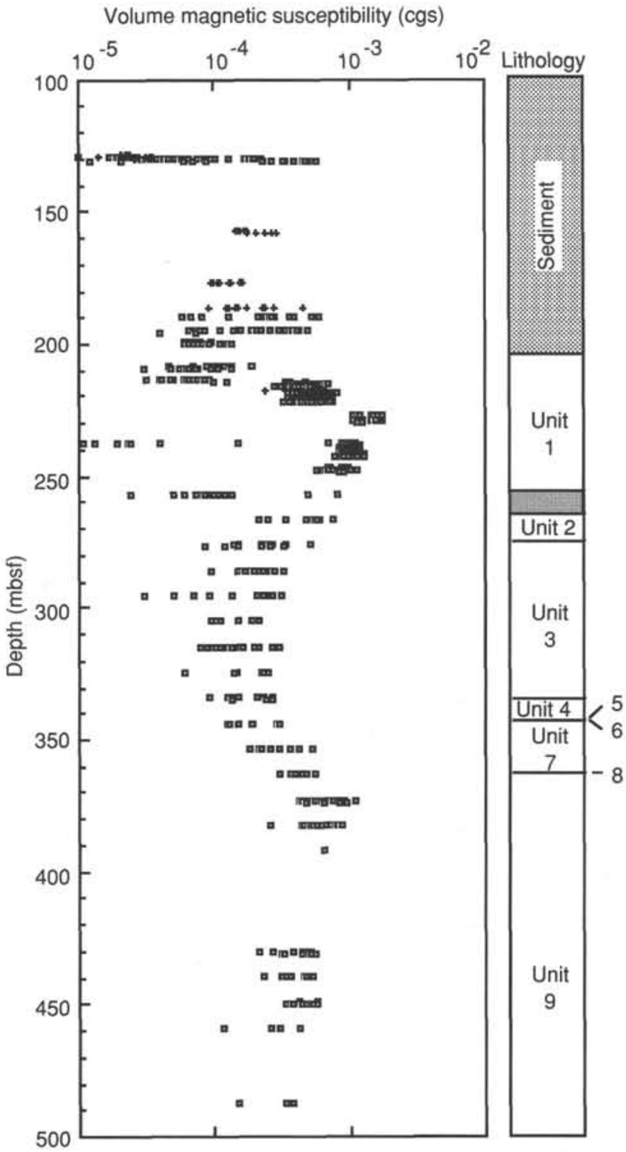

Figure 27. Volume magnetic susceptibility, Holes 839A and 839B combined. Susceptibility scale is logarithmic. Squares = susceptibility values from Hole 839B, and plus signs = values from Hole 839A. Column at right shows igneous unit boundaries.

Mn decrease is observed. The variation in the Mn data probably results both from water-mineral interactions that cause a Mn increase with depth and a dilution effect that causes a pore-water Mn decrease in the lower part of the sedimentary cover. These features also have been observed at Sites 834, 835, and 838, and argue for low advection of seawater at the boundary between hemipelagic sediment and the basaltic basement. This circulation seems to be helped by the occurrence of permeable volcanic material overlying the basement.

ORGANIC GEOCHEMISTRY

Shipboard organic geochemical analysis of samples from Hole 839A consisted of 10 determinations of volatile hydrocarbons in sediments using the Carle gas chromatograph, 10 determinations of total nitrogen, carbon, and sulfur using the Carlo Erba NCS analyzer, and 46 determinations of total inorganic carbon using the Coulometrics 5011 coulometer equipped with a System 140 carbonate/carbon analyzer. In addition, one determination of the volatile hydrocarbons in Hole 839B was also made. Details of the analytical procedures used are outlined in the "Organic Geochemistry" section of the "Explanatory Notes" chapter (this volume) and are described in detail by Emeis and Kvenvolden (1986).

The volatile hydrocarbon gases were obtained from the bulk sediment using the head-space sampling technique and were routinely monitored for methane, ethane, and propane. Samples were taken from Cores 135-839A-1H, -6H, -8H, -10H, -11H, and -15H and Core 135-839B-11R. Methane concentrations in all of the samples were between 2 and 3 ppm, which is very low and at the laboratory background level. Ethane and propane were not detected. The extremely low concentration of methane indicates that methanogenesis is not occurring in these sediments. As was the case at Sites 837 and 838, a significant contributing factor could be the very low levels of organic carbon (see below) in these sediments, which are probably not enough to sustain microbial activity. A second sample from Core 135-839A-11H was analyzed using the NGA instrument. This showed that the composition of the head-space gas was very similar to that of air with the exception that carbon dioxide was ten times more abundant (approximately 3000 ppm).

Determinations of inorganic carbon (IC) contents were performed on the samples used for physical properties and on additional samples selected by the sedimentologists. Percent $CaCO_3$ is calculated according to the equation:

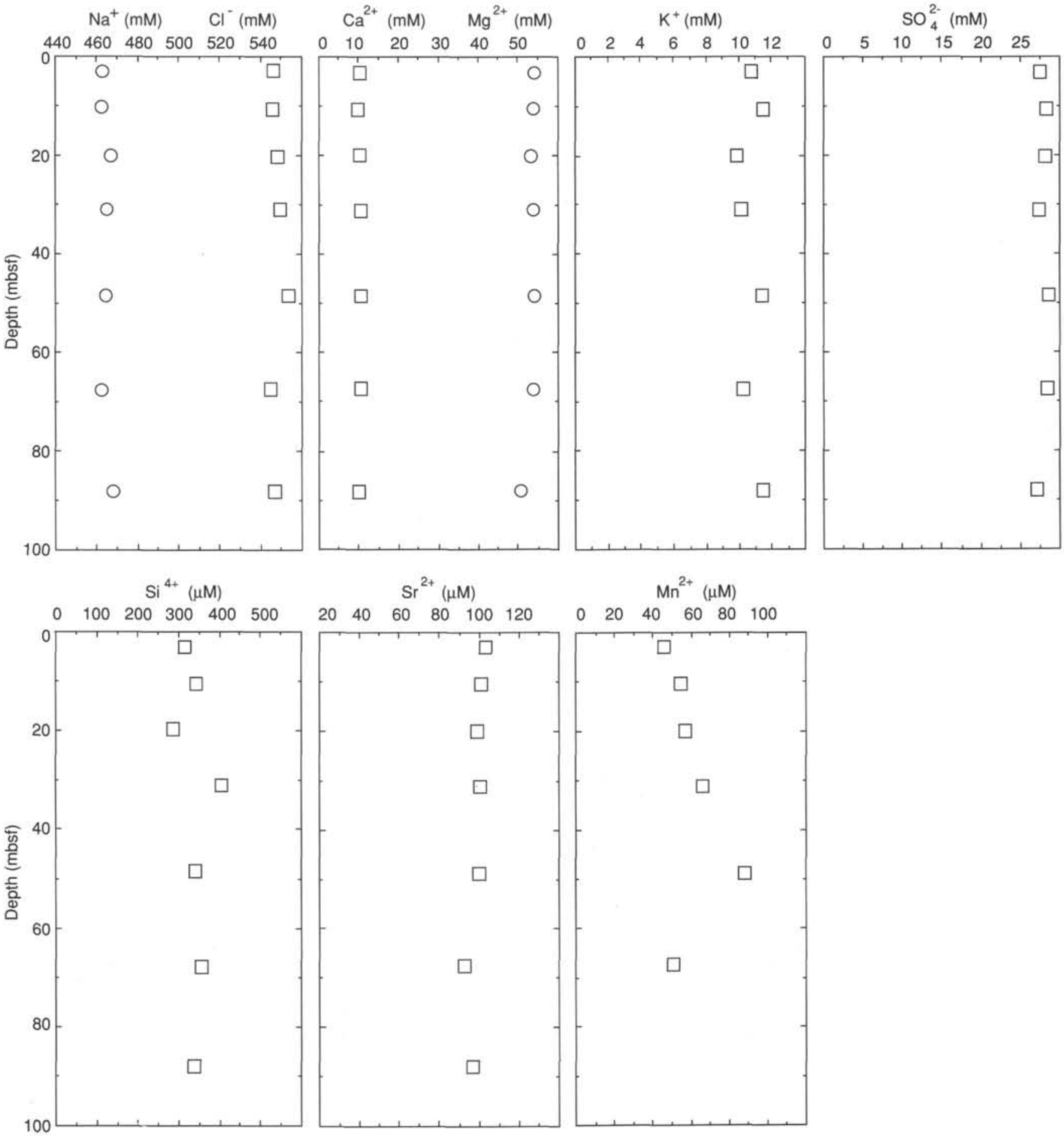

Figure 28. Concentration vs. depth profiles for chloride and sodium, calcium and magnesium, potassium, sulfate, silica, strontium, and manganese, Hole 839A.

$$CaCO_3 = IC \cdot 8.334.$$

This equation assumes that all the carbonate is present as calcite. The data from these analyses are presented in Table 8. Carbonate values range from <1.5% to 60.6%. Samples from Unit I (down to 17.37 mbsf) show values between 22.8% and 60.6%, whereas Unit II, which is dominated by volcaniclastic sediments, shows much lower carbonate values except where the occasional interval of nannofossil ooze was present. This is discussed in more detail and related to the lithologic units in the "Lithostratigraphy" section of this site chapter.

Also shown in Table 8 are the percentages of total carbon for the 10 samples measured. Total organic carbon (TOC) is defined here as the difference between the total carbon and the inorganic carbon values. The sediments from Site 839 have organic carbon contents between 0.01% and 0.17% and hence were considered

Table 8. Concentrations of inorganic and organic carbon at Hole 839A.

Core, section, interval (cm)	Depth (mbsf)	Total carbon (%)	Inorganic carbon (%)	Total organic carbon (%)	$CaCO_3$ (%)
135-839A-					
1H-1, 79–80	0.79		2.74		22.8
1H-2, 78–79	2.28		4.07		33.9
1H-3, 69–70	3.69	5.54	5.37	0.17	44.7
2H-2, 79–80	6.79		7.21		60.1
2H-4, 79–80	9.79		7.12		59.3
2H-6, 94–95	12.94	5.16	5.15	0.01	42.9
3H-1, 68–69	14.68		6.27		52.2
3H-2, 78–79	16.28		6.61		55.1
3H-3, 37–38	17.37	7.37	7.28	0.09	60.6
3H-4, 53–54	19.03		3.3		27.5
3H-4, 78–79	19.28		0.32		2.7
3H-4, 111–112	19.61		0.25		2.1
3H-6, 78–79	22.28		0.42		3.5
4H-2, 88–89	25.88		0.18		1.5
4H-5, 6–7	29.56		6.78		56.5
4H-5, 27–28	29.77		5.58		46.5
4H-5, 81–82	30.31	6.17	6.08	0.09	50.6
4H-5, 129–130	30.79		7.07		58.9
4H-6, 81–82	31.81		0.58		4.8
5H-2, 104–105	35.54		5.6		46.6
5H-3, 52–53	36.52		6.07		50.6
5H-3, 86–87	36.86	0.55	0.54	0.01	4.5
5H-5, 80–81	39.8		3.74		31.2
5H-6, 13–14	40.63	7.06	6.96	0.1	58
5H-6, 134–135	41.84		0.76		6.3
6H-1, 86–87	43.36		4.15		34.6
7H-2, 87–88	54.37	0.55	0.47	0.08	3.9
7H-4, 81–82	57.31		0.79		6.6
7H-5, 120–121	59.2		0.89		7.4
7H-7, 41–42	61.41		0.34		2.8
8H-1, 74–75	62.24		0.39		3.2
8H-3, 74–75	65.24		0.42		3.5
8H-5, 60–61	68.1		0.33		2.7
8H-7, 19–20	70.69		0.24		2
9H-2, 52–53	73.02		0.27		2.2
9H-3, 51–52	74.51		0.28		2.3
10H-5, 55–56	87.05	6.14	6.12	0.02	51
10H-6, 52–53	88.52		5.17		43.1
10H-CC, 16–17	89.27		5.73		47.7
11H-1, 98–99	90.98		5.29		44.1
11H-2, 31–32	91.81		5.01		41.7
11H-3, 51–52	93.51	4.09	3.95	0.14	32.9
11H-4, 52–53	95.02		0.87		7.2
11H-5, 40–41	96.4		0.96		8
11H-6, 91–92	98.41		0.37		3.1
11H-7, 31–32	99.31	0.9	0.89	0.01	7.4

too low for analysis by the Rock-Eval instrument. These are very low and, as for Holes 837A and 838A, probably reflect the amount of volcaniclastics in these sediments. The nitrogen and sulfur contents were also measured, but each element was only detected in one of the samples analyzed and then in very low concentrations. There was 0.01% nitrogen in the sample from 12.94 mbsf (Hole 839A) and 0.04% sulfur in the sample from 99.31 mbsf (Hole 839A).

IGNEOUS PETROLOGY

Introduction

Igneous rocks were recovered from 205.85 to 218.20 mbsf in Hole 839A and from 214.15 to 497.26 mbsf in Hole 839B (Fig. 29). An interbedded sedimentary unit was recovered in Hole 839B from 256.81 to 266.40 mbsf. The igneous rocks are the most arclike of the basement materials recovered from the backarc sites drilled on Leg 135. Two principal rock types were found: sparsely to highly phyric olivine-clinopyroxene basalts and moderately to highly phyric plagioclase basaltic andesites. The separation into basalt and basaltic andesite is supported by major and trace element XRF data.

Four major (>10 m thick) and four minor (<10 m thick) igneous lithologic units were identified on the basis of hand specimen and thin section descriptions. The unit names used in visual core descriptions are based on hand-specimen observations; Unit 9, for example, is described as a pyroxene-plagioclase basalt in the visual core descriptions, but as a clinopyroxene-orthopyroxene-plagioclase basalt in the thin section descriptions. Lithologic units were defined as sequences of cooling units having similar lithology and petrography (Fig. 29).

The uppermost igneous unit (Unit 1) is a thick (42 m) aphyric to moderately phyric clinopyroxene-olivine basalt comprising only a small number of cooling units (Fig. 30). This unit is overlain by upper Pliocene sediments (nannofossil Zone CN13; see Biostratigraphy section, this chapter). Recovery in Core 135-839B-12R and the results of the downhole logging indicate that the sedimentary-igneous contact at the top of Unit 1 is at about 214 mbsf (Fig. 29).

Unit 2 is a thin sequence of moderately phyric clinopyroxene-orthopyroxene-plagioclase basaltic andesite which is separated from Unit 1 by an interbed of upper Pliocene sediments (nannofossil Zone CN12d, see Biostratigraphy section, this chapter). This basaltic andesite overlies a moderately to highly phyric clinopyroxene-olivine basalt (Unit 3, 334.33–353.3 mbsf) which shows a marked increase in phenocryst content near its base. There is a sharp contact between the olivine-rich base of Unit 3 and the sparsely phyric olivine-clinopyroxene basalt which constitutes Unit 4 (334.33–353.3 mbsf).

Units 5, 6, 7, and 8 are represented by eight pieces constituting <0.5 m of recovery from Cores 135-839B-27R and 28R. Units 5 and 7 are moderately phyric pyroxene-plagioclase basalts much like those of Units 2 and 9. Units 6 and 8 are phyric clinopyroxene-olivine basalts similar to rocks in Unit 3. Units 5, 6, 7, and 8 may represent interfingering of flows related to Units 3 and 9. However, these four units were recovered in a very short segment of core during a time of hole instability. This sequence of small (<10 cm) fragments could instead represent pieces of rock that originated higher in the hole, and may be pieces of Units 2 and 3 displaced downhole.

Unit 9, the lowermost 135 m (49%) of the recovered volcanic section, comprises a series of flows of moderately to highly phyric clinopyroxene-orthopyroxene-plagioclase basalt. There is a small chemical change within Unit 9 at 410 m, at which depth there is also a discontinuity in the downhole logs (Fig. 29).

The lithologic and petrographic characteristics of the igneous section from Site 839 are described in detail in the next section. A synopsis of the petrographic characteristics of the igneous units is included in Table 9; representative modal analyses are shown in Table 10.

Lithology and Petrography

Unit 1

Aphyric to Moderately Phyric Clinopyroxene-Olivine Basalt

Unit 1 is an aphyric to moderately phyric clinopyroxene-olivine basalt (Fig. 31). Although the grain size is dominantly <1 mm, it is holocrystalline and is generally diabasic. The material from the uppermost part of the unit (Cores 135-839A-23X to -25N-1, and Core 135-839B-12R) is somewhat finer grained than that in the lower cores. The unit is intercalated with upper Pliocene sediments; the upper contact appears to be depositional. The small number of intra-unit-chilled margins recovered (Fig. 30) indicates a massive eruptive unit, perhaps consisting of a number of thick (e.g., >5 m) flows. The basalt is sparsely to moderately phyric at

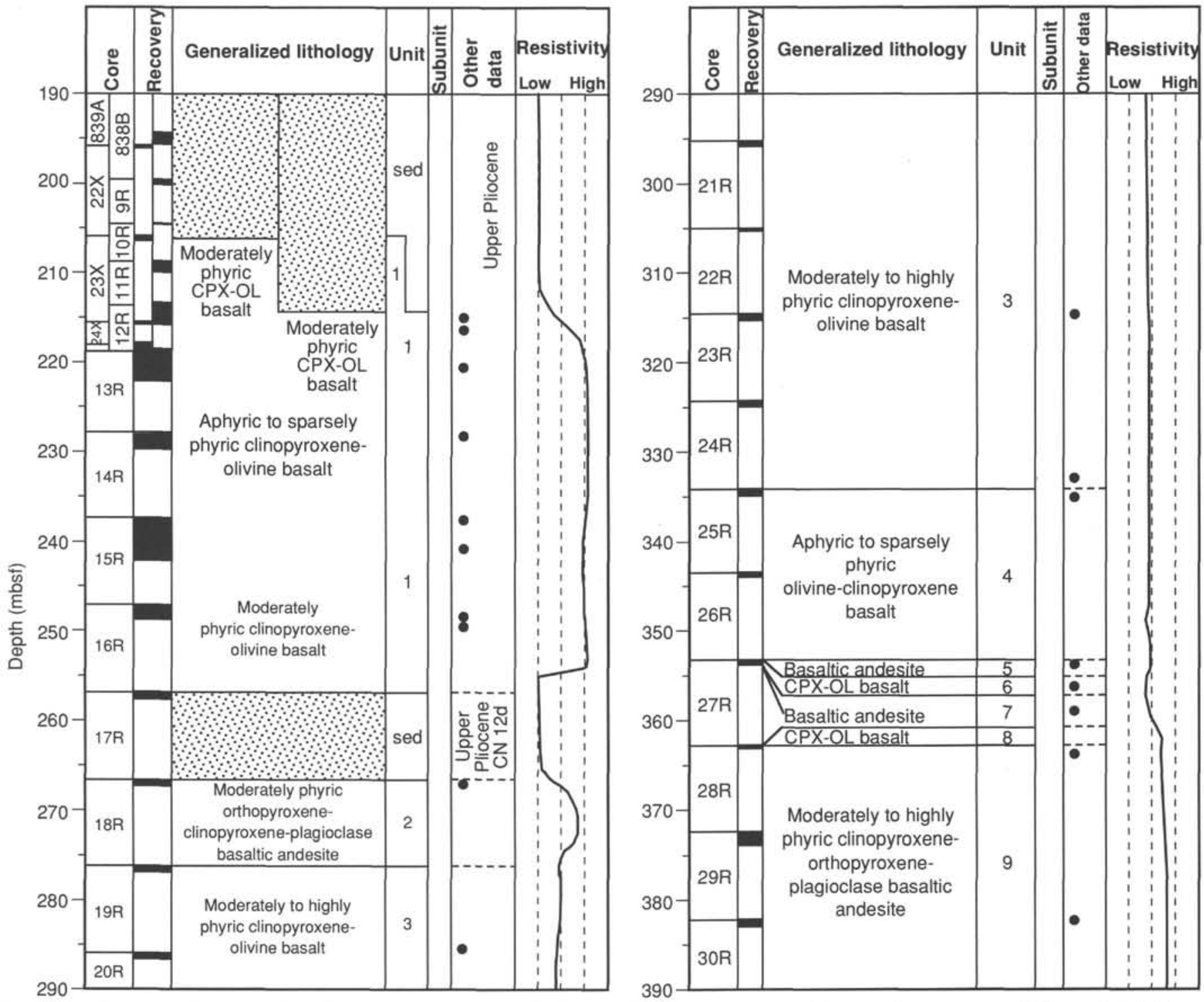

Figure 29. Summary of igneous lithologies recovered from Holes 839A and 839B. Stippled pattern indicates sedimentary material. Large dots indicate shipboard thin-section locations. Resistivity data are a simplified summary of results from downhole logging.

its top (Core 135-839B-12R) and its base (Core 135-838B-16R) and aphyric to sparsely phyric in the interior.

The basalt is highly vesicular, with vesicle abundances ranging between 20 and 40 modal% in the upper part of the unit to 10–20 modal% in the lower part of the unit. Vesicle sizes range from 0.05 to 10 mm, and tend to be bimodally distributed, being predominantly <0.7 or >1 mm. The larger vesicles are much less common and are irregularly distributed throughout the unit, whereas the smaller vesicles are abundant and interconnected and give the groundmass a pervasive porosity. Very dark gray, quenched, vesicular fillings line pre-existing vesicles and also occur as thin (approximately 1 mm thick) stringers and veinlets. Prominent subvertical vesicle trains occur in Section 135-839B-14R-1.

Petrographic analysis reveals considerable mineralogic and textural variation throughout the unit. The samples all have markedly seriate textures, and the distinction between phenocrysts and groundmass is arbitrary. Modal data (Table 10) confirm that the basalt is mostly aphyric, becoming moderately phyric toward the base. Phenocrysts present are olivine (0.3–1.4 modal%, typically subhedral, as large as 2 mm in size, with resorption evident in some crystals), and clinopyroxene (up to 1.5 modal%; euhedral to subhedral, usually forming glomerocrysts, as large as 1 mm in size, and commonly exhibiting sector zoning, twinning, and undulatory extinction), and rare large (as much as 1 mm), euhedral Cr-spinel. The Cr-spinel forms discrete, deep red-brown glomerocrysts, the individual crystals varying between euhedral and subhedral. In addition, small (<0.05 mm in size) Cr-spinel inclusions occur within olivine phenocrysts.

Plagioclase, clinopyroxene, olivine, and magnetite form the groundmass throughout the unit. Of particular significance is the occurrence of orthopyroxene coexisting (though not necessarily in equilibrium) with, and forming rims on, olivine (Fig. 32). This assemblage is especially prominent in the central portion of the unit. The groundmass plagioclase (20–39 modal%) forms elongated, euhedral to subhedral, lath-shaped crystals, extending to microlite size (<0.6 mm in size). The plagioclase crystals are randomly oriented and developed into an interlocking network with interstitial clinopyroxene (Fig. 32). Zoning to distinct sodic rims is visible on some of the crystals. Clinopyroxene (16–26

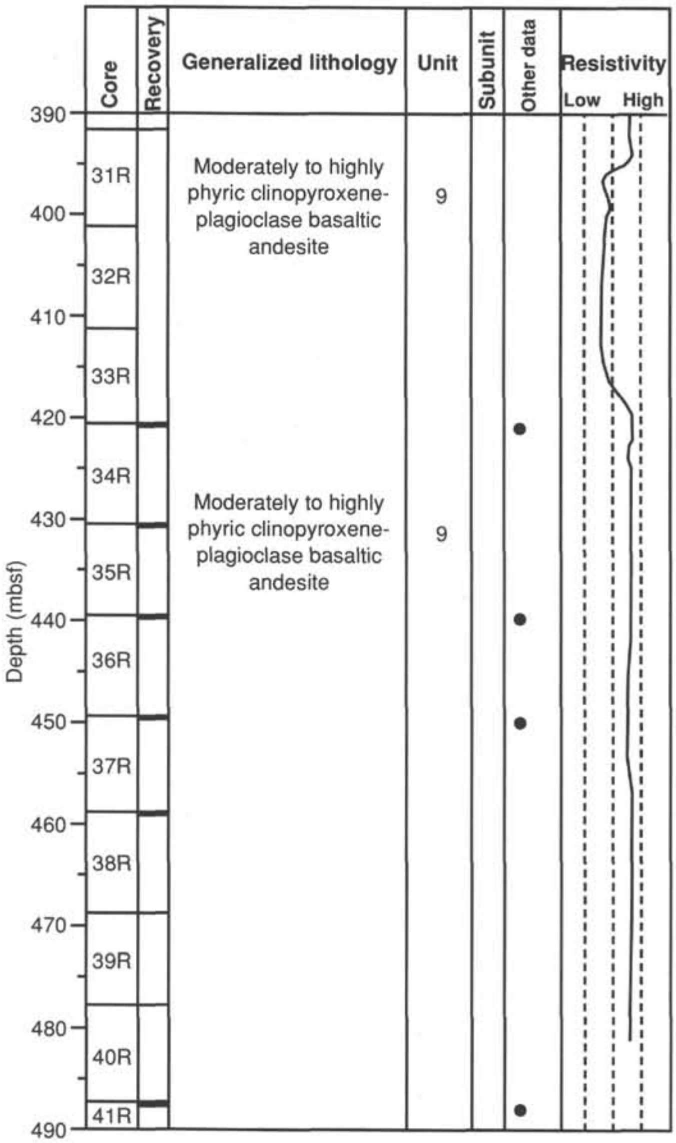

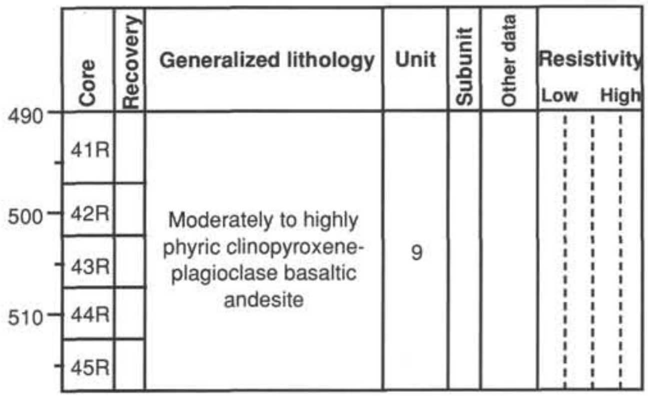

Figure 29 (continued).

modal%) occurs as subhedral to anhedral single grains and in grain clusters. Lamellar twinning and undulatory extinction are notable in some crystals; the pyroxene commonly interstitial to plagioclase. Olivine (1.3–4.8 modal%) occurs as isolated and discrete, subhedral to anhedral crystals and, less commonly, as anhedral interstitial grains between plagioclase. Some of the olivine grains are partially to completely enclosed by orthopyroxene and/or clinopyroxene (Fig. 32) in orthopyroxene-bearing samples. Orthopyroxene (as high as 3.3 modal%) is common in the central parts of the unit (Cores 135-839B-14R to -15R). It forms distinctive euhedral to subhedral, often elongated, prismatic crystals (0.1–1.0 mm long). It is faintly pleochroic (pale green to pink), and sometimes occurs in partial intergrowths with plagioclase or clinopyroxene. It is sporadically present in low abundances in the upper (e.g., Section 135-839B-13R-4) and lowest parts of the unit (e.g., Section 135-839B-16R-2). Magnetite is a conspicuous groundmass mineral (up to 1.9 modal%) in Unit 1, forming octahedral to irregular and skeletal grains (0.01–0.30 mm in size), occurring almost entirely within the mesostasis. The octahedra are easily visible on weathered surfaces in hand specimens. The mesostasis, which constitutes between 20 and 35 modal% of the rock, is microcrystalline, locally has radiating quench textures, and contains very fine-grained and delicate globular clusters and rods of magnetite together with plagioclase microlites with swallowtail textures and plumose clinopyroxene aggregates.

Alteration of Unit 1 is slight to moderate. In parts of the unit (below Core 135-839B-14R), the basalt is gray brown in color resulting from the early stages of alteration. This is associated with the development of iron-oxyhydroxide-staining, secondary zeolite linings to cavities and vesicles, and the replacement of mesostasis by yellow-brown clays and zeolitic aggregates.

Unit 2

Moderately Phyric Orthopyroxene-Clinopyroxene-Plagioclase Basaltic Andesite

Unit 2 is a dark-gray to gray, moderately phyric, orthopyroxene-clinopyroxene-plagioclase basaltic andesite. It is depositionally overlain by upper Pliocene sediments in Core 135-838B-17R and is stratigraphically above Unit 3 in Core 135-839B-25R. Glassy margins on the recovered pieces indicate that this unit

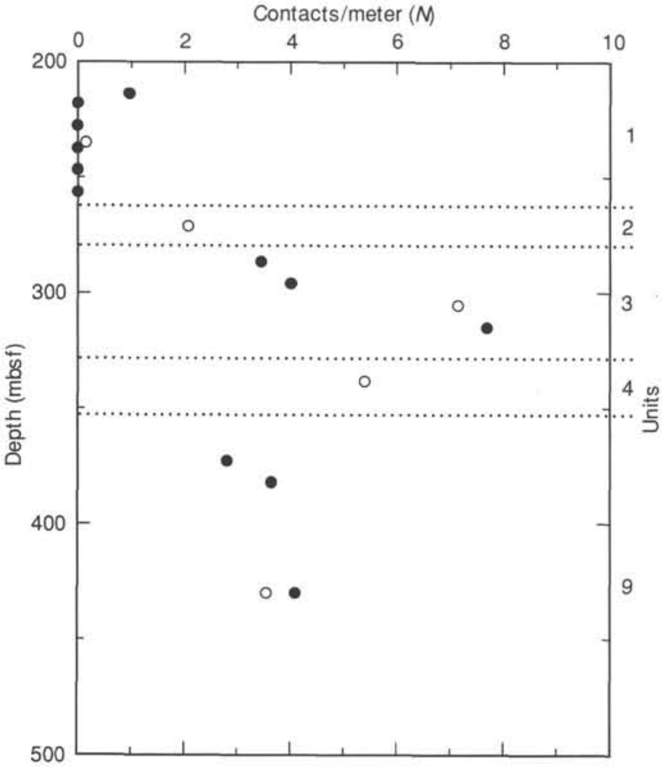

Figure 30. Contacts per meter of recovered rock for igneous units from Hole 839B. Only cores with >0.5-m recovery are included in the data for individual sections (filled circles). All sections have been included in the unit averages (total contacts in unit/total meters of recovery for unit). See Site 834, "Igneous Petrology" section, for a discussion of the methodology in preparing these data. The low contacts per meter suggest thick cooling units. Note the contrast between the very low values for Unit 1 (implying thick flows) and the high values characteristic of Units 3 and 9. Units 5, 6, 7, and 8 are too small to yield any useful data. Data for Units 2 and 4 are from a single core of each. Open circles = unit averages.

represents a series of thinly bedded flows (Fig. 30). Several pieces in the top part of the unit (Section 135-839B-18R-1, Pieces 1 and 2) are glassy with microlitic zones, whereas groundmass plagioclase and clinopyroxene are visible throughout the main part of the unit.

The basaltic andesite has 10–30 modal% vesicles, 0.1–11 mm in size; some groups of vesicles have coalesced to form small vesicle pipes. Darker gray quenched segregation vesicles are present throughout. Adjacent to glass rims in Pieces 1 and 2 (Section 135-839B-18R-1) vesicles are ovoid and there is some alignment subparallel to the margins.

Plagioclase is the principal phenocryst phase (5–10 modal%). It appears as euhedral, tabular crystals with oscillatory zoning. Crystals are up to 1.5 mm across, often contain melt inclusions, and generally form monomineralic glomeroporphyritic clusters. Clinopyroxene occurs in minor amounts (<1%) and forms discrete subhedral phenocrysts up to 2 mm across and rare glomerocrysts with olivine. Orthopyroxene phenocrysts (0.3 modal%) occur as elongate subhedral grains up to 0.5 mm in size. Isolated olivine crystals (1–2 mm in size) have been recognized in hand specimens but have not been observed in thin section.

The groundmass comprises plagioclase (15 modal%), clinopyroxene (15 modal%), minor, but significant, orthopyroxene (1–3 modal%), and cryptocrystalline mesostasis. Plagioclase forms euhedral, randomly oriented microlites (up to 0.5 mm in size) which commonly exhibit quench morphologies. Clinopyroxene forms subhedral, elongated, tabular and equant crystals (up to 0.3 mm in size) in the groundmass. Within the segregation vesicles, the clinopyroxene forms very fine-grained, quenched feathery aggregates. Orthopyroxene occurs as subhedral, usually elongated, prismatic crystals with inclusions of fine-grained magnetite. The mesostasis is mainly microcrystalline but locally is vitreous and extremely fresh. Magnetite forms very small (<0.05 mm in size) skeletal grains, commonly with cruciform morphologies.

Unit 3

Sparsely to Highly Phyric Clinopyroxene-Olivine Basalt

This unit varies from a sparsely to highly phyric clinopyroxene-olivine basalt. The unit thickness of 58.3 m is well-constrained as the transitions from Unit 2 to Unit 3 and from Unit 3 to Unit 4 were both recovered. Olivine is the principal phenocryst phase throughout (modal olivine/modal clinopyroxene >4; Table 10). The high number of contacts per meter indicate an eruptive unit characterized by very thin flows or pillows (Fig. 30). Modal phenocryst contents increase systematically downward (Fig. 33) from <2 modal% to about 10 modal% (Fig. 34), but vary widely within each core. The maximum phenocryst size increases from about 1.5 mm in size at the top of Unit 3 to about 4 mm in size one-third of the way down the unit (Fig. 33). There is clearly an increase of phenocryst concentration toward the base of Unit 3, but there does not appear to be any systematic settling of olivine within individual cooling units (Fig. 35).

The rocks are uniformly vesicular with 10–20 modal% rounded to irregular vesicles that range from 0.1 to 10 mm in maximum dimension. There is a bimodal size distribution of vesicles, with those <0.2 mm in size giving the samples a pervasive groundmass porosity (Fig. 34). Dark segregation vesicles with quench-textured fillings are common.

The samples have pronounced seriate porphyritic textures. Olivine phenocrysts (1 to 5 modal%) form euhedral to subhedral, mostly isolated crystals that are commonly 3–4 mm in size. The largest crystals exhibit kink bands, fractured margins, and overgrowths (Fig. 36). The fractures are infilled by mesostasis, suggesting that they formed during eruption, perhaps in response to sudden temperature and/or pressure drops. Small Cr-spinel inclusions (up to 0.05 mm in size) are commonly included in the olivines. Cr-spinel euhedra up to 2.0 mm in diameter also occur as separate crystals and glomerocrysts. Clinopyroxene phenocrysts occur as glomeroporphyritic intergrowths and as subhedral to euhedral, tabular to equant, isolated crystals up to 1.2 mm in length. Some are sector zoned.

Groundmass varies from fine-grained, with visible plagioclase, clinopyroxene, and olivine (Fig. 36), to cryptocrystalline and variolitic (in which very fine clinopyroxene-plagioclase quench intergrowths occur), to glassy. Microphenocrysts of euhedral to subhedral olivine (0.08–0.5 mm in size) and clinopyroxene (0.05–0.5 mm in size; equant to elongate, euhedral to subhedral crystals, with wavy extinction patterns) make up about 5 modal% and 10–15 modal%, respectively, of the groundmass. The remaining clinopyroxene occurs as smaller, equant to quench-textured grains. Plagioclase constitutes 10–20 modal% of the groundmass, occurring as small (up to 0.6 mm in size) laths to microlites with quench morphologies. Fine-grained opaque minerals (0.002–0.06 mm in size) are ubiquitous in the groundmass.

Unit 4

Aphyric to Sparsely Phyric Olivine-Clinopyroxene Basalt

Unit 4 is an aphyric to sparsely phyric olivine-clinopyroxene basalt. Its upper contact is marked by a sharp transition from the

Table 9. Principal lithologic units defined at Hole 839B, based on recovered core.

Unit	Lithology	Top depth (mbsf) Core, section, interval (cm)	Bottom depth (mbsf) Core, section, interval (cm)	Distinguishing features
1	(Hole 839A) Moderately phyric clinopyroxene-olivine basalt	205.85 23X-1, 25 cm (Piece 1)	218.20 25N-1, 78 cm (Piece 15)	Moderately phyric (2%–5% olivine), diabasic groundmass, 25%–30% vesicles, abundant octahedral opaques
1	(Hole 839B) Aphyric to moderately phyric clinopyroxene-olivine basalt	214.15 12R-1, 78 cm (Piece 1)	256.81 17R-1, 13 cm (Piece 2)	Aphyric to olivine-bearing (13R to 15R), moderately phyric (2%–5% olivine, 12R, 16R) diabasic groundmass, 25%–30% vesicles, abundant octahedral opaques, large Cr-spinel aggregates
2	Moderately phyric orthopyroxene-clinopyroxene-plagioclase basaltic andesite	266.40 18R-1, 0 cm (Piece 1)	276.06 19R-1, 10 cm (Piece 1)	5%–10% glomeroporphyritic plagioclase, 1% pyroxene, 10%–15% vesicles
3	Sparsely to highly phyric clinopyroxene-olivine basalt	276.06 19R-1, 10 cm (Piece 2)	334.33 25R-1, 40 cm (Piece 7)	3%–15% olivine + clinopyroxene, olivine>clinopyroxene, seriate, 20%–30% vesicular, olivine increases downward
4	Aphyric to sparsely phyric olivine-clinopyroxene basalt	334.33 25R-1, 40 cm (Piece 8)	353.3 26R-1, 42 cm (Piece 7)	1%–2% olivine + clinopyroxene, clinopyroxene >= olivine, seriate, 30% vesicles, somewhat similar to less phyric parts of Unit 3
5	Moderately phyric orthopyroxene-clinopyroxene-plagioclase basaltic andesite	353.3 27R-1, 0 cm (Piece 1)	353.43 27R-1, 18 cm (Piece 3)	5%–8% plagioclase glomerocrysts, <2% pyroxene phenocrysts (plagioclase > pyroxene) 8%–10% vesicles, similar to Unit 9
6	Moderately to highly phyric clinopyroxene-olivine basalt	353.43 27R-1, 18 cm (Piece 4)	353.54 27R-1, 33 cm (Piece 5)	5%–10% olivine phenocrysts, 1%–2% clinopyroxene, 15%–20% vesicles, similar to Unit 3
7	Moderately phyric clinopyroxene-orthopyroxene-plagioclase basaltic andesite	353.54 27R-1, 33 cm (Piece 6)	362.9 28R-1, 0 cm (Piece 1)	4%–7% plagioclase glomerocrysts, 1%–2% pyroxene phenocrysts, 10%–15% vesicles, similar to Unit 9
8	Moderately to highly phyric clinopyroxene-olivine basalt	362.9 28R-1, 0 cm (Piece 1)	362.93 28R-1, 5 cm (Piece 1)	7%–10% olivine phenocyrsts, 1%–2% clinopyroxene phenocrysts, 15%–20% vesicles, similar to Units 3 and 6
9	Moderately to highly phyric clinopyroxene-orthopyroxene-plagioclase basaltic andesite	362.93 28R-1, 5 cm (Piece 2)	497.26 42R-1, 6 cm (Piece 1)	7%–15% plagioclase phenocrysts, 2%–3% pyroxene phenocrysts, orthopyroxene >= clinopyroxene, 10%–15% vesicles

Note: Unit boundaries reflect changes in principal lithology defined in visual and thin section descriptions. Unit I was recovered in Holes 839A and 839B. Other units were recovered only from Hole 839B.

densely olivine phyric base of Unit 3 in Section 135-839B-25R-1 (between Pieces 7 and 8). The unit thickness is estimated to be 19 m, but the lower contact with Unit 5 was not recovered (Fig. 29). The large number of recovered flow margins indicates a series of thin flows or pillows (Fig. 30). Unit 4 is distinguished from Unit 3 by the absence of large phenocrysts, the pronounced development of microphenocrysts (0.1–0.5 mm in size), and the predominance of clinopyroxene over olivine (10:1) in those microphenocrysts (Table 10 and Figs. 31 and 37). Vesicle content is generally high, ranging from 5 to 30 modal% with some vesicles as large as 1.5 cm across. The largest vesicles have formed by coalescence of several smaller vesicles. Dark segregation vesicles and vesicle trains are common.

Phenocrysts consist of euhedral to subhedral olivine and clinopyroxene up to 1.5 and 1.0 mm, respectively, and are present in approximately equal portions. The very pronounced seriate texture makes the distinction between microphenocrysts and groundmass somewhat arbitrary. The phenocrysts (>0.5 mm in size) and microphenocrysts (0.1–0.5 mm in size) occur as isolated grains and in small glomerocrysts. Cr-spinel inclusions occur in olivine grains of all sizes. The groundmass constitutes 50–60 modal% glassy to cryptocrystalline mesostasis with small quench clinopyroxene crystallites and very small (<0.01 mm in size) skeletal and rodlike granules. Other groundmass phases are (in decreasing abundance) clinopyroxene (0.02–0.5 mm in size, euhedral microphenocrysts to anhedral interstitial grains), plagioclase (elongated laths, euhedral to subhedral, up to 0.5 mm in size), olivine (0.05–0.5 mm in size, euhedral to subhedral and skeletal microphenocrysts), and rare magnetite. The clinopyroxene phenocrysts and microphenocrysts commonly show curved cleavages and shadowy extinctions indicative of rapid crystal growth.

The rock is extremely fresh, with much of the mesostasis existing as fresh dark-brown glass. Rare patches of yellow to yellow-brown amorphous clays are found replacing the mesostasis, and there is minor development of iron-oxyhydroxide coatings and globular zeolites in some vesicles.

Unit 5

Moderately Phyric Orthopyroxene-Clinopyroxene-Plagioclase Basaltic Andesite

Unit 5 is a moderately phyric orthopyroxene-clinopyroxene-plagioclase basaltic andesite comprising the first three pieces in Section 135-839B-27R-1. In hand specimen the rocks of this unit are dark gray, with approximately 10 modal% visible phenocrysts set in a glassy to aphanitic groundmass. The rock is characterized by a high proportion of plagioclase to pyroxene phenocrysts

Table 10. Modal analyses of representative samples from Hole 839B.

Core, section	12R-2	13R-4	14R-1	15R-1	15R-4	16R-1	16R-2	18R-1	19R-1	20R-1	25R-1
Interval (cm)	29–32	2–6	132–135	34–37	95–98	106–108	10–12	54–58	50–53	74–77	35–38
Piece	6	1	23	6	17	19	3	14	9	12	7
Depth (mbsf)	214.95	221.60	228.67	237.59	241.90	247.84	248.60	266.78	276.30	286.19	334.23
N	1143	1123	1005	1081	1051	1019	1005	1055	1158	1214	1070
Unit no.	1	1	1	1	1	1	1	2	3	3	3
Phenocrysts:											
Olivine	0.7	0.8	0.3	0.8	0.6	0.8	1.4		7.1	4.0	14.1
Clinopyroxene	1.0	0.4		<0.1		0.9	1.5	0.1	1.5	1.3	0.4
Plagioclase								6.6			
Orthopyroxene								0.3			
Total phenocrysts	1.7	1.2	0.3	0.9	0.6	1.7	2.9	7.0	8.6	5.3	14.5
Groundmass:											
Plagioclase	19.8	24.7	39.4	32.6	28.7	31.2	33.9	13.8	15.9	18.7	8.7
Clinopyroxene	16.5	19.3	15.8	21.0	26.2	19.7	21.8	*13.7	10.2	15.2	9.2
Orthopyroxene		0.2	3.0	2.0	3.3		0.4	0.3			
Olivine	2.3	2.9	1.3	2.7	4.8	2.4	1.8		3.0	6.5	4.5
Opaques		0.9	1.4	1.9	1.1	1.7	1.6	2.9	0.2	0.3	
Cr-spinel					0.1	0.5		0.2	0.1	0.1	
Mesostasis	35.9	27.8	21.9	25.4	23.5	21.5	20.3	43.9	38.4	33.1	52.0
Total groundmass	74.5	75.8	82.8	85.6	87.7	77.0	79.8	74.6	67.9	73.9	74.5
Vesicles:											
Open	23.5	23.0	16.8	13.7	11.7	21.1	17.3	17.8	23.2	20.8	11.1
Filled	0.4		<0.1		<0.1	0.2		0.5	0.3		
Total	23.9	23.0	16.9	13.7	11.8	21.3	17.3	18.3	23.5	20.8	11.1

Core, section	25R-1	26R-1	27R-1	27R-1	27R-1	28R-1	30R-1	34R-1	36R-1	37R-1	41R-1
Interval (cm)	46–48	23–26	15–17	21–24	38–41	8–10	74–76	15–18	25–28	50–53	5–7
Piece	8	5	3	4	7	2	13	3	6	9	2
Depth (mbsf)	334.30	343.77	353.42	353.47	353.59	363.98	382.67	420.99	439.82	449.55	487.55
N	1070	1115	1082	1199	1082	2167	1103	1013	1100	1042	1346
Unit no.	4	4	5	6	7	9	9	9	9	9	9
Phenocrysts:											
Olivine	0.1	0.2		5.6							
Clinopyroxene	0.1		0.2	0.6	<0.1	0.4	0.1	1.0	0.3	0.3	
Plagioclase			8.6		7.1	9.4	11.7	11.9	7.5	7.6	3.5
Orthopyroxene			0.2		0.5	0.3	0.7	0.3	0.1	0.5	0.2
Total phenocrysts	0.2	0.2	9.0	6.2	7.6	10.1	12.5	13.2	7.9	8.4	3.7
Groundmass:											
Plagioclase	13.8	6.4	10.7	0.4	9.2	10.3	14.4	20.6	16.2	12.1	17.2
Clinopyroxene	17.5	17.1	*3.8	4.8	*3.9	*3.4	*9.8	*10.5	*5.0	*6.3	*11.7
Orthopyroxene			0.7		0.5	0.8	2.1	1.5	0.4	1.0	0.1
Olivine	2.0	2.7		3.3							
Opaques			0.9		0.5	1.6	2.8	1.2	1.2	6.0	0.4
Cr-spinel				0.1							
Mesostasis	50.6	59.6	60.0	61.1	66.1	58.3	43.5	45.0	56.5	47.4	43.1
Total groundmass	83.9	85.8	76.1	69.7	80.2	74.4	72.5	78.8	78.1	72.8	72.5
Vesicles:											
Open	15.9	14.0	14.9	24.2	12.2	14.8	15.0	7.4	11.2	18.4	23.8
Filled						0.7		0.6	2.8		
Total	15.9	14.0	14.9	24.2	12.2	15.5	15.0	8.0	14.0	18.4	23.8

Notes: Phenocrysts were considered as grains that were distinct in size and shape from the average groundmass constituents. The designation of phenocrysts in samples with pronounced seriate porphyritic textures is somewhat arbitrary and may vary from unit to unit as the groundmass textures change. Unit 4 samples have abundant microphenocrysts (0.1–0.5 mm in size); these are essentially aphyric in hand specimen and the microphenocrysts have been counted with the groundmass. Mesostasis includes alteration products of original mesostasis and crystallites too small to be identified. An asterisk (*) indicates that the groundmass clinopyroxene count includes both clinopyroxene and unidentified pyroxenes; the groundmass orthopyroxene was positively identified where listed. *N* = number of points counted.

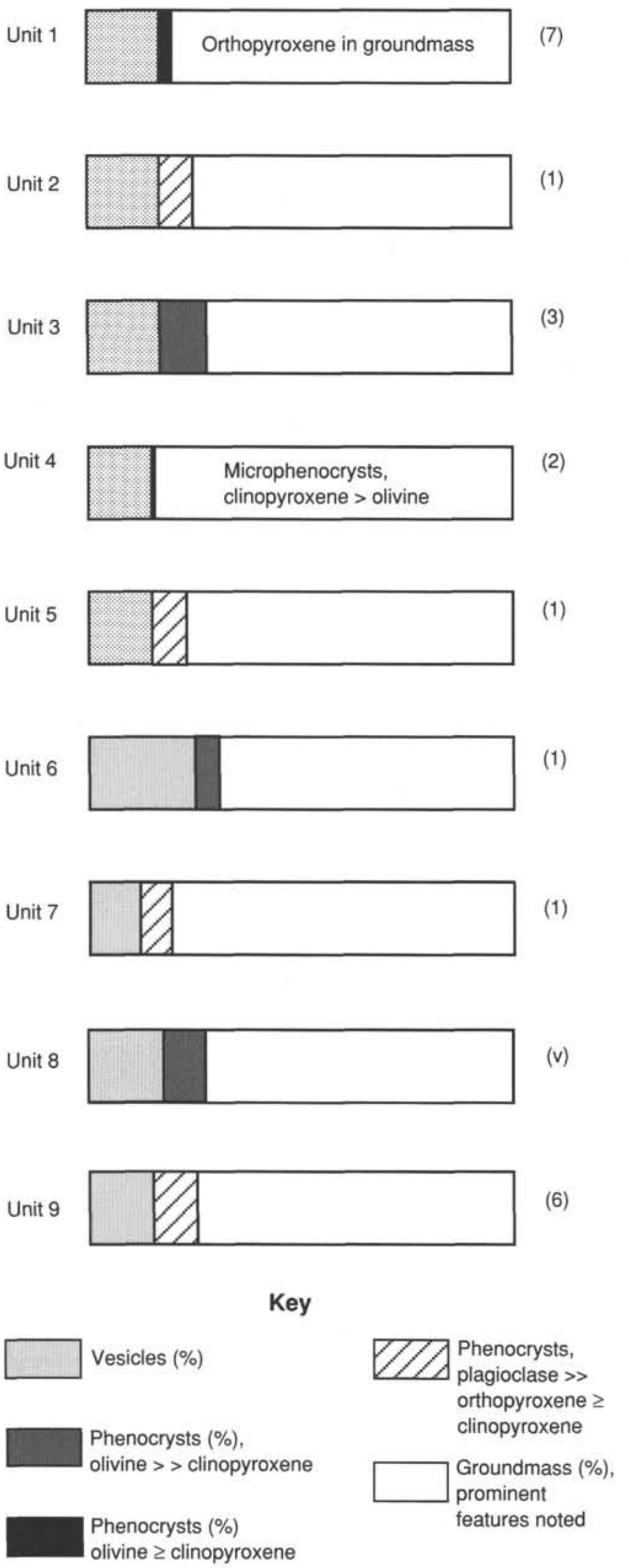

Figure 31. Summary of modal data for Units 1–9 showing the principal differences used in defining lithologic units. Note the very high vesicularity of all of the units. Number of point counts indicated in parentheses at right; v = visual estimate.

Figure 32. Photomicrograph of coarsely crystalline groundmass showing network of interlocking plagioclase, clinopyroxene and orthopyroxene; Unit 1, Sample 135-839B-14R-1, 132–133 cm, Piece 23; field of view = 1.5 mm, crossed polarized light. The orthopyroxene in the center of the photograph completely encloses a subhedral grain of olivine.

(> 8:1). The vesicle content is approximately 15 modal%; irregularly shaped vesicles up to 5 mm across occur. Some vesicles are lined with yellow-white to gray zeolites.

Phenocryst phases are plagioclase (7–10 modal%, individual crystals to 3 mm in size, showing oscillatory zoning), orthopyroxene (<1 modal%; up to 1 mm in size, subhedral to prismatic crystals), and clinopyroxene (<1 modal%; up to 0.5 mm in size, subhedral). Most of the phenocrysts form glomerocrystic clusters up to 5 mm across; monomineralic plagioclase clusters dominate, but there are also plagioclase-pyroxene clusters. The groundmass is cryptocrystalline to microcrystalline with discernible plagioclase, clinopyroxene, orthopyroxene, and magnetite. Cryptocrystalline mesostasis makes up 60 modal% or more of the groundmass. Orthopyroxene (euhedral to subhedral isolated crystals and small star-shaped glomerocrysts) is subordinate to clinopyroxene (subhedral equant microphenocrysts to elongate groundmass grains), although it is difficult to distinguish the two pyroxene types in the small grains characteristic of the groundmass. Fine-grained skeletal to granular magnetite is ubiquitous in the mesostasis.

Alteration is relatively minor and is limited to moderate replacement of the mesostasis by fine-grained clays. Locally, patches of red-orange amorphous material occur as a mesostasis replacement.

The samples are petrographically and chemically identical to lithologies in the upper portions of Unit 9 and in Units 2 and 7 (Table 10 and Fig. 31). The fragments identified as Unit 5 may have been dislodged from Unit 2 during drilling operations.

Unit 6

Moderately to Highly Phyric Clinopyroxene-Olivine Basalt

Unit 6 is a moderately phyric clinopyroxene-olivine basalt; it is represented by two fragments in Section 135-839B-27R-1. A fresh glassy rim is present on Piece 5. The basalt is highly vesicular with 10–25 modal% rounded vesicles up to 7 mm across. The vesicles have a bimodal size distribution with both large, sparser, rounded vesicles and abundant, very small (<0.2 mm in size) interconnected vesicles that give the rock a high groundmass porosity.

Olivine (up to 3 mm in size; as isolated euhedral and sometimes skeletal crystals) is the dominant phenocryst and comprises 5–6 modal% of the rock. The largest phenocrysts exhibit cracking

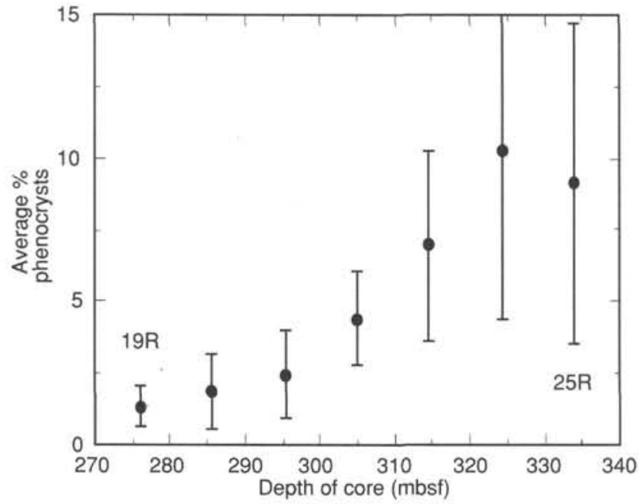

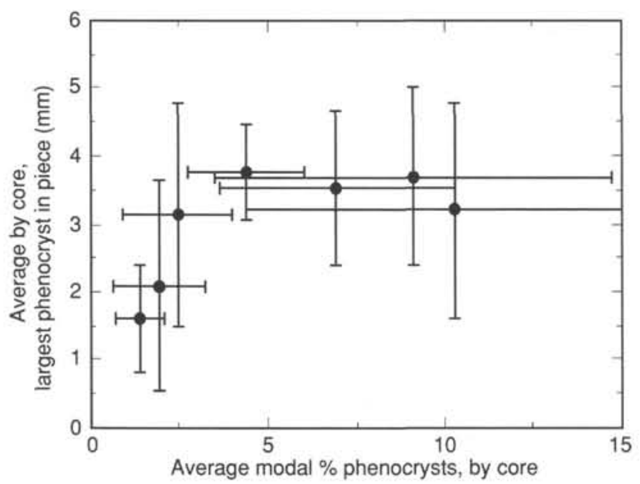

Figure 33. Variation in modal olivine plus clinopyroxene for Unit 3, Hole 839B. All pieces from Unit 3 were counted using a binocular microscope and a 1 × 1 mm grid overlay. Modal estimates are lower than thin-section estimates because only grains larger than about 0.5 mm were counted here. The maximum dimension of the largest phenocryst in each piece (generally olivine) was also measured. The results presented here are averages and standard deviations for each core.

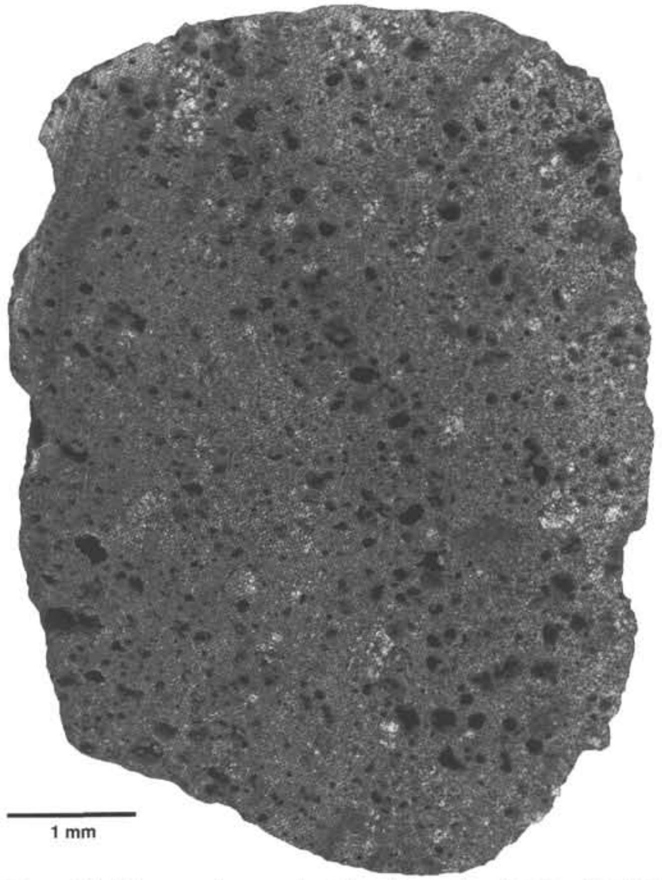

Figure 34. Close-up photograph of basalt sample showing abundant olivine phenocrysts (approximately 10%) and trails of coarse vesicles; Unit 3, Section 135-839B-25R-1, 34–42 cm, Piece 7. Note the bimodal size distribution of the vesicles.

on their margins and melt infilling, which is believed to result from quenching during eruption. Euhedral clinopyroxene grains up to 0.4 mm across are also visible. A few large (<0.3 mm in size), euhedral, Cr-spinel grains occur as single grains and in 3–6 grain glomerocrysts ranging from 0.15 to 0.8 mm across. Cr-spinel inclusions (0.005–0.01 mm in size) are also present in many of the olivine phenocrysts. Most of the phenocrysts occur as isolated crystals, but small glomerocrysts are also present. The seriate texture produces a gradation between phenocrysts, microphenocrysts, and groundmass-sized crystals.

The groundmass is dominantly cryptocrystalline to variolitic. Very fine-grained radiating, acicular, and plumose aggregates of clinopyroxene, plagioclase, and skeletal magnetite grains are visible components.

Unit 6 differs from Unit 4 in the dominance of olivine over clinopyroxene, both as phenocryst and microphenocryst populations. It is, however, petrographically and chemically identical to rocks from Unit 3 and may represent fragments of Unit 3 displaced downhole.

Unit 7

Moderately Phyric Clinopyroxene-Orthopyroxene-Plagioclase Basaltic Andesite

Unit 7 consists of two fragments of dark gray, moderately phyric orthopyroxene-clinopyroxene-plagioclase basaltic andesite, recovered at the bottom of Section 135-839B-27R-1. Plagioclase is the dominant phenocryst phase (7.1 modal%; up to 1.5 mm in size, isolated crystals and glomerocrysts to 4 mm in size). It contains melt inclusions and displays oscillatory zoning. Both clinopyroxene (<1 modal%; up to 0.5 mm in size, mainly in glomerocrysts) and orthopyroxene (0.5 modal%; up to 0.8 mm in size, as euhedral to subhedral elongate prismatic crystals, and as glomerocrysts) are present as phenocrysts. Plagioclase to pyroxene ratios are greater than 10. The same phases occur in the groundmass, which has intergrown swallowtail plagioclase crystals and acicular clinopyroxene crystals. Orthopyroxene develops star-shaped crystal aggregates. The groundmass is mostly very fresh, and brown glass is visible in thin section. Vesicle content is 15 modal% and vesicles are round and empty. Alteration is confined to minor localized replacement of the mesostasis by green-brown clays, which may be filling microvesicles.

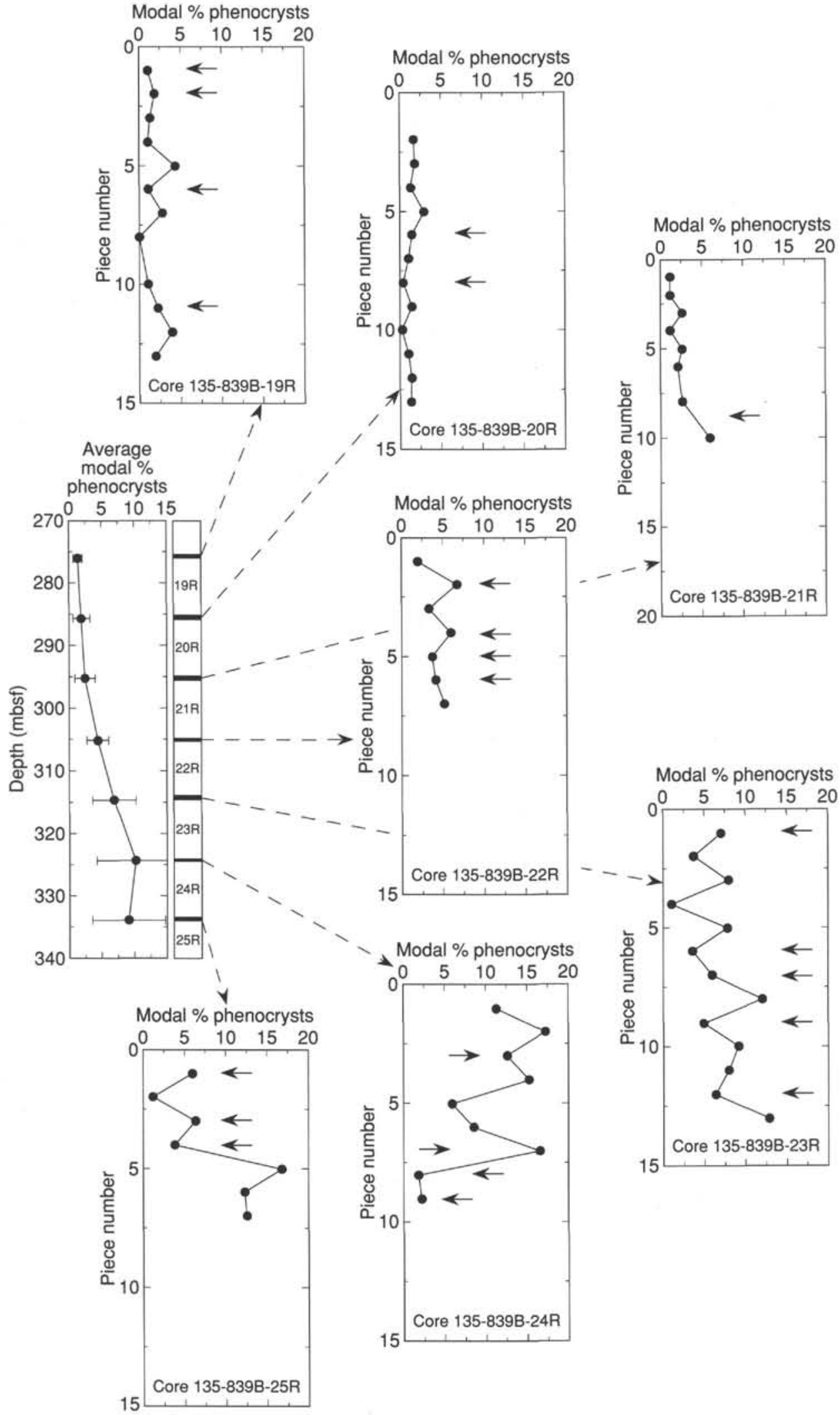

Figure 35. Olivine modal data, collected as described in Figure 33, for individual pieces in Unit 3. Arrows indicate the location of glassy cooling unit margins. There is no consistent increase of phenocryst abundances within individual cooling units. Phenocryst percentages increase in the piece below a piece with a glassy margin in ten cases and decrease in five cases. Olivine(+clinopyroxene)-rich and olivine(+clinopyroxene)-poor glassy margins occur. The increase in phenocryst percentages downward is characteristic of the unit as a whole.

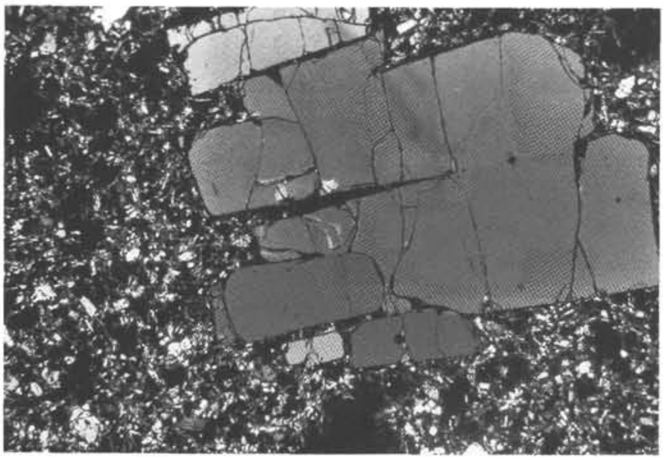

Figure 36. Photomicrograph of euhedral olivine glomerocrysts, showing extensive cracking, enclosed in fine grained groundmass of plagioclase, clinopyroxene, and olivine; Unit 3, Sample 135-839B-25R-1, 35–38 cm, Piece 7; field of view = 6 mm, crossed polarized light. Note small Cr-spinel inclusion in central right-hand portion of the olivine.

Figure 37. Photomicrograph showing abundant clinopyroxene microphenocrysts with interstitial glass, plagioclase microlites, and olivine; Unit 4, Sample 135-839B-25R-1, 46–48 cm, Piece 8; field of view = 3 mm, crossed polarized light. Many of the clinopyroxene microphenocrysts exhibit curved cleavages and shadowy extinction.

The two pieces identified as Unit 7 are petrographically and chemically identical to the rocks from Units 2, 5, and 9 and may represent fragments displaced from higher in the hole.

Unit 8

Moderately to Highly Phyric Clinopyroxene-Olivine Basalt

Unit 8 is a single piece of gray, moderately to highly phyric clinopyroxene olivine basalt. Vesicle abundance ranges between 15 and 20 modal% and the vesicles occur in two distinct size populations. Vesicles >0.5 mm in size make up about 1 modal% of the sample and include segregation infillings; the remainder, mostly <0.2 mm in size, are interconnected and give the groundmass a high porosity. Olivine is the dominant phenocryst, forming 7–10 modal% of the rock. There are 1–2 modal% clinopyroxene phenocrysts and rare aggregates of Cr-spinel up to 0.3 mm in diameter. The sample is very slightly altered with some iron-oxyhydroxide surface coatings and minor alteration of olivine along fractures.

The sample designated as Unit 8 is petrographically identical to samples from Units 3 and 6 (Fig. 31). As is the case with Unit 6, it is likely that Unit 8 is a fragment of Unit 3 that has been displaced downcore during operations with the drill string.

Unit 9

Moderately to Highly PhyricClinopyroxene-Orthopyroxene-Plagioclase Basaltic Andesite

Unit 9 comprises a series of flows of clinopyroxene-orthopyroxene, plagioclase basaltic andesite forming an eruptive unit at least 135 m thick. It extends from Core 135-839B-28R at 362.93 mbsf to the bottom of the hole at 497.26 mbsf. Core recovery was poor but the number of glassy or fine-grained flow margins suggests a series of thin- to medium-bedded flows or pillows (Fig. 30). The typical flow thickness appears to be somewhat larger than is characteristic of Unit 3 (Fig. 30).

The rocks of Unit 9 are conspicuously vesicular, with vesicle concentrations estimated between 10 and 20 modal%, increasing in some sections (e.g., Section 135-839B-39R-1) to as high as 35 modal%. There is no clear evidence for any systematic changes in vesicularity within the unit. Vesicle sizes are commonly bimodal, with one size range <0.5 mm and another from 1 to 8 mm. The vesicle shapes range from round to ovoid to elongated. Some of the larger vesicles have formed by the coalescence of smaller vesicles. The smaller vesicles are uniformly distributed, whereas the larger vesicles are erratically distributed and often develop into linear vesicle trails, pipe vesicles, and segregation vesicles. The segregation vesicles are darker colored, frothy blebs of quenched basaltic lava, representing refilling of earlier vesicles by local melt segregation (Figs. 38). In some examples, these have near circular cross sections (Fig. 38), whereas others develop as vesicle trails. In one case (Section 135-839-37R-1), some of the spherical segregation vesicles show small offsets across gently dipping planes, with concentrations of small vesicles along them.

The phenocryst assemblage is plagioclase, clinopyroxene, and orthopyroxene, with total phenocryst contents (see modal data in Table 10) ranging between 3 and 13 modal% and averaging 9.4

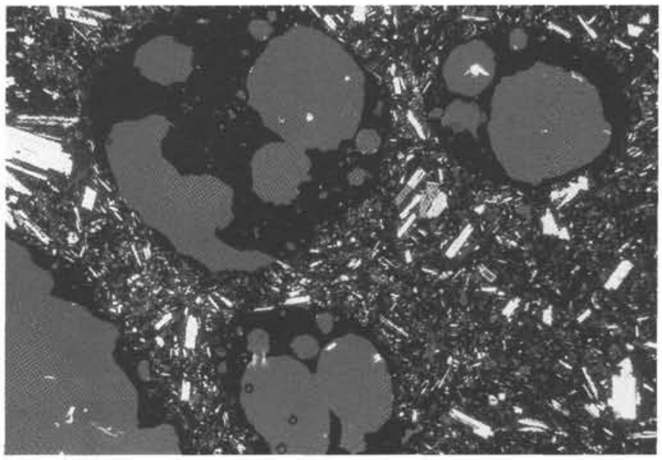

Figure 38. Photomicrograph of near-spherical vesicle infillings by melt segregation; Unit 9, Sample 135-839B-28R-1, 8–10 cm, Piece 2; field of view = 6 mm, partially crossed polarizers. This melt itself has experienced extensive vesiculation. Note the quenched nature of these segregation infillings and their sharp contacts with the enclosing groundmass.

modal%. Plagioclase ranges from 3.5 to 11.9 modal% (average 8.6 modal%), with the clinopyroxene and orthopyroxene phenocrysts together constituting only 0.2–1.3 modal% of the total rock. This high modal plagioclase/pyroxene phenocryst ratio is characteristic of the basaltic andesites from the Kermadec-Tonga arc (e.g., Ewart et al., 1973, 1977). The plagioclase occurs as single crystals and more commonly as monomineralic glomerocrysts (0.5–2.5 mm in size, rarely to 5 mm in size) of euhedral to subhedral crystals. The plagioclase phenocrysts commonly contain melt inclusions in the core region or distributed throughout the crystal (Fig. 39). Oscillatory-zoned crystals with distinct narrow sodic rims are common (Fig. 40). Augite occurs as single euhedral to subhedral crystals (0.5–2.0 mm in size, rarely to 4.5 mm in size), but more commonly in plagioclase-pyroxene, monomineralic clinopyroxene, or orthopyroxene-clinopyroxene glomerocrysts (Fig. 41). The crystals commonly exhibit lamellar twinning. Pigeonite has not been identified. Orthopyroxene occurs as isolated, euhedral to subhedral, prismatic crystals (up to 1.2 mm in size) and in small star-shaped glomerocrysts (Fig. 42).

Groundmass phases are dominantly plagioclase (10.3–20.6 modal% of the rock) and clinopyroxene (3.4–11.7 modal%), with minor orthopyroxene (0.1–1.0 modal%). Magnetite is confined to the mesostasis as small anhedral to skeletal grains. Plagioclase typically forms euhedral to subhedral randomly oriented laths and quenched swallowtail hopper-form microlites. Clinopyroxene forms discrete, equant to elongate subhedral grains, usually <0.3 mm in size, with shadowy extinction patterns attributed to growth during rapid cooling. Orthopyroxene characteristically forms isolated subhedral elongated tabular grains that often occur in star-shaped clusters. The interstitial mesostasis varies from glassy to cryptocrystalline to microcrystalline.

Unit 9 samples are uniformly very fresh, with only minor alteration. Rare, thin, white-yellow, yellow, and red-brown coatings of clays, zeolite, iron-oxyhydroxides, and manganese oxide are present at vesicle margins and as minor replacements of the mesostasis. There are occasional occurrences of very fine-grained, globular and barrel-shaped zeolites, but the largest vesicles generally appear free of secondary mineral infillings.

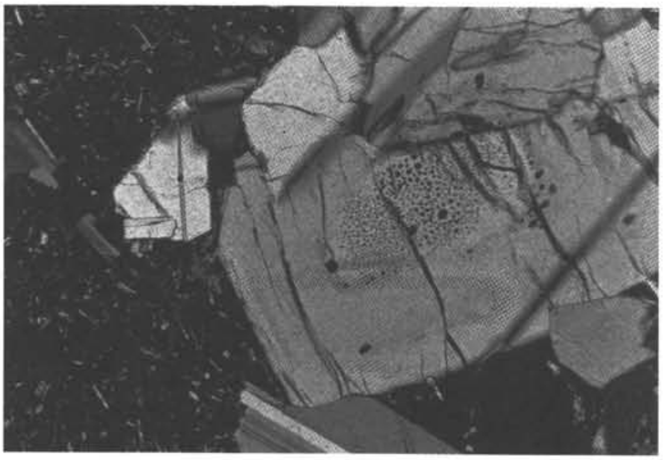

Figure 39. Photomicrograph of plagioclase glomerocryst showing concentration of near-spherical melt inclusions in core of crystal; Unit 9, Sample 135-839B-36R-1, 25–28 cm, Piece 6; field of view = 1.5 mm, crossed polarized light.

Figure 40. Photomicrograph of plagioclase phenocryst showing oscillatory zoning, distinct sodic rims, and deformation sector; Unit 9, Sample 135-839B-34R-1, 15–18 cm, field of view = 3 mm, crossed polarized light.

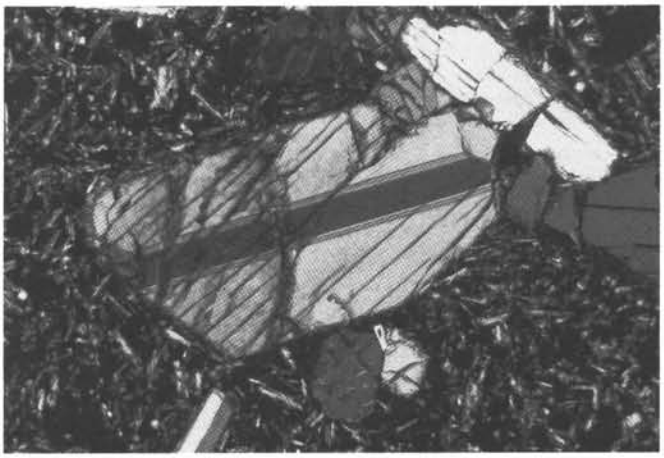

Figure 41. Photomicrograph of clinopyroxene-orthopyroxene glomerocrysts; Unit 9, Sample 135-839B-37R-1, 50–53 cm, Piece 9; field of view = 1.5 mm, crossed polarized light. Clinopyroxene shows lamellar twinning.

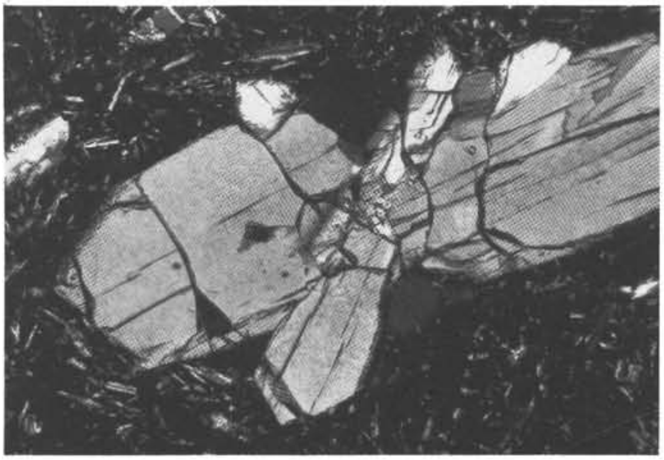

Figure 42. Photomicrograph of pure orthopyroxene glomerocrysts arranged in starlike form; Unit 9, Sample 135-839B-28R-1, 8–10 cm, Piece 2; field of view = 1.5 mm, crossed polarized light.

Alteration

Macroscopically visible alteration features at Site 839 are restricted to the basalts in Unit 1 (214.15–256.8 mbsf). Below Unit 1, the rocks are remarkably fresh and appear unaffected by high-temperature circulating fluids despite their high porosity. Rb values in Unit 1 are higher (averaging 9.3 ppm) than in any of the other units (which average 3–4 ppm in mafic samples and up to 7–8 ppm in the more evolved samples). The elevated Rb values of Unit 1 may indicate minor amounts of water-rock interaction.

Prominent secondary mineral occurrences in Unit 1 basalts include clear, radiating, euhedral aragonite crystals in cavities (Fig. 43A) and talc on fractures (Fig. 43B). In addition, globular to acicular zeolites and a white, prismatic mineral (analcime/chabazite?) occur on the rims of vesicles.

The occurrence of talc is surprising, as it is considered to require elevated temperatures for formation. No other characteristic greenschist facies mineral has been detected in the unit nor is there any alteration halo observed along the fracture. The breakdown of olivine in this unit may be supplying the Mg necessary for talc crystallization.

In thin section, a white, rectangular mineral is common as a vesicle lining and as a replacement of the mesostasis in parts of Unit 1. This mineral has very low relief and birefringence and may be analcime or chabazite. Olivine is partially altered to iddingsite and small amounts of yellow-brown clay. The mesostasis, when altered, yields a somewhat darker colored clay. Zeolites (likely phillipsite) occur rarely in vesicles. A single, highly birefringent mineral has been observed in a cavity of a thin section of Sample 135-839B-15R-4, Piece 17, and resembles aragonite. Talc has not been identified in any of the thin sections studied; its only occurrence has been found by macroscopic examination.

The volcanic rocks recovered below Unit 1 appear extremely fresh macroscopically and microscopically. The only observed alteration feature is the localized breakdown of volcanic glass showing an early stage of the formation of yellow (Fe-rich?) smectite and the formation of a minor amount of iron-hydroxide. The smectite is not well crystallized and in most cases appears isotropic under crossed nicols. Occasionally, a weak but typical radiating extinction can be seen in globular aggregates. These alteration features within the rocks are consistent with a reaction with seawater.

Igneous Geochemistry

Site 839 was drilled 75 km west of the active ELSC approximately midway between the Lau Ridge and the active Tofua Arc. In view of their proximity to the ELSC, we expected that the Site 839 basalts would show a pronounced "MORB-like" signature. This expectation was based on a pre-cruise assumption that there had been a progressive change in the geochemical character of Lau Basin basalts from "arc-like" to "MORB-like" with basin evolution and that this portion of the Lau Basin had formed by normal seafloor spreading. However, all of the samples, both olivine- and orthopyroxene-bearing, have incompatible-element ratios and abundances more like those of island-arc tholeiitic series lavas.

Twenty-four samples from Holes 839A and 839B were analyzed by XRF for major and selected trace elements. One of these samples is a pumice fragment from lithologic Subunit IIE. Its origin is not known and it will not be discussed in detail.

The geochemical variations within the Site 839 basalts support the lithologic unit designations made on the basis of hand sample and petrographic observations. The rock types range from high-MgO (15%) tholeiites to basaltic andesites with 4% to 6% MgO. In general, values for loss on ignition (LOI) are relatively low, confirming that these rocks have undergone only minor alteration.

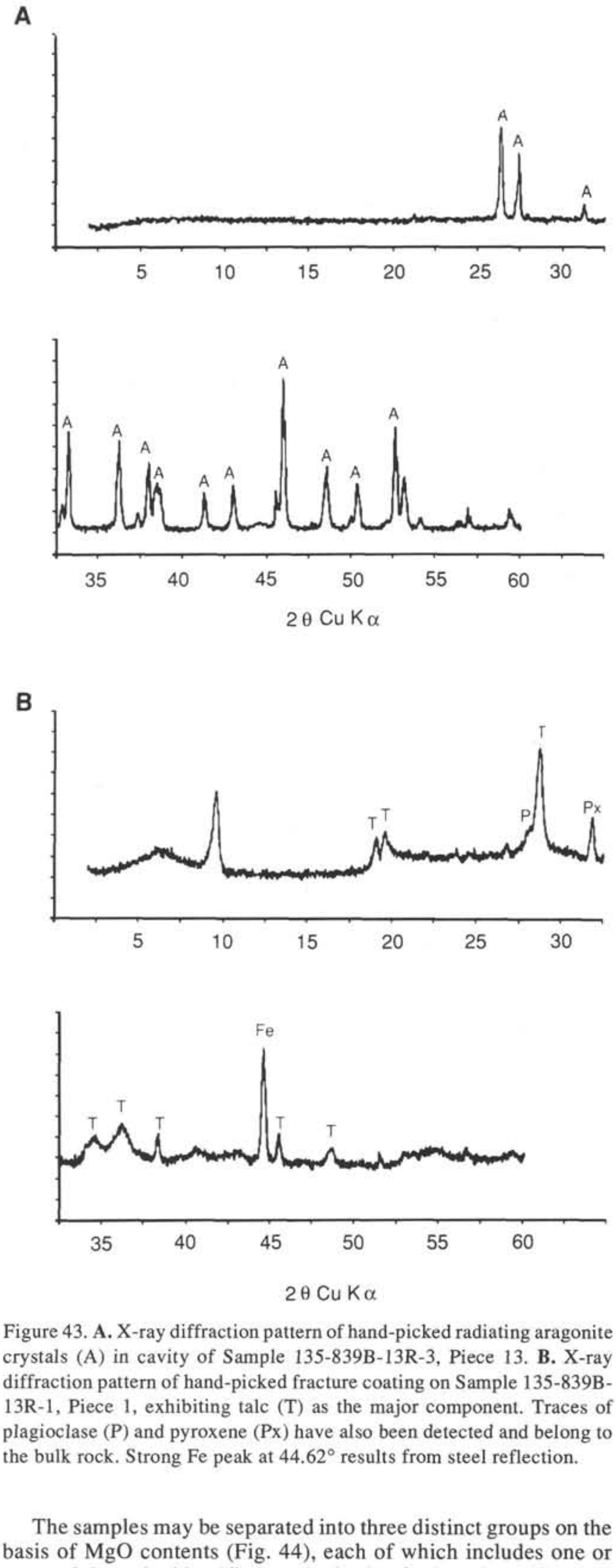

Figure 43. **A.** X-ray diffraction pattern of hand-picked radiating aragonite crystals (A) in cavity of Sample 135-839B-13R-3, Piece 13. **B.** X-ray diffraction pattern of hand-picked fracture coating on Sample 135-839B-13R-1, Piece 1, exhibiting talc (T) as the major component. Traces of plagioclase (P) and pyroxene (Px) have also been detected and belong to the bulk rock. Strong Fe peak at 44.62° results from steel reflection.

The samples may be separated into three distinct groups on the basis of MgO contents (Fig. 44), each of which includes one or more of the units identified on the basis of mineralogy. Group 1 has MgO greater than 13% and includes rocks from Units 3 and 6. Group 2 samples are basalts (ranging to basaltic andesites) from

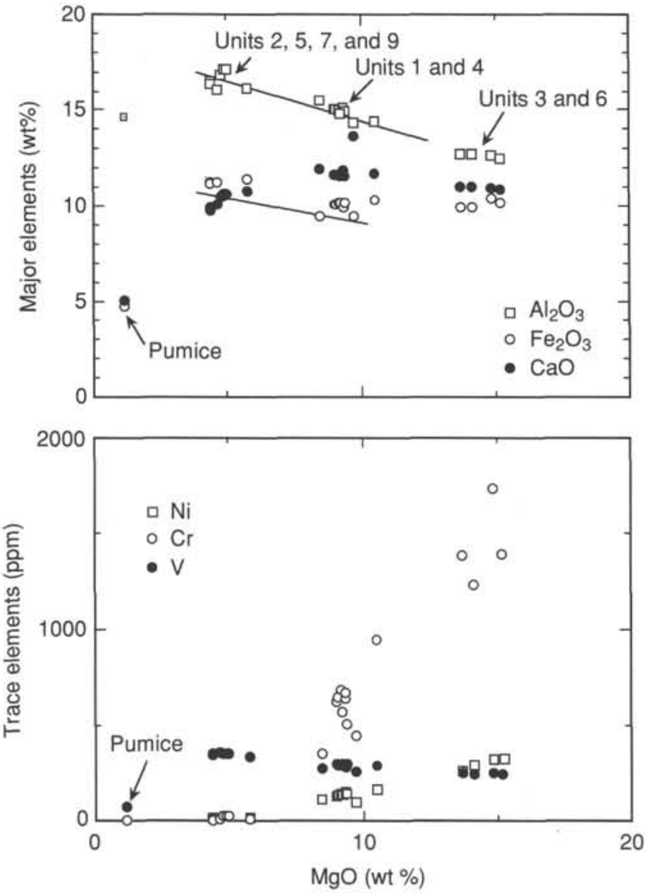

Figure 44. Representative variation diagrams from bulk-rock analyses of samples from Site 834. The pumice sample is from sedimentary Subunit 2E. Note the grouping of samples. Group 1 referred to in text includes Units 3 and 6, Group 2 includes Units 1 and 4, and Group 3 includes Units 2, 5, 7, and 9. Note the coherent trends of all the samples from the basement and the very high Cr and Ni contents of lavas from Units 3 and 6. The upper and lower lines indicate, respectively, the trends of Al_2O_3 and Fe_2O_3 in glasses from Mariana Trough basalts sampled at 18°N in the neovolcanic zone (Hawkins et al., 1990).

Units 1 and 4 with 8%–11% MgO. Group 3 samples are the most evolved and have MgO <6%; these include rocks from Units 2, 5, 7, and 9. Analyses of samples from Units 5 and 7 (represented by three and two pieces, respectively) are nearly identical to those from Unit 2 and the upper portion of Unit 9 (Table 11), whereas samples from Unit 6 (represented by two pieces) are very similar to Unit 3 lavas. There are no analyses of Unit 8, but its petrographic characteristics indicate it is also quite similar to Unit 3.

The Group 1 rocks are strongly enriched in compatible trace elements (Cr = 1229–1740 ppm; Ni = 258–320 ppm) indicating that they are relatively primitive melts. These rocks are olivine and hypersthene normative (Fig. 45) and have concentrations of Ti, Zr, and Y similar to those of the least fractionated lavas from the Tonga and Kermadec arcs (Table 12 and Fig. 46). There is an increase in Cr downward in Unit 3 (Fig. 47); otherwise the unit is quite homogeneous. The increase in Cr may reflect a local concentration of Cr-spinel.

The basalts in Group 1 are remarkable in their high MgO, Cr, and Ni contents. There is no question that in parts of the core, olivine accumulation has modified bulk rock compositions. However, the high MgO, Cr, and Ni in the analyzed Group 1 samples cannot be solely related to olivine accumulation. First, the compatible element concentrations are high (e.g, Ni up to 320 ppm), even in samples that are only moderately phyric (e.g., 135-839B-20R-1, 74–77 cm, with 4 modal% olivine, 1.5 modal% clinopyroxene; Tables 10 and 11). In addition, there is no correlation of MgO or Ni concentrations with modal% olivine, the olivines show little evidence of disequilibrium or reaction, and olivine also occurs as a groundmass phase in the lavas. This evidence supports the conclusion that the high MgO, Cr, and Ni are primary features of the Group 1 lavas.

The variation diagrams and normative plots suggest olivine control as an important factor in the development of the Site 839 volcanic rocks, but separating the effects of olivine removal and olivine accumulation is not straightforward. Major element plots suggest that Group 1 basalts could represent mixing of magnesian olivine into Group 2-type volcanics (Fig. 48). However, incompatible element abundances (e.g., K_2O, Ba, Zr) require mixing of olivine into a Group 3-type basaltic andesite (Fig. 48) to produce the Group 1 rocks. Least-squares calculations confirm that mixing of olivine and clinopyroxene into Group 3-type volcanics can yield compositions like those of Group 1. Such mixing requires addition of about 50% crystals (olivine: clinopyroxene of about 1:1) to the Group 3 basaltic andesites to yield acceptable fits to the major and trace element abundances of the Group 1 basalts. Group 2 volcanics are not a suitable end member for such mixing. Neither are the Cr-MgO systematics consistent with simple mixing of magnesian olivine with Group 2 or 3 volcanics to produce the Group 1 basalts (Fig. 48). In short, both the chemical and petrographic evidence are consistent with an interpretation of high MgO as a primary feature of the Unit 3 volcanics, although the MgO contents may have been locally modified by olivine redistribution.

Group 2 basalts include Units 1 and 4 and have average concentrations of 9.3%–9.8% MgO, 440–620 ppm Cr, and 90–140 ppm Ni (Tables 11 and 12). These values are considered to be representative of near-liquid compositions, as the analyzed samples are not highly phyric. The Group 2 rocks span the SiO_2 division between basalt and basaltic andesite (Unit 1 has an average SiO_2 = 52.6%, Unit 4 has an average SiO_2 = 51.6%). We have referred to them, as a group, as basalts throughout this discussion and in visual and microscopic descriptions. Unit 4 basalts are distinguished by lower Na_2O, Sr, Ba, and P_2O_5 than rocks from either Unit 3 or Unit 1 (Tables 11 and 12). All of the lavas in Group 2, despite their high MgO contents, are quartz-normative (Fig. 45). They have incompatible element ratios similar to those of the more magnesian rocks in Unit 3 (Fig. 46 and Table 12) but have much lower abundances of Cr and Ni, higher concentrations of SiO_2, Al_2O_3, and CaO, and similar concentrations of V and Fe_2O_3 (Fig. 44). Unit 1 within Group 2 is the only interval that shows macroscopic evidence of alteration. This alteration may be illustrated in the large scatter observed within the unit for elements such as Rb (Fig. 47).

The basaltic andesites of Group 3 (Units 2, 5, 6, and 9) are very homogeneous and also are the most fractionated lithology recovered. These rocks have very low Cr and Ni, 4%–6% MgO, and higher Fe_2O_3, Al_2O_3, V, and incompatible element concentrations than either of the more magnesian groups (Fig. 44; Tables 11 and 12). They have average Zr/Y (1.7–2.1), Y/Zr (0.42–0.43), Ba/Ce (7–9), and K/Ba (41–55) within the same ranges as the more primitive samples (Table 12 and Fig. 46). There is some downcore variation observed within Unit 9. The samples below about 400 mbsf are slightly less fractionated than those in the top of Unit 9, with lower Ba and Sr and higher MgO and CaO (Table 11). The basaltic andesites in Unit 2 are most like the lower portion of Unit 9 (Table 11). This break in Unit 9 occurs in an interval of no recovery where the downhole logs show a resistivity and density change. The unrecovered interval may include a separate flow

Table 11. Representative major and trace element analyses of igneous rocks from Holes 839A and 839B.

Hole	839A	839B	839B	839B	839B	839B	839B	839B	839B	839B	839B	839B	839B	839B
Core, section	10H-3	24X-1	12R-2	13R-2	13R-4	14R-1	15R-1	15R-4	16R-1	16R-2	18R-1	19R-1	20R-1	23R-1
Interval (cm)	116–135	0–6	25–32	72–77	22–26	128–135	34–39	95–100	106–111	15–16	54–60	50–56	74–80	24–27
Unit no.	IIE	1	1	1	1	1	1	1	1	1	2	3	3	3
Depth (mbsf)	84.66	215.20	215.23	220.42	222.89	228.48	237.64	242.41	248.06	248.61	266.94	276.50	286.44	314.84
Major elements (wt%):														
SiO_2	70.73	53.03	52.36	52.70	52.31	53.01	53.28	52.30	52.28	52.50	54.92	50.63	50.20	50.43
TiO_2	0.55	0.65	0.60	0.62	0.60	0.60	0.65	0.60	0.66	0.63	0.90	0.58	0.57	0.59
Al_2O_3	14.66	15.06	15.15	15.05	14.98	15.54	14.98	14.45	14.94	14.84	16.08	12.75	12.48	12.66
Fe_2O_3	4.76	10.04	9.94	10.06	9.93	9.42	10.16	10.33	10.14	10.16	11.22	9.93	10.18	10.36
MnO	0.13	0.17	0.16	0.16	0.16	0.16	0.19	0.18	0.18	0.17	0.18	0.16	0.17	0.17
MgO	1.17	9.00	9.35	9.04	9.36	8.48	9.40	10.51	9.18	9.21	4.64	14.15	15.20	14.86
CaO	5.07	11.66	11.88	11.62	11.64	11.92	11.52	11.68	11.61	11.57	10.08	10.98	10.88	10.92
Na_2O	3.64	1.35	1.66	1.36	1.20	1.55	1.37	1.14	1.36	1.16	1.90	1.28	1.23	1.21
K_2O	0.92	0.23	0.24	0.31	0.27	0.21	0.30	0.20	0.29	0.24	0.56	0.32	0.29	0.26
P_2O_5	0.11	0.07	0.08	0.07	0.08	0.06	0.07	0.06	0.08	0.07	0.12	0.07	0.07	0.07
Total	101.73	101.26	101.40	101.00	100.53	100.95	101.90	101.44	100.69	100.56	100.62	100.85	101.27	101.54
LOI	3.65	−0.22	0.33	0.30	0.10	−0.21	−0.06	0.00	−0.08	−0.07	1.09	0.61	0.27	0.37
Mg#		64.0	65.1	64.0	65.1	64.1	64.7	66.8	64.2	64.2	45.0	73.8	74.7	74.0
Trace elements (ppm):														
Nb	2	1	1	1	1	1	0	1	1	1	0	1	1	1
Zr	85	32	29	29	29	29	30	28	32	31	49	33	33	33
Y	30	16	14	14	15	15	15	13	15	15	21	14	14	15
Sr	180	148	143	143	141	149	145	139	146	145	191	137	163	137
Rb	11	5	11	13	11	10	14	8	7	5	8	4	5	4
Zn	46	55	63	54	54	44	58	52	58	51	75	56	55	57
Cu	28	102	95	111	101	43	131	82	104	124	108	72	72	83
Ni	0	126	143	130	145	109	139	166	136	135	15	283	320	320
Cr	0	618	637	644	666	347	503	945	686	566	7	1229	1398	1740
V	71	294	279	289	286	271	295	288	290	295	357	242	243	245
Ce	19	5	8	7	6	8	9	6	5	8	12	12	9	10
Ba	234	78	45	59	70	59	63	55	77	54	85	62	55	54

Hole	839B	839B	839B	839B	839B	839B	839B	839B	839B	839B
Core, section	26R-1	27R-1	27R-1	27R-1	28R-1	30R-1	34R-1	36R-1	37R-1	41R-1
Interval (cm)	23–29	15–19	21–24	38–42	24–29	74–79	15–20	26–31	50–56	5–10
Unit	4	5	6	7	9	9	9	9	9	9
Depth (mbsf)	343.83	353.45	353.51	353.68	363.14	382.94	421.05	439.86	449.70	487.55
Major elements (wt%):										
SiO_2	51.64	54.15	50.45	55.02	54.57	54.68	53.41	53.76	54.06	53.41
TiO_2	0.57	0.85	0.58	0.87	0.86	0.85	0.81	0.80	0.82	0.81
Al_2O_3	14.33	16.55	12.75	16.46	16.39	16.50	16.84	17.16	17.14	16.12
Fe_2O_3	9.42	11.05	9.90	11.23	11.16	11.25	10.49	10.62	10.65	11.38
MnO	0.17	0.19	0.17	0.20	0.19	0.18	0.18	0.18	0.18	0.19
MgO	9.72	4.36	13.71	4.35	4.36	4.34	4.77	4.95	4.86	5.76
CaO	13.64	9.85	11.00	9.80	9.89	9.77	10.50	10.60	10.56	10.80
Na_2O	1.15	1.99	1.71	1.96	2.33	2.00	1.94	1.90	1.80	1.72
K_2O	0.22	0.65	0.29	0.78	0.64	0.68	0.41	0.45	0.44	0.39
P_2O_5	0.04	0.13	0.07	0.13	0.13	0.14	0.09	0.08	0.10	0.08
Total	100.92	99.78	100.63	100.80	100.53	100.40	99.42	100.47	100.60	100.64
LOI	0.00	1.02	0.65	1.46	1.16	0.95	2.77	0.66	0.58	0.28
Mg#	67.1	43.9	73.3	43.4	43.6	43.3	47.4	48.0	47.5	50.1
Trace elements (ppm):										
Nb	1	1	1	1	1	1	1	2	1	1
Zr	27	52	33	52	53	54	45	44	44	45
Y	15	20	14	21	21	20	20	21	20	20
Sr	117	217	140	215	219	218	185	185	183	185
Rb	3	9	5	12	9	10	5	6	6	5
Zn	51	77	59	78	79	75	70	75	70	77
Cu	105	77	85	83	84	82	97	97	93	82
Ni	92	12	258	11	11	11	20	20	21	20
Cr	445	3	1391	4	1	0	22	25	24	10
V	256	347	247	341	348	343	348	346	346	332
Ce	6	9	2	15	14	11	8	15	7	10
Ba	44	114	58	127	118	123	117	84	96	72

Notes: Mg# represents 100 · (Mg /[Mg + Fe^{2+}]), where Fe^{3+}/Fe^{2+} is assumed to be 0.2. Mg# was not calculated for samples with SiO_2 > 65%. LOI = loss on ignition.

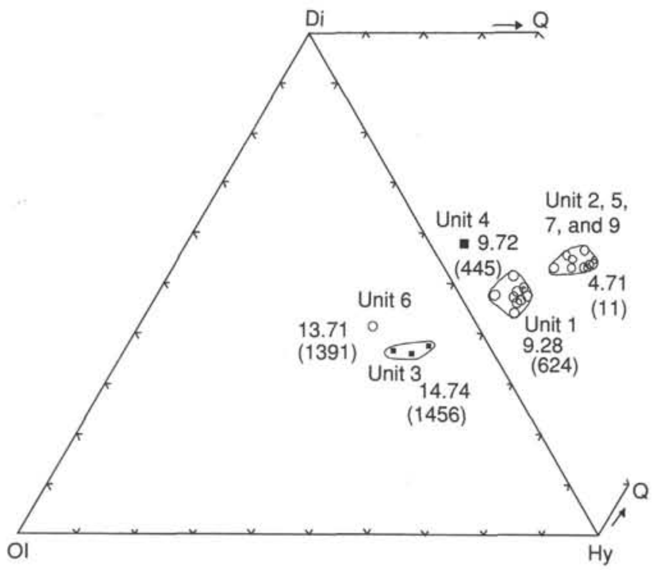

Figure 45. CIPW normative mineralogy of Site 839 volcanic samples shown in Di-Hy-Ol-Q projection from plagioclase. Iron was partitioned assuming $Fe_2O_3/FeO = 0.2$. Decimal numbers by each group are the average weight % MgO in the group; numbers in parentheses are average Cr contents in ppm. Note that Units 1 and 4 are quartz normative despite their very high MgO and Cr contents.

unit, a sedimentary interbed, or a flow top between two major eruptive units of the basaltic andesite.

The three groups of lavas from Site 839 have a number of features in common. All of the samples, regardless of MgO concentration, have very low abundances of Na_2O, TiO_2, P_2O_5, Y, and Zr (Table 11). The concentrations of these elements are lower than the range shown in present-day CLSC and ELSC lavas (Table 12). Similarly depleted basalts have, however, been recovered in the eastern Lau Basin northwest of Tofua (Hawkins and Melchior, 1985; Table 12). The patterns of depletions are similar to those shown by lavas in the modern Tonga and Kermadec arcs, although the Site 839 rocks are not as depleted in Zr or Y (Table 12 and Fig. 49).

The Site 839 lavas, taken together, display coherent trends in their major and trace element variations. They have similar ranges of incompatible element ratios (Fig. 46 and Table 12) and have trace element patterns with the Nb depletion and Rb, Ba, K, and Sr enrichments characteristic of arc lavas from Tonga and Kermadec arcs. Cr, and to a lesser extent Ni, decrease rapidly with decreasing MgO (Fig. 44). Al_2O_3, Na_2O, and SiO_2 increase, Fe_2O_3 and V increase slightly, and CaO increases very slightly and then drops, as MgO decreases (Fig. 44). These variations are consistent with derivation of the Site 839 lavas from similar parental melts by fractionation dominated by olivine and lesser amounts of clinopyroxene, joined by plagioclase in the later stages. The rapid decrease of Cr and the increase in CaO with decreasing MgO (Fig. 48) is consistent with the crystallization and fractionation of Cr-spinel, olivine, and clinopyroxene.

Table 12. Average compositions of principal lithologic units from Site 839.

	Site 839											
Unit no.	1	2	3	4	9	Lau Basin	Lau Basin	Lau Basin	Lau Basin	Tonga-Kermadec	Tonga boninite	Mariana forearc tholeiite
N	9	1	3	1	6	18-1-1	25-2-1	ANT 225-1	ANT 225-3			
Major elements (wt%):												
SiO_2	52.64	54.92	50.42	51.64	53.98	48.00	52.60	53.59	49.27	53.21	54.35	51.08
TiO_2	0.62	0.90	0.58	0.57	0.83	1.12	1.94	1.05	0.70	0.51	0.20	0.24
Al_2O_3	15.00	16.08	12.63	14.33	16.69	16.88	13.92	14.56	16.09	17.09	10.67	14.88
Fe_2O_3	10.02	11.22	10.16	9.42	10.93	9.84	14.54	12.83	9.92	10.92	10.45	8.94
MnO	0.17	0.18	0.17	0.17	0.18	0.15	0.23	0.21	0.14	0.18	0.19	0.15
MgO	9.28	4.64	14.74	9.72	4.84	10.00	4.13	5.27	8.31	5.37	14.99	9.37
CaO	11.68	10.08	10.93	13.64	10.35	11.82	8.30	10.22	13.40	11.45	8.66	12.98
Na_2O	1.35	1.90	1.24	1.15	1.95	2.46	3.08	2.34	1.43	1.57	1.14	1.51
K_2O	0.25	0.56	0.29	0.22	0.50	0.05	0.32	0.17	0.08	0.34	0.35	0.27
P_2O_5	0.07	0.12	0.07	0.04	0.10	0.03	0.17	0.11	0.06	0.07	0.03	0.04
Mg#	64.7	45.0	74.2	67.1	46.7	66.8	36.0	44.9	62.4	49.3	74.0	67.5
Trace elements (ppm):												
Nb	0.9	0	1	1	1.2	0.8	2.1	7	6	0.6	<1	BDL
Zr	30	49	33	27	47.5	50	115	45	22	18	12	17
Y	14.7	21	14.3	15	20.3	24.5	44.8	26	17	12	7	9
Sr	144	191	146	117	196	104	93	98	94	196	151	151
Rb	9.3	8	4.3	3	6.8	<2	<2	0.5	1	4.4	6	1
Zn	99	108	76	105	74	68	126	—	—	84	—	—
Cu	54.3	75	56	51	89.2	114	42	107	97	—	—	—
Ni	137	15	308	92	17.2	206	10	33	112	23	275	112
Cr	624	7	1456	445	14	424	7	50	320	54	1095	348
V	287	357	243	256	344	249	514	359	300	305	247	180
Ce	6.9	12	10.3	6	10.8	5.4	13	—	—	3.7	4.1	—
Ba	62	85	57	44	102	16.1	34.5	32.5	62.2	88	88	12
Ba/Zr	2.1	1.7	1.7	1.6	2.1	0.3	0.3	0.7	2.8	4.9	88	0.7
Y/Zr	0.49	0.43	0.43	0.60	0.42	0.49	0.39	0.58	0.77	0.67	0.60	0.53
Ba/Ce	9.0	7.1	5.5	7.0	9.4	3.0	2.7			23.8	26	—
K/Ba	33	55	42	42	41	26	77	43	11	32	27	187

Notes: N = number of analyses. Note the extremely high Cr and Ni contents of the Unit 3 samples. Lau Basin analyses from samples from *Charles Darwin* Cruise 33 (Ernewein et al., in press) and for ANT samples, from Hawkins (1976) and Hawkins and Melchior (1985); Tonga-Kermadec analysis from Ewart and Hawkesworth (1987); Mariana forearc analysis from Bloomer (1983); Tongan boninite analysis from Falloon et al. (1987) with Ce value from Falloon and Crawford (1991). Mg# calculation as in Table 11.

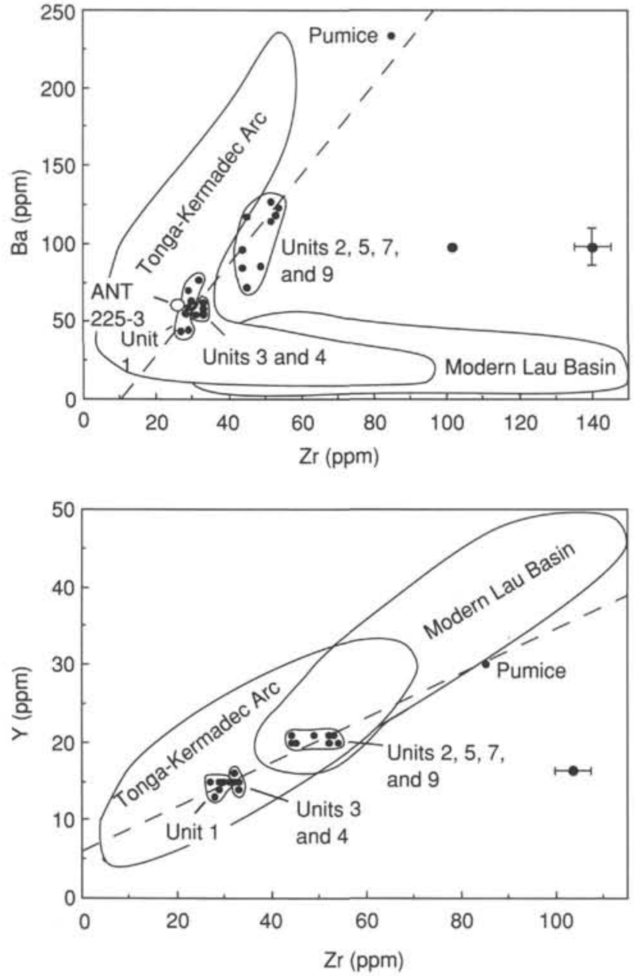

Figure 46. Y and Ba vs. Zr for Site 839 samples (filled circles). Note the very constant Ba/Zr and Y/Zr values; the very low Y and Zr contents of the mafic lavas from Units 1, 3, and 4; and the high Ba/Zr of the samples as a group. Fields for Tonga-Kermadec are from Ewart and Hawkesworth (1987); fields for the Lau Basin neovolcanic zone are from Ernewein et al. (in press), Hawkins (1976), and Hawkins and Melchior (1985). Note the overlap of the arc and basin samples in Y and Zr abundances and the similarity in Ba and Zr of backarc Sample ANT 225-3 (dredged close to the Tofua Arc at 19°S; Hawkins, 1976) to the Unit 1 volcanics. The dashed lines represent an estimate of a best fit through the data, but they do not pass through the origin. Error bars indicate ±1 standard deviation based on precision estimates (see "Explanatory Notes" chapter, this volume).

The entire section at Site 839 cannot represent flows derived from a single batch of parental magma, despite their gross similarities in chemical trends and ratios. The downhole stratigraphy shows no systematic or simple trends between more and less fractionated compositions (Fig. 47). The most primitive flows (Unit 3) occur midway through the section, whereas intervals of the most evolved lavas occur above and below Unit 3. Furthermore, the more fractionated basalts in Unit 4 have lower Ba, Sr, and Na_2O than the magnesian basalts of Unit 3. It is unlikely, given these complexities in the volcanic stratigraphy, that all of the flows at Site 839 were derived from the crystallization of a single parental melt. The chemical and petrographic data are, however, consistent with the derivation of these flows by similar types and degrees of crystal fractionation of similar parental melts. It is likely that the magma sequence sampled at Site 839 represents several eruptive episodes of variously fractionated melts from multiple, similar batches of parental magma.

The N-MORB-normalized, incompatible trace element patterns for Site 839 rocks illustrate two important points (Fig. 49). First, all of the samples from Site 839 have patterns typical of island-arc tholeiites despite their range in degree of fractionation. The basaltic andesites, in both pattern and mineralogy, are virtually identical to samples from the active Tofua Arc (Ewart and Hawkesworth, 1987). Their patterns are different in abundance, but not in form, from those of the magnesian basalts from Unit 3. These arclike patterns are consistent with the high Ba/Zr of the Site 839 lavas (Fig. 46). The second point is that the rhyolitic pumice from the sedimentary section has an almost identical normalized pattern, although with higher absolute abundances. This similarity in trace element signature suggests (1) that the pumice is arc derived and (2) that the series of lavas found at Site 839 could represent parental lavas for these types of rhyolitic pumices. Deviations exist in Sr, P, and Ti, all of which are lower in the pumice sample. This could reflect significant fractionation of plagioclase, oxide, and apatite, as would be required to produce the rhyolitic pumice from a basaltic andesite.

Summary

A 292-m sequence of volcanic rocks was sampled at Site 839. The lowermost 49% of the section is a series of phyric clinopyroxene-orthopyroxene-plagioclase basaltic andesite flows. These are characterized by very high plagioclase/pyroxene phenocryst ratios. The thick sequence of basaltic andesites is overlain by more magnesian aphyric to sparsely phyric olivine-clinopyroxene basalts to basaltic andesites (9% MgO), and high MgO (13%) moderately to highly phyric clinopyroxene-olivine basalts. The most magnesian of these units (Unit 3) shows a pronounced concentration of olivine in its lowermost flows. The magnesian lavas constitute 86% of the upper half of the basement section. The more magnesian Units 1 and 3 are separated by a sedimentary interbed and a thin flow of basaltic andesite identical to that in the lower half of Hole 839B.

The igneous rocks from Site 839 all have trace element ratios and variations considered characteristic of island-arc volcanics. Ba/Zr values are greater than 1.5, Zr is less than 35 ppm, Y is less than 15 ppm, Na_2O is less than 1.5%, and Ba is about 40–60 ppm in the most primitive samples. The basaltic andesites of Units 2 and 9 are very similar to basaltic andesites from the active Tonga Arc (Table 12). The basalts from Unit 3 are remarkable in their very high MgO (to 15.2%), Ni (to 320 ppm), and Cr (to 1740 ppm) contents, but they are not boninitic, as they lack both the mineralogic and textural characteristics of boninite and the extreme silica enrichment and CaO and Al_2O_3 depletions typical of most boninite lavas (Table 12). Neither are they as depleted as primitive arc tholeiites, which occur with boninitic lavas in the Mariana forearc (Table 12). The aphyric and nearly aphyric Unit 3 basalts are, however, close to compositions that have been postulated as parental to the island-arc tholeiite series of the Tonga and Kermadec arcs (Ewart and Hawkesworth, 1987).

PHYSICAL PROPERTIES

Introduction

A full suite of standard ODP physical properties measurements was made at Site 839. Index properties of sediments and sedimentary rocks from Holes 839A and 839B were determined by using a pycnometer and balance, and include bulk density, grain density, porosity, water content, and void ratio. Bulk density was also measured using the continuous gamma-ray attenuation porosity evaluator (GRAPE) on full APC cores from Hole 839A. All basalt

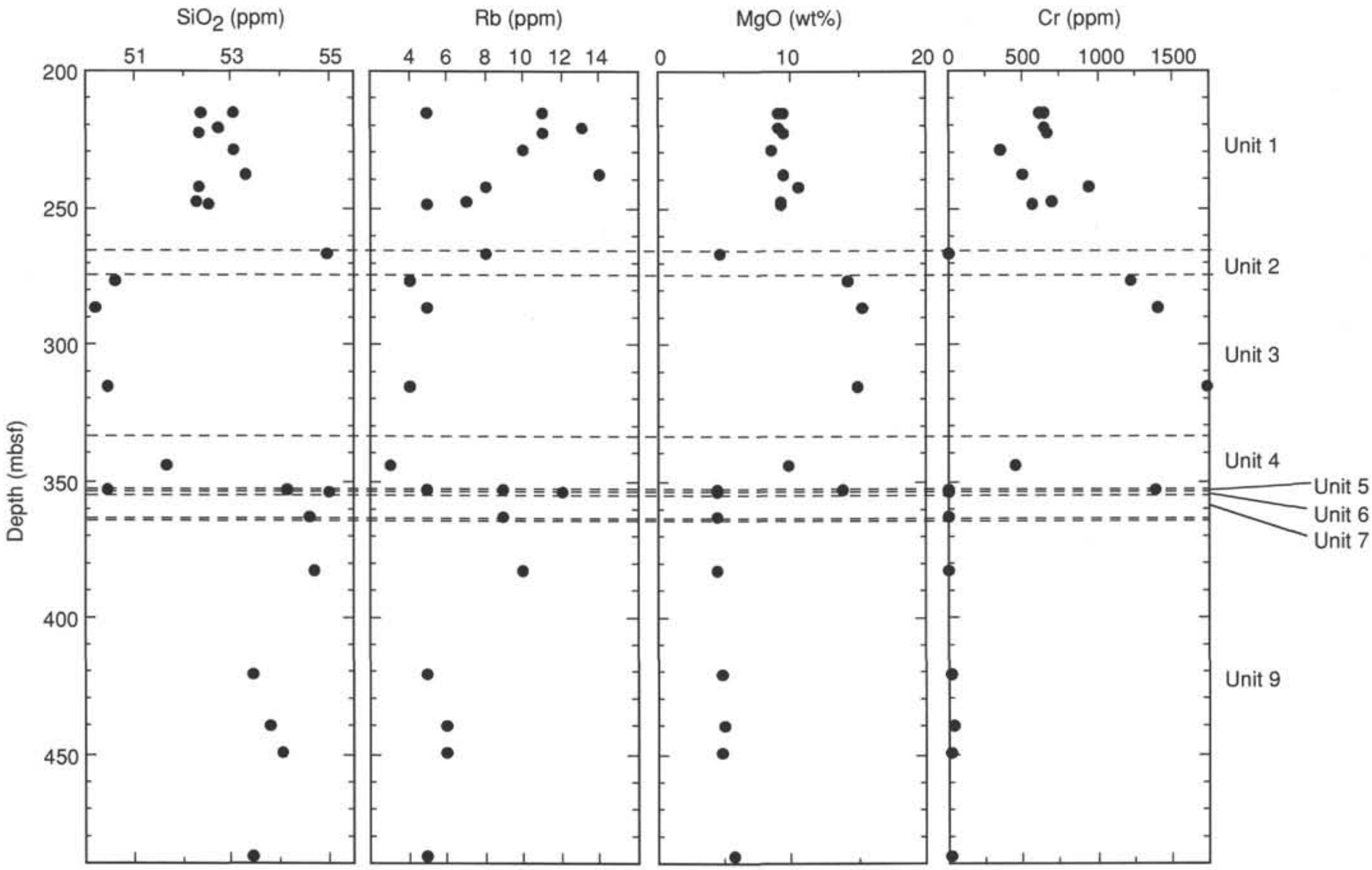

Figure 47. Downhole chemical variations of Site 839 lavas. The units are not arranged in a simple chemical sequence from more to less fractionated, or vice versa. The increase in Cr downward in Unit 3, from its essentially aphyric top to the densely phyric base, may reflect some accumulation of Cr-spinel. The large scatter in Rb values in Unit 1 may be a consequence of low-temperature reaction with seawater.

samples from Hole 839B were run through the 2-min GRAPE process to determine bulk densities. These samples (42 discrete samples) were also powdered, and the weight and volume of the dried powder determined, to give grain density.

Compressional wave velocities were measured on whole cores using the continuous *P*-wave logger and on discrete samples using the Hamilton Frame apparatus. Velocities of unconsolidated sediment that could not be removed from the core liner were measured in only one direction. Velocities were measured in both horizontal and vertical directions when possible in unconsolidated sediment and on most of the consolidated sedimentary rocks and basalts.

Vane-shear strength was measured on selected undisturbed intervals of the core samples from Hole 839A until degrees of rotation exceeded 90° or the sediment cracked, indicating that the assumption of uniform shear by the vane was no longer valid.

Thermal conductivity was measured on undisturbed sediment cores from Hole 839A and on two basalt samples from Hole 839B.

The lithologic units referenced in this section are those described in the "Lithostratigraphy" section (this chapter). Results from laboratory measurements are listed on Tables 13 and 14 and plotted on Figures 50 through 63.

Index Properties

Hole 839A

Wet-bulk density, grain density, water content, porosity, and void ratio for sediments and sedimentary rocks from Hole 839A are plotted vs. depth in Figure 50, and values for the gravimetrically determined index properties are listed in Table 13.

Index properties vary cyclically downhole throughout much of Hole 839A, predominantly reflecting the total amount of calcium carbonate in the sediments. For example, there are several cycles between 0 and 18, 18 and 48, and 48 and 80 mbsf. Within each of these cycles, density decreases, whereas water content, porosity, and void ratio increase (Fig. 50). The carbonate content within each cycle is indicative of the amount of nannofossil ooze within the cycle. Nannofossil ooze, the dominant lithology, is positively correlated with water content (Fig. 51), and thus the remaining index properties. Within each of the cycles, therefore, the index properties depend on the proportion of nannofossil ooze to sands and gravels.

Between 80 and 100 mbsf, the scatter in the data results from sampling multiple lithologies within a small depth interval. The few indurated sediment samples measured below 100 mbsf are more dense and contain less water than the overlying sediments. Average index property values for the entire hole are bulk density = 1.52 g/cm^3, grain density = 2.72 g/cm^3, porosity = 73%, water content = 107%, and void ratio = 4.23.

The GRAPE bulk density data have been processed by initially averaging at 5-cm intervals to remove spurious data points caused by core section ends and void spaces within the core (Fig. 52A) and then by applying a 15-point running average (Fig. 52B). Data were not obtained on core sections between 18 and 52 mbsf because of problems with the GRAPE electronics. Of the core material processed, the values plotted within the upper 18 mbsf display a signal typical of nannofossil ooze in the Lau Basin (e.g.,

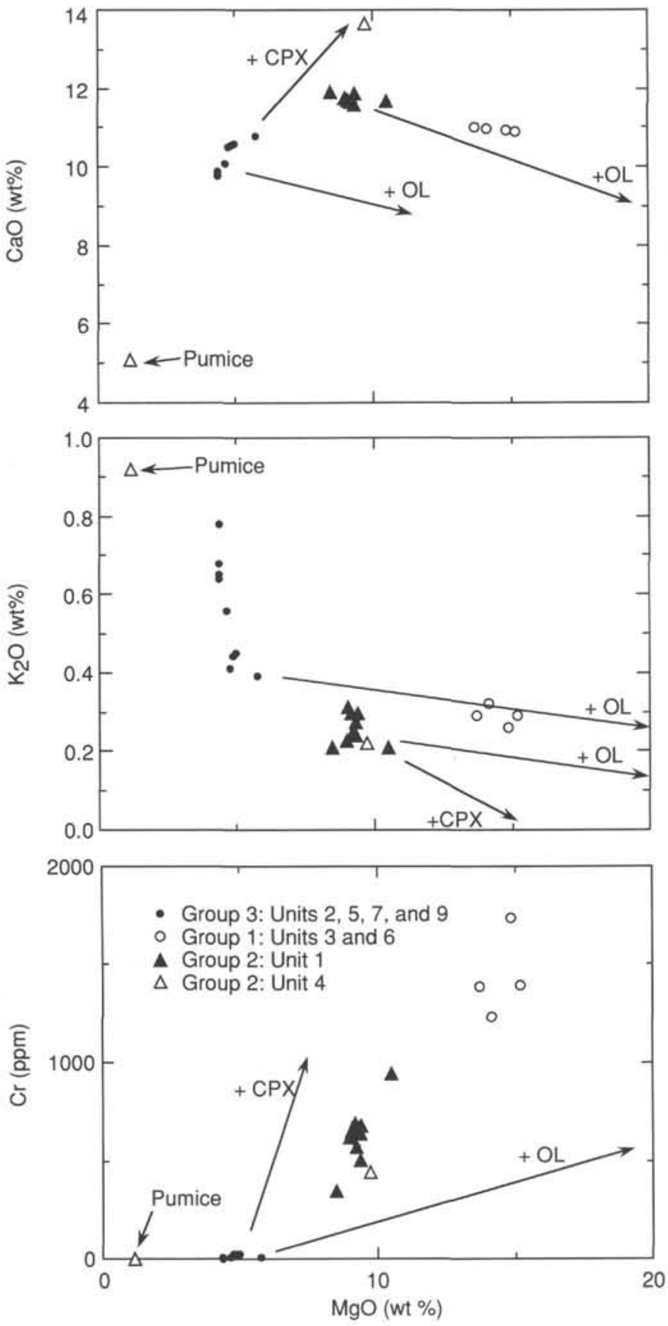

Figure 48. Representative variation diagrams showing the kinds of mixing lines expected for adding magnesian olivine (OL) and clinopyroxene (CPX) to volcanic rocks from Units 1 and 9. Note that no single solution is appropriate to produce the more magnesian basalts by mixing. Least-squares mixing calculations indicate that producing the Group 1 basalts from the Group 3 basaltic andesites requires accumulation of about 50% olivine and clinopyroxene (in 1:1 proportions), with small amounts of Cr-spinel and plagioclase. Conversely, the Group 3 volcanics could be derived from the Group 1 compositions by fractionation of the same minerals in the same proportions.

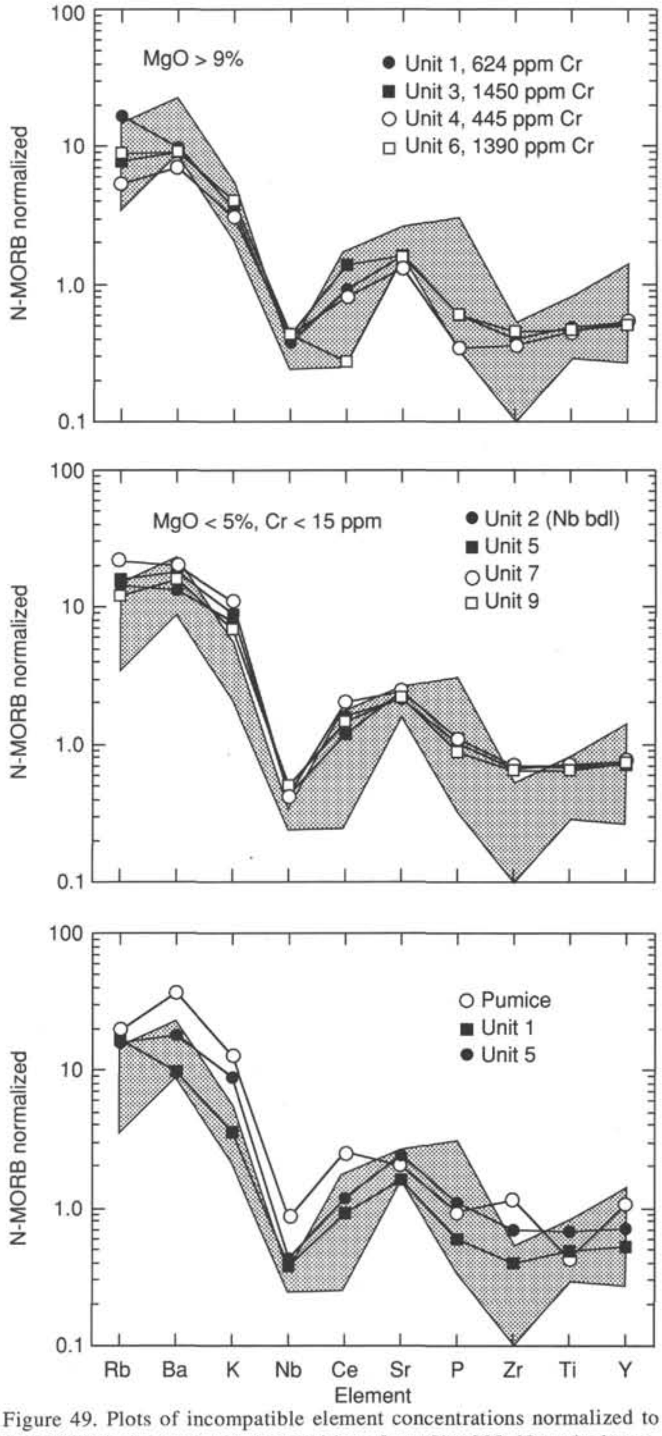

Figure 49. Plots of incompatible element concentrations normalized to N-MORB for average unit compositions from Site 839. Note the homogeneity of the basaltic andesite samples in Units 1, 5, 7, and 9; their higher overall concentrations of incompatible elements compared to Units 1, 3, 4, and 6; the similarity of patterns for the more and less fractionated samples; and the similarity of the pattern for the rhyolitic pumice from the sedimentary section to those of basement samples from the site. Stippled field is range of Tonga-Kermadec Arc lava compositions from Ewart et al. (1973, 1977) and Ewart and Hakesworth (1987). N-MORB normalizing values from Sun and McDonough (1989). Unit 2 has Nb below detection limit (Nb bdl).

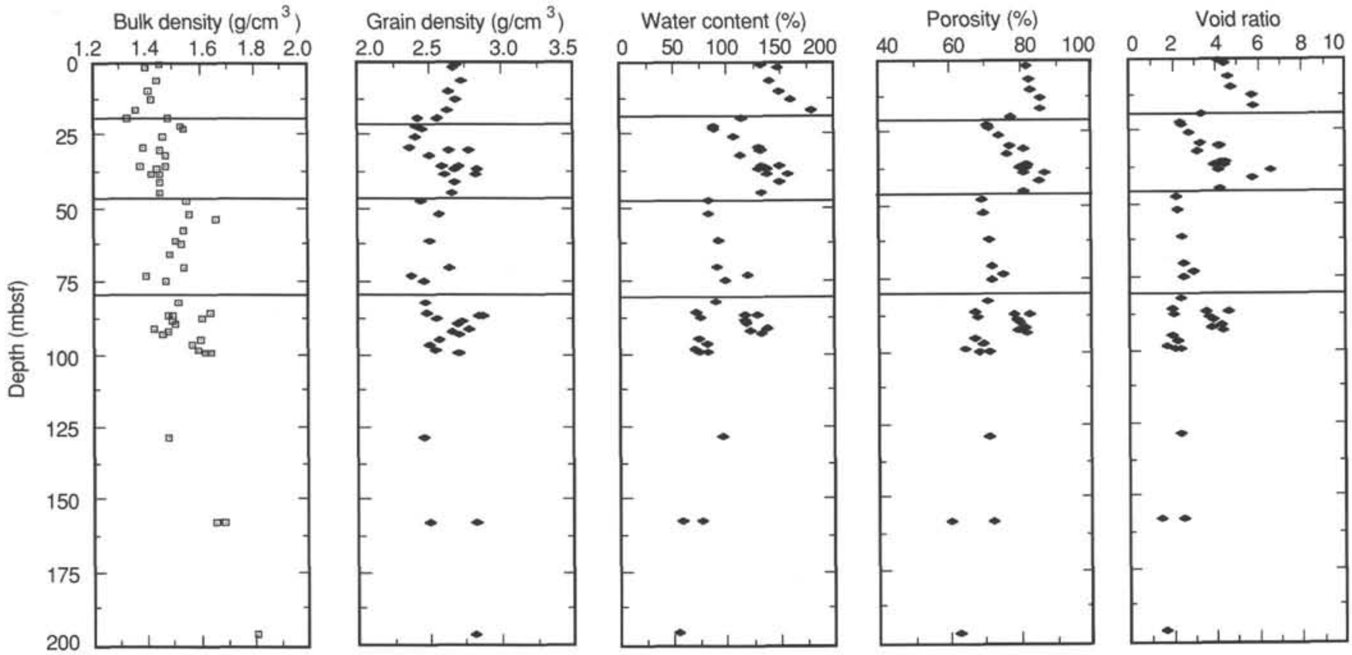

Figure 50. Index property data (bulk density, grain density, water content, porosity, and void ratio) vs. depth for the sedimentary section from Hole 839A.

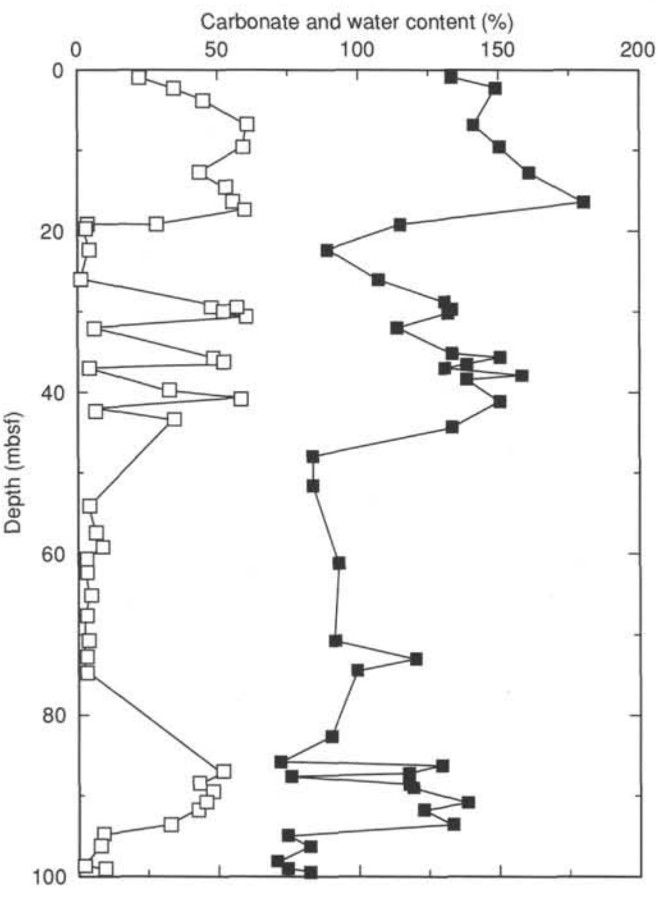

Figure 51. Total carbonate content (open squares) and water content (filled squares) vs. depth in Hole 839A, illustrating similar trends downhole.

a gently oscillating curve with an average value of 1.45 g/cm³ and a very small increase downhole). In the lower sections of Hole 839A, GRAPE density decreases from approximately 1.70 to 1.6 g/cm³, reflecting the generally decreasing sand- to silt-size grains within the proportionally increasing amount of matrix material (nannofossil ooze). The variation in GRAPE density between 80 and 100 mbsf reflects the varying layers of nannofossil ooze with silt and sand interbeds (see "Lithostratigraphy" section, this chapter).

Hole 839B

GRAPE 2-min bulk density and gravimetrically measured grain density results are presented in Figure 53 and Table 14. GRAPE 2-min counts average 2.54 g/cm³ over the sediments and basalt samples measured. The variation in bulk density reflects the highly vesicular nature of the basalts. Grain density for the basalt samples averages 2.89 g/cm³ and shows little significant increase downhole. These values are slightly lower than reported average results for basalts (Johnson and Olhoeft, 1984).

Compressional Wave Velocity

Hole 839A

Compressional-velocity data measured with a Hamilton Frame device and the *P*-wave logger on sediments from Hole 839A are shown in Figures 54 and 55, respectively, and are listed in Table 13. Compressional wave velocity measured on these sediments averages 1603 m/s. The velocity of the unconsolidated sediments (predominantly nannofossil ooze) increases only slightly downhole, from 1473 to 1558 m/s. Higher velocities were measured on sands and indurated sediments. The expanded scale and the more dense coverage of the *P*-wave logger provide more detailed velocities for the sedimentary column in Hole 839A (Fig. 55). Nannofossil ooze between 0 and 18 mbsf displays a 1500 m/s, zero-gradient velocity profile that is characteristic of the Leg 135 oozes. The variation in measured results below that depth reflects the alternation of silt and sandstone interbeds within the nannofossil ooze. Overall, no pronounced gradient is present within the top 100 mbsf. However, individual units display internal gradi-

Table 13. Physical properties data, Hole 839A.

Core, section, interval (cm)	Depth (mbsf)	TC (W/[m · °K])	Su (kPa)	Bulk density (g/cm^3)	Grain density (g/cm^3)	Porosity (%)	Water content (%)	Void ratio	V_p (m/s)	V_p dir.
135-839A-										
1H-1, 60–60	0.60	0.756								
1H-1, 75–76	0.75		1.2							
1H-1, 76–78	0.76			1.45	2.69	81	133	4.2	1474	A
1H-1, 76–78	0.76									A
1H-2, 60–60	2.10	0.908								
1H-2, 75–76	2.25		3.7							
1H-2, 78–80	2.28			1.40	2.67	82	149	4.5	1484	A
1H-3, 30–30	3.30	0.865								
1H-3, 60–60	3.60	0.875								
2H-2, 60–60	6.60	0.806								
2H-2, 75–76	6.75		3.2							
2H-2, 78–80	6.78			1.44	2.73	82	141	4.6	1502	A
2H-3, 60–60	8.10	0.925								
2H-4, 60–60	9.60	0.904								
2H-4, 75–76	9.75		5.5							
2H-4, 78–80	9.78			1.41	2.64	83	150	4.8	1516	A
2H-6, 60–60	12.60	0.891								
2H-6, 90–91	12.90		12.0							
2H-6, 92–94	12.92			1.42	2.69	85	161	5.8	1513	A
3H-2, 60–60	16.10	0.825								
3H-2, 75–76	16.25		8.7							
3H-2, 76–78	16.26			1.36	2.63	85	181	5.8	1461	C
3H-3, 60–60	17.60	0.968								
3H-4, 50–51	19.00		5.9							
3H-4, 51–53	19.01			1.48	2.56	77	116	3.4	1501	A
3H-4, 60–60	19.10	0.864								
3H-4, 75–76	19.25		7.7							
3H-4, 77–79	19.27			1.33	2.42	45	52	0.8	1572	A
3H-4, 110–112	19.60		5.3						1554	A
3H-6, 60–60	22.10	0.811								
3H-6, 75–76	22.25		4.5							
3H-6, 76–78	22.26			1.53	2.41	71	89	2.4	1534	A
3H-6, 110–112	22.60	0.706		1.54	2.45	71	90	2.5		
4H-2, 76–78	25.76			1.46	2.40	74	107	2.8		
4H-2, 85–88	25.85								1598	A
4H-3, 60–60	27.10	0.865								
4H-4, 60–60	28.60	0.755								
4H-4, 77–79	28.77			1.39	2.36	77	131	3.3	1523	A
4H-5, 10–12	29.60								1519	C
4H-5, 20–21	29.70		37.4							
4H-5, 22–24	29.72			1.45	2.77	81	133	4.2		
4H-5, 24–26	29.74		141.3							
4H-5, 75–76	30.25		8.1							
4H-5, 77–78	30.27			1.45	2.64	81	132	4.2		
4H-6, 60–60	31.60	0.809								
4H-6, 75–76	31.75		16.6							
4H-6, 77–78	31.77			1.47	2.50	76	113	3.2	1511	A
5H-2, 72–73	35.22		152.3	1.47	2.71	82	134	4.5		
5H-2, 77–78	35.27								1525	C
5H-2, 60–60	35.40	0.810								
5H-2, 100–101	35.50		22.1							
5H-2, 102–104	35.52			1.38	2.59	81	150	4.3	1502	A
5H-3, 51–53	36.51		38.6	1.44	2.83	82	139	4.5	1492	A
5H-3, 60–60	36.60	0.978								
5H-3, 87–89	36.87			1.44	2.68	80	131	4.0		
5H-3, 90–91	36.90		56.3							
5H-4, 50–51	38.00		199.8	1.45	2.82	87	158	6.6		
5H-4, 57–59	38.07								1532	C
5H-4, 60–60	38.10	0.894								
5H-4, 92–93	38.42			1.42	2.61	81	139	4.2		
5H-6, 60–60	41.10	0.855								
5H-6, 75–76	41.25		53.0							
5H-6, 76–78	41.26			1.45	2.68	85	150	5.8		
5H-6, 78–80	41.28								1472	A
6H-2, 45–47	44.45								1506	C
6H-2, 50–51	44.50		60.7							
6H-2, 52–54	44.52			1.45	2.66	81	133	4.2		
6H-2, 60–60	44.60	0.833								
6H-2, 145–146	45.45		30.9						1523	C
6H-3, 60–60	46.10	0.900								
6H-4, 60–60	47.60	0.857								
6H-4, 80–82	47.80			1.55	2.44	69	84	2.2		
6H-6, 60–60	50.60	0.832								
6H-7, 26–27	51.76			1.56	2.57	70	83	2.3	1625	A
6H-7, 26–28	51.76									A

Table 13 (continued).

Core, section, interval (cm)	Depth (mbsf)	TC (W/[m · °K])	Su (kPa)	Bulk density (g/cm^3)	Grain density (g/cm^3)	Porosity (%)	Water content (%)	Void ratio	V_p (m/s)	V_p dir.
135-839A- (cont.)										
7H-2, 76–78	54.26			1.66	10.57	6	7	35.0	1619	A
7H-2, 125–125	54.75	0.717								
7H-3, 60–60	55.60	0.895								
7H-4, 60–60	57.10	0.855								
7H-4, 75–76	57.25		76.1							
7H-4, 77–79	57.27								1527	A
7H-6, 60–60	60.10	0.780								
7H-7, 30–31	61.30		8.8							
7H-7, 36–38	61.36			1.51	2.50	71	93	2.5	1552	A
8H-1, 75–76	62.25		15.5							
8H-2, 60–60	63.60	0.774								
8H-3, 60–60	65.10	0.874								
8H-3, 75–76	65.25		8.8							
8H-3, 75–77	65.25								1540	A
8H-4, 60–60	66.60	0.801								
8H-6, 60–60	69.60	0.802								
8H-7, 15–16	70.65			1.54	2.64	72	92	2.5	1571	A
9H-2, 56–58	73.06			1.40	2.37	75	121	3.0	1612	C
9H-2, 115–115	73.65	0.709								
9H-3, 50–52	74.50			1.47	2.46	72	100	2.5		
9H-3, 60–60	75.50	0.891								
9H-4, 60–60	77.00	0.821								
10H-2, 60–62	82.60			1.52	2.47	71	91	2.4	1678	C
10H-4, 78–80	85.78			1.64	2.48	67	72	2.0		
10H-4, 138–140	86.38		73.9	1.50	2.84	82	129	4.7		
10H-4, 139–141	86.39								1573	C
10H-5, 56–58	87.06			1.48	2.87	78	117	3.6	1528	C
10H-5, 60–61	87.10	0.933	101.5							
10H-5, 118–120	87.68			1.61	2.55	68	76	2.1	1590	C
10H-6, 51–53	88.51			1.50	2.73	79	117	3.7		
10H-6, 60–60	88.60	0.873								
10H-6, 106–108	89.06								1564	C
10H-6, 108–110	89.08			1.51	2.70	80	119	3.9		
11H-1, 94–96	90.94			1.43	2.77	81	139	4.3	1589	C
11H-1, 100–101	91.00		119.2							
11H-2, 50–52	92.00			1.48	2.66	79	123	3.8	1558	C
11H-2, 60–60	92.10	0.804								
11H-3, 50–52	93.50			1.46	2.71	81	134	4.4		
11H-3, 60–60	93.60	0.949								
11H-4, 50–52	95.00			1.60	2.57	67	75	2.0		
11H-4, 60–60	95.10	0.848								
11H-5, 40–42	96.40			1.57	2.50	69	83	2.3	1573	C
11H-6, 60–60	98.10	0.874								
11H-6, 68–70	98.18								1625	C
11H-6, 88–90	98.38			1.59	2.54	64	71	1.8		
11H-7, 29–31	99.29			1.64	2.70	68	75	2.2		
12X-1, 6–9	99.56			1.62	2.71	71	82	2.4	1863	A
12X-1, 24–25	99.74								1691	A
12X-2, 24–25	101.24			1.66	2.80	70	77	2.3		
15X-1, 60–62	129.10			1.48	2.46	71	97	2.4		
15X-1, 60–62	129.10								1558	A
18X-CC, 8–10	157.68			1.66	2.50	60	59	1.5		
18X-CC, 31–33	157.91			1.69	2.82	72	77	2.6	1947	A
20X-1, 5–6	176.55			1.71	2.74	72	75	2.5	2196	A
20X-1, 10–11	176.60			1.89	2.66	58	46	1.4	2196	A
22X-CC, 1–2	195.91			1.81	2.81	63	55	1.7	2005	A

Notes: TC = thermal conductivity, Su = undrained vane shear strength, V_p = compressional (*P*-wave) velocity, and V_p dir. = velocity direction, where A is the vertical velocity along the core and C is the horizontal velocity perpendicular to the core face.

ents reflecting an increase in grain size. For example, within Subunit IIC between 40 and 55 mbsf, velocity increases from 1500 to 1590 m/s as grain size increases from silts to sands (see "Lithostratigraphy" section, this chapter).

Hole 839B

Compressional wave velocity measured on sediments from the upper portions of Hole 839B agree well with measurements made on sediments sampled from the lower portions of Hole 839A (Fig. 54). Velocity measurements made on basalts between 214 and 487.5 mbsf average 4226 m/s and display some variation in values around the mean but no appreciable gradient with depth. The variability in velocity values reflects the vesicularity variations within the measured basalt samples. There is excellent correlation between grain density and compressional wave velocity in samples from Hole 839B (Fig. 56).

Undrained Vane Shear Strength

Values of undrained shear strength were obtained using the standard on-board miniature vane shear apparatus on unconsoli-

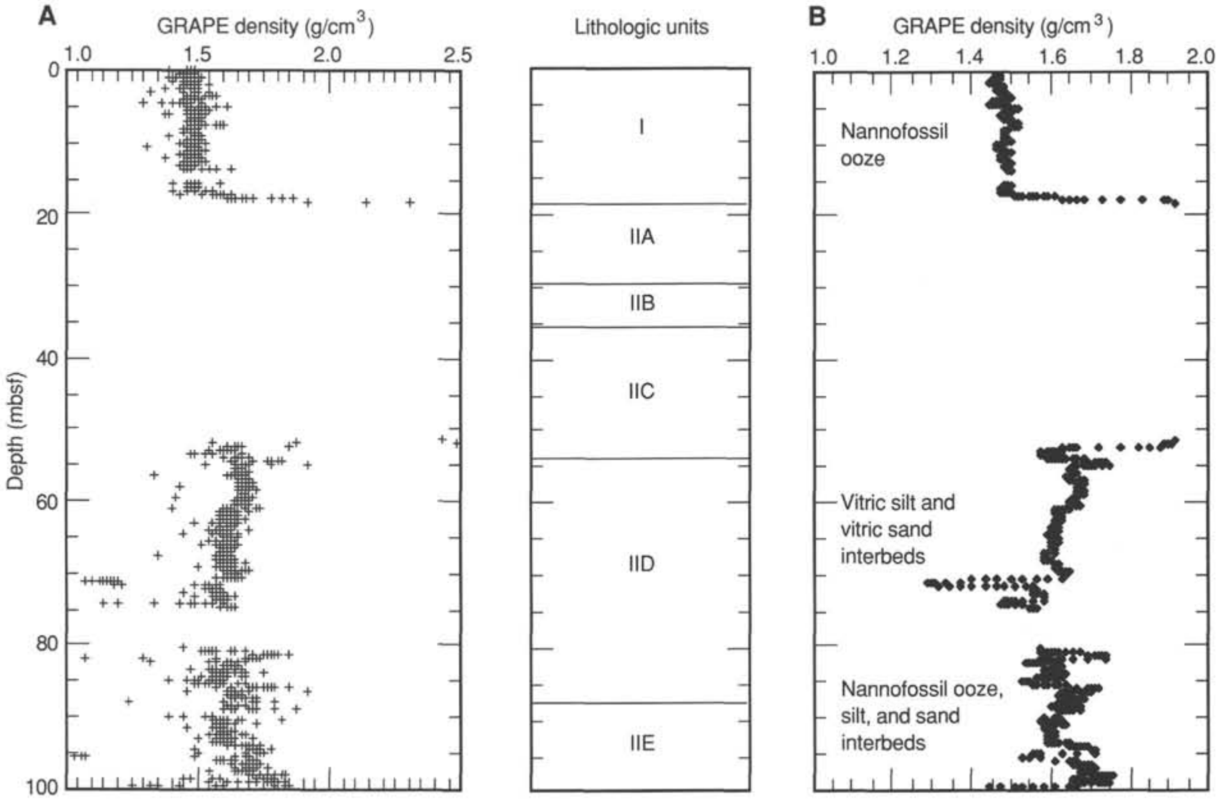

Figure 52. GRAPE bulk density vs. depth at 5-cm intervals (**A**) and after 15-point running average has been applied (**B**), Hole 839A.

dated sediments in Hole 839A; the results are plotted in Figure 57 and reported in Table 13.

In general, measurements are made on representative sections of core, which means that the matrix material, generally the finer grained sediment, is sampled preferentially. Initial shear strengths within the upper 20 m are low (about 5 kPa) and increase downhole to 50 kPa at 40 mbsf with a few excursions to >150 kPa, which represent individual measurements in small consolidated layers within the section. Below 40 mbsf, few measurements were made because many sections contained silts and sands for which this technique is inappropriate.

Thermal Conductivity

All thermal conductivity values in soft sediment cores were obtained using needle probes inserted through core liners into full core sections. For lithified sedimentary rocks and basalts, the thermal conductivity was measured on a split core face. The thermal conductivity results for both full and split cores from Holes 834A and 839B are shown in Figure 58 and listed in Tables 13 and 14. The thermal conductivity averages 0.846 W/(m · °K) for the unconsolidated sediments in Hole 839A and 1.472 W/(m · °K) for the consolidated sediments and basalts tested in Hole 839B. The variability in the thermal conductivity values measured in the unconsolidated sediments reflects the water content and mimics the index property trends outlined earlier. Within Hole 839B, the low thermal conductivity (1.100 W/[m · °K]) was measured on consolidated sediment (sandstones) and the high values (1.500 W/[m · °K] and higher) on basalt samples.

Temperature Measurements

The downhole water sampler temperature probe (WSTP) was used to make temperature measurements at four depths in Hole 839A. The results of the three shallowest measurements are shown in Figure 59. A measurement made at 90 mbsf was not used because the temperature curve did not decay. The temperature history in the sedimentary section should be such that after 5 min in the sediment, the decay curve is approximated by

$$T(t) = A/t + T_{eq},$$

where A is a constant determined experimentally, t is time, and T_{eq} is the equilibrium formation temperature (Hyndman et al., 1987). The temperature gradient defined by these measurements is about 0.71 °C/100 m (Fig. 60A) compared to 5.00°C/100 m at Site 834, 1.53°C/100 m at Site 835, 2.11°C/100 m at Site 837, and 8.70°C/100 m at Site 838 (Fig. 60B). Thermal conductivity measurements (Fig. 57) were used to calculate thermal resistivity and integrated over depth. When the resulting thermal resistance is plotted with the temperature measurements from the WSTP temperature probe (Fig. 61), the slope of the regression line indicates that the heat flow in the region is 9.1 mW/m^2. For comparison, heat flow was 50 mW/m^2 at Site 834, 14.5 mW/m^2 at Site 835, 24.4 mW/m^2 at Site 837, and 50.6 mW/m^2 at Site 838 (Fig. 62). Heat flow predicted by theoretical heat flow curves approaches 200 mW/m^2 for young crust (Anderson et al., 1977).

Discussion

The physical properties data, particularly the index properties, correlate with the lithologic changes at Site 839. For example, the increase in carbonate content corresponds to an increase in density and a decrease in water content, porosity, and void ratio within the upper portion of Hole 839A. The *P*-wave logger, compressional-wave velocity data varies with the alternation of silts and sands interbedded within the nannofossil ooze. An increase in silt and sand content corresponds to an increase in compressional wave velocity. Within Hole 839B there is an excellent correlation between grain density and compressional wave velocity of the basalt samples measured. The correlation between bulk density

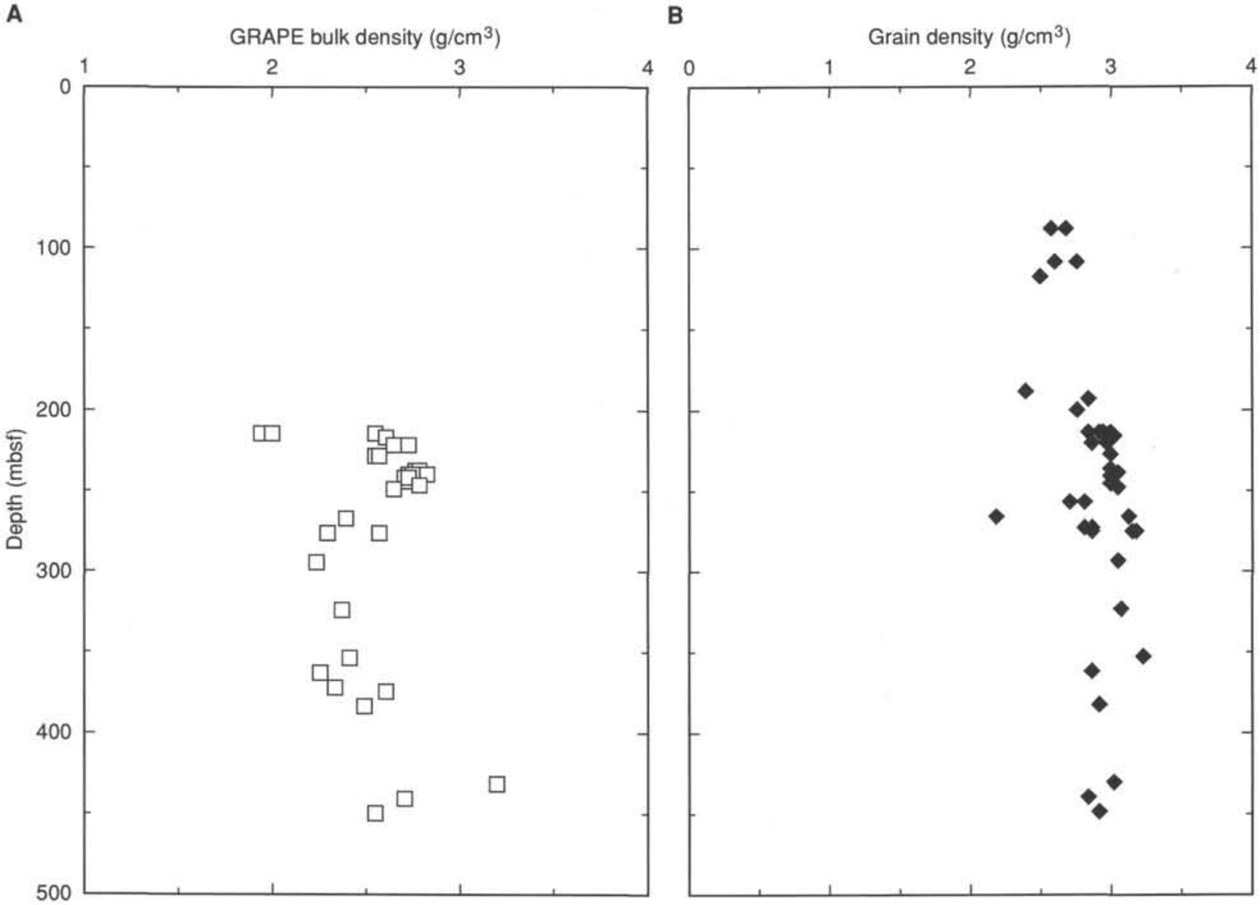

Figure 53. GRAPE 2-min bulk density (**A**) and grain density (**B**) for consolidated sediments and basalt samples recovered from Hole 839B.

and velocity in these same basalt samples is poor, probably because the vesicularity of the basalts is random.

The temperature gradient at Site 839 is 7.1°C/km and is the lowest found in the Lau Basin during Leg 135. The calculated heat flow, 9.1 mW/m^2, is also the lowest measured to date on this leg. These observations suggest that there is a considerable amount of heat being removed by seawater convection processes. Site 839, situated close to the spreading center, may be the site of downwelling convective flow for such low temperatures to be measured. Nearby Site 838 has a higher measured heat flow (50 mW/m^2) and may be the site of less vigorous downflow.

PHYSICAL PROPERTIES PACKER EXPERIMENT

Packer Experiment

A single-element, nonrotating packer was run in Hole 839B following logging. The objectives of the packer experiment were to measure the bulk permeability and pore pressure between the packer element and the bottom of the hole, and to set the packer at two different depths to determine if the permeability changed through the hole.

Equipment and Operations

During logging, possible sites for a packer experiment were observed on caliper logs obtained during logging, with final site selections made from the FMS caliper. Based on these logs, two sites were selected, at 398.2 and 326.9 mbsf. At the deeper site, the target section was 8.5 m long, with a borehole diameter between 28 and 33 cm (11 and 13 in.). The second site was 7.3 m long, with a borehole diameter from 33 to 38 cm (13 to 15 in.). Both sites were moderately elliptical, but this was not considered to be a serious problem in sealing the hole with the packer element. These locations were selected because of the relative smoothness of the borehole and the lack of obvious breakouts, because the width was sufficiently narrow for the packer to close off the borehole successfully, and because a sufficient length of smooth section was present to give a good target for final positioning of the packer element. Following site selection, a detailed packer test plan was made up based on an outline for ODP packer experiments in Becker (1990a).

The packer used was a nonrotatable, single drill-string packer from TAM International of Houston, Texas; the operation of this packer on board the *JOIDES Resolution* is described by Becker (1990a), from which much of the following discussion is taken. Inflation of the packer element is enabled by free-falling a retrievable go-devil, which keys into the packer plumbing system. This go-devil also carries the Kuster Company pressure recorders that acquire the borehole pressure data needed to determine permeability. Once the go-devil is sealed properly in the packer control assembly, the rig pumps can be used to pressurize the packer element. When the packer is inflated and gripping the borehole wall, the heave compensator is adjusted to put weight on the packer (about 15,000 lb), which in turn shifts a control tube in the packer to close off the inflate/deflate ports and lock the packer element in the inflated position. After completion of testing, the packer is deflated by pulling up on the drill string at the rig floor, opening the inflate/deflate port. About ½ hr is then needed for the packer to deflate before it can be moved.

Two types of tests were run. Pulse tests require rapidly pumping fluid into the shut-in borehole and monitoring the decay rate

Table 14. Physical properties data, Hole 839B.

Core, section, interval (cm)	Depth (mbsf)	TC (W/[m · °K])	Bulk density (g/cm^3)	Grain density (g/cm^3)	V_p (m/s)	V_p dir.
135-839B-						
2W-1, 15–16	90.15			2.66		
2W-1, 78–80	90.15			2.55	1474	C
2W-1, 78–80	90.78				1553	C
3R-CC, 7–8	110.07			2.74	1847	C
3R-CC, 15–16	110.15			2.60	1816	C
4R-CC, 1–2	119.17			2.48	1633	A
7R-CC, 4–5	189.74			2.37		
8R-1, 30–31	195			2.82		
9R-1, 60–62	199.9			2.75		
10R-CC, 1–5	204.31				1567	C
11R-1, 30–35	208.8				2266	C
11R-1, 69–75	209.19				2157	C
12R-1, 9–11	213.59		1.94	2.94	2082	A
12R-1, 9–11	213.59			2.91	2135	B
12R-1, 9–11	213.59				2092	C
12R-1, 38–45	213.88	1.142				
12R-1, 49–51	213.99		2.00	2.91	2287	A
12R-1, 49–51	213.99			2.83	2312	B
12R-1, 49–51	213.99				2353	C
12R-1, 117–119	214.67		2.54	2.98	4089	A
12R-1, 117–119	214.67				4169	B
12R-1, 117–119	214.67				4273	C
12R-2, 80–82	215.78		2.61	3.00	4091	A
12R-2, 80–82	215.78				4128	B
12R-2, 80–82	215.78				3900	C
13R-1, 57–59	218.77		2.60	2.98	4110	A
13R-1, 57–59	218.77				4326	B
13R-1, 57–59	218.77				4152	C
13R-2, 67–69	220.37		2.65	2.96	4318	A
13R-2, 67–69	220.37				4262	B
13R-2, 67–69	220.37				3877	C
13R-3, 29–36	221.49	1.526				
13R-3, 72–74	221.89		2.72	2.85	4340	A
13R-3, 72–74	221.89				4474	B
13R-3, 72–74	221.89				4427	C
14R-1, 18–20	227.38		2.54	2.97	4009	A
14R-1, 18–20	227.38				3866	B
14R-1, 18–20	227.38				3909	C
14R-1, 23–28	227.93	1.450				
14R-2, 17–19	228.87		2.56	2.99	3802	A
14R-2, 17–19	228.87				3964	B
14R-2, 17–19	228.87				3802	C
15R-1, 67–69	237.91			2.99		
15R-1, 67–69	237.97		2.79		4251	A
15R-1, 67–69	237.97				4298	B
15R-1, 67–69	237.97				4044	C
15R-1, 80–87	238.10	1.730				
15R-2, 80–82	239.31		2.75	3.02	4114	A
15R-2, 80–82	239.31				4285	B
15R-2, 80–82	239.31				4184	C
15R-2, 73–79	239.53	1.663				
15R-3, 47–49	240.43		2.83	3.00	4402	A
15R-3, 47–49	240.43				4479	B
15R-3, 47–49	240.43				4123	C
15R-4, 62–64	242.08		2.72	2.99	4298	A
15R-4, 62–64	242.08				4385	B
15R-4, 62–64	242.08				4260	C
15R-4, 70–78	242.50	1.531				
16R-1, 52–60	247.52	1.812				
16R-1, 64–66	247.64		2.79	2.97	4226	A
16R-1, 64–66	247.64				4364	B
16R-1, 64–66	247.64				4257	C
16R-2, 14–16	248.6		2.64	3.04	4363	A
16R-2, 14–16	248.6				4485	B
16R-2, 14–16	248.6				4263	C
17R-1, 20–28	256.90	1.074				
17R-1, 27–29	256.97			2.69	1927	A
17R-1, 50–52	257.2			2.79	1815	A
17R-1, 50–52	257.2				1847	B
18R-1, 27–29	266.67		2.40	3.12	4367	A
18R-1, 27–29	266.67			2.17	4569	B
18R-1, 27–29	266.67				4166	C
29R-1, 43–45	273.03			2.80		
29R-1, 118–120	273.78			2.85		

Table 14 (continued).

Core, section, interval (cm)	Depth (mbsf)	TC (W/[m · °K])	Bulk density (g/cm^3)	Grain density (g/cm^3)	V_p (m/s)	V_p dir.
135-839B- (cont.)						
19R-1, 5–7	276.05		2.56	2.86	4731	A
19R-1, 5–7	276.05				4728	B
19R-1, 5–7	276.05				4748	C
19R-1, 1–5	276.10	1.322				
19R-1, 44–46	276.44		2.29	3.17	4295	A
19R-1, 44–46	276.44			3.15	4471	B
19R-1, 44–46	276.44				4158	C
20R-1, 9–12	285.79				4412	A
21R-1, 35–37	295.65		2.23	3.04	4223	A
21R-1, 35–37	295.65				4388	B
21R-1, 35–37	295.65				4397	C
23R-1, 57–59	315.17				4196	C
24R-1, 25–27	324.55		2.37	3.05	3970	A
24R-1, 25–27	324.55				3829	B
24R-1, 25–27	324.55				3996	C
25R-1, 44–47	334.44				4675	C
26R-1, 10–12	343.7				4330	C
27R-1, 20–23	353.5		2.41	3.21	4413	A
28R-1, 107–110	363.97		2.26	2.84	4606	
29R-1, 43–45	373.03		2.34		4506	A
29R-1, 43–45	373.03				4557	B
29R-1, 43–45	373.03				4366	C
29R-1, 118–120	373.78		2.60		4414	A
29R-1, 118–120	373.78				4362	B
29R-1, 118–120	373.78				4222	C
30R-1, 35–37	382.55		2.49	2.91	4288	A
30R-1, 35–37	382.55				4398	B
30R-1, 35–37	382.55				4151	C
31R-1, 18–20	392.08				3943	C
34R-1, 2–4	420.92			1.50	4379	C
34R-1, 32–34	421.22				4652	C
35R-1, 58–60	430.88		3.19	3.00	4542	A
35R-1, 58–60	430.88				4608	B
35R-1, 58–60	430.88				4500	C
36R-1, 33–35	439.93		2.70	2.83	4905	A
36R-1, 33–35	439.93				4809	B
36R-1, 33–35	439.93				4797	C
37R-1, 10–12	449.3		2.54	2.89	4767	A
37R-1, 10–12	449.3				4724	B
37R-1, 10–12	449.3				4632	C
38R-1, 18–20	459.08				4275	C
41R-1, 5–7	487.55				4009	A

Notes: TC = thermal conductivity, V_p = compressional (P-wave) velocity, and V_p dir. = velocity direction, where A is the vertical velocity along the core, B is the horizontal velocity parallel to the cut core face, and C is the horizontal velocity perpendicular to the core face.

of the pressure buildup from the pulse. If the rate of decay is sufficiently slow (perhaps 30 min to 1 hr), then the permeability can be determined from the resulting record of pressure vs. time. If the decay rate after a pulse test is rapid (less than about 15 min), then the pulse test will give inaccurate results, and an injection test is run. During an injection test, water is pumped into the shut-in hole at a constant rate for a period of time, commonly about 20 min to an hour, and the gradual buildup of pressure in the hole allows a calculation of permeability (see Becker, 1990a).

During pulse or injection tests, water is pumped into the hole at rates of from 50 to 100 strokes/min with the mud pump, which pumps about 5 gal/stroke (18.931 L/stroke). Pumping pressures are obtained from pressure transducers in the high-pressure lines leading into the hole and are read from the driller's operating station. The on-board pressure is monitored as an indication of what is happening in the hole. The primary pressure data is recorded on the Kuster gauges in the hole and is acquired when the gauges are retrieved at the end of testing at a particular location in the hole.

At Hole 839B, the packer was set at two depths: 398.2 and 326.9 mbsf. At both locations, successful inflation and setting of the packer was achieved with 1500 psi of packer inflation pressures and 15,000–18,000 lb of weight set down on the packer with the drill string (see "Operations" section, this chapter, for details). In both cases, all signs on board indicated that a successful set was achieved, and that the packer should have shut-in the hole.

At the first set at 398.2 mbsf, two pulse tests were run, at 500 psi and 1000 psi. In both cases, pressure in the on-board system decayed immediately to 0 psi. Although a packer leak was suspected, two injection tests were run to test the possibility that all of the water pumped into the hole was moving into permeable basalt surrounding the borehole. The first injection test was run for 41 min at 50 strokes/min (50 strokes/min = 250 gal/min or 15.78 L/s). A flat pressure response of 365 to 375 psi was obtained with no significant rise or drop of pressure in the hole. Pressure decayed to 0 psi immediately after pumping stopped. The second test was run for 33 min at 100 strokes/min (100 strokes/min = 500 gal/min or 31.55 L/s). As before, a flat pressure response was

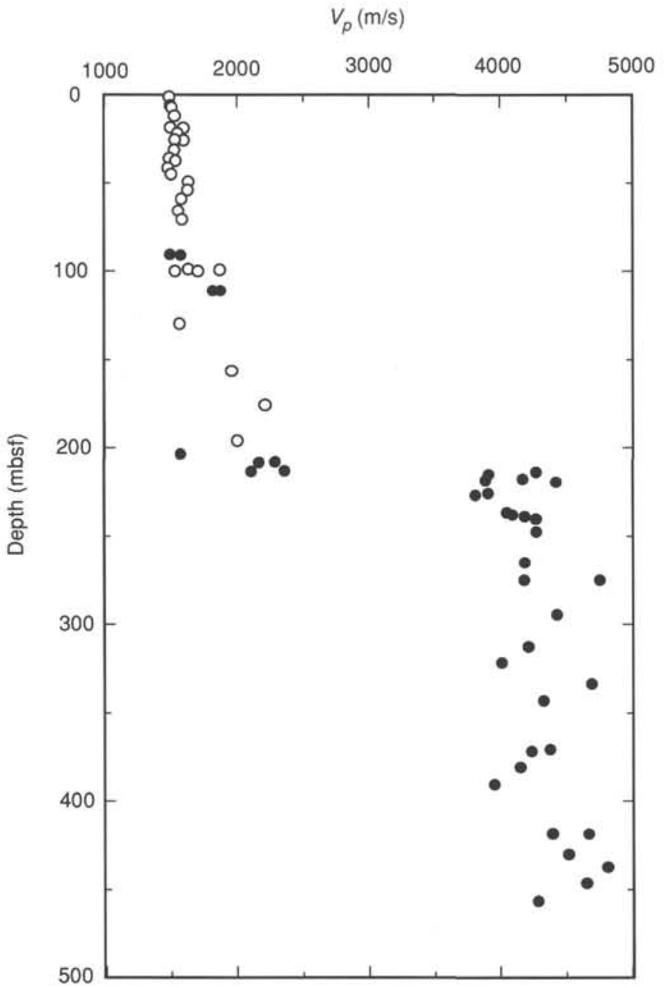

Figure 54. Compressional velocity vs. depth for sediments from Hole 839A (open circles) and lithified sediments and basalt samples from Hole 839B (filled circles).

obtained, between 1365 and 1370 psi, and pressure again decayed to 0 psi immediately after pumping ceased. Based on these tests, we felt that the packer may have been leaking and decided to move it to the second location. After the second test, the packer was deflated and unseated, and the Kuster recorders were recovered, reset, and sent back down the hole with the go-devil.

The packer was set a second time at 326.9 mbsf. Two pulse tests of 500 and 1000 psi decayed rapidly to 0 psi after pumping ceased. Three injection tests were run. The first was begun with a goal of pumping 100 strokes/min, based on the results from the first set, but an immediate pressure buildup to 2530 psi caused the test to be stopped at 50 strokes/min (50 strokes/min = 250 gal/min = 15.78 L/s), as the pumps were only rated to 3000 psi. The test was ended after only a few minutes and was followed by an immediate pressure decay. The second test was for 20 min at 35 strokes/min (35 strokes/min = 175 gal/min or 11.04 L/s); it yielded a flat pressure response of 1205 to 1235 psi. A third injection test was run for 30 min at 45 strokes/min (45 strokes/min = 225 gal/min or 14.20 L/s), and again yielded a generally flat pressure response of 1805 to 1820 psi. The final injection test was run at the maximum sustainable pressures to try and reach the limits of what the formation could absorb. This test was run for 1 hr at 59 strokes/min (59 strokes/min = 295 gal/min or 18.61 L/s), again yielding a flat pressure response with minor fluctuations between 2940 and 2960 psi.

After the fourth test the packer was unseated, deflated, and retrieved. Overpull of the drill string was required to pull the packer from the hole, indicating that the packer element may not have been entirely deflated and that it probably hung up within the hole. When the packer was recovered at the rig floor, the packer rubber element was pulled inside-out, and several steel cables within the element were broken. However, the surface of the recovered element showed no signs of water jetting or sand cutting as would be expected if high-pressure water were leaking around the packer seal. The element was only slightly worn and abraded. It showed some striations and pockmarking caused by pressure from the hole wall, but basically was in excellent condition with no holes or tears other than the tear presumably caused by extraction of the packer from the hole.

Kuster Pressure Recorder Results and Implications

The Kuster pressure chart for the first packer set confirmed the observations made during the test—that pressure decayed to 0 psi almost immediately after each pulse and injection test (Fig. 63). The pressure increase over hydrostatic pressure during the first injection test was 33 psi on Kuster gauge N9542, and 50 psi on Kuster gauge 860909. A pressure rise at the start of the test is observed in the Kuster pressure data; this pressure rise may potentially be processed/converted to a permeability measurement by means other than the constant pressure injection test calculation given below. During the second injection test, the pressure increase for the two gauges was 65 and 71 psi, respectively. On the second test, the Kuster-recorded pressure appears to decay slightly rather than increase during the course of the test.

The Kuster pressure charts for the second packer test indicate that something was mechanically wrong with Kuster gauge 860909 and with the packer. Kuster gauge 860909 gave pressure readings about 565 psi higher than both Kuster gauge N9542 and the calculated hydrostatic pressure for the depth of the second packer set. Thus, the results from gauge 860909 are considered invalid and cannot be used to calculate a permeability.

Mechanical problems with the packer are indicated by the small pressure rise observed in the borehole on Kuster gauge N9542. The first injection test, aborted because of the high pump pressures, produced a maximum downhole pressure increase over hydrostatic of only 11 psi. The second injection test did not cause any appreciable increase. The third injection test resulted in a steadily increasing pressure to a maximum of 9.5 psi over hydrostatic. The fourth and longest injection test created a peak pressure increase of 14 psi, which decayed to about 7.5 psi during the course of the test. Yet the on-board pumping pressure of 2950 psi approached the limits of the equipment. Calculated frictional pressure drops through the pumps, connecting hoses, and drill pipe for 59 strokes/min are only about 387 psi, leaving a residual borehole pressure of around 2563 psi that should have been observed on the Kuster recorders. Clearly, mechanical problems within the packer created the high observed pressures instead, and the borehole never saw a high pressure increase over hydrostatic.

On recovery of the go-devil after the second packer set, a seal separation ring on the go-devil was found to have rotated 45° with respect to the mandrel flow holes. With the ring rotated, pressure would be required to pump water through the plugged go-devil mandrel flow holes. However, calculated pressure losses caused by this possibility (pumping frictional losses through the equipment and drill pipe plus pressure required to pump water through the plugged go-devil flow holes) were 1617 psi, only about half of the observed pressure. As these flow holes are also used in deflating the packer element, partial blockage of them could lead to only partial deflation of the packer element, resulting in the damage to the element that occurred when the packer was pulled from the hole.

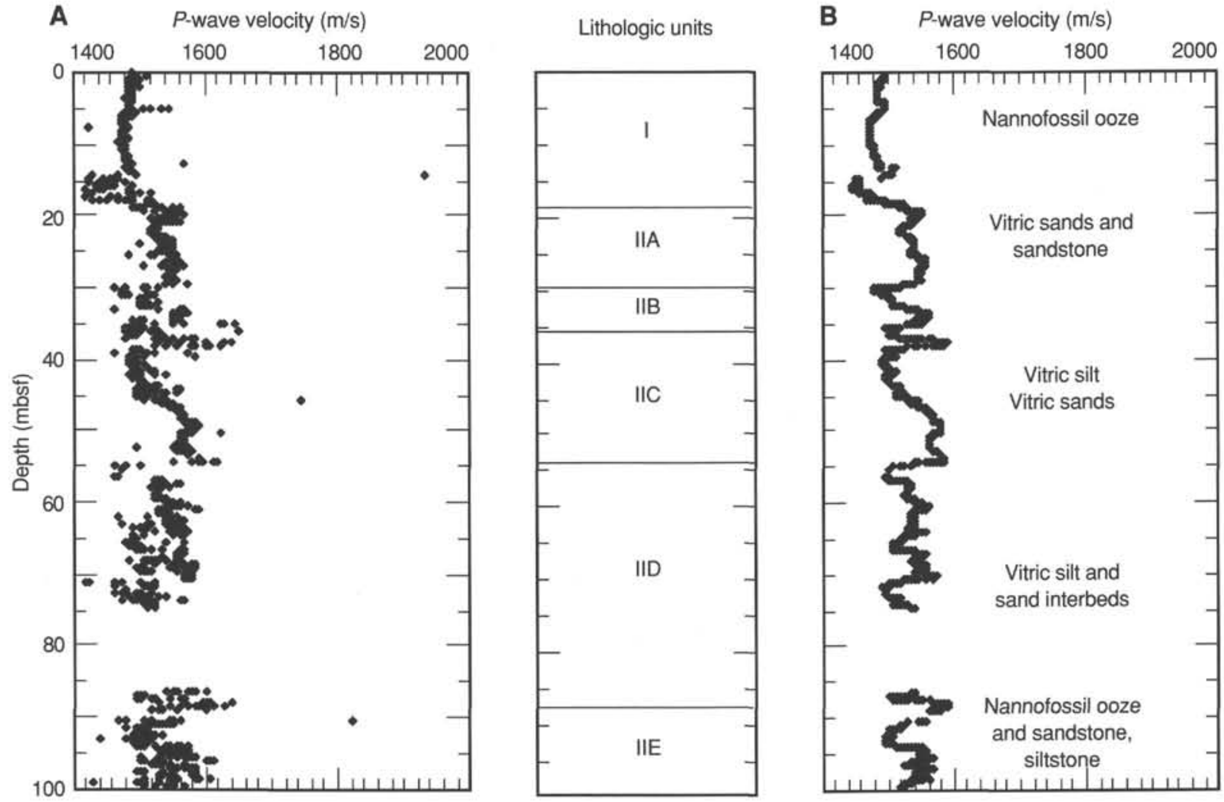

Figure 55. *P*-wave logger data after the initial 5-cm averaging (**A**) and after applying a 15-point running average (**B**) vs. depth, Hole 839A.

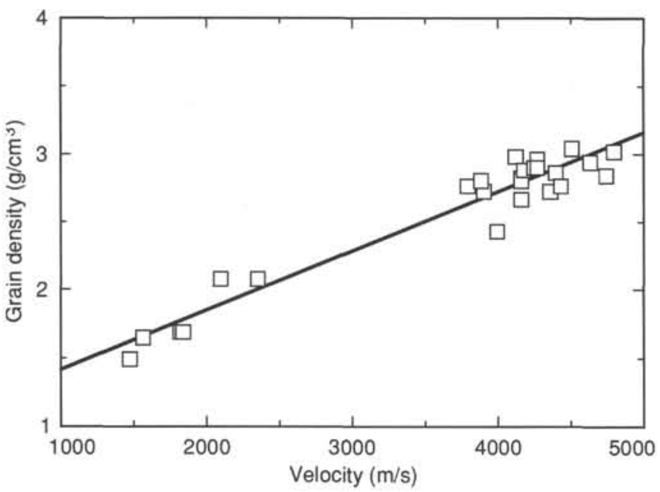

Figure 56. Compressional wave velocity vs. grain density measured on discrete samples from Hole 839B. Line shows least-squares fit to data, where grain density = 0.98 + 4.4 ± 10^{-4} ± velocity, with a correlation coefficient of 0.93.

At the end of Leg 135, tests were done on-board ship to measure experimentally pressure losses for this possible mechanical malfunction. The pressure rise obtained when the seal separation ring on the go-devil was rotated 45° and closed off the mandrel flow holes was 2955 psi at 50 strokes/min, very similar to what was observed during the second packer set. As the seal separation ring on the go-devil was in a rotated position when the packer was recovered, we conclude that this was the cause of the high pressures observed during the packer experiment. Therefore, the pumped water went into the borehole, and the second packer set is a valid test of the formation permeability, if we assume that a packer seal was achieved.

Results

The observed pump rates and pressure increases recorded on the Kuster charts can be used to calculate a permeability for both packer sets. For a constant rate injection test, Glover's formula (Anderson and Zoback, 1982; Zoback and Anderson, 1983) gives formation permeability k:

$$k = cQ\ \ln(2L/D)/\pi 2LP,$$

where Q = quantity of water pumped per unit time (l/s), L = length of hole below the packer (m), D = hole diameter (m), P = net head acting on the formation (Pa), and $c = \mu/gr$ where μ is the fluid viscosity, g is the acceleration caused by gravity, and r is the fluid density. This term converts from hydraulic conductivity (with units of m/s) to permeability (with units of m^2) or darcys.

In the first packer set we used the following values:

μ = 0.0048 Pa' s (assumed temperature = 4°C),
g = 9.8 m/s^2,
r = 1025 kg/m^3,
D = 0.3 m (estimated average hole diameter),
$P = 2.28 \times 10^5$ Pa (injection test 1, Kuster gauge N9542, Fig. 63),
$P = 3.45 \times 10^5$ Pa (injection test 1, Kuster gauge 860909),
$P = 4.48 \times 10^5$ Pa (injection test 2, Kuster gauge N9542),
$P = 4.90 \times 10^5$ Pa (injection test 2, Kuster gauge 860909),
q = 0.01578 m^3/s (injection test 1),
q = 0.03156 m^3/s (injection test 2), and
L = 67.7 or 119 m.

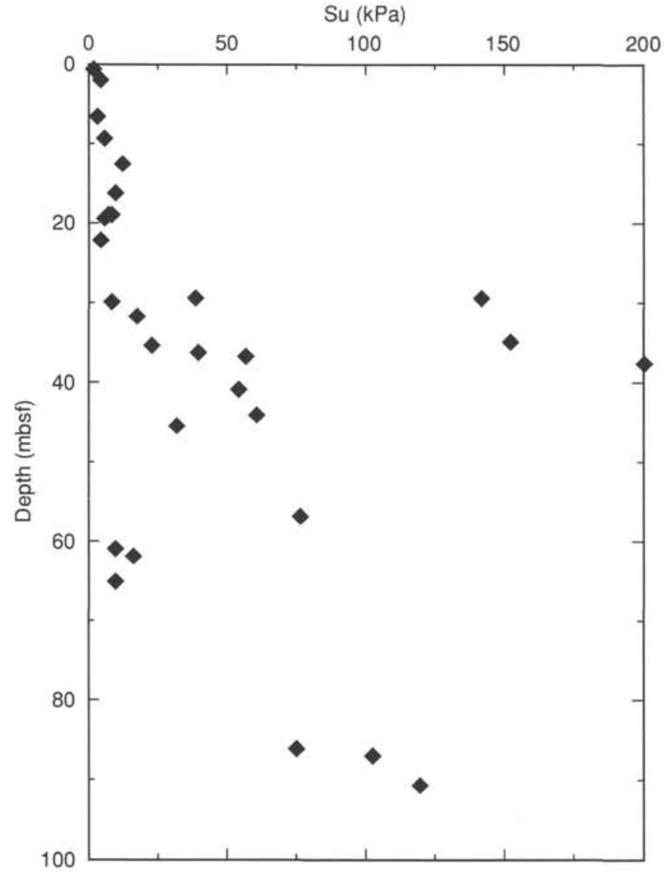

Figure 57. Undrained shear strength vs. depth, Hole 839A.

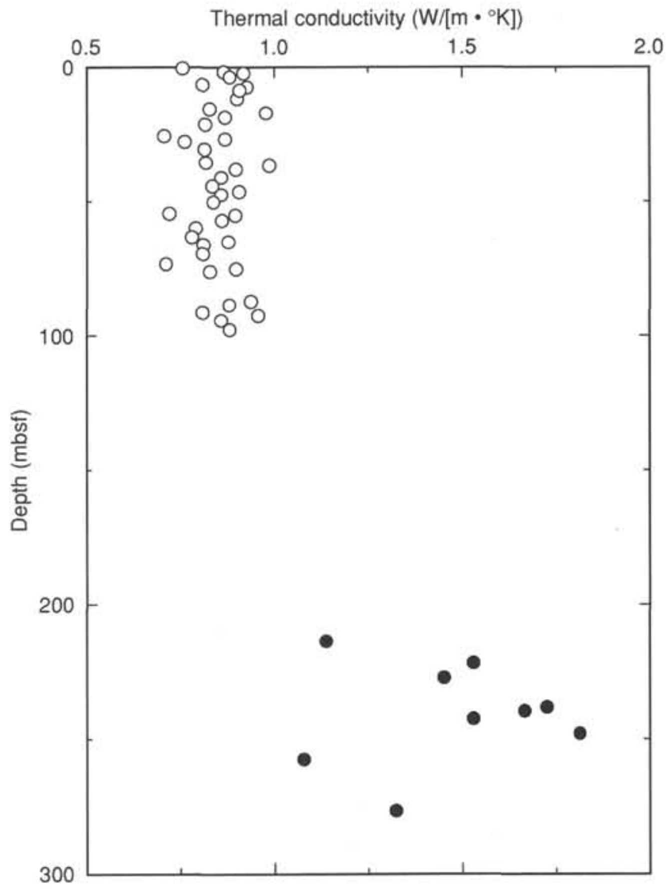

Figure 58. Thermal conductivity vs. depth for sediments from Hole 839A (open circles) and consolidated sediments and basalt samples from Hole 839B (filled circles).

For the second packer set, we used the following values (calculating only for the third and fourth injection tests and using data only from Kuster gauge N9542):

$P = 6.55 \times 10^4$ Pa (injection test 3),
$P = 9.65 \times 10^4$ Pa (injection test 4),
$q = 0.0142$ m^3/s (injection test 3),
$q = 0.0186$ m^3/s (injection test 4),
$L = 139$ or 190.3 m.

The length of borehole tested (variable L above) is an unknown quantity. The total borehole below the first packer set was about 119 m (TD = 517.2 mbsf and packer depth = 398.2 mbsf). However, the last logging run with the FMS tool found bottom 51.3 m above the drilled TD (at 465.9 mbsf), in which case the total borehole exposed below the packer could be as little as 67.7 m. More likely, some part or all of the borehole below the blockage remained open to the fluid pumped into the hole. The minimum and maximum lengths of the borehole thus give a range of possible permeabilities. Similarly, for the second packer set, the borehole length could range from 139 to 190.3 m.

The permeability calculated for the above values gives a range of 2×10^{-16} m^2 to 5×10^{-16} m^2 for the first packer set, and 5×10^{-16} m^2 to 8×10^{-16} m^2 for injection tests 3 and 4 at the second packer set. The calculated permeabilities show some consistency, falling within the range of $2–8 \times 10^{-16}$ m^2 for all calculations. However, these calculations are preliminary and are subject to substantial change during post-cruise processing.

The permeabilities calculated for Hole 839B are lower than expected, based on the recovered core and lithology and when compared with values measured elsewhere. Hole 839B penetrated

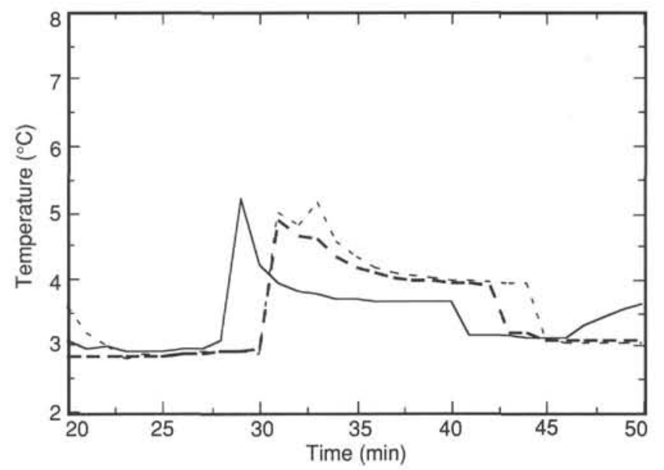

Figure 59. Heat flow measurements, Hole 839A, from various depths, based on WSTP probe temperature runs. Solid line = 33 mbsf, short dashed line = 52 mbsf, and bold dashed line = 71 mbsf.

mainly pillow lavas and flow units, and the recovered core showed a high vesicularity that we expected would translate into high permeability. However, packer experiments elsewhere in pillow lavas measured permeabilities of 10^{-14} to 10^{-13} m^2 in Hole 504B and Hole 395. Permeability values of 10^{-17} to 10^{-18} m^2 were

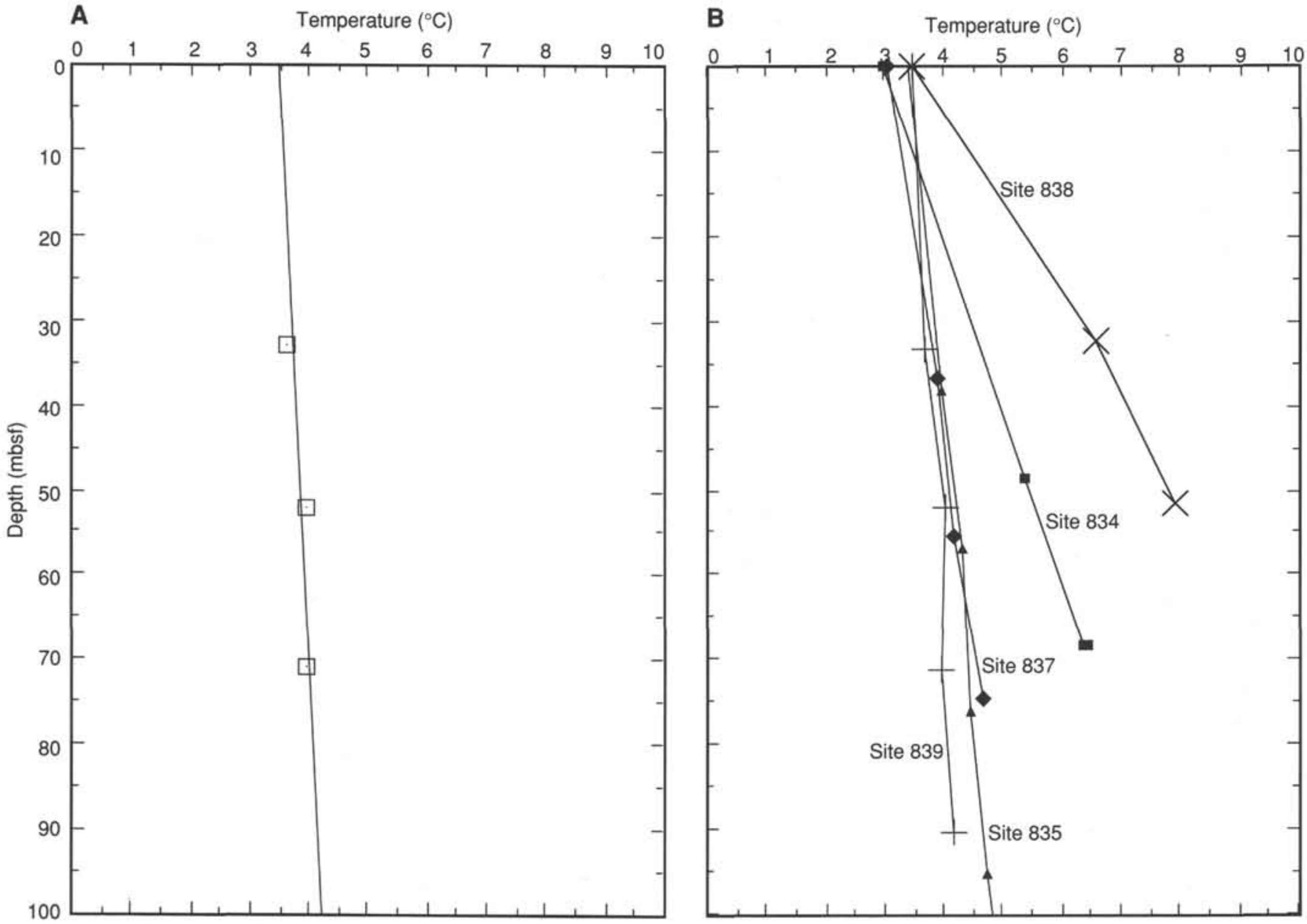

Figure 60. **A.** Temperature gradients vs. depth, Hole 839A, with line showing geothermal gradient of 0.71°C/100 m. **B.** Composite of temperature gradients measured at ODP Leg 135 Lau Basin sites.

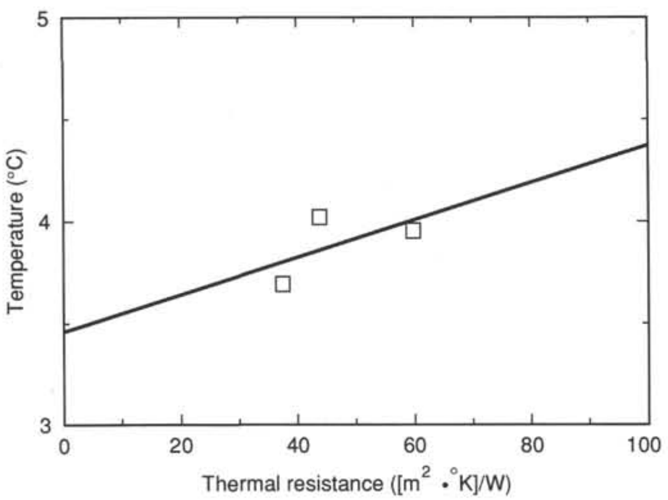

Figure 61. Thermal resistance vs. temperature, Site 839. The slope of the line indicates that the magnitude of the heat flow for this site is about 9.1 mW/m^2.

measured in sheeted dikes in these same holes (Anderson and Zoback, 1982; Zoback and Anderson, 1983; Anderson et al., 1985; Becker et al., 1983a, 1983b; Becker, 1989, 1990a, 1990b). Thus, our preliminary calculated results for the permeability in pillow basalts and flows of Hole 839B are smaller by 2 orders of magnitude than measured elsewhere in similar units and approach the permeabilities measured in the sheeted dike complex below the pillow lavas.

Summary of Results

The packer experiment was run between 0600 and 1800 on 23 January 1991. A narrative of the packer deployment and pressure tests are given in the "Operations" section (this chapter). Two packer sets were achieved at two different sites, with the quality of the set considered to be excellent based on the ability of the packer element to hold applied weight. At the first site, two pulse tests and two injection tests were run, and a lower limit for the permeability of the tested section may have been measured, although this conclusion is still tentative. At the second site, two pulse tests and four injection tests were run. Mechanical problems occurred during this second set, and only a small pressure rise was observed on pressure charts from below the packer. Testing on board after the experiment showed that the mechanical problem was a stuck separator ring on the go-devil, and that the pumped fluid therefore vented into the borehole. The preliminary result of permeability calculations is that the permeability measured in Hole 839B, about 2×10^{-16} m^2 to 8×10^{-16} m^2, is lower than

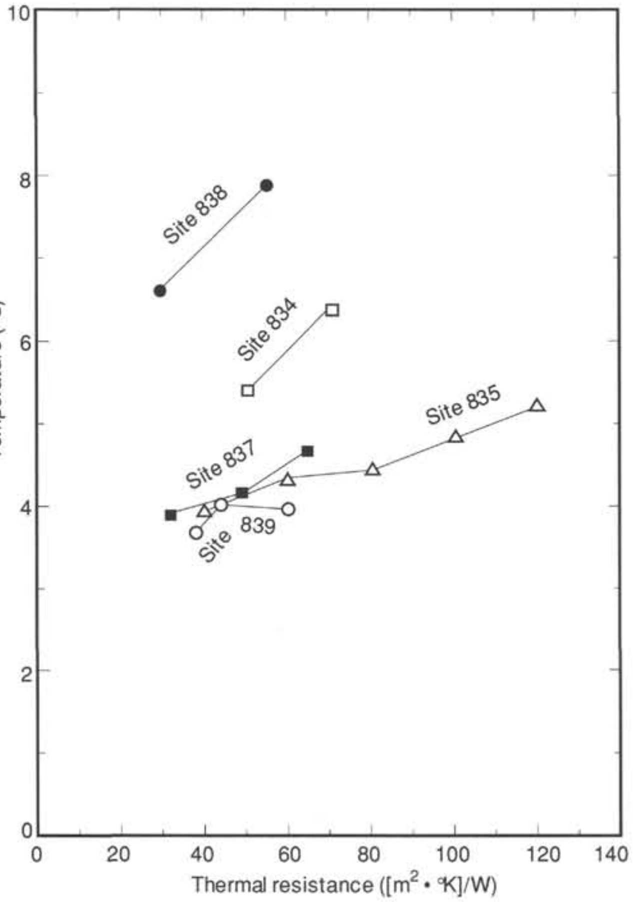

Figure 62. Composite plot of thermal resistance vs. temperature for all the Lau Basin backarc sites. The slopes of the lines indicate the magnitude of heat flow for each site.

expected for fractured and highly vesicular pillow basalts like those in Hole 839B. All observations on the ship indicate that the packer achieved a good mechanical seal. However, the low pressures measured during pulse and injection texts, and the sharp observed pressure rises and drop-offs, all suggest that the packer may not have achieved a hydraulic set. Post-cruise processing is necessary to fully evaluate the results of the packer test.

DOWNHOLE MEASUREMENTS

Operations

Logging operations at Hole 839B began at 1945 hr UTC, 20 January 1991, and ended at 0300 hr UTC, 22 January. The driller's mud line was at 2628.5 mbrf, and the driller's total depth was 473.8 mbsf. During logging the end of the drill pipe was set at 89.2 mbsf, although some openhole logs were obtained at shallower depths when it was safe for the driller to raise the pipe. Well logging operations consisted of five logging runs using the seismic stratigraphic string, the lithoporosity string, the geochemical string, the formation microscanner logging string, and the analog borehole televiewer (BHTV).

The first logging run was made with the seismic stratigraphic tool string, which includes the long-spaced sonic, the phasor induction, and the natural gamma-ray tools, plus a three-arm caliper to center the tool string in the hole. The seismic stratigraphic tool combination measures (1) compressional sound-wave velocity through rocks and sediments surrounding the borehole; (2) resistivity, which is sensitive to the porosity and the conductivity of the pore fluids; and (3) the natural gamma-ray response, which is sensitive to the naturally emitted radiation of the rocks. The logging sequence with the seismic stratigraphic tool string consisted of a downlog through pipe from 15.9 to 89.2 mbsf, a continued downlog open hole from 89.2 to 456.4 mbsf, a main uplog from 485.6 to 68.5 mbsf openhole, and another uplog from 181.0 to 68.5 mbsf openhole.

The second logging run consisted of three passes with the lithoporosity tool-string combination, which includes a high-temperature lithodensity tool, compensated neutron porosity tool, and natural gamma-ray tool. This combination measures density, porosity, gamma ray, thorium, uranium, potassium, photoelectric effect, and a caliper (with maximum hole diameter of 48 cm or 19 in.). The first pass was a downlog from mud line to 89.2 mbsf in pipe, continuing into the open hole to 454.7 mbsf. The second pass was an uplog from 470.4 to 81.9 mbsf (openhole), and the third was also an uplog from 156.3 to 81.8 mbsf (openhole). The logging speed for both uplog passes was 549 m/hr (1800 ft/hr).

The third logging run was made with the geochemical tool string, which is a combination of the aluminum clay tool, the gamma-ray spectrometry tool, the natural gamma-ray tool, and a compensated neutron tool. This tool string is run at 183 m/hr (600 ft/hr). The main uplog was recorded openhole from 469.5 to 61.7 mbsf, continuing into pipe up to the mud line, and a repeat section was logged from 143.2 to 82.1 mbsf openhole.

The fourth logging run was made with the FMS string. Pass 1 was recorded openhole from 469.9 to 80.3 mbsf and Pass 2 was recorded from 471.5 to 80.0 mbsf openhole. The logging speed for both passes was 549 m/hr (1800 ft/hr).

The fifth logging run was made with the analog BHTV, which records the acoustic reflectivity of the borehole wall as a function of depth and azimuth. A single pass was made, and data were recorded openhole from 457.6 to 213.8 mbsf.

On-board Processing and Data Quality

The data tapes were corrected by subtracting 10 ft from the depth measurement to account for the logging cable heave compensator, and depths were converted from feet below rig floor to meters below seafloor. The aluminum data recorded during the geochemical tool run is not valid, as a result of a tool malfunction (and is not presented in the figures). The in-pipe section of the main pass of the geochemical log will be corrected for the effect of the pipe, post-cruise. The repeat section of the geochemical log showed evidence of spurious gamma-ray emission resulting from previous irradiation by the radioactive source in the geochemical tool. The resistivity curve was edited to remove spurious peaks (>9600 ohm-m).

Raw sonic logs exhibited several areas of cycle skipping; these data were reprocessed (see "Downhole Measurements" section, "Explanatory Notes" chapter, this volume). Velocity values less than 1.39 km/s and greater than 7.62 km/s were discarded during reprocessing. FMS processing was done on board using a VAX-station 3200 and proprietary Schlumberger software (see "Explanatory Notes" chapter, this volume). It was not possible to digitize the analog signal collected with the analog BHTV tool on-board ship; the data will be digitized, formatted, and analyzed on shore. When the diameter of the hole is greater than 39.4 cm (15.5 in.), the FMS pads do not make sufficient contact with the borehole walls to produce images of satisfactory quality.

Results and Interpretation

The results of the logging in Hole 839B are shown in Figures 64 through 69. The lithology of Site 839 can be summarized as follows: lithologic Unit I (0–17.85 mbsf) is a clayey nannofossil

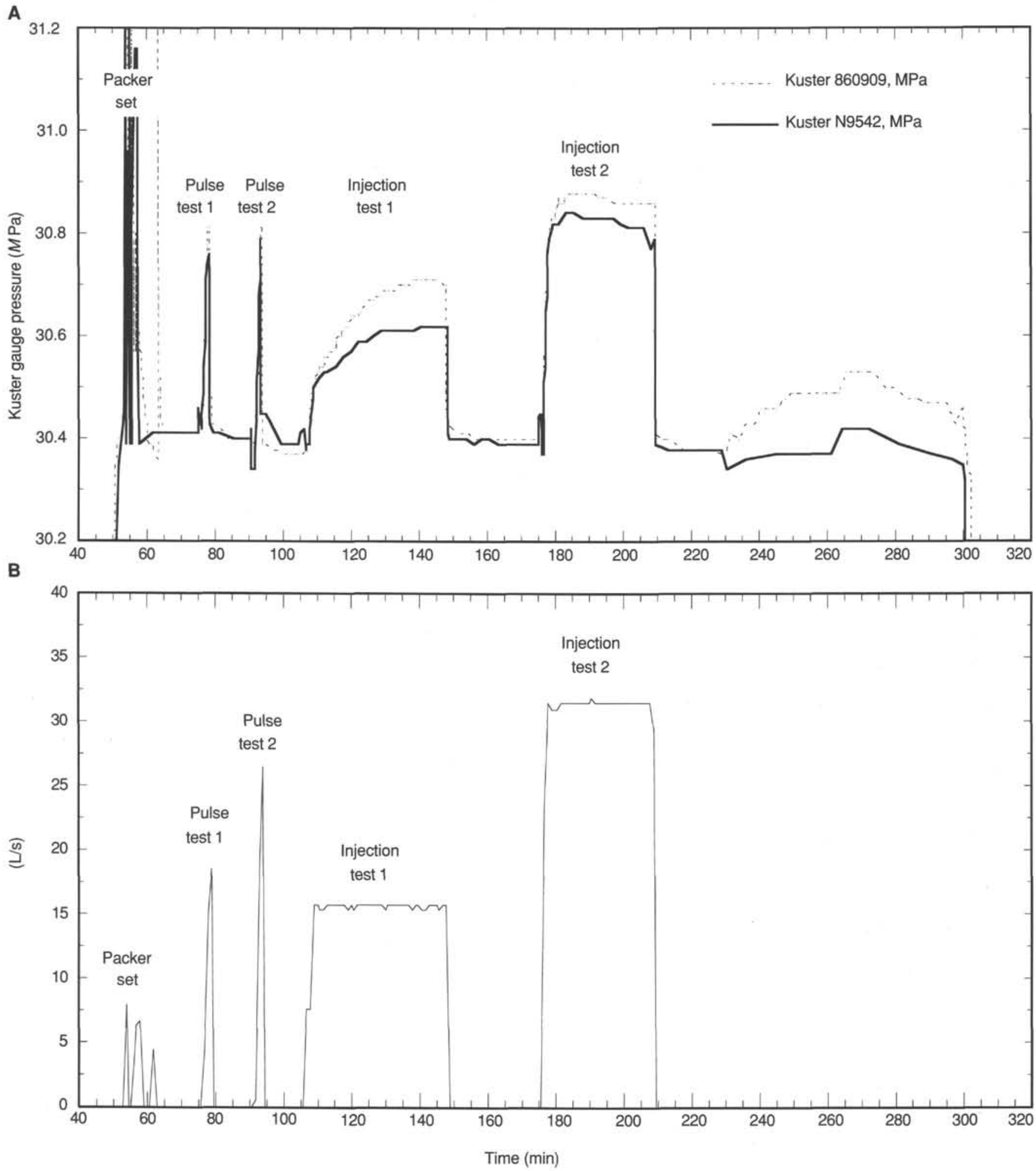

Figure 63. **A.** Pressure vs. time for Kuster gauges N9542 and 860909 for packer set at 398.2 mbsf. Only the segment of the chart from when the Kuster gauge reached the packer is shown here. **B.** Flow rate vs. time for packer set at 398.2 mbsf.

ooze containing thin vitric sand and silt layers; lithologic Unit II (Subunits IIA–IIF; 17.85 and 99.5 mbsf), is described as increasing amounts of vitric sands and silts; and lithologic Unit III comprises all sediments recovered below 99.5 mbsf in Holes 839A and 839B (see "Lithostratigraphy" section, this chapter). Below 99.5 mbsf, core recovery of Unit III in Hole 839A was very low (only 2.7%); and in Hole 839B, core recovery below 99.5 mbsf was 5.6%. Two main types of igneous rocks underlying the sediments at 214 mbsf have been described: olivine-clinopyroxene phyric basalt and orthopyroxene-clinopyroxene-plagioclase phyric basaltic andesite; these types are subdivided into nine units (see "Igneous Petrology" section, this chapter).

The boundaries between some of the lithologic and igneous units are marked by changes in measured values recorded by the logs, as discussed below.

Caliper Logs

The caliper logs record the diameter of the hole and are useful in evaluating whether information from the logs is valid (see "Downhole Measurements" section, "Explanatory Notes" chapter, this volume). At Hole 839B, the FMS caliper logs (Fig. 64) show that the diameter of the hole is well within 10–15 in. (25.4–38.1 cm), with the exception of the interval above 214 mbsf and from 253 to 265 mbsf, where the calipers are at the maximum extension of 15.5 in. (39.4 cm). The FMS calipers indicate that the hole is mostly elliptical below 265 mbsf, with diameter ranging from 10 to 15 in. The shape of the calipers indicates a rough borehole surface below 214 mbsf.

Resistivity and Sonic Velocity Logs

The resistivity logs (ILM, ILD, and SFLU; Fig. 65) and the sonic velocity log (VEL; Fig. 65) are, for the most part, positively correlated. These logs are primarily controlled by density, porosity, and fracturing within the formation. The velocity and resistivity values (<2000 m/s and <2.0 ohm-m) are low in the upper part of the logged hole between 89 and 214 mbsf, corresponding to the sedimentary section (parts of lithologic Units II and III). At 162 mbsf, velocity and resisitivity values show a marked positive excursion from relatively flat and low values to variable and high values. This pattern continues to the base of the sedimentary section at 214 mbsf. This strongly suggests a subdivision of lithologic Unit III, in a section of the core for which recovery was poor.

Velocity and resistivity values increase in the region of 214 mbsf (and continue to do so until 253 mbsf), corresponding to the sediment/igneous contact at the top of igneous Unit 1 identified in the core at that depth. Because core recoveries were low, however, the contact could be either higher or lower in the section. The steepest rate of change in the resistivity value is most marked at 218 mbsf, with a smaller increase at 214 mbsf.

In the sediment section encountered from 256 to 266 mbsf, the resistivity and velocity values decrease to values slightly higher than those seen in the sedimentary section corresponding to lithologic Unit III, but significantly lower than igneous Unit 1 (from 214 to 256 mbsf). From 266 to 276 mbsf (the Unit 2 boundaries), resistivity values increase dramatically, although change in the velocity curve is negligible.

The division between igneous Units 3 and 4 is not apparent in the resistivity and velocity logs. From 276 to 360 mbsf, which is the combined interval for Units 3 and 4, values for both logs are slightly lower than Unit 2 values.

Examination of the resistivity and velocity logs may help resolve the question referred to in the "Igneous Petrology" section (this chapter) of whether or not Units 5, 6, 7, and 8 are artifacts of drilling operations. A single break in lithology appears to be present at 360 mbsf, based on the increase in resistivity and velocity logs, supporting a sharp change from igneous Unit 4 to Unit 9, rather than an interfingered contact. Thus, the identification of Units 5, 6, 7, and 8 may be more plausibly explained as the result of mixing of fragments from other units higher in the hole.

Another decrease in resistivity values occurs from 395 to 420 mbsf, suggesting a subunit within igneous Unit 9, a unit in which recovery was very low. Resistivity values above and below this interval within igneous Unit 9 are similar. Calipers from the FMS tool (see Fig. 64) indicate that the hole was strongly elliptical in that interval. The FMS images also show lower resistivity values in this same interval. This possible subunit is also marked by higher velocity values.

Density Log

The bulk density log (RHOB; Fig. 66) obtains measurements using gamma-ray scattering from a radioactive source on the caliper arm. The caliper arm was in contact with the wall of the borehole throughout Hole 839B (see CALI, RHOB, and DRHO; Fig. 66); therefore, the data are generally valid.

In the interval from 162 to 214 mbsf discussed above, where a change in velocity and resisitivity occurs, a comparable change from relatively flat and low values to variable and high values in the character of the density and photoelectric curves occurs. This may support the subdivision of lithologic Unit III, from which there was very poor recovery. The lithology of Subunit IIIA has low resistivity, velocity, and density, whereas Subunit IIIB is characterized by a lithology with relatively high values of resistivity, velocity, and density.

From 214 to 253 mbsf, an increase in density and photoelectric effect values occurs at the contact between lithologic Unit III and the basalt of igneous Unit 1. This agrees with the increase in both velocity and resistivity at the same depth. Between 253 and 266 mbsf the density values drop to between 1.8 and 2.0 g/cm^3, which corresponds to the sediment interbed. The change from Unit 4 to Unit 9 observed at about 360 mbsf in the resistivity and velocity curves is not apparent in the density curve.

As seen in the resistivity and velocity logs, the interval from 395 to 420 mbsf within igneous Unit 9 is marked by a change in character of the density curve from high-frequency alternations between higher and lower values to a more uniform and constant trend, thus supporting suggestions of a subunit in the igneous section. The curve is flatter and has lower densities in this interval than in the rest of Unit 9 (values around 2.0 g/cm^3).

Neutron Porosity Log

In Hole 839B, porosity (NPHI; Fig. 66) and density are inversely correlated, lending confidence to the porosity trends measured. Average porosity values in the upper 214 mbsf vary between 40% and 75%, with average values of about 60%. Below 216 mbsf, porosity values decrease to values as low as 25%, ranging to values of 70%.

Gamma-ray Log

The gamma-ray log (SGR, Fig. 67) records the natural gamma-ray spectrum from the total thorium, uranium, and potassium content of the formation. At about 162 mbsf, where the lithologic Subunit IIIB suggested by the log data begins, there is a sharp decrease in gamma-ray values. An increase in gamma-ray levels occurs below 266 mbsf, corresponding with the top of igneous Unit 2. At 360 mbsf, a significant increase in the total gamma-ray curve (which is essentially reflecting potassium concentrations) correlates well with the change in petrology from igneous Unit 4 to Unit 9.

Geochemical Yields

The gamma-ray spectrometry tool (GST) measures the relative yield of gamma rays resulting from the interactions of neutrons emitted from a 14-MeV source with the elements present in the formation (see "Downhole Measurements" section in "Explanatory Notes" chapter, this volume). Geochemical logs for Site 839 are presented in Figure 68. Positive and negative excursions in Si, Fe, and other elemental concentrations at the sedimentary/igneous boundaries are observed. The significance of their values will be reexamined following correction for variations in borehole size.

Few igneous unit boundaries can be correlated with log signal variations at this stage.

Formation Microscanner

The formation microscanner images are presented on microfiche in the back of this volume. The images were of poor quality above 214 mbsf because of enlarged hole size, corresponding to the sediment section. However, in igneous Unit 1 from 214 to 256 mbsf, low-resistivity vertical and horizontal fractures on the order of 2–10 cm wide are evident in the images (Fig. 69). The caliper values change rapidly through this zone, indicating a rugose surface. In the sediment sections the hole was enlarged and the tool did not make contact with the borehole wall; therefore, no good FMS images were collected in any of the sediment sections. Below 266 mbsf, vertical and horizontal fractures are not as common as in igneous Unit 1.

Summary

The well logs provide a continuous *in situ* record of the lithologies at Hole 839B. Based on velocity, resistivity, and density logs, lithologic Unit III may be subdivided into two subunits at 162 mbsf, the lower subunit being characterized by distinctly higher resistivity, velocity, and density values than that of the upper. In this hole, the sediment-igneous boundaries are easily distinguishable in the resistivity, velocity, and density logs, as well as in the gamma-ray logs.

Unit boundaries identified in the "Igneous Petrology" section of this chapter are also seen in the well logs, although igneous Units 5, 6, 7, and 8 are seen as one distinct change in lithology in the velocity and resistivity curves, rather than as a switch from one to another in sequence. The suggestion (see "Igneous Petrology" section, this chapter) that the sequence seen in the core is a result of drilling disturbance agrees with the evidence seen in the logging data.

Igneous Unit 9 may be divided by a subunit on the basis of resistivity, velocity, density, and FMS data.

DISCUSSION

The primary objectives for Site 839 remained the same as for Sites 836, 837, and 838: to obtain a deep penetration of the basement section, to identify the composition and affinities of the volcanics both in the basement and in the volcaniclastics, to determine the age of the initial formation of the basin, and to assess the history of basin fill and its correlation with that of adjacent sites.

All of the objectives outstanding from Sites 836, 837, and 838 in the central Lau Basin were successfully attained at Site 839. Basement age was determined, and the recovery of 283.11 m of basaltic basement revealed a magma lineage having the strongest affinities to the island-arc tholeiitic series of any of the Leg 135 backarc sites. Olivine-phyric basalts, interleaved with two-pyroxene andesitic flows, comprise the lower volcanic section. Some units have very primitive characteristics and may represent near-parental primary magmas for some of the arclike volcanics sampled from other Leg 135 sites. The volcanic basement is overlain by 214.15 m of oozes, vitric turbidites, and volcanic gravels. The oldest sediments recovered are of late Pliocene age (1.9–2.2 Ma), comparable with the oldest sediments at Site 837. Site 837, however, lies 20 km west of the position of Site 839 if projected along strike, and Site 837 would thus have a predicted age up to 1 m.y. older than that at Site 839 if the crust at both sites had formed by seafloor spreading from the same spreading center. Sediments at Site 839 are predominantly oozes in the uppermost unit, but the central section is dominated by volcaniclastics composed of basaltic andesite and andesite fragments, as well as siliceous pumice.

During late Pliocene extensional deformation, basement block faulting resulted in the development of a northwest-tilted half-graben, which was subsequently buried with onlapping mixed volcanic gravels, vitric sands, and silts with nannofossil clays. These rapidly deposited units were eventually overlain by latest Pliocene and Pleistocene clayey nannofossil oozes and silts in pelagic and hemipelagic dominated sequences. The present northwest dip of the seafloor and the uppermost sedimentary units suggest that recent extensional deformation has affected the basin.

REFERENCES

Anderson, R. N., Langseth, M. G., and Sclater, J. G., 1977. The mechanisms of heat transfer through the floor of the Indian Ocean. *J. Geophys. Res.*, 82:3391–3409.

Anderson, R. N., and Zoback, M. D., 1982. Permeability, underpressures, and convection in the oceanic crust near the Costa Rica Rift, eastern equatorial Pacific. *J. Geophys. Res.*, 87:2860–2868.

Anderson, R. N., Zoback, M. D., Hickman, S. H., and Newmark, R. L., 1985. Permeability versus depth in the upper oceanic crust: in situ measurements in DSDP Hole 504B, eastern equatorial Pacific. *J. Geophys. Res.*, 90:3659–3669.

Becker, K., 1989. Measurements of the permeability of the sheeted dikes in Hole 504B, ODP Leg 111. *In* Becker, K., Sakai, H., et al., *Proc. ODP, Sci. Results*, 111: College Station, TX (Ocean Drilling Program), 317–325.

———, 1990a. A guide to formation testing using ODP drillstring packers. *ODP Tech. Note*, No. 14.

———, 1990b. Measurements of the permeability of the upper oceanic crust at Hole 395A, ODP Leg 109. *In* Detrick, R., Honnorez, J., Bryan, W. B., Juteau, T., et al., *Proc. ODP, Sci. Results*, 106/109: College Station, TX (Ocean Drilling Program), 213–222.

Becker, K., Langseth, M. G., and Von Herzen, R. P., 1983a. Deep crustal geothermal measurements, Hole 504B, Deep Sea Drilling Project Legs 69 and 70. *In* Cann, J. R., Langseth, M. G., Honnorez, J., Von Herzen, R. P., White, S. M., et al., *Init. Repts. DSDP*, 69: Washington (U.S. Govt. Printing Office), 223–236.

Becker, K., Langseth, M. G., Von Herzen, R. P., and Anderson, R. N., 1983b. Deep crustal geothermal measurements, Hole 504B, Costa Rica Rift. *J. Geophys. Res.*, 88:3447–3457.

Berger, A. L., 1978. Long-term variations of caloric solar insolation resulting from earth's orbital variations. *Quat. Res.*, 9:139–167.

Berggren, W. A., Kent, D. V., Flynn, J. J., and Van Couvering, J. A., 1985a. Cenozoic geochronology. *Geol. Soc. Am. Bull.*, 96:1407–1418.

Berggren, W. A., Kent, D. V., and Van Couvering, J. A., 1985b. The Neogene: Part 2. Neogene geochronology and chronostratigraphy. *In* Snelling, N. J. (Ed.), *The Chronology of the Geological Record*. Geol. Soc. London Mem., 10:211–260.

Bloomer, S. H., 1983. Distribution and origin of igneous rocks from the landward slopes of the Mariana Trench. *J. Geophys. Res.*, 88:7411–7428.

Bouma, A. H., 1962. *Sedimentology of Some Flysch Deposits*: Amsterdam (Elsevier).

Church, B. N., and Johnson, W. M., 1980. Calculation of the refractive index of silicate glasses from chemical composition. *Geol. Soc. Am. Bull.*, 91:619–625.

Clement, B. M., and Robinson, F., 1987. The magnetostratigraphy of Leg 94 sediments. *In* Ruddiman, W. F., Kidd, R. B., Thomas, E., et al., *Init. Repts. DSDP*, 94, Pt. 2: Washington (U.S. Govt. Printing Office), 635–650.

deMenocal, P., Bloemendal, J., and King, J., 1991. A rock-magnetic record of monsoonal dust deposition to the Arabian Sea: evidence for a shift in the mode of deposition at 2.4 Ma. *In* Prell, W. L., Niitsuma, N., et al., *Proc. ODP, Sci. Results*, 117: College Station, TX (Ocean Drilling Program), 389–407.

Emeis, K.-C., and Kvenvolden, K. A., 1986. Shipboard organic geochemistry on *JOIDES Resolution*. *ODP Tech. Note*, No. 7.

Ernewein, M., Pearce, J. A., Bloomer, S. H., Parson, L. M., Murton, B. J., Johnson, L. E., in press. Geochemistry of Lau Basin volcanic rocks: influence of ridge segmentation and arc proximity. *Contrib. Mineral. Petrol.*

Ewart, A., Brothers, R. N., and Mateen, A., 1977. An outline of the geology and geochemistry, and the possible petrogenetic evolution of the volcanic rocks of the Tonga-Kermadec-New Zealand island arc. *J. Volcanol. Geotherm. Res.*, 2:205–250.

Ewart, A., Bryan, W. B., and Gill, J., 1973. Mineralogy and geochemistry of the younger volcanic islands of Tonga, southwest Pacific. *J. Petrol.*, 14:429–465.

Ewart, A., and Hawkesworth, C. J., 1987. The Pleistocene-Recent Tonga-Kermadec arc lavas: interpretation of new isotope and rare earth data in terms of a depleted mantle source model. *J. Petrol.*, 28:495–530.

Falloon, T. J., and Crawford, A. J., in press. The petrogenesis of high-calcium boninite lavas dredged from the north Tonga Ridge. *Earth Planet. Sci. Lett.*

Falloon, T. J., Green, D. H., and Crawford, A. J., 1987. Dredged igneous rocks from the northern termination of the Tofua magmatic arc, Tonga and adjacent Lau Basin, *Aust. J. Earth Sci.*, 34:487–506.

Harland, W. B., Cox, A. V., Llewellyn, P. G., Pickton, C.A.G., Smith, D. G., and Walters, R., 1982. *A Geologic Time Scale:* Cambridge (Cambridge Univ. Press).

Harms, J. C., Southard, J. B., and Walker, R. G., 1982. Structures and sequences in clastic rocks. *SEPM Short Course*, No. 9.

Hawkins, J. W., 1976. Petrology and geochemistry of basaltic rocks of the Lau Basin. *Earth Planet. Sci. Lett.*, 28:283–297.

_______, 1989. Cruise Report—ROUNDABOUT Expedition, Legs 14, 15, R/V *Thomas Washington. SIO Ref. Ser.*, No. 89-13.

Hawkins, J. W., Lonsdale, P. F., Macdougall, J. D., and Volpe, A. M., 1990. Petrology of the axial ridge of the Mariana Trough back arc spreading center. *Earth Planet. Sci. Lett.*, 100:226–256.

Hawkins, J. W., and Melchior, J. T., 1985. Petrology of Mariana Trough and Lau Basin basalts. *J. Geophys. Res.*, 90:11431–11468.

Hyndman, R. D., Langseth, M. G., and Von Herzen, R. P., 1987. Deep Sea Drilling Project geothermal measurements: a review. *Rev. Geophys.*, 25:1563–1582.

Johnson, G. R., and Olhoeft, G. R., 1984. Density of rocks and minerals. *In* Carmichael, R. S. (Ed.), *CRC Handbook of Physical Properties of Rocks* (Vol. 3): Boca Raton, FL (CRC Press), 1–38.

Lowe, D. R., 1975. Water escape structures in coarse-grained sediments. *Sedimentology*, 22:157–204.

Nilsson, K., Florendo, F. F., and Hawkins, J. W., et al., 1989. Petrology of a nascent triple junction, northeastern Lau Basin. *Eos*, 70:1389.

Okada, H., and Bukry, D., 1980. Supplementary modification and introduction of code numbers to the low-latitude coccolith biostratigraphic zonation (Bukry, 1973; 1975). *Mar. Micropaleontol.*, 5:321–325.

Parson, L. M., et al., 1989. RRS *Charles Darwin* Cruise 33/88, 5 May–1 June 1988. Geophysical and geological investigations of the Lau back-arc basin, SW Pacific. *Inst. Oceanogr. Sci. Deacon Lab. Cruise Report*, No. 206.

Parson, L. M., Pearce, J. A., Murton, B. J., Hodkinson, R. A., Bloomer, S., Ernewein, M., Huggett, Q. J., Miller, S., Johnson, L., Rodda, P., and Helu, S., 1990. Role of ridge jumps and ridge propagation in the tectonic evolution of the Lau back-arc basin, southwest Pacific. *Geology*, 18:470–473.

Schmincke, H.-U., 1981. Ash from vitric muds in deep sea cores from the Mariana Trough and fore-arc regions (south Philippine Sea) (Sites 453, 454, 455, 458, 459). *In* Hussong, D. M., Uyeda, S., et al., *Init. Repts. DSDP*, 60: Washington (U.S. Govt. Printing Office), 473–481.

Sun, S.-S., and McDonough, W. F., 1989. Chemical and isotopic systematics of oceanic basalts: implications for mantle composition and processes. *In* Saunders, A. D., and Norry, M. J. (Eds.), *Magmatism in the Ocean Basins*. Geol. Soc. Spec. Publ. London, 42:313–345.

von Stackelberg, U., 1990. R.V. *Sonne* cruise SO48: summary of results testing a model of mineralisation. *Mar. Min.*, 9:135–144.

Walker, R. G., 1978. Deep water sandstone facies and ancient submarine fans: models for exploration of stratigraphic traps. *AAPG Bull.*, 62:932–966.

Wollin, G., Ericson, D. B., and Ryan, W.B.F., 1971. Magnetism of the Earth and climate changes. *Earth Planet. Sci. Lett.*, 12:175–183.

Zoback, M. D., and Anderson, R. N., 1983. Permeability, underpressures, and convection in the oceanic crust at Deep Sea Drilling Project Hole 504B. *In* Cann, J. R., Langseth, M. G., et al., *Init. Repts. DSDP*, 69: Washington (U.S. Govt. Printing Office), 245–254.

Ms 135A-109

NOTE: All core description forms ("barrel sheets") and core photographs have been printed on coated paper and bound separately as Part 2 of this volume, beginning on page 681.

Formation microscanner images for this site are presented on microfiche in the back of Part 2.

[Blank page]

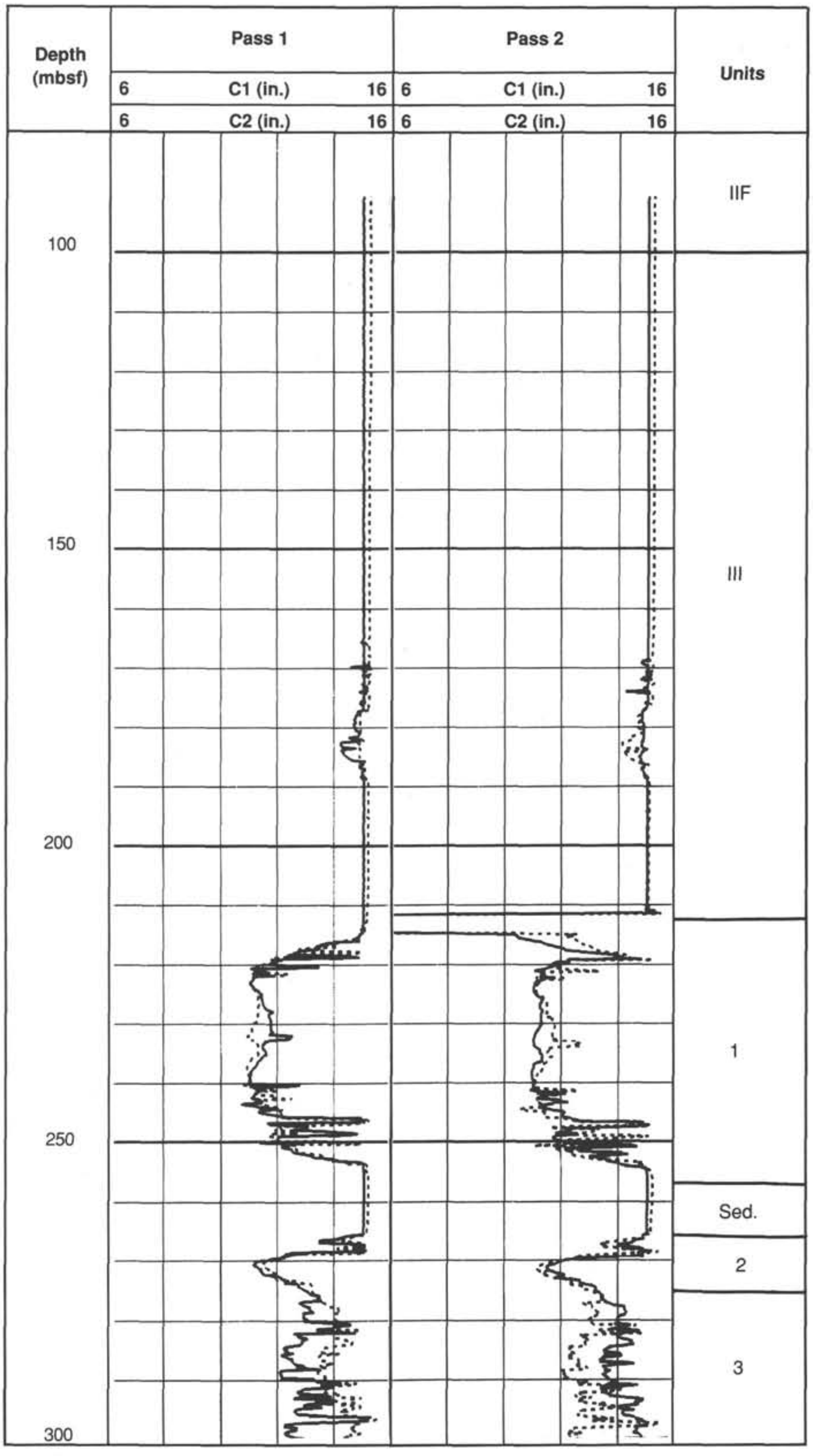

Figure 64. Caliper data obtained for Hole 839A from both passes of the formation microscanner tool. C1 (caliper 1–3, solid line) and C2 (caliper 2–4, dashed line) are plotted at a scale of 6–16 in. Lithostratigraphic and igneous unit boundaries are plotted to right of leg curves.

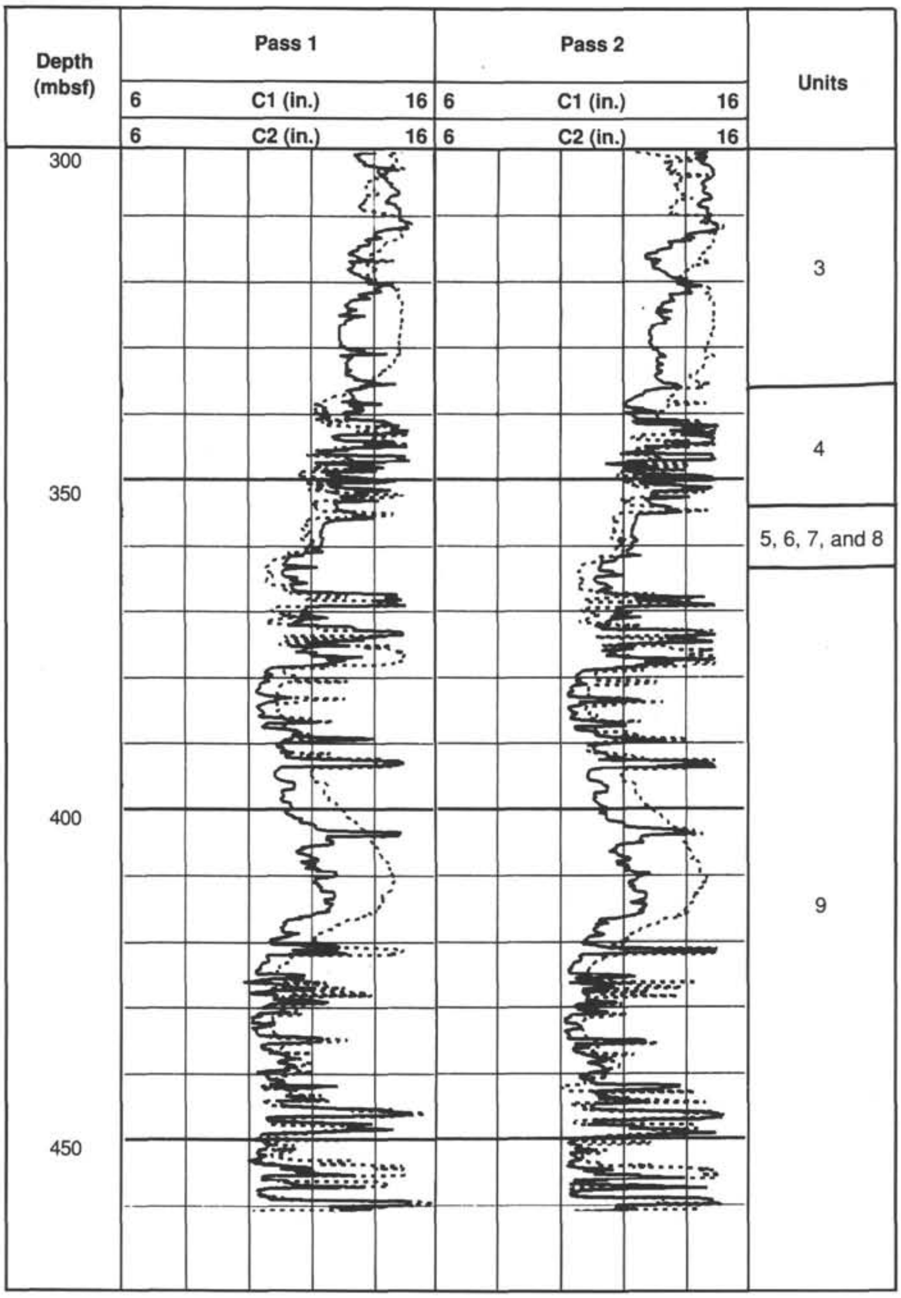

Figure 64 (continued).

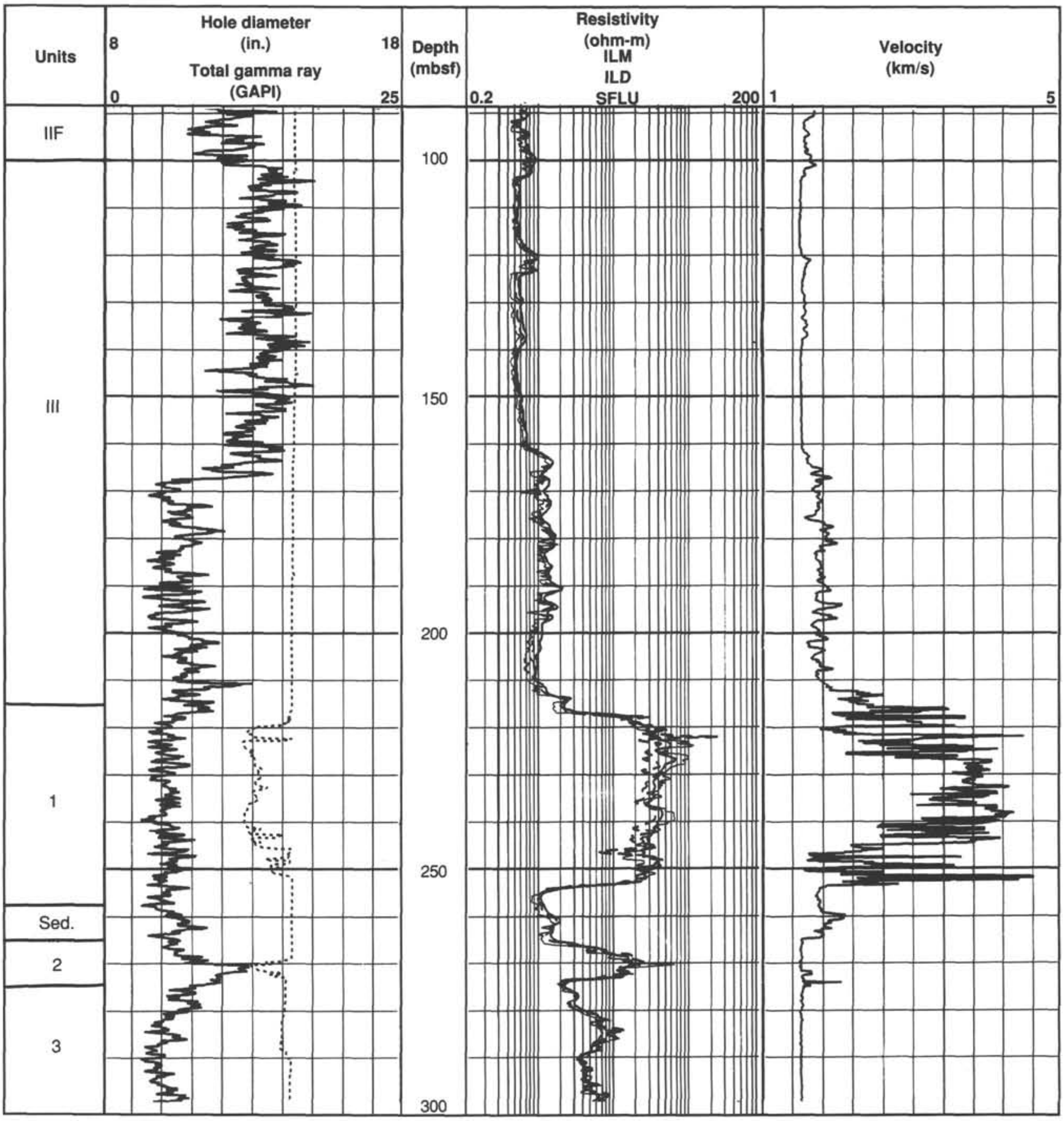

Figure 65. Seismic stratigraphic tool-string logs vs. depth (mbsf), Hole 839A. The logs illustrated are as follows: total gamma ray (SGR, in American Petroleum Institute [API] units), caliper hole diameter (in inches), sonic velocity, and medium (ILM), deep (ILD), and spherically focused (SFLU) resistivity (on a logarithmic scale). Lithostratigraphic and igneous units are given to the left of the log curves.

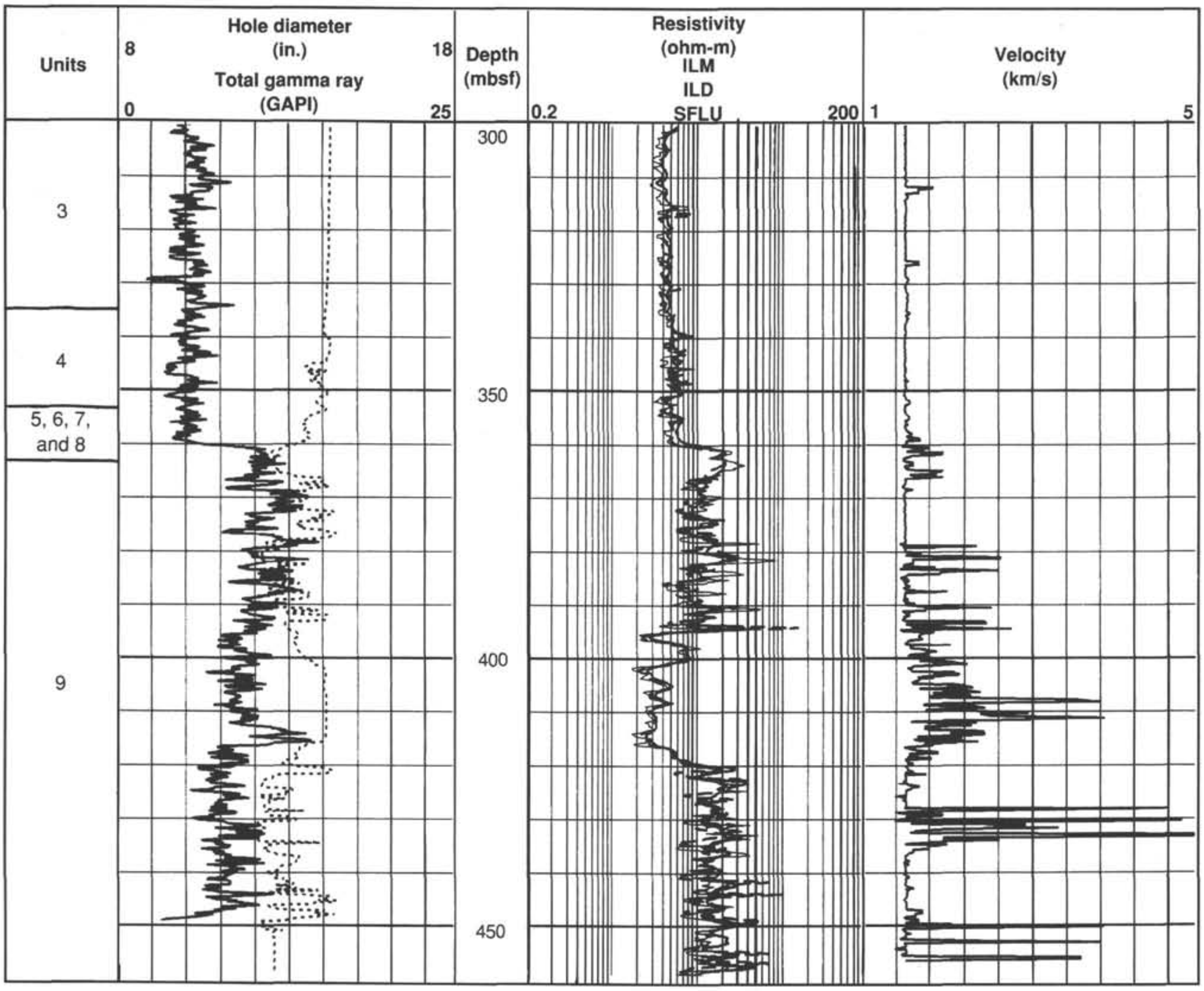

Figure 65 (continued).

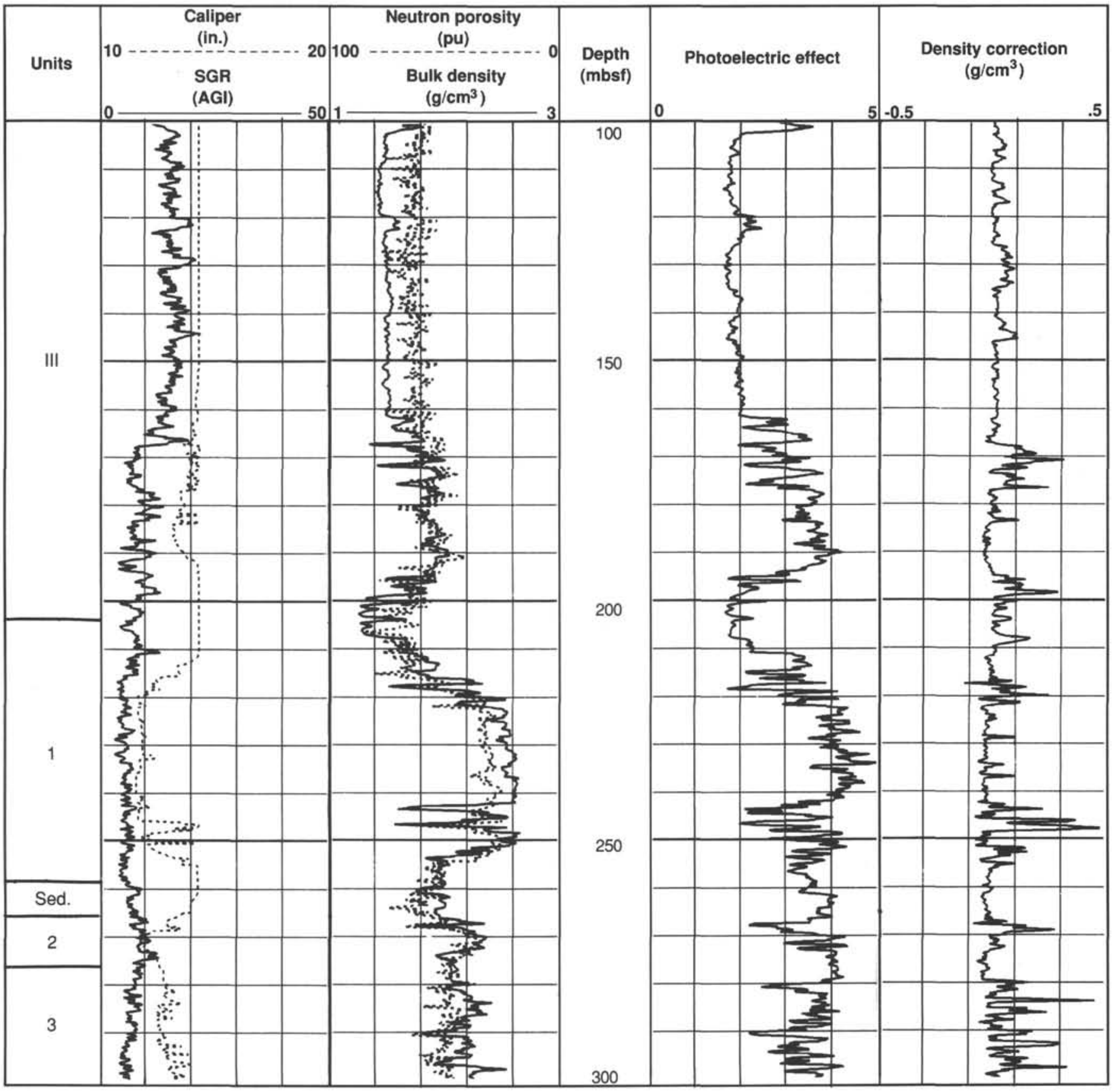

Figure 66. Lithoporosity tool-string logs vs. depth, Hole 839A. The logs illustrated are as follows: total gamma ray (SGR, in American Petroleum Institute [API] units), caliper hole diameter (in inches); density compensation (DRHO), bulk density (RHOB), neutron porosity (NPHI), and photoelectric effect (PEF, in barns/electrons). Lithostratigraphic and igneous units are given to the left of the log curves.

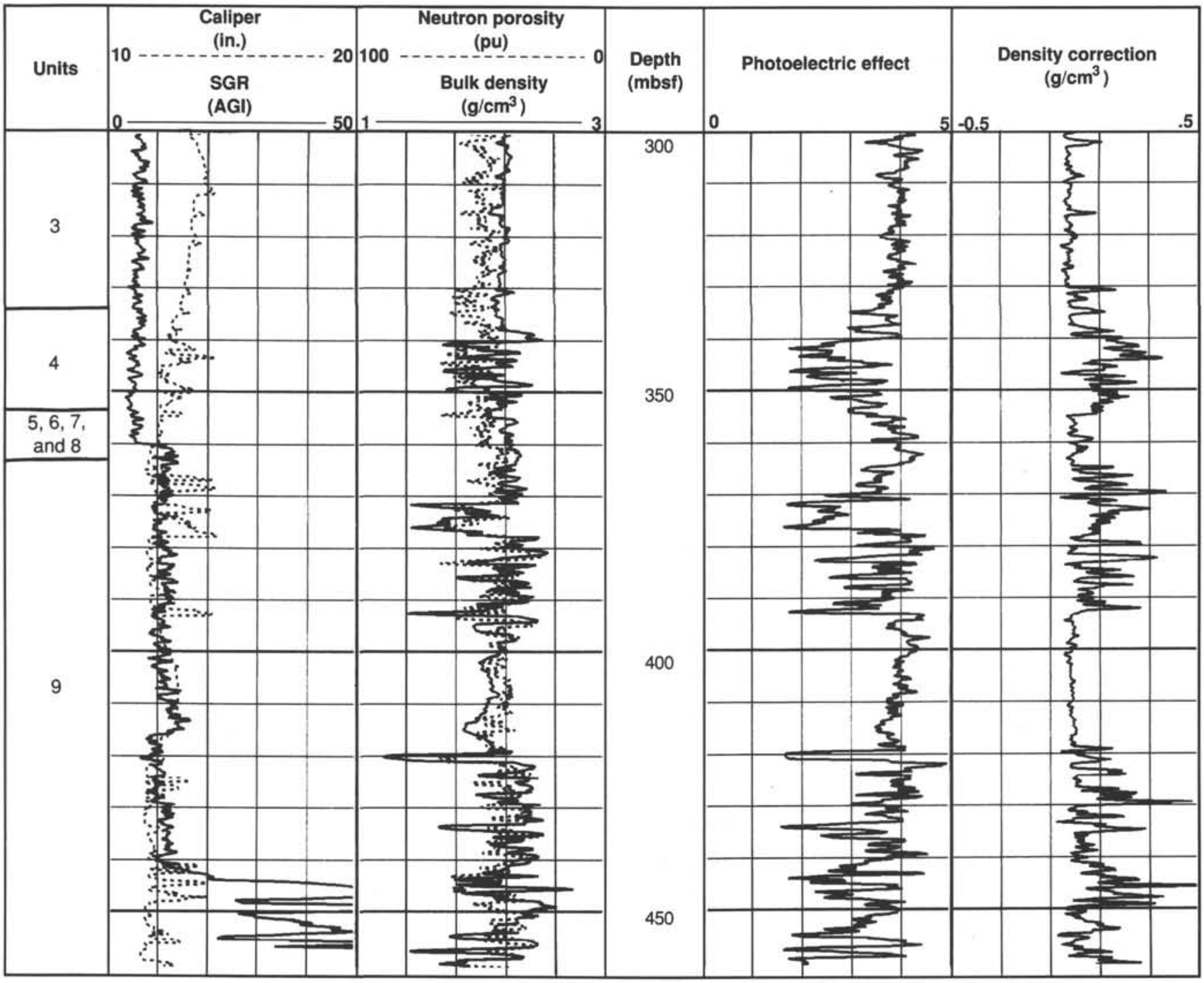

Figure 66 (continued).

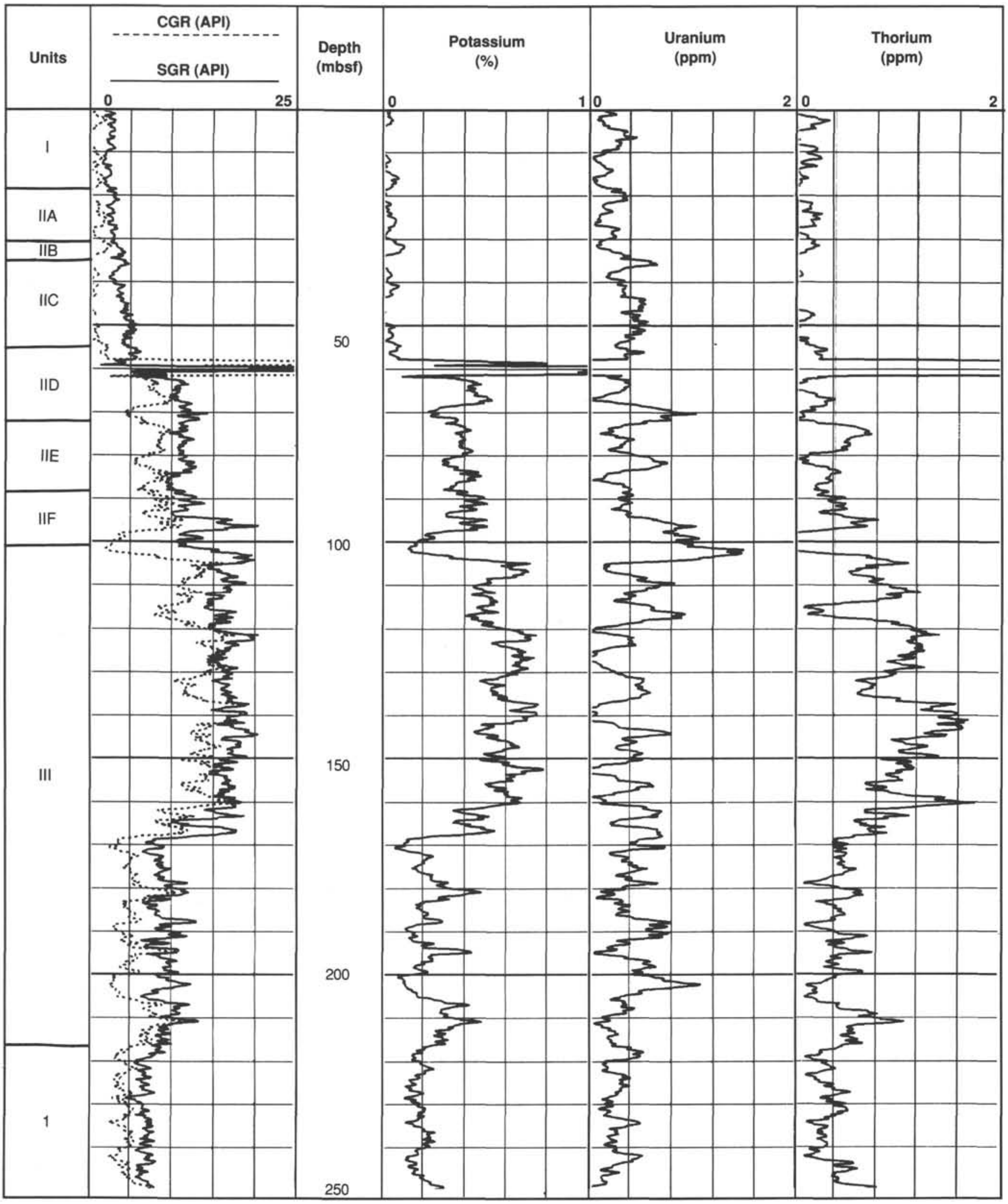

Figure 67. Natural gamma-ray intensity from the geochemical tool string vs. depth, Hole 839A. The logs illustrated are as follows: total gamma ray (SGR, in American Petroleum Institute [API] units), computed gamma ray (CGR, in API units) thorium, uranium, and potassium. Lithostratigraphic and igneous units are given to the left of the log curves.

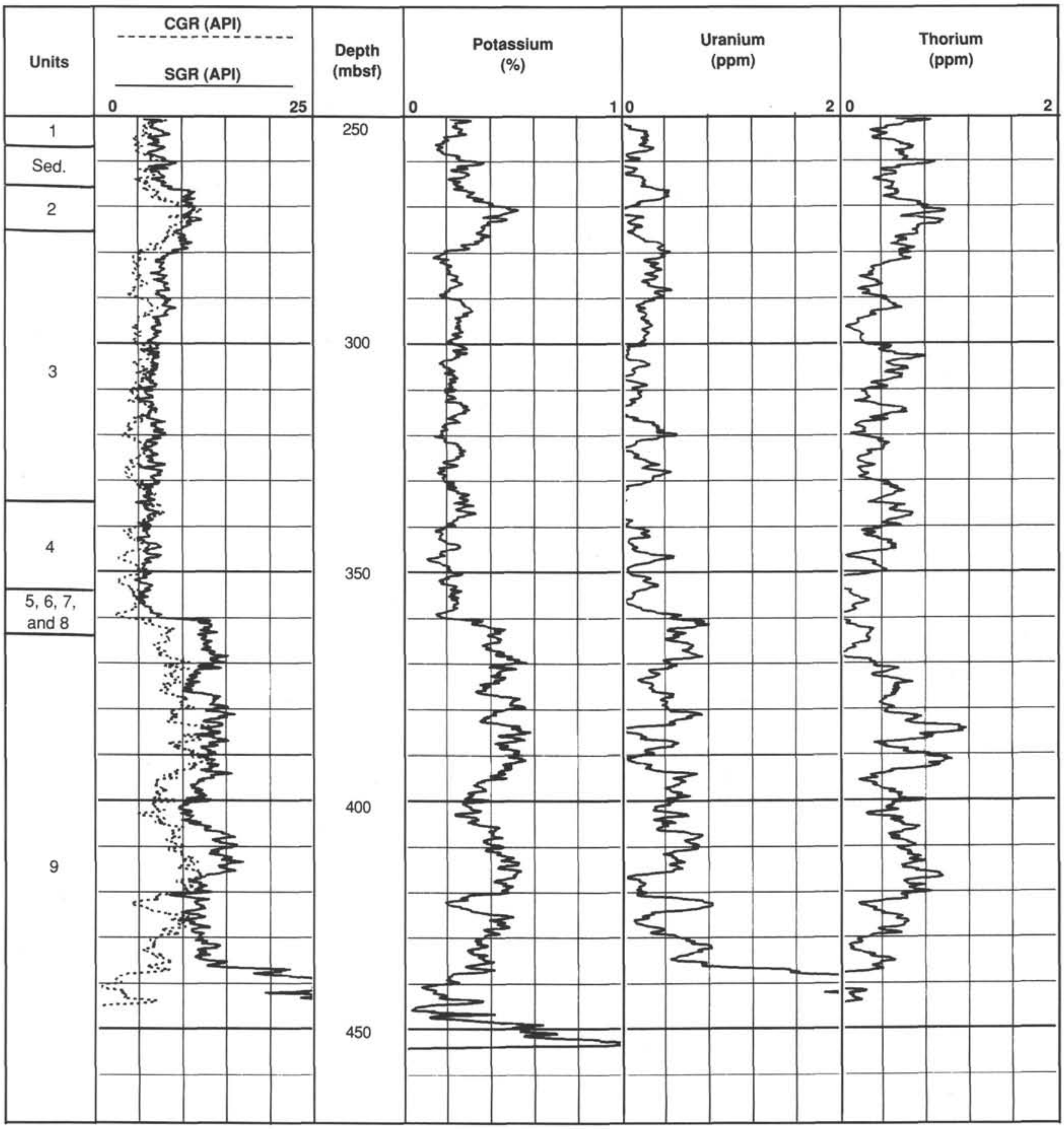

Figure 67 (continued).

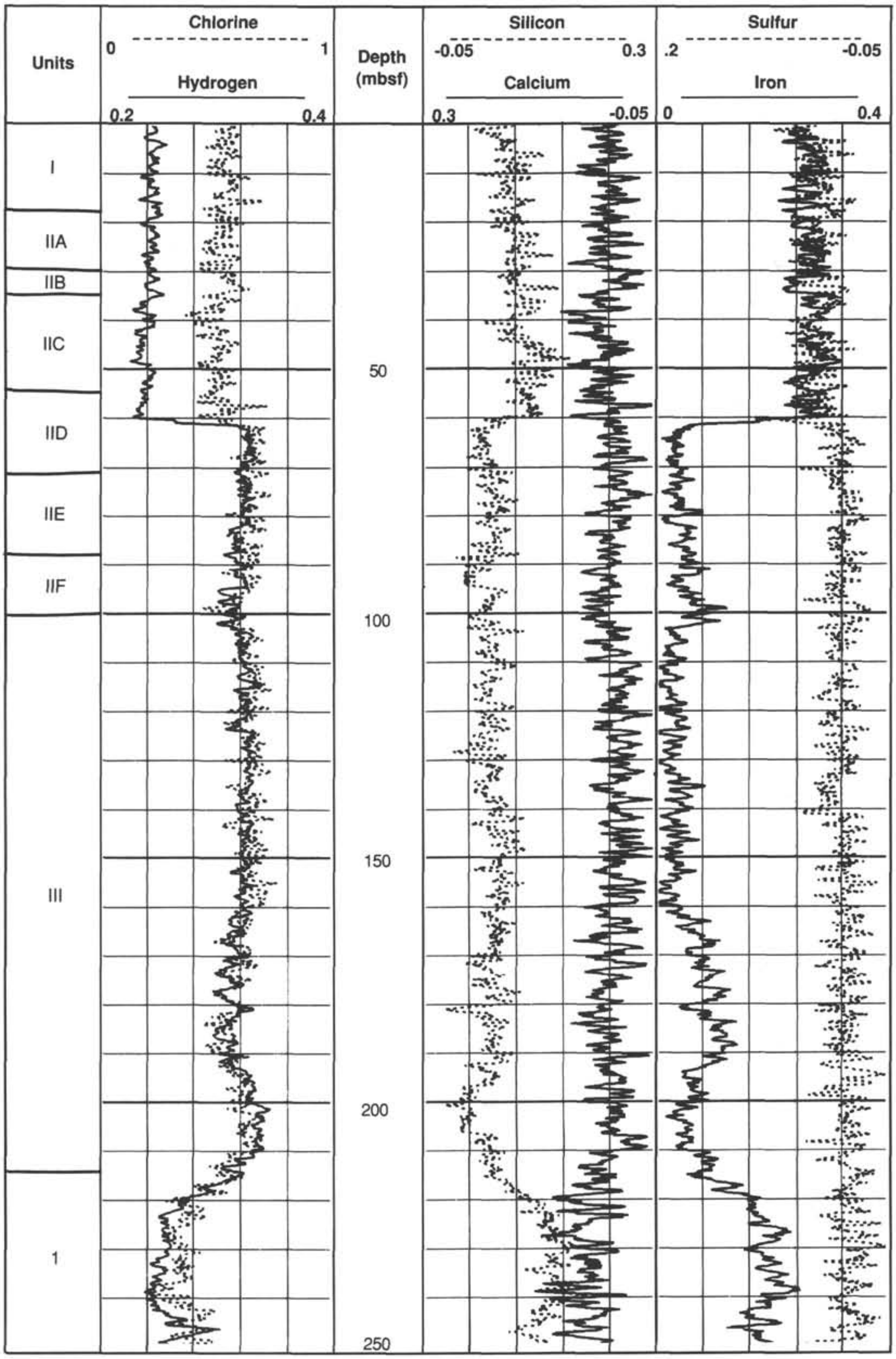

Figure 68. Geochemical yield logs vs. depth, Hole 839A. The logs illustrated are as follows: calcium, silicon, iron, sulfur, hydrogen, and chlorine. Lithostratigraphic and igneous units are given to the left of the log curves.

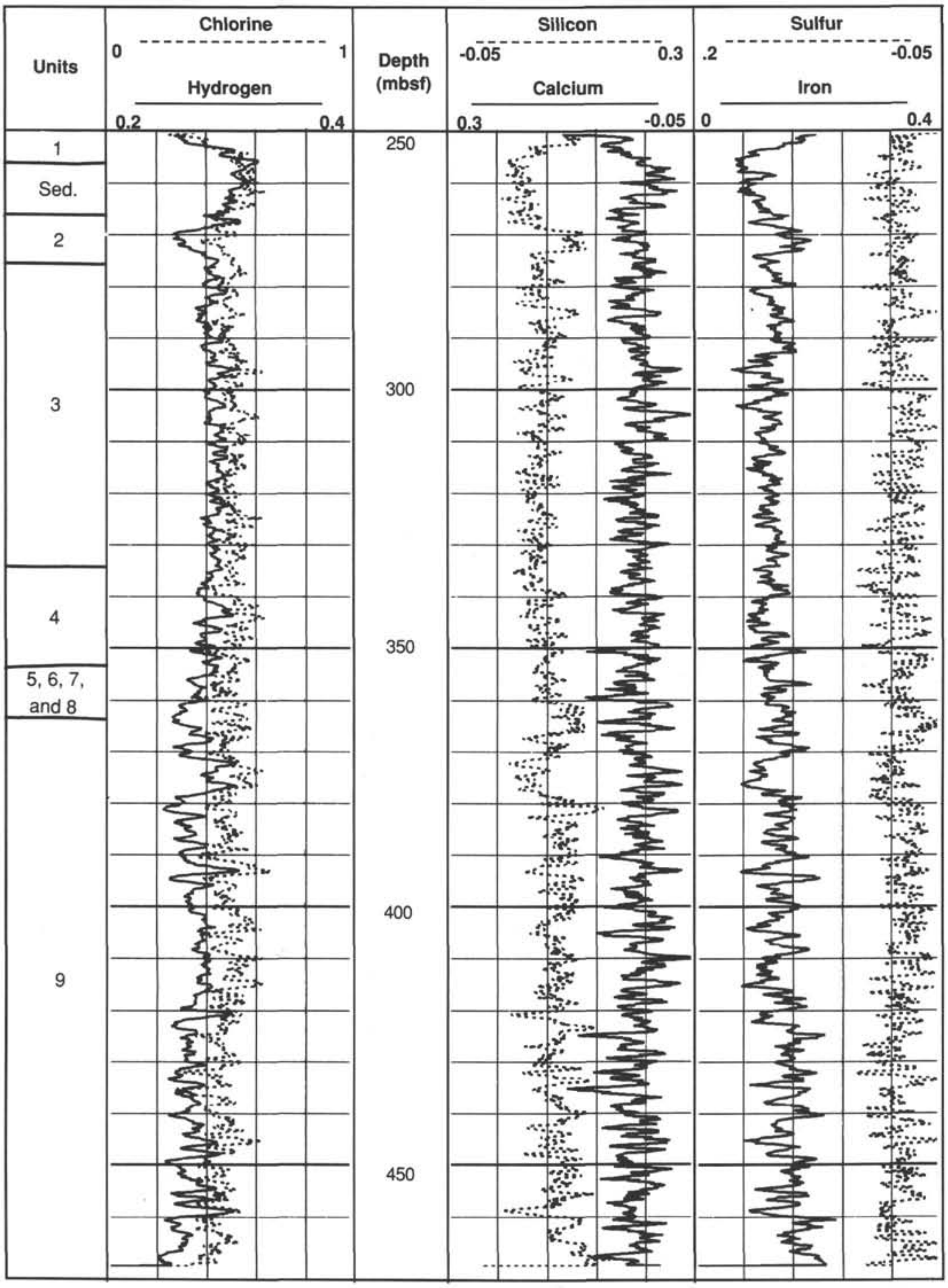

Figure 68 (continued).

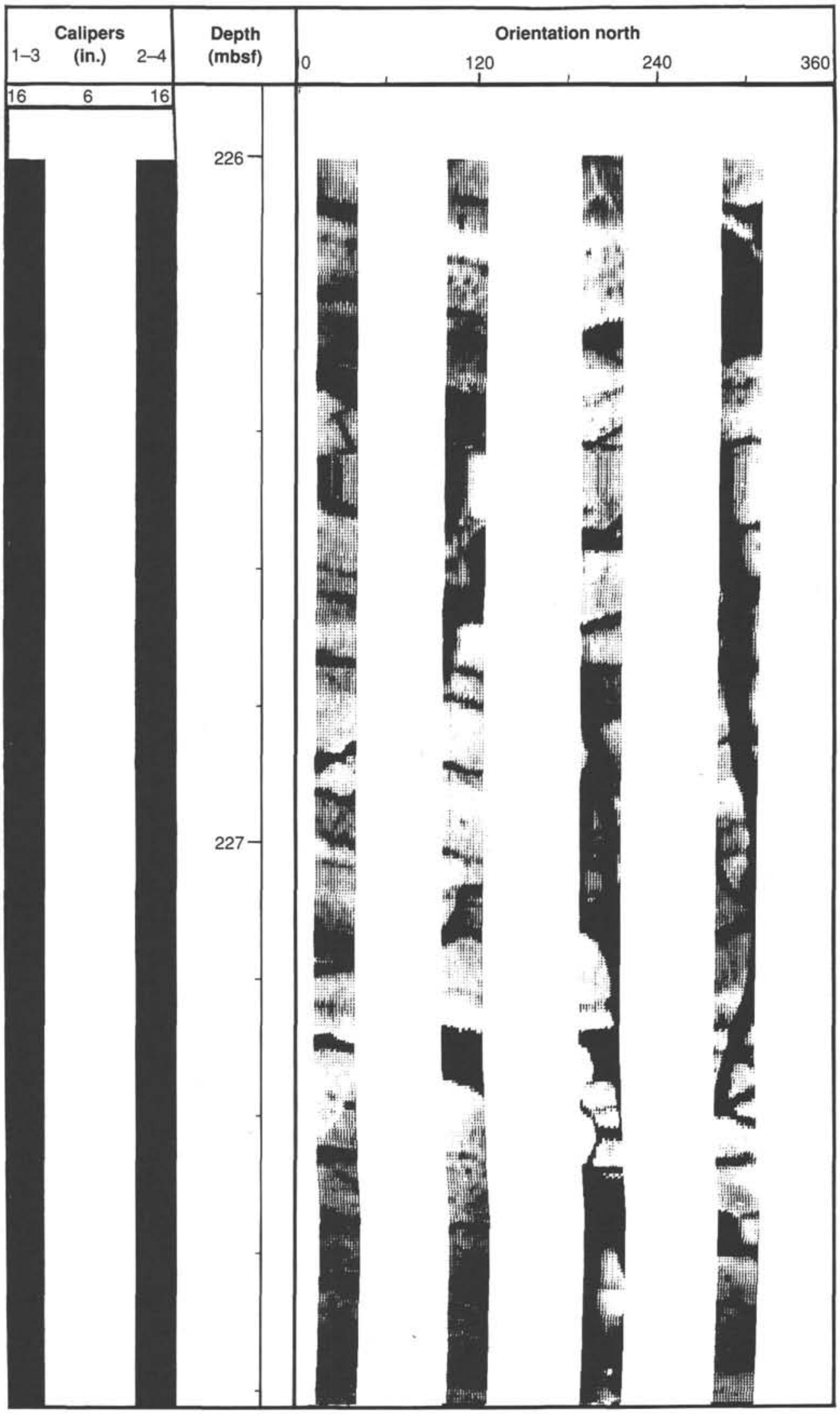

Figure 69. Formation microscanner images from 226 to 227 mbsf illustrating vertical and horizontal fractures. The horizontal to vertical ratio is 1:1. The FMS caliper log is shown to the left of the FMS image.

Hole 839B: Resistivity-Natural Gamma Ray Log Summary

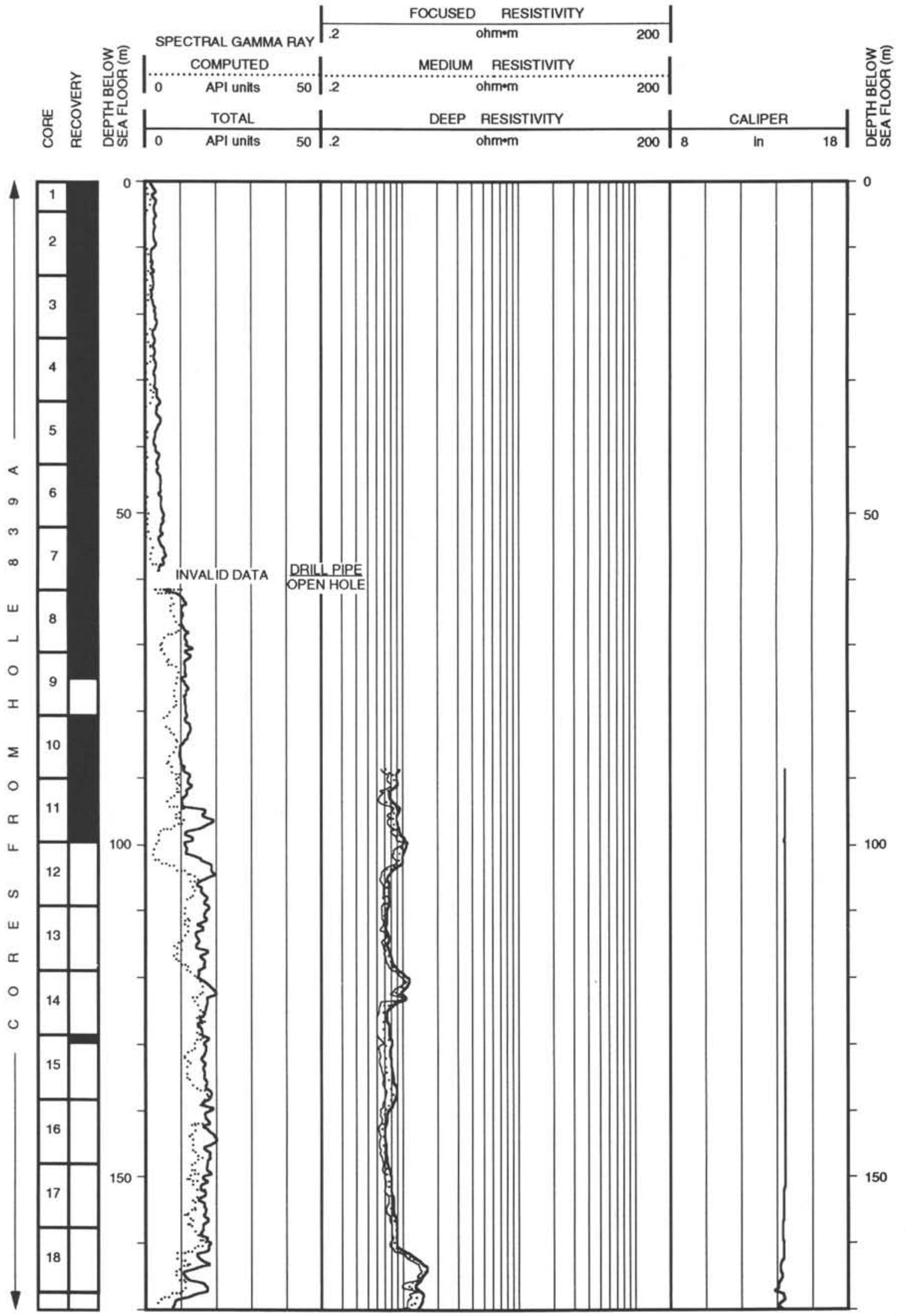

Hole 839B: Resistivity-Natural Gamma Ray Log Summary (continued)

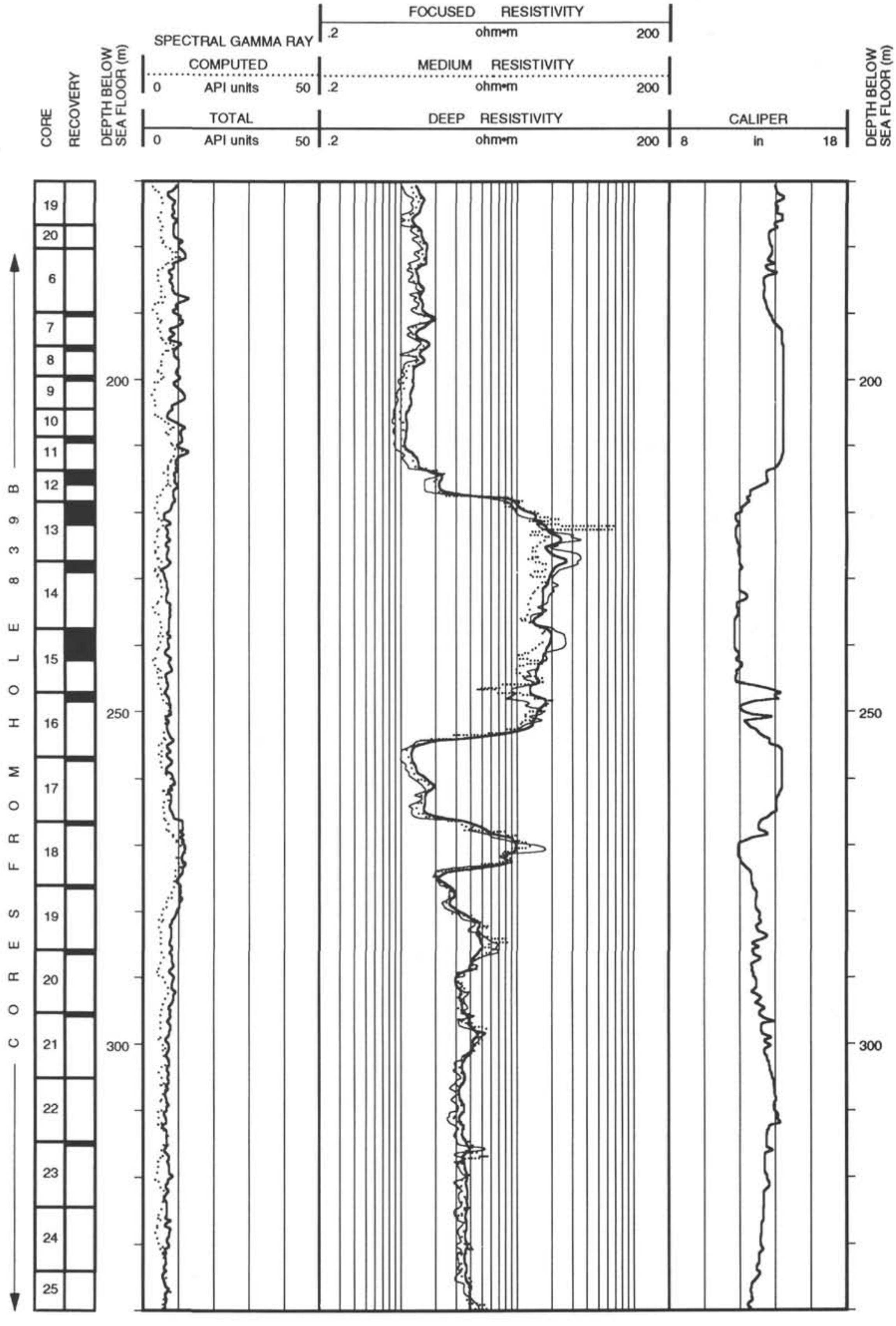

Hole 839B: Resistivity-Natural Gamma Ray Log Summary (continued)

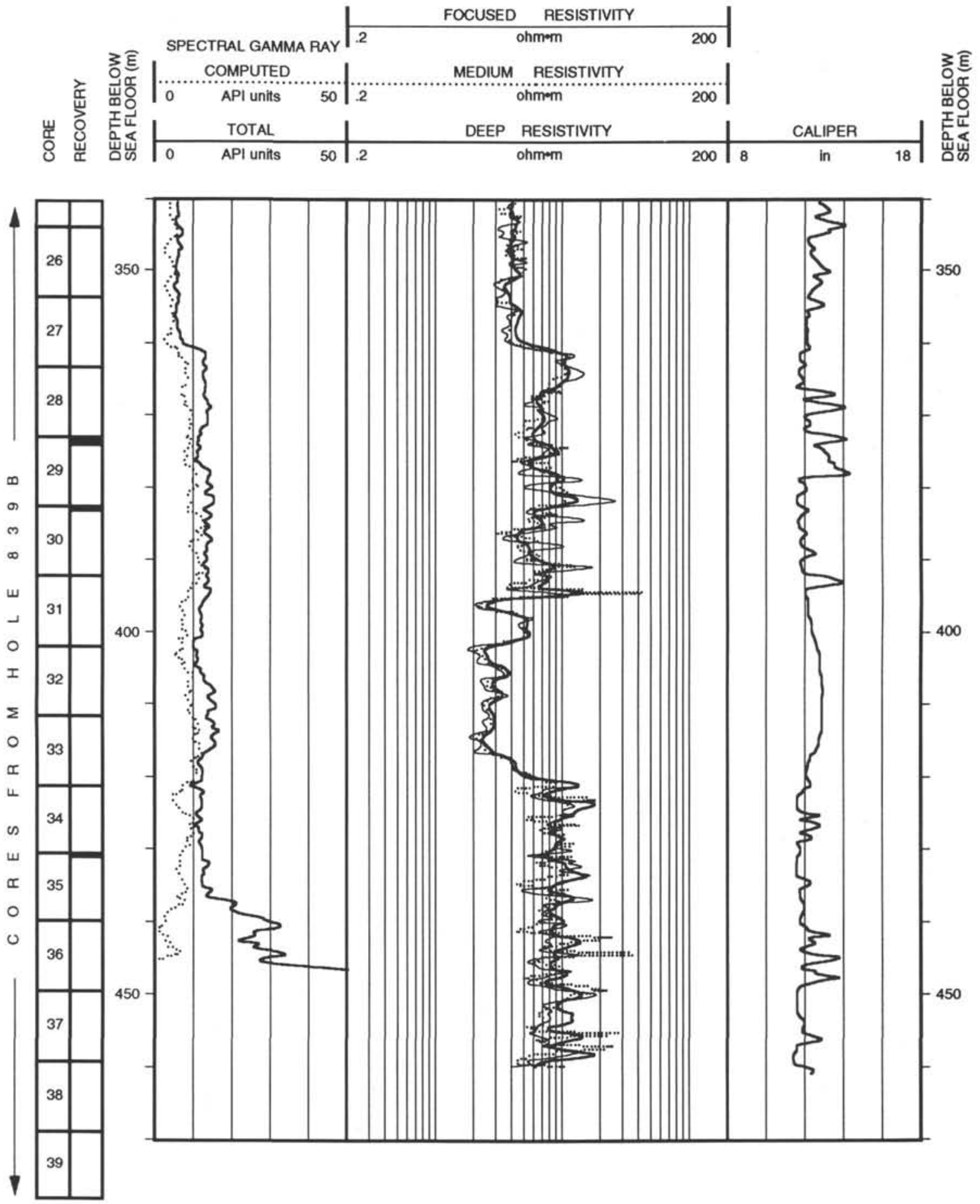

Hole 839B: Density-Natural Gamma Ray Log Summary

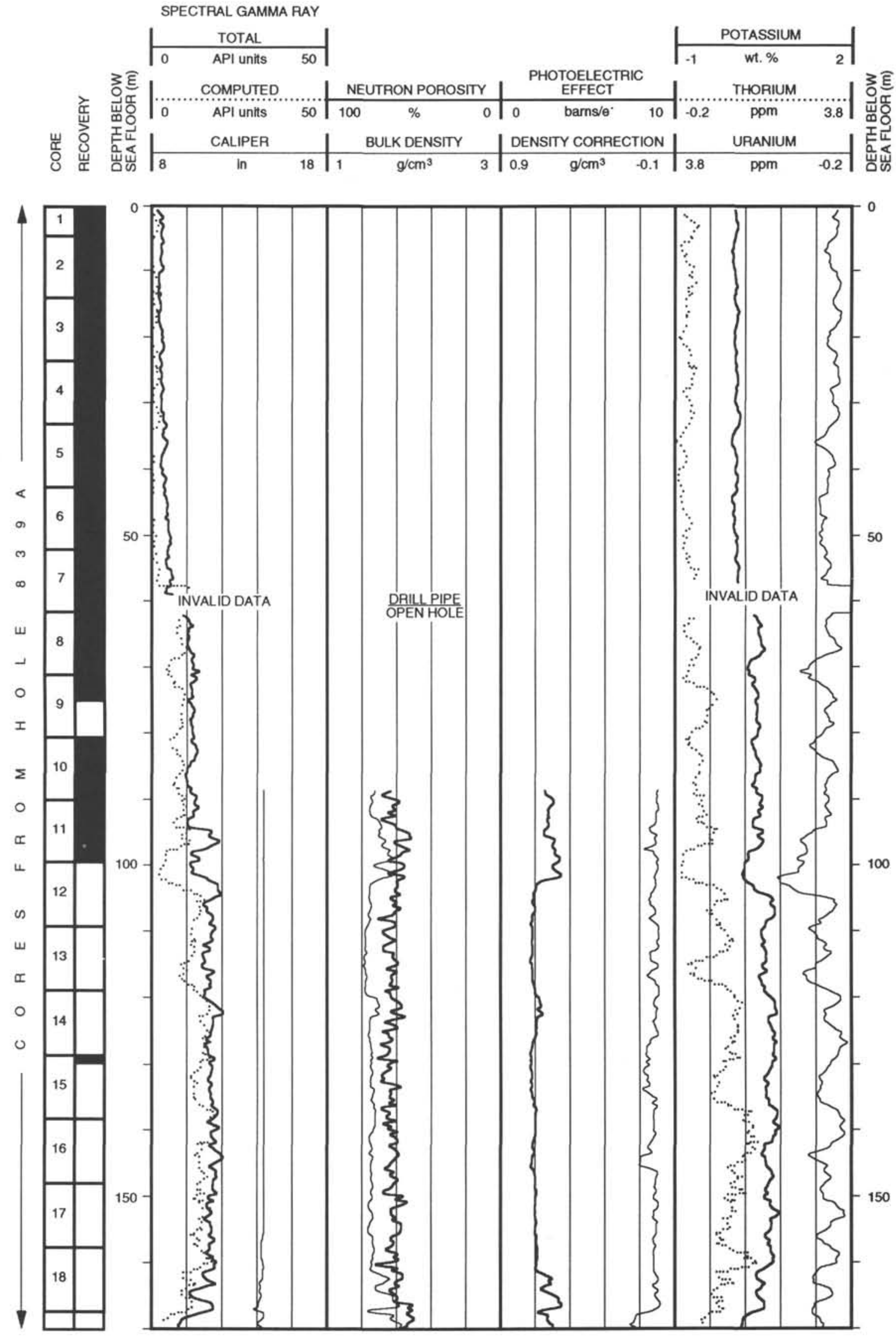

Hole 839B: Density-Natural Gamma Ray Log Summary (continued)

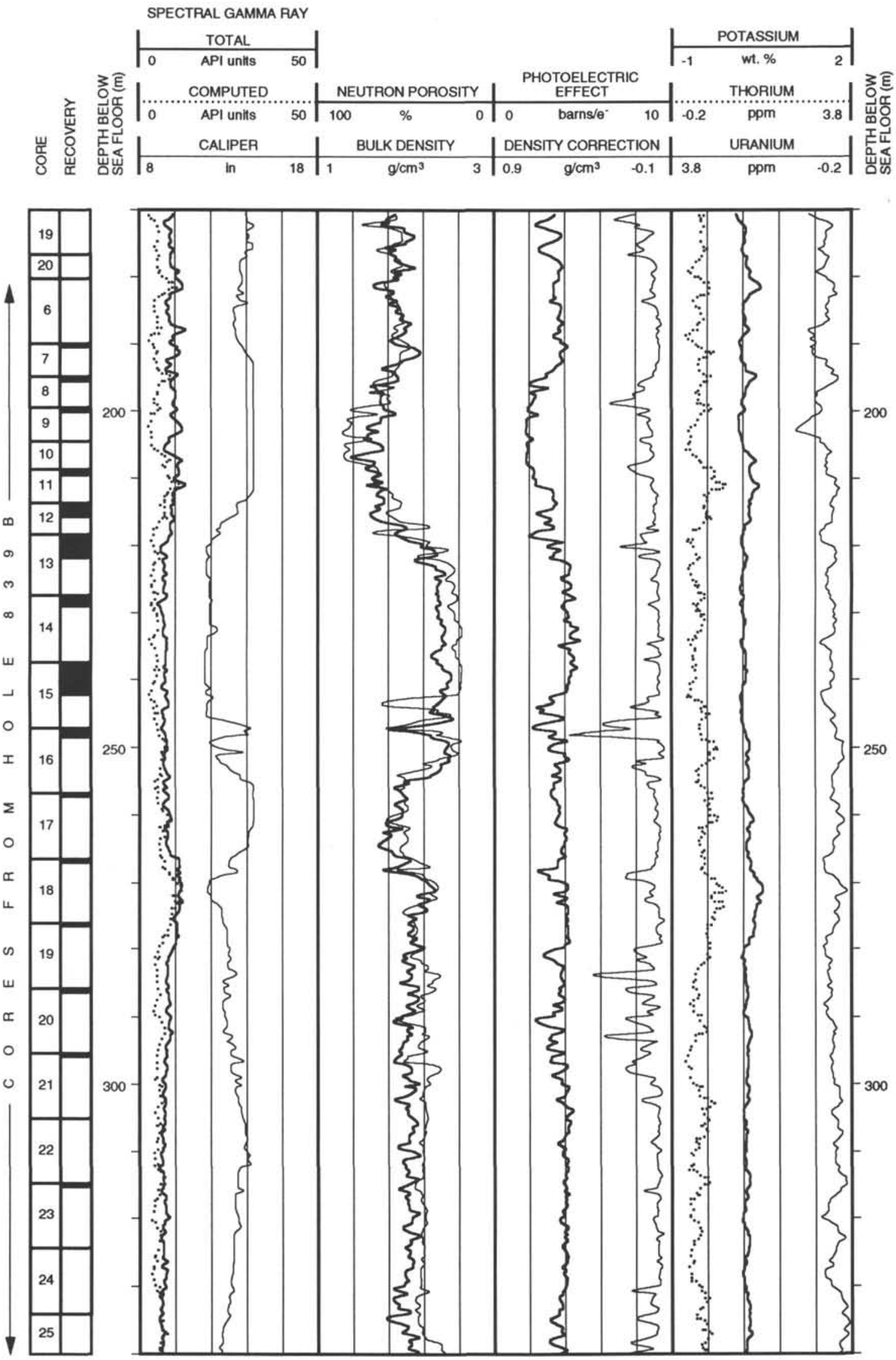

Hole 839B: Density-Natural Gamma Ray Log Summary (continued)

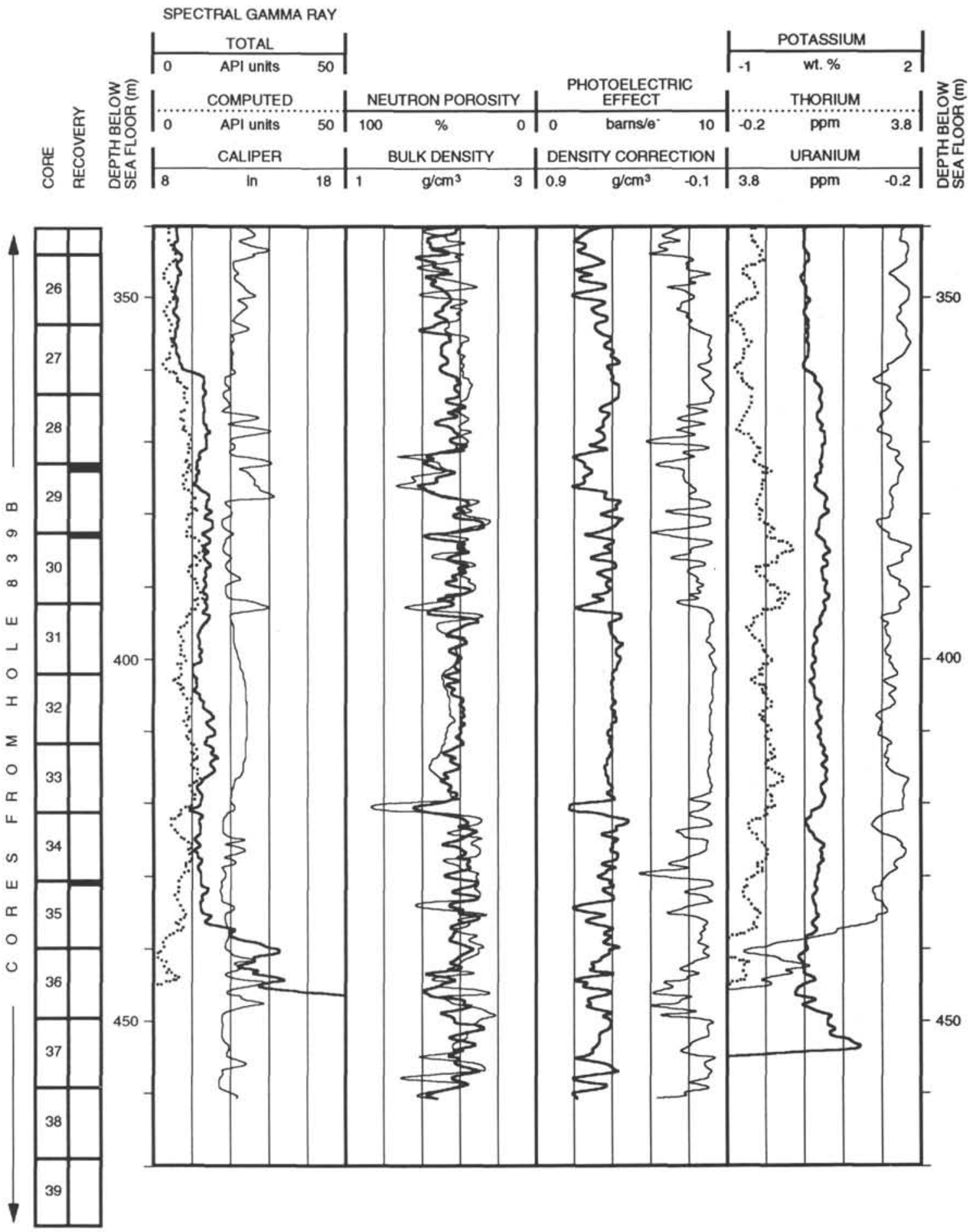

Hole 839B: Geochemical Log Summary

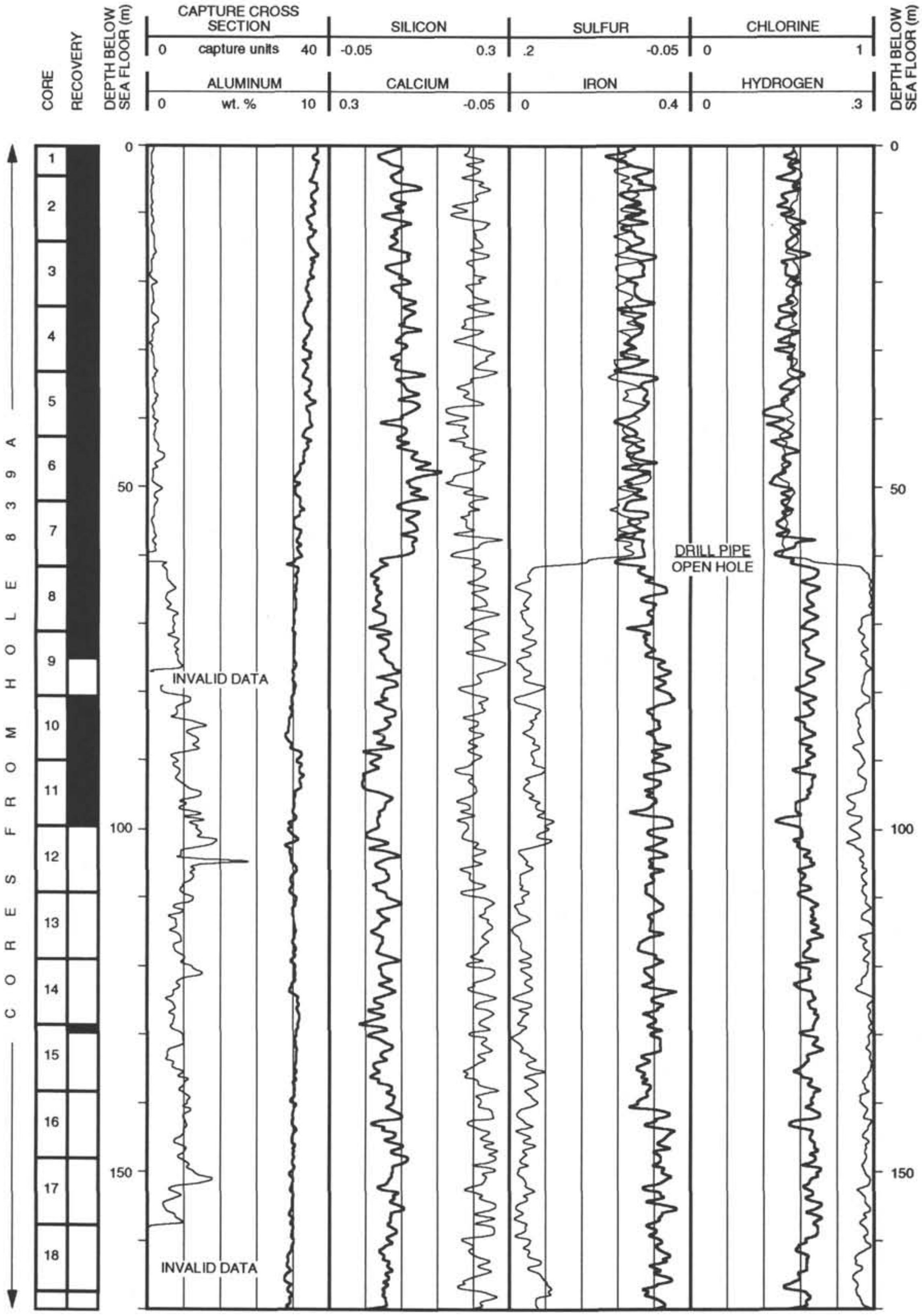

Hole 839B: Geochemical Log Summary (continued)

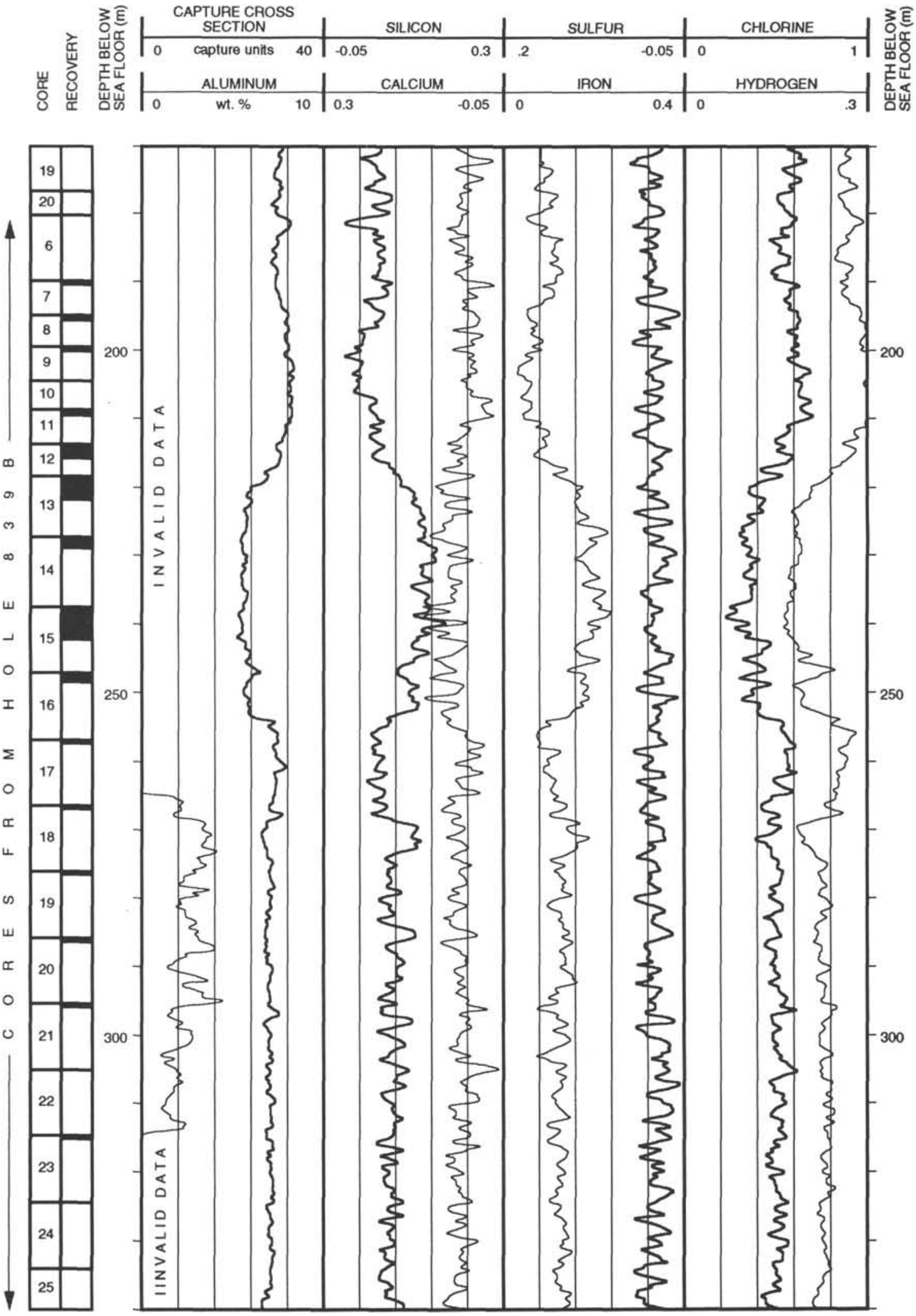

Hole 839B: Geochemical Log Summary (continued)